Striated domains in biological model membranes

AFM and computer simulation studies of lipid bilayers and the model peptide WALP

Yarrow, F.
Ph.D. thesis, Utrecht University, May 2009
Met een samenvatting in het Nederlands
Printed by Ponsen & Looijen B.V.

ISBN 978-90-393-5063-8

Striated domains in biological model membranes

AFM and computer simulation studies of lipid bilayers and the model peptide WALP

Gestreepte domeinen in biologische modelmembranen

Een AFM en computer simulatie studie van lipide bilagen en het modelpeptide WALP

(met een samenvatting in het Nederlands)

Proefschrift

ter verkrijging van de graad van doctor aan de Universiteit Utrecht op gezag van de rector magnificus, prof. dr. J.C. Stoof, ingevolge het besluit van het college voor promoties in het openbaar te verdedigen op woensdag 10 juni 2009 des ochtends te 10.30 uur

door

Fiona Yarrow

geboren op 11 mei 1973 te Delft

Promotor: Prof. dr. J.P.J.M. van der Eerden

This thesis was accomplished with financial support from the Dutch Organization for Scientific Research (NWO)

Contents

Chapter 1

Introduction

1.1 Self-assembly and biomembranes

Self-assembly of mixed systems into ordered patterns has attracted a lot of attention during the last decade. Miniaturization of technological devices requires new production methods. In that perspective, spontaneous assembly of the separate components is attractive because of its simplicity and low cost [1]. Research into self-organization in 2-dimensional, nanoscale systems has been motivated by the desire to determine the physical parameters necessary for the formation of such regular structures [1, 2]. One of the best examples of self-assembly is found in nature, where the biomembranes present in each living organism are largely held together by non-covalent forces [3, 4]. Moreover, many biological processes that are essential for their functioning are self-regulated through a complicated interplay of effects involving the lipid composition of the membrane. The forces governing these processes have been studied through the use of model membranes that contain a limited number of lipids and model peptides. The use of such model systems allows a more systematic approach compared to 'living' membranes, as these generally contain a large number of different types of lipid and large, complex proteins. Understanding the nature of the interactions in model membranes does not only help to elucidate biophysical aspects, but can also lead to technological improvements. A good example of this is the development of electronic and optical devices based on biologically relevant molecules [5 - 8].

This thesis focuses on a special case of self-assembly, *i.e*. the spontaneous formation of microdomains with a striated appearance in model biomembranes in the presence of the model peptide WALP23. Better insight into lipid-mediated peptide-peptide interactions can be obtained by studying the conditions under which these domains are formed. In this thesis, Atomic Force Microscopy (AFM) and coarse-grained computer simulations are used to study these striated domains. The remainder of this chapter will describe some general properties of biological membranes and the relevant parameters that determine their organization (sections 1.1.a and b), followed by a more specific overview of the striated domains (section 1.1.c). The techniques of AFM and computer simulation and their application to biological systems will be introduced in sections 1.2 and 1.3, respectively. A detailed outline of the remainder of the work in this thesis can be found in section 1.4.

1.1.a Biomembranes

Lipids

Biomembranes envelope all cells in living organisms and form a semi-permeable barrier, while giving structure to the cells. These membranes organize in a highly complex manner and consist mainly of lipids and proteins, as depicted in Fig. 1.1. A diversity of lipids can be found in biological membranes. They are characterized by the presence of a polar and a non-polar part, but large variations are found in their exact chemical composition. The most

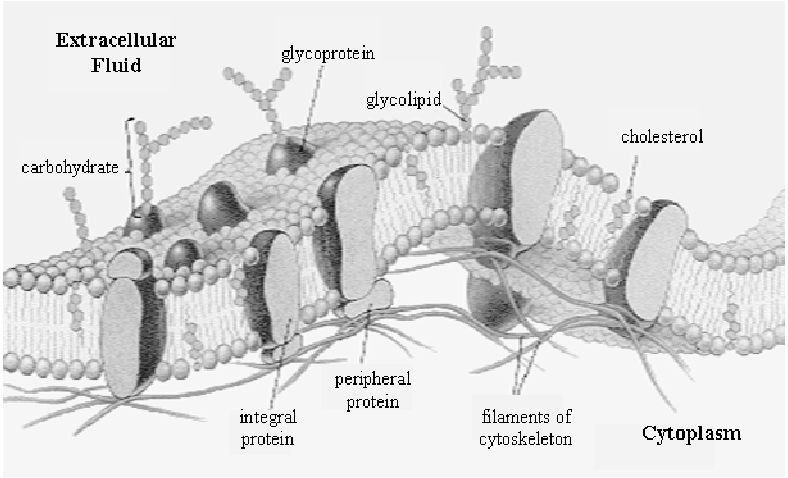

Fig. 1.1 Artist's impression of a biological membrane containing lipids and proteins. The lipids are depicted schematically by a spherical polar group and two tails [9]

abundant class of lipids found in animal-cell membranes is that of the diacyl-glycerophospholipids [3]. They have two apolar hydrocarbon tails linked to the 1 and 2 position of a glycerol (1,2,3-propanetriol) backbone. These fatty-acid chains can vary in length and degree of saturation. The 3-position of the glycerol is linked to a polar phosphate moiety. The nature of the polar groups can vary, but the zwitterionic phosphatidylcholine (PC, see Fig. 1.2.a) and phosphatidylethanolamine (PE) groups are the most common [3, 4]. Sphingolipids and sterols are two main lipid classes with a backbone different from glycerol (see Fig. 1.2.b).
The amphiphatic character of the lipids generally leads to the formation of different assembled structures in aqueous environments, such as vesicles (also called liposomes), micelles and lamellar bilayers (see Fig. 1.3 [10]). The polar groups are on the outside of the layer and are in contact with the aqueous environment, while the hydrophobic acyl chains are shielded in the interior. Membranes are organized as bilayers. The lipid acyl chains (or tails) in this structure tend to pack together closely in order to maximize their mutual Van der Waals interactions [3, 4].

Phase behaviour of lipids

The detailed mechanical and structural properties of the bilayer as a whole depend on the exact nature of the lipids and their physical state [3, 10 - 13]. Lipid bilayers are known to exhibit extensive polymorphism depending on factors such as lipid chemistry [14 - 18], temperature [14, 19 - 21], hydration [22], pH [23, 24] and the presence of certain solutes [12, 14, 25 - 27]. For example, the extensively studied DPPC (= 1,2-dipalmitoyl-*sn*-glycero-3-phosphocholine or di-16:0-PC) has been shown to form four successive thermotropic phases in its fully hydrated state. Each of these has its own characteristic properties as the stiffness of the chains decreases and the lateral and rotational motions of the molecules increase. The lamellar bilayer structure is retained. A schematic overview of these phases is shown in Fig. 1.4 [3, 10, 22, 28].

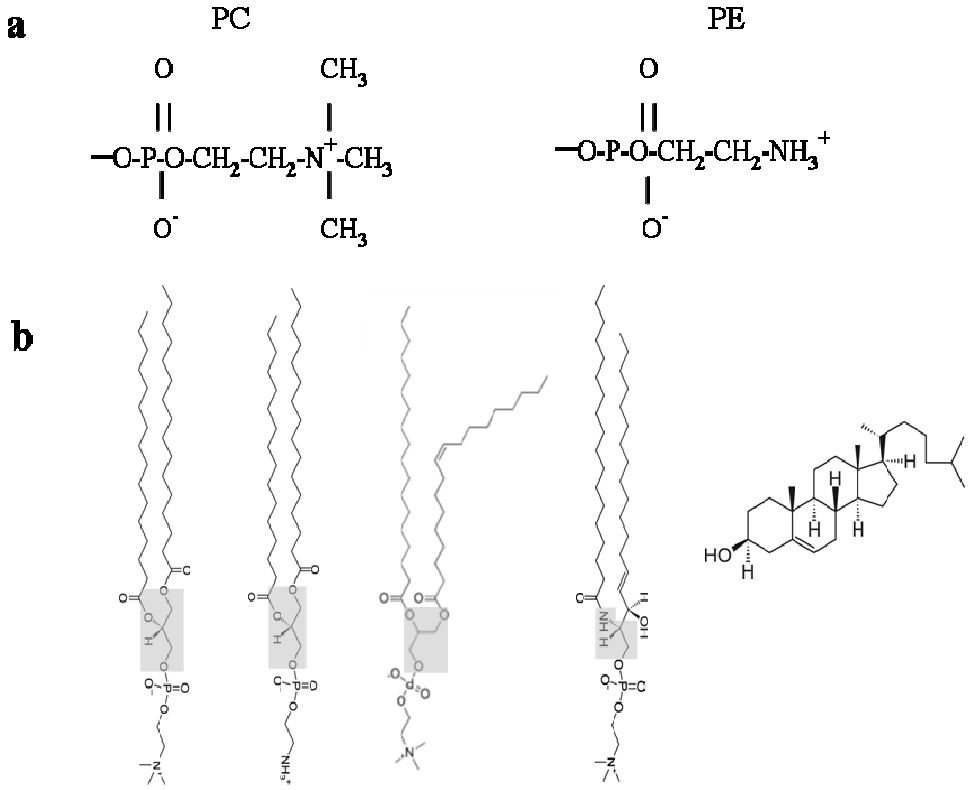

Fig. 1.2 Chemical structures of different lipids and headgroups: **a.** Phosphatidylcholine PC and phosphatidylethanolamine PE headgroup. **b.** From left to right: DPPC, DPPE, OPPC, sphingomyelin and cholesterol. The names of the first three types of lipid are derived from both the polar region and the hydrocarbon region. For example, DPPC = 1,2-dipalmitoyl-*sn*-glycero-3-phosphocholine and contains a PC headgroup, a glycerol backbone and two palmitoyl chains (16:0 with = 16 the number of carbon atoms and 0 the number of unsaturated bonds in the chain). OPPC = 1-oleyl (18:1), 2-palmitoyl-*sn*-glycero-3-phosphocholine. Sphingomyelin is a representative of the sphingosine class of lipids and cholesterol of the sterol class [3, 10]. The carbon and oxygen or nitrogen atoms making up the glycerol and sphingosine backbone are shaded in **b**

First, a crystalline, low-temperature solid phase is encountered: the subgel L_c' phase. Its hydrocarbon chains are fully extended and tightly packed in a configuration where they are tilted with respect to the bilayer normal (*z*-axis in Fig. 1.3) [19, 28 - 30]. The apostrophe ' denotes a tilted configuration of the lipid acyl chains. Almost no motions of the molecules occur [3, 19, 21, 31, 32]. Heating transforms this phase to the gel L_β' phase where the chains are packed slightly looser and slow rotational motions around the long-axis take place [28]. A phase with a corrugated, sawtooth appearance (ripple or P_β' phase) is formed above the pre-transition temperature ($T_{pre,DPPC}$ = 34 - 35 ˚C [19,

21, 29, 33 - 35]), while further heating transforms this into the fluid or liquid-crystalline L_α phase at the main transition temperature T_M ($T_{M,DPPC}$ = 41.4 - 41.5 ˚C [21, 29, 33]). The chains become fully disordered when the chain isomerism changes from a predominantly *trans*-state to one with a substantial number of *gauche*-kinks [34, 36, 37]. Both lateral and rotational diffusion are high. The chain disordering is accompanied by an expansion of the in-plane area [38, 39] and a concomitant decrease in the thickness of the bilayer [40]. Obviously, the much looser packing of the chains in the L_α phase gives rise to different collective membrane properties than the stiff gel L_β' phase [29, 37].

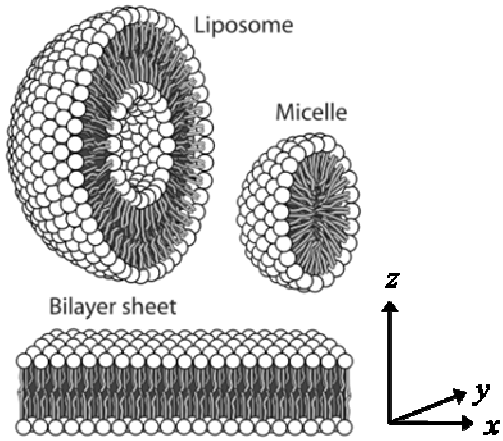

Fig. 1.3 Lipid structures formed in aqueous environments: a liposome (or vesicle), a micelle and a lamellar bilayer [41]. The lipid polar groups are depicted by white spheres and the hydrocarbon chains in grey. The apolar hydrocarbon chains are shielded from the aqueous phase in all structures

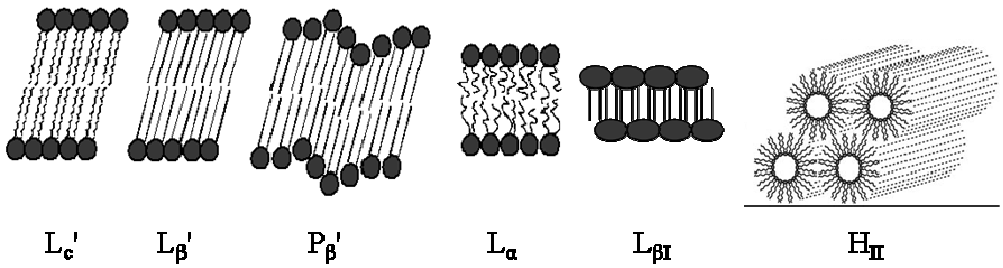

Fig. 1.4 Different lipid phases. From left to right: the subgel L_c', gel L_β', ripple P_β', liquid-crystalline or fluid L_α, interdigitated $L_{\beta I}$ and the non-lamellar inverted hexagonal H_{II} phase, where the lipid headgroups are located on the inside of the tubular structure [3, 10]

Additional phases can be encountered when chemical changes in the polar or hydrocarbon region [12, 17, 42, 43] of the lipids take place or in the presence of organic solvents [25, 26, 44, 45]. Replacement of the PC headgroup by PE leads to a conversion of the tilted L_{β}' to a non-tilted gel L_{β} phase [46, 47], while ethanol can induce an overlap of the hydrocarbon chains of opposing leaflets of the bilayer: the interdigitated $L_{\beta I}$ phase (Fig. 1.4) [25, 26]. Addition of bulky cholesterol molecules induces microdomains ('rafts') with an enlarged thickness in otherwise fluid bilayers. The lipids in these domains adopt the liquid-ordered L_o phase, where the fluid chains are more ordered than in the regular L_{α} phase [3, 48]. Finally, unsaturated PE lipids have a large propensity for highly-curved phases and can organize in the 3-dimensional inverted hexagonal H_{II} (Fig. 1.4) or cubic Q_{II} phase [12, 42].

Living membranes are generally in the liquid-crystalline L_{α} phase [3, 29], but lipids with a different phase-preference are frequently encountered. Their presence provides a mechanism through which membrane properties can be adapted to suit different biological purposes. For example, the presence of H_{II} -preferring ('non-bilayer') lipids in a lamellar bilayer is believed to alter curvature in order to allow the formation of highly curved regions during fusion of two membranes [49 - 51]. Model membranes with a limited number of different lipids have been employed successfully to help elucidate these relationships [19, 35, 52]. The extensive studies of biologically less-relevant lipid phases, such as the gel phase, help to demonstrate the effects of lipid packing on membrane collective properties and their influence on proteins (see below). Large differences have been found for the relative lateral packing densities within the polar and/or apolar regions when the type and phase of the lipids alters. This in turn alters the collective properties of the membrane such as permeability [53], curvature and elastic properties [42, 52, 54].

Proteins

Proteins are the other main constituents of biological membranes. They fulfil the many different tasks necessary for the adequate functioning of living organisms. Some proteins catalyze biochemical reactions, while others have a role in signalling, growth or transportation, such as the oxygen-carrying haemoglobin. Highly specific proteins (antibodies) help to eliminate foreign viruses and bacteria [4, 55].

Proteins are built up from a number of covalently linked amino acids with different chemical structures. Generally, they are large, complex structures containing a number of separate structural sub-units. Shifts in the relative positions of these units can alter the functioning of the protein as a whole [13, 57]. Association of proteins with the bilayer can occur in an orientation parallel or perpendicular to the bilayer surface. The former type is called peripheral, whereas the latter is known as integral or transmembrane (TM, see Fig. 1.1) [4, 56, 58].

Small proteins, which are commonly referred to as peptides, are frequently employed as model proteins in biophysical studies of lipid-protein interactions. Natural peptides, such as gramicidin [57, 59, 60], as well as synthetic peptides, such as WALP*m* [61 - 66] and $(LA)_{12}$ [67

- 69], have been used. The use of these latter peptides allows for a more systematic pinpointing of relevant physical factors than their oligomeric, biological counterparts do [67, 70, 71].

1.1.b Protein-lipid interactions

A number of direct and lipid-mediated interactions govern the association and distribution of proteins in membranes. Various experimental techniques have been used to study numerous aspects of lipid-protein interactions, *e.g.* NMR [72, 74], X-ray [73, 75] and neutron diffraction [12, 73], Raman scattering [36, 76], IR-spectroscopy [67, 77, 78], ESR [74, 79], DSC [14, 78, 80, 81], circular dichroism [33, 82, 83], fluorescence spectroscopy [75, 84] and various forms of microscopy [75, 85, 86]. The conformation, mode and extent of insertion, aggregation and functioning of proteins generally show great susceptibility to the surrounding lipid matrix [11, 13, 53, 57, 59, 87 - 93]. Many pore-forming proteins, *e.g.* alamethicin [79], KcsA [13] and gramicidin A [57, 59, 94, 95], are stabilized in the presence of certain types of lipid, switching them from a non-active to an active, functional state ('gating'). Lipid heterogeneity, such as raft formation, is linked to the lateral distribution of the proteins over the membrane as some proteins are targeted preferentially to certain lipid areas [48, 96]. Some proteins are known to aggregate and form 2-D crystals in membranes, such as bacteriorhodopsin [97]. Conversely, proteins themselves are more than merely passive constituents and can play an active role in affecting lipid phase behaviour, for instance by locally disordering the conformation of the lipid tails and lowering T_M [14, 98], or by changing the bilayer's tendency towards non-lamellar phases [99 - 101]. This complexity makes it difficult to fully catalogue and quantify all factors involved in the mutual relationship between proteins and the surrounding (model) bilayers.

A number of theories to explain indirect, lipid-induced protein-lipid interactions have been put forward thus far. The first and probably most cited concept is that of the hydrophobic mismatch between lipid and proteins [62, 91, 94, 102, 103], which occurs when the thickness of the hydrophobic interior of the lipid bilayer does not match that of the hydrophobic part of the protein. Evidently, this leads to the energetically unfavourable exposure of hydrophobic parts of the longer species to the surrounding aqueous environment. A variety of responses from the protein and/or lipid bilayer is aimed at minimizing this [60, 102]. The protein or peptide can change its extent or mode of association with the membrane or alter its backbone conformation or tilt [62, 83, 104], while lipids bordering the protein can locally assume a more (dis)ordered conformation [60, 94, 98]. Aggregation of the proteins will reduce the area of interfacial contact between the lipids and proteins [86, 105, 106]. Additionally, proteins may become regionalized when they localize preferentially in the best-matching parts of inhomogeneous membranes [48, 71]. A number of proteins reach their optimal activity or insertion efficiency in situations where they are closely matched to the lipids [84, 87, 107].

Nevertheless, other mechanisms must be operational as some proteins reside in the less tightly packed lipid phases (*e.g.* L_α phase), irrespective of what their relative lengths dictate [69, 89,

108]. The looser lipid organization can also lead to disaggregation of proteins that are clustered in the more tightly packed gel phase [75, 88, 109, 110].

Another relevant parameter put forward in literature is the intrinsic radius of curvature of the membrane. This can be correlated with the molecular shape of the constituting lipids [111] and depends on the type and physical state of the lipids [57, 92, 112]. For example, the large projected area of the acyl chains on the *xy*-plane and small headgroup give POPE (di-18:1-PE) an overall conical shape, while the smaller acyl-chain area of DPPC (di-16:0-PC) gives it a more cylindrical shape. Highly curved structures are favoured when POPE molecules are packed together in a layer, whereas DPPC lipids pack into flat layers [11, 12, 52, 113]. Proteins respond to alterations in curvature stress (*i.e.* stress resulting from forcing two monolayers with a certain intrinsic curvature into a bilayer) through their extent of oligomerization [57], functioning and insertion topology [13, 79, 114].
A related concept is that of the lateral pressure within the membrane. The various regions of the bilayer each give different relative contributions to the total, net-zero pressure. The interfacial tension in the polar region generally gives a negative contribution, which is counterbalanced by positive contributions resulting from the loss of entropy of the hydrocarbon chains and the electrostatic repulsion of the headgroups [13, 51, 115]. This can be described by a depth (z)-dependent profile representing these different contributions. POPE bilayers give a different overall profile than DPPC bilayers as the more conical molecular shape of POPE alters the relative contributions of the polar and hydrocarbon region [112]. The pressure can convey itself to the incorporated proteins and can force them together mechanically [114, 116], as has been shown for the mechanosensitive channel MscL [114].

1.1.c Striated domains in lipid/WALP mixed bilayers

It is clear that structural parameters of the membrane can play a large role in determining the lateral distribution of proteins and their sub-units. In this light, the highly ordered, self-assembled striated microdomains found in mixtures of saturated PC lipids and the model peptide WALP are highly interesting. In these domains, the peptides pack together with lipids in a ~ 1:10 ratio [117]. Closer inspection of these structures can help to understand the relevant physical forces governing lateral heterogeneity in lipid-protein systems.

The synthetic peptide WALP*m* (with *m* the total number of amino acid groups, see Fig. 1.5) and its derivatives were designed to mimic one membrane-spanning structural sub-unit of a larger, multi-spanning protein. Its highly hydrophobic, α-helical core of alternating leucine (Leu or L) and alanine (Ala or A) amino acids assures insertion into the hydrophobic region of the bilayer [118]. The tryptophan (Trp or W) groups provide a stable anchor point at the interface between the polar and the hydrocarbon region [63, 119, 120]. These large aromatic anchoring groups are encountered frequently in biological proteins at this position in the membrane [56, 63, 118 - 121].
The length of the Ala-Leu stretch of WALP*m* can be varied and the Trp can be replaced with other anchoring groups. These peptides have been used to identify the responses of the

membrane and peptide to hydrophobic mismatch conditions. This includes deformation of the lipid chains in the immediate vicinity of the peptide, altered phase behaviour of the lipid bilayer, and conformational changes and aggregation of the peptide. The effect of different flanking residues on these was also studied [61, 63 - 66, 101].

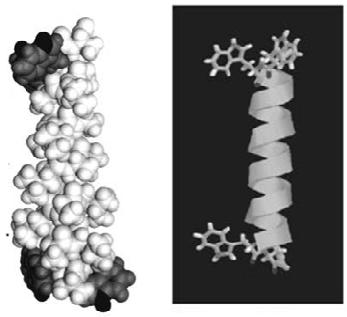

NH_2 A W W L A L A L A L A L A L A L A L W W G Ac

Fig. 1.5 Space-filling model (left) of WALP23 [149]. Tryptophan groups are represented in dark grey and other amino acid residues in white. The schematic depiction of the same WALP23 (right) [70] clearly shows the α-helical alanine-leucine centre and the large aromatic rings of the tryptophan residues. The amino acid sequence of WALP23 is given below the pictures, where A = alanine, W = tryptophan, L = leucine and G = glycine amino acid residues. Ac = acetyl group [61]

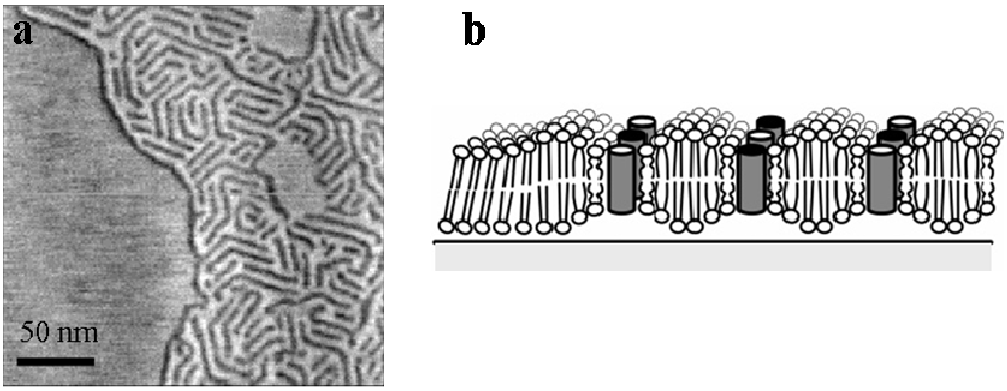

Fig. 1.6.a. AFM topograph (Contact Mode) of a striated domain in a supported DPPC bilayer with 2 mol% WALP23. The featureless grey area on the left is the unperturbed, pure DPPC bilayer. The domains consist of alternating lighter and darker lines, respectively representing higher and lower features. **b.** Schematic model of the proposed molecular organization of a striated domain [119]. The rows of grey cylinders with alternating black and white termini depict single rows of WALP23 in an anti-parallel orientation (white N terminus next to black C terminus). These correspond to the darker lines in **a**. The lipids between the rows of WALP (lighter lines in **a**) have an adjusted conformation compared to the pure DPPC bilayer (= the 3 lipid molecules on the left hand side, grey area in **a**)

The assembly of WALP into striated domains in gel-state PC lipid layers was previously investigated with AFM by Rinia *et al.* [33, 122, 123] and Ganchev *et al.* [119] and with X-ray diffraction and fluorescence spectroscopy by Sparr *et al.* [75, 110]. The repeat distance between the lines in the striated domains has a constant value of 7.5 - 8 nm. Angles of ~ 120° are formed at places where the lines change direction, reflecting the hexagonal packing of the lipid gel state. It was concluded that single lines of the shorter, perpendicular orientated WALP alternate with rows of lipids that have an increased height compared to the surrounding pure PC bilayer. These peptide and lipids rows appear as alternating dark and lighter lines in the AFM height image in Fig. 1.6.a. The lipids making up the lighter lines still have a gel-like packing, but the commonly adopted polar tilt angle of ~ 30° [19, 29, 30] of the pure DPPC phase is reduced to a much smaller angle of 6º [110]. This gives the lines an increased height with respect to the surrounding bilayer. The lipids in the immediate vicinity of the peptides have somewhat disordered hydrocarbon chains to bridge the mismatch in length that otherwise exists between the shorter peptide and longer lipid [110, 117]. A schematic representation of the proposed structure within the striated domain is given in Fig. 1.6.b. The striped ordering is thought to result from opposing tendencies of expulsion of the peptide from the tightly packed gel-phase bilayer and attractive lipid-WALP interactions [117, 124].

Remarkably, the striped structure was preserved when the tryptophan anchoring groups of WALP were replaced with other neutrally charged moieties (*i.e.* histidine at high pH, phenylalanine or tyrosine) [33]. This suggests a generic mechanism that is not dependent on chemical details. Disordering of the striated domains was observed only when a positive charge on the peptide was introduced through a charged arginine, lysine or histidine (at low pH) amino acid group [33]. Moreover, aggregation of WALP was reduced significantly upon going from the gel L_{β}' to the liquid-crystalline L_{α} phase, demonstrating the importance of the structural organization of the lipid surroundings [75, 110].

Many features of these striated domains have not yet been elucidated, such as the details of the mechanism by which they are formed and the exact response to structural changes in the lateral organization of the lipids. In this thesis, this is studied by altering various lipid characteristics, such as the phase and type of lipid. Both liquid-AFM and computer simulations are used to study the effect of these factors on the striated domains.

1.2 Atomic Force Microscopy

Atomic Force Microscopy (AFM) was introduced in 1986 by Binnig *et al*. [125]. Since then, it has become a widespread technique used in many different fields of science. AFM allows imaging of topographical features on the surface of a large variety of samples with a high horizontal and vertical resolution of ~ 0.2 and 0.02 nm, respectively, in air [126]. This resolution exceeds that of other microscopic techniques such as electron and fluorescence

microscopy [127], and is so high that the observation of separate atoms is achievable in crystalline materials [126].

1.2.a The technique of AFM

The principle of the Atomic Force Microscope is based on probing a sample surface with a sharp tip (radius typically 2 - 10 nm [127, 128]) mounted on a flexible cantilever. This cantilever deflects when features with a different height are encountered during the raster-scanning of a surface in a series of horizontal sweeps. The extent of deflection is monitored by a laser beam that reflects from the cantilever onto a position-sensitive photodiode. The position of this back-reflected light on the photodiode changes as function of deflection. This signal is then used in a feedback loop that aims to maintain a constant, preset deflection and, thus, a constant force between tip and sample. Deviations from this constant value are corrected by moving the sample, or alternatively the tip, in the vertical z-direction by means of a piezo-electrical element (see Fig. 1.7). The local height variation is reconstructed from the vertical movements and a 2-D topographic image is obtained, where higher features are depicted by a lighter colour and lower features by a darker one [125, 127, 129, 130].

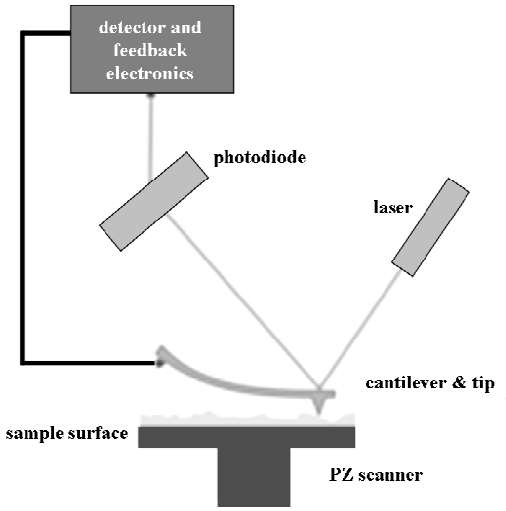

Fig. 1.7 Schematic representation of the set-up of an Atomic Force Microscope [138]. The tip scans the sample surface, while its deflection is monitored by reflecting a laser-beam of the back of the cantilever onto a position-sensitive photodiode. The piezo-electric scanner PZ is used to maintain a constant deflection of the cantilever when it encounters features with a different height on the surface of the sample

In the so-called Contact Mode, the tip is in continuous contact with the surface. Lateral and axial forces are exerted by the tip, which can deform the sample or even sweep parts away in extreme cases. Intermittent contact of the tip with the surface in the so-called Tapping Mode eliminates the lateral friction. The sinusoidal movement of the tip perpendicular to the surface

is either driven by its self-resonance frequency (AAC Mode) [125, 127, 131] or magnetically (MAC Mode) [132]. The scanning rate in Tapping Mode is much lower than in Contact Mode and the resolution for biological samples seems lower [127, 129, 133].
Relevant forces between the AFM probe and sample include electrostatic forces, Van der Waals attraction and a repulsive short-range hydration force arising from compression of the ordered water-structure around the sample [127, 133, 134].

An essential prerequisite for stable imaging is good adhesion of the sample to an underlying, solid support to prevent dislodgement of the sample. Attachment of the sample to the substrate can be either through covalent bonding or by physisorption [135, 136]. The often-used muscovite mica ($KAl_2(OH)_2AlSi_3O_{10}$ [136]) provides an atomically flat, weakly negatively charged surface that is readily cleaned before use by cleaving the layered crystal [128, 137].

1.2.b AFM and biological samples

AFM has many advantages for studying biological samples. It allows direct observation of the sample without the need for fluorescent or other labels, combined with a high spatial resolution and the ability to image under aqueous [139], and thus physiological, conditions. The soft and deformable biological samples, however, pose a limitation upon the achievable resolution. The maximal achievable resolution is lowered to ~ 0.5 nm in the lateral and ~ 0.1 nm in the vertical direction [129, 140]. Irreversible damage and deformation of the sample have to be minimized by using low scanning forces of typically a few tens to hundred pico-Newton [54, 129]. Fortunately, liquid-AFM allows for significantly lower imaging forces than AFM in air where ~ 1 nN is the limit due to capillary forces acting on the tip [127, 129, 141]. Damage of the sample can be further minimized by fine-tuning the long-range electrostatic forces between tip and sample through changes in electrolyte concentration or pH [134, 142].

One of the first applications of AFM to biological specimens was the imaging of DNA strands in air [143]. After that, innumerable studies of native proteins and supported lipid mono- and bilayers have been published [127, 130, 140, 144]. Supported planar lipid bilayers (SPBs) are more convenient to image than liposomes. SPBs exhibit many of the characteristics of free-standing membranes and are therefore regarded as good model systems [7, 145]. They can be prepared by either the Langmuir-Blodgett technique [73, 136, 137] or the vesicle fusion method [132, 136, 146, 147].
AFM on single-component SPBs of gel-state DPPC, DMPC and DPPE showed flat, smooth surfaces [26, 144, 146, 148]. Holes provided information on the thickness of the layer and confirmed the existence of a bilayer with a thin layer of water intercalated between the sample and the substrate [26, 78, 149]. Other lipid polymorphs have been imaged as well, such as the ripple $P_{\beta'}$ phase [35, 150], the interdigitated $L_{\beta I}$ phase [26, 78] and liquid-crystalline L_α phase [3, 19, 38]. Lateral heterogeneity in DPPC and DMPC bilayers was observed when the temperature was elevated and the coexistence-region between the low-temperature gel phase

and high-temperature liquid-crystalline phase was entered [151]. Microdomains were also imaged in binary and ternary bilayer systems (*e.g.* DPPC/POPC [127], DMPC/DSPC [35, 152] and cholesterol/sphingomyelin/DOPC [153]).

AFM has been also applied to native proteins, *e.g.* bacteriorhodopsin [128, 135] and cholera toxin B-oligomer [154]. The identification of separate structural sub-units and their rearrangements as response to ionic strength or force has led to valuable information on protein folding [135, 155, 156]. Ordered patterns that were formed when embedding the integral peptides gramicidin A [85] and WALP [122, 123] in SPBs could be resolved clearly by AFM. AFM, however, is a much more versatile tool. Local elastic properties and friction coefficients can be quantified [144]. Additionally, inter- and intra-protein interactions are revealed when membrane proteins are dislodged and sequentially unfolded in response to pulling with the AFM tip [130, 156]. Ganchev *et al.* [119] have demonstrated the resistance against dislodgement of the tryptophan anchoring groups of the α-helical peptide WALP when pulling it out of a phospholipid bilayer.

1.3 Computer simulations of biomembranes

Experimental techniques are indispensable in the study of model membranes and incorporated peptides or proteins. Various thermodynamic, structural and dynamical aspects have been investigated with a wide variety of techniques. On the other hand, many fundamental, collective and individual quantitative properties of the participating molecules are not accessible or have to be derived indirectly from measurable quantities. Computer simulations are employed increasingly to overcome these shortcomings [157 - 160].
Historically, two techniques of molecular simulation have been used: Molecular Dynamics (MD) and Monte Carlo (MC). Both methods make use of a chosen set of inter- and intra-particle interactions. MD is based on the calculation of particle trajectories by integrating Newton's equations of motion, whereas MC has a stochastic character without a direct temporal interpretation [160, 161]. Its dynamics are such that it calculates the same ensemble averages of system observables as MD. These observables are expressed in terms of the momenta and coordinates of all particles in the system. They correspond to macroscopic, thermodynamic quantities. Both MC and MD need some model that describes the system under study. A division can be made into atomistic models and larger-scale models that have been simplified to some extent [157, 158, 162].

1.3.a Atomistic or all-atom models

Usually, MD is used in conjunction with atomistic models to investigate the organization of lipids and, often, one membrane-associated protein, on a molecular scale [159, 160, 163, 164]. Conformation, orientation, short-time motions, as well as the insertion dynamics of transmembrane helices and pore-forming peptides (*e.g.* alamethicin, melittin, bacterio-rhodopsin, glycoporin, gramicidin A) have been studied in this way [57, 165, 166].

The atoms of the lipids and proteins are modelled explicitly, while the solvent can be represented atomically or as a continuum [158, 165]. Interactions between the atoms are represented by potential-energy expressions and the forces are calculated as gradients thereof. The intramolecular part of the potential-energy function includes terms for bonds, dihedral and torsional angles [158, 160]. The intermolecular part is usually represented by a so-called Lennard-Jones potential of the form $A / r^{12} - B / r^{6}$, which describes excluded volume effects at small inter-atom distances *r*, while allowing for a long-range attraction due to Van der Waals dispersion forces [167]. Electrostatic terms can be added [168]. The required input parameters, such as equilibrium bond distances and force constants, are usually derived from spectroscopy or quantum chemistry [160]. A reasonably accurate picture of the molecular architecture of the protein must be known beforehand, which is not always straightforward. Nowadays, many parameter sets are available commercially, such as the often-used CHARMM [169] or GROMOS [170] force fields.

Severe limitations of these atomistic simulation models are the high computational costs, restricting the simulations to small time (~ tenths of ns) and length scales (few hundred lipids and one protein; ~ tens of nm) [160, 165] that are not adequate to describe collective processes of the membrane occurring on time scales of milliseconds [157, 162]. This makes atomistic simulations unsuitable for the study of processes such as melting, membrane fusion and the formation of compositional heterogeneities such as striated domains.

1.3.b Simplified models

The restrictions mentioned above are reduced by introducing simplified models that eliminate a number of degrees of freedom [162, 171]. Essential physical parameters for the description of collective phenomena are sought to be retained, despite the unavoidable loss of chemical detail. Basically, one can distinguish between models that retain some notion of molecules and models that treat the lipid membrane purely as a continuous surface or mean field [157, 165, 172]. Collective properties such as bending rigidity, spontaneous curvature, density and surface tension are used as key parameters in the latter case [115, 158, 165, 173, 174]. In the perspective of this thesis, however, a particle-based model is required for describing the correlation between the observed striated phases and lipid structural properties.

Coarse graining by grouping several atoms into a larger effective particle (‘superatom’ or ‘bead’) reduces the degrees of freedom, while retaining part of the chemical details [171, 175, 176]. Molecules are built up by connecting different types of spherical beads, to form single chain amphiphiles [177], or double-chain lipid layers, either with or without proteins [124, 171, 175, 176, 178].

1.3.c Dissipative Particle Dynamics (DPD)

The coarse-grained connected bead lipid model described above has been implemented in the Dissipative Particle Dynamics (DPD) algorithm [158, 175, 179, 180]. Its success in replicating essential experimental results in a computationally less costly manner makes DPD an obvious choice for simulating the mixed WALP/lipid striated domains.
DPD was first introduced by Hoogerbrugge and Koelman [180] in 1992 and was later refined by Español and Warren [181]. It was developed originally to simulate complex fluids. DPD is derived from MD, but adds a random $\boldsymbol{F}_{ij}^{R}$ and dissipative $\boldsymbol{F}_{ij}^{D}$ force to the conservative interaction force $\boldsymbol{F}_{ij}^{C}$. The total, pairwise-additive force $\boldsymbol{f}_i$ acting on one particle i is the sum of the three forces $\boldsymbol{F}_{ij}^{C}$, $\boldsymbol{F}_{ij}^{R}$ and $\boldsymbol{F}_{ij}^{D}$ [182, 183]. The conservative force between DPD particles i and j is usually chosen as a soft repulsive potential [184], which allows for much longer time-steps during the simulation compared to the conventional hard-core, repulsive part of the Lennard-Jones potential. This is allowed from a physical point of view because the beads represent the centre of mass of soft fluid particles rather than real, impenetrable atoms [184]. The dissipative force $\boldsymbol{F}_{ij}^{D}$ corresponds to a frictional force which tends to reduce velocity differences between the different particles. The random force $\boldsymbol{F}_{ij}^{R}$ and the frictional dissipative force $\boldsymbol{F}_{ij}^{D}$ are interrelated through the fluctuation-dissipation theorem so that they act as thermostat, while ensuring a correct description of the hydrodynamics on a mesoscopic scale [181, 185]. The total force $\boldsymbol{f}_i$ is then used to calculate the particle's trajectories based on Newton's equations of motion in a manner similar to that used in Molecular Dynamics [161]. A more complete treatise of the DPD method and its mathematical basis can be found in [161, 180, 186, 187].

1.3.d CG-DPD simulations of lipid bilayers with and without proteins

DPD simulations with a coarse-grained (CG) model were used by Smit and co-workers to study the phase behaviour of single- and double-chain lipids of varying geometries [158, 171, 179, 182]. The models contain different types of beads to mimic the various components: water w, the hydrophilic headgroup H and the hydrophobic hydrocarbon chain T (see Fig. 1.8).
The intra-chain coupling of the beads occurs via harmonic or Hookean springs. Stiffness of the chain is added through a bending potential, which is set to an equilibrium angle of 180° for saturated lipid acyl chains [179]. Empirical or MD-derived interaction parameters have been used to describe the bonded interactions [158, 187]. Various, slightly differing, parameter sets have been proposed [175, 178]. The density of the fluid particles and their self-interaction parameters are tailored to mimic the compressibility of water [187], while the interactions between unlike particles i and j can be derived from the Flory-Huggins theory for immiscible polymers [187, 188]. An experimentally correct tensionless state (surface tension $\gamma = 0$) of the bilayers can be ensured by including Monte Carlo moves that change the area of the simulation box until the desired γ is reached [182].

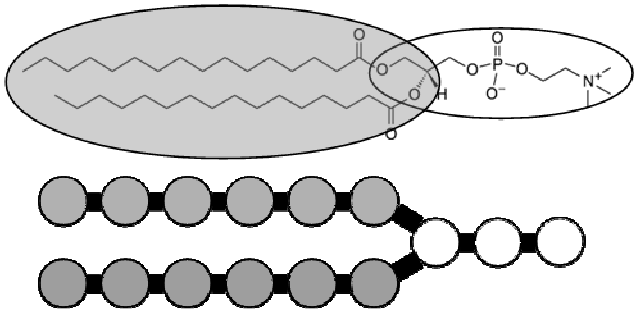

Fig. 1.8 Chemical structure of a DPPC molecule (above) and the coarse-grained description used for computer simulations (below): 3 H beads describe the polar PC head (white), while 2 x 6 T beads are used to describe both lipid tails (grey) [179]

The lipid model of Kranenburg and Venturoli [179, 183] has been successful in describing the different polymorphs known from experimental data. Other CG species can be included in the bilayers, such as small molecules and peptides [158, 183]. In this thesis, the same CG lipid model is used, together with a similarly coarse-grained peptide model to calculate the perturbation of the lipids caused by the single rows of WALP in the striated domains.

1.4 Outline of this thesis

In this thesis, the effect of various packing-related aspects of the lipids upon the striated domains in mixed phospholipid/WALP23 supported bilayers is studied. It is shown that the ability of the lipid/WALP23 systems to form striated domains strongly depends on the lipid environment. The packing of the lipids is altered when the temperature [14] or the chemical composition of the lipids [3, 12] is changed.

Liquid-AFM is a convenient tool to study these systems with a high resolution in a biologically relevant hydrated state. Chapter 2 describes some general AFM results, illustrating the properties of the striated domains and the influence of the concentration of WALP, hydrophobic mismatch and modifications of the WALP upon these. Chapter 3 deals with the main phase melting transition of the PC lipids and the influence of WALP upon this. It is also shown that the loosely packed fluid lipid phase affects the lateral ordering of the peptide within the domains. In Chapter 4, the lipid packing of the bilayer is modified by choosing other lipids than the saturated PC lipids of the other chapters. Replacement of DPPC (di-16:0-PC) by increasing amounts of DPPE (di-16:0-PE) leads to a removal of the intrinsic tilt angle of the lipid acyl chains, while addition of *n*-hexadecane to DPPC bilayers has the same effect without altering the headgroups. *Cis*-unsaturated (di-*n*:1-PC and 16:0,18:1-PC) lipids have a looser lateral packing due to a kink in their chains at the position of the double C=C bond. It is shown

that both the modifications in unsaturation and tilt angle remove the tendency to form striated domains.

In Chapter 5, computer simulations are applied to gain information on an almost molecular level about the respective lipid and peptide conformations within the striated domains. A coarse-grained model of both species is applied and implemented in the Dissipative Particle Dynamics (DPD) simulation scheme [180]. The bead model of Kranenburg and Venturoli *et al.* [179, 183] is used to model the lipids, where the molecules are thought to be built up from a relatively small number of 'superatoms' or 'beads'. Various parameters of these pure lipid bilayers are investigated as function of temperature and lipid acyl-chain tilt. In section 5.4, rigid rows of WALP molecules are incorporated in the bilayer to mimic the single rows of the peptide in the striated domains. The perturbation of the lipids around these inclusions is investigated for different temperatures, peptide lengths, and in the presence and absence of an intrinsic tilt of the lipid's acyl chains. These data complement the information obtained by AFM.

Finally, in the closing Chapter 6, the previously stated model (see section 1.1.c and [117]) is extended to include the new results of Chapters 1 to 5.

Chapter 2

General properties of striated domains

Abstract

Microdomains with a striated appearance are formed spontaneously in mixed bilayers of saturated gel phase PC lipids and the model peptide WALP. WALP is a synthetic, transmembrane peptide consisting of a single, α-helical core flanked by two tryptophan anchoring groups on each end. Earlier studies showed that these domains consist of single rows of peptide that alternate with rows of ~ 8 - 10 lipid molecules with a significantly reduced acyl-chain tilt. The overall striated packing has been previously explained in terms of generic lipid-peptide and peptide-peptide interactions [117].

In this chapter, a further study of these striated domains is performed with liquid-Atomic Force Microscopy (AFM) in Contact Mode. General properties of the domains are described, such as their area, height and the repeat distance between the lines. Next, it is shown that the extent of hydrophobic mismatch between the gel-state PC bilayer and WALP plays only a minor role in determining the morphology of the striated domains. Striated domains with a similar appearance are formed when varying the length n of the saturated hydrocarbon chain between $14 < n < 20$ carbon atoms. A very large mismatch ($n = 22, 24$) leads to severe reduction of the amount of WALP that is incorporated in the bilayer. Finally, covalent linkage of a palmitoyl chain to the N terminus of the WALP (Pa-WALP23) leads to a less regular packing of the stripes in the domains, which is explained in terms of steric effects.

2.1 Introduction

The discovery of highly ordered striated domains in mixed bilayers of saturated PC lipids and the model peptide WALP is interesting (see section 1.1.c and [117, 122, 123]), as insight into lipid-mediated lipid-peptide interactions can be obtained by studying the physical forces that underlie the formation of these patterns. The lipid environment has been shown to exert a large influence on the lateral distribution and conformation of a number of other proteins and can even switch a protein from a functional to a non-functional state by altering the relative position of its sub-units [13, 57, 91, 95, 173]. However, not all forces involved are yet fully understood.

In the striated domains, single lines of the single α-helical model peptide WALP23 (black lines in Fig. 1.6.a) alternate with higher rows of lipids whose acyl chains have a reduced tilt angle [110, 117] (white lines in Fig. 1.6.a). Some features of these domains have been studied experimentally with AFM, such as the influence of the length of the peptide and the type of anchoring group [33, 122, 123]. The only other peptide known so far to form similar regular patterns in lipid bilayers is gramicidin A [85]. The formation of the striated domains is believed to involve competing peptide-peptide and lipid-peptide interactions [117], but a more detailed description of the various contributions made by the lipid-matrix and the peptide to this self-assembly is still lacking.

In this chapter, some general features of the striated domains in hydrated, mixed bilayers of saturated PC lipids and WALP23 are investigated with AFM in Contact Mode. Experimental conditions are varied to study issues such as the concentration of WALP in the bilayer, influence of the substrate, and ionic strength and pH of the aqueous medium. These data serve as reference for the remainder of the work described in this thesis. Next, the hydrophobic mismatch between the peptide and the lipid matrix is altered by systematically changing the length of the acyl chains of the disaturated PC lipids from 14 to 24 carbon units. The length of WALP is kept constant. A large hydrophobic mismatch (*i.e*. a non-concurrent length of the hydrophobic parts of the protein and the lipids) can affect the aggregation of proteins or peptides [60, 92, 102, 189] and their affinity for associating with the membrane [71, 83, 105, 190, 191]. Hydrophobic matching is of biological relevance, as many theoretical and experimental studies have shown the importance of favourable matching conditions for the functioning of various proteins [13, 84, 87, 94, 107, 113].

In the final section, WALP is modified by covalent attachment of a palmitoyl C16 chain to the N terminus (Pa-WALP23). This can not only help to identify the effect of modification of the peptide on the formation of the striated phase, but can also provide more insight into the biological role of palmitoylation. Covalent attachment of a fatty-acid chain such as palmitate or myristate is encountered frequently in biological membranes. For soluble, peripheral proteins, the long hydrocarbon chain increases hydrophobicity and thus enhances association with the membrane [96, 192].

However, palmitoylation has also been observed to occur close to hydrophobic, transmembrane segments [193]. The exact role of this modification remains elusive, although it has been proposed that palmitoylation can facilitate partitioning of proteins to lipid rafts [48, 96] and alter the orientation, conformation [194] and functioning [193, 195] of the protein.

2.2 Materials & Methods

Materials

The lipids DMPC (di-1,2-myristoyl-*sn*-glycero-3-phosphocholine = di-14:0-PC, with n =14 the number of carbon atoms in the chain and 0 the number of unsaturated bonds u), DPPC (1,2-dipalmitoyl-*sn*-glycero-3-phospocholine = di-16:0-PC), DSPC (di-1,2-stearoyl-*sn*-glycero-3-phosphocholine = di-18:0-PC), DAPC (di-1,2-arachidoyl-*sn*-glycero-3-phosphocholine = di-20:0-PC), DBPC (di-1,2-beheneoyl-*sn*-glycero-3-phosphocholine = di-22:0-PC) and DLgPC (di-1,2-lignoceroyl-*sn*-glycero-3-phosphocholine = di-24:0-PC) were purchased from Avanti Polar Lipids Inc., Alabaster, USA at > 99.0 % purity. Lipids were dissolved in a solution of 1:3 v/v chloroform ($CHCl_3$)/methanol (MeOH) of analytical grade. NaCl was obtained from Merck (Darmstadt, Germany, p.a. grade). MilliQ-water with a resistivity of 18 MΩ/cm was used throughout.

WALP23 and the N-palmitoylated WALP23 (Pa-WALP23) were a gift from prof. J.A. Killian (Dept. Biochemistry of Membranes, Utrecht University). Its synthesis has been described in [99]. The peptide essentially consists of an α-helical stretch of alanine (Ala or A) and leucine (Leu or L) amino acids, symmetrically flanked by a total of four tryptophan (Trp or W) groups. The N terminus is capped by an acetyl (Ac) group, while the C terminus is capped by amide or ethanolamine to avoid charges on the molecule. Amide-capped WALP was used here, although identical results are obtained with the ethanolamine-capped peptide. The amino-acid composition of WALP23 is:

$$NH_2\text{-A-W-W-(L-A)}_8\text{-L- W-W- G-Ac}$$

where A = alanine, W = tryptophan, L = leucine, G = glycine amino acid residues and Ac = acetyl group

The alanine and leucine groups make the helix highly hydrophobic. This ensures a transmembrane orientation of WALP when it is incorporated into lipid bilayers [33, 196]. The tryptophan groups provide a stable anchoring of the peptide [63, 119, 120]. The total length of WALP23 is 3.6 nm [74] and the length of the Ala-Leu hydrophobic stretch d_{HPH} (WALP23) is 2.6 nm [190]. [1] Pa-WALP23 has the same composition as WALP23 but has a palmitoyl (C16:0) chain covalently attached to its N terminus.

[1] Following [74], it is assumed that every amino acid residue contributes 0.15 nm to the total length. The ethanolamine has the length of an additional amino acid

Bilayer preparation

Supported bilayers (SPBs) were prepared according to the vesicle fusion protocol [127, 147]. First, dry mixed films were prepared by mixing appropriate amounts of solutions of the lipid (dissolved in 1:3 v/v $CHCl_3$/MeOH) and WALP23 (dissolved in TFE, 2,2,2-trifluorethanol, Sigma-Aldrich, 99,5+ % NMR-grade) and subsequently removing the solvent with a rotary evaporator. Residual traces of organic solvent were removed by overnight storage under vacuum. The films were then hydrated by adding 20 mM NaCl solution to a final lipid concentration of ~ 1 mM. After that, the sample underwent 8 - 10 freeze-thawing cycles by alternatively freezing the sample in an EtOH/CO_2 bath and thawing it above its main transition temperature under mild shaking (T ~ 55 °C was used for DPPC). This leads to the formation of multi-walled vesicles or liposomes (*i.e.* closed, spherical bilayer structures containing multiple bilayers, also called multi-lamellar vesicles MLVs). These were sonicated in a Branson bath-sonicator for 45 - 60 minutes under nitrogen-flow until the dispersion became clear, indicating the presence of smaller, single-walled SUVs (small or sonicated uni-lamellar vesicles, see Fig. 1.3) [197]. Remaining large aggregates were removed by centrifuging at 20800 *g* at 4 °C for 45 minutes. Dispersions were stored at 5 °C if not used immediately, but were not kept for more than 4 days.

Supported bilayers were made by depositing ~ 75 µl of the SUV dispersion on a mica disk with a diameter of 14 mm (muscovite mica, $KAl_2(OH)_2AlSi_3O_{10}$ [136], Regular V-5 sheets PK/10, SPI supplies Structure Probe R, West Chester, USA) glued on to a larger, metal disk. Mica is often used as substrate for AFM as it forms atomically flat, hydrophilic surfaces [136]. It is cleaned prior to use by cleaving the layered crystal. A hydrophobic layer was applied to the perimeter of the metal disk in order to prevent the liquid from flowing off. The disk with the lipid dispersion was heated at 65 °C (for DPPC) for 45 minutes, in a sealed container to prevent dehydration. This causes the vesicles to collapse and spread to form continuous, flat bilayers [132, 198, 199], which adhere to the mica through physisorption [135, 199]. The sample was removed from the oven and allowed to cool to room temperature before rinsing it three times with 20 mM NaCl solution. The sample was then placed in the liquid-cell of the AFM and 0.2 - 0.3 ml of the measuring solution was added. Care was taken to keep the sample hydrated at all times. All samples were made and measured at least twice to ensure reproducibility. A 20 mM NaCl solution is chosen here as aqueous medium to allow comparison with previous studies on striated domains [33, 110, 119, 122, 123]. Often-used buffers such as Tris often leave debris on top of the bilayer surface that can obscure its features.

The temperatures of all heating steps were adjusted for the longer lipids with $n > 16$ carbon atoms so that they were above their respective melting transition temperatures T_M, which increase with chain length [29]. An exception was made for di-22:0-PC (DBPC) and di-24:0-PC (DLgPC), which have a T_M of ~ 75 °C [200] and 80 °C [201] respectively. A lower 70 °C was used there to prevent dehydration in the oven. The unaltered morphology of a similarly treated DPPC/WALP23 sample indicated that no degradation of the WALP takes place at this temperature. The experiments at different NaCl concentrations (2 - 2000 mM) were performed

by replacing the 20 mM NaCl solution with one of the desired concentration at the onset of the sample preparation. Likewise, a 20 mM NaCl solution with the correct pH (through addition of HCl or NaOH) was used to prepare and image the samples at pH 4 and 10. The regular 20 mM NaCl solution has a pH of ~ 5.6.

AFM measurements

Atomic Force Microscopy (AFM) was done in Contact Mode on a commercially available PicoScan Microscope (Molecular Imaging Corporation, Phoenix, USA, model 305-0002 157) with an S-1286 scanner. Measurements were performed in 20 mM NaCl (unless stated otherwise) at room temperature (22 - 23 °C), with the exception of DMPC. This sample was cooled to 13 °C to ensure gel-phase behaviour. A Peltier I sample stage (Molecular Imaging Corporation, Phoenix, USA) controlled by a LakeShore 330 Temperature Controller was used. The temperature on top of the mica disk, immersed in 20 mM NaCl, was calibrated with a Pt-100 (Sensycon, Alzenau, Germany) with a flat metal disk (ø 4.8 mm) as probe. This temperature was found to deviate significantly from the setpoint value given by the controlling device, which is measured at the underside of the sample holder. Calibrated values are used throughout.

Pyramidal shaped Si_3N_4 oxide-sharpened tips mounted on a triangular cantilever with a nominal spring constant of 0.06 N/m and a typical radius of 5 - 20 nm were used (NP-S, NanoProbe, Digital Instruments Inc., Santa Barbara, USA). A silicon calibration grid that had a square wave with a pitch of 3 µm and step height of 24 nm (TGZ01 UltraSharp grating set, NT-MDT Co., Moscow, Russia) was used for the calibration of the AFM scanner. Scans of the bilayers were made at the lowest possible force that allowed stable imaging, which was typically ~ 0.4 nN. This level was maintained by decreasing the force setpoint manually during the scan, as thermal drift can cause large deviations in force during the time interval it takes to complete a scan (~ few minutes/image). A scan rate of 3 - 4 lines/s was used. All presented images are in the height (topographic) mode and are background-corrected (‘flattened’) with the use of the PicoScan 5.2 software (Molecular Imaging). The relative height of the features in the images is represented by a grey scale, where a lighter colour indicates a greater height.

The thickness of the bilayer d_{bil} is defined here as the difference in height between the top of the bilayer and the top of the mica substrate (see Fig. 2.1). This is the sum of the thickness of the pure bilayer d^0_{bil} and the layer of water d_w between the underside of the sample and the mica [26, 78, 149]. d_{bil} is measured through holes piercing the layer [26]. The number of such holes can be increased by applying a smaller amount of the vesicle dispersion to the mica substrate. The height of the striated domains d_{dom} is the difference in height between the higher parts of the domains (white lines) and the surrounding, pure bilayer. The repeat distance r_{rep} is defined as the distance from one dark stripe to the next. Averages were taken of at least 50 separate measurements.

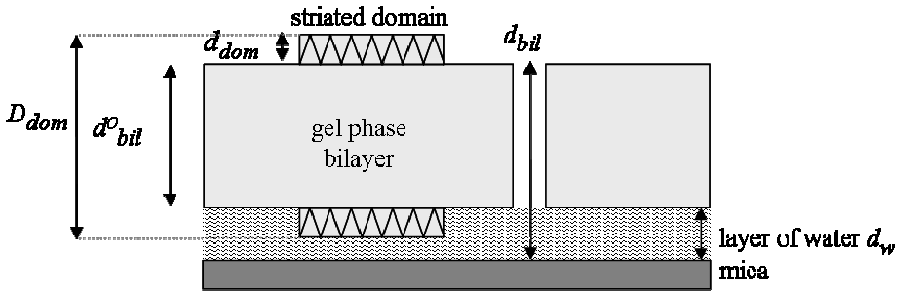

Fig. 2.1 Definition of the various heights. The light grey rectangle depicts a gel-phase bilayer with a hole, while the striped rectangles depict the striated domains that protrude on either side of the bilayer. The layer of water d_w between the bilayer and the mica support is also drawn (thickness largely exaggerated). d_{bil} is the bilayer thickness measured by AFM and includes the layer of water ($d_{bil} = d^0_{bil} + d_w$). d_{dom} is the difference in height between the top of the striated domain and the surrounding bilayer as measured by AFM. Note that only the upper part of the domain contributes to d_{dom}. In contrast, both halves contribute to the total thickening caused by the striated domains that is measured by X-ray diffraction (D_{dom})

2.3 Results

2.3.a Gel-state di-*n*:0-PC lipid bilayers

Supported bilayers of different di-*n*:0-PC lipids in the gel state were imaged with AFM for the even n = 14 - 24 and for an equimolar n = 16/n = 18 mixture. All topological images (Figs. 2.2.a to f) showed the flat surfaces of the bilayers (= *xy*-plane in Fig. 1.3). A number of interspersing, meandering dark lines with a depth of ~ 0.2 - 0.3 nm were frequently observed at low scanning forces and large magnifications. In some instances, curves of 120º were observed. These dark lines have been attributed to packing defects in previous studies [122, 202]: the so-called grain boundaries. They separate areas where the lipid acyl chains have a different azimuth tilt angle, while maintaining the same polar angle $\theta \sim 30°$ [29, 30] with respect to the bilayer normal [53, 117, 211] (see Fig. 5.3 for the definition of these angles). The formation of these defects upon solidification from the high-temperature L_α phase will be shown in more detail in Chapter 3. The lipids immediately adjacent to the boundaries are most likely forced to a more ordered and/or less tilted conformation to accommodate packing frustrations at these borders. This gives rise to elevated strips bordering the grain boundaries with Δd = 0.05 - 0.1 nm with respect to the surrounding bilayer (see Fig. 2.2.b). They can only be imaged at very low scanning forces of $F \leq 0.3$ nN and with sharp tips and are not visible in the other images of Fig. 2.2 for this reason. Occasionally, holes (black features; see, for instance, Figs. 2.2.d, f) and unopened vesicles were found (white spherical structures with dimensions in the order of 50 - 250 nm, see Figs. 2.2.b, e and f).

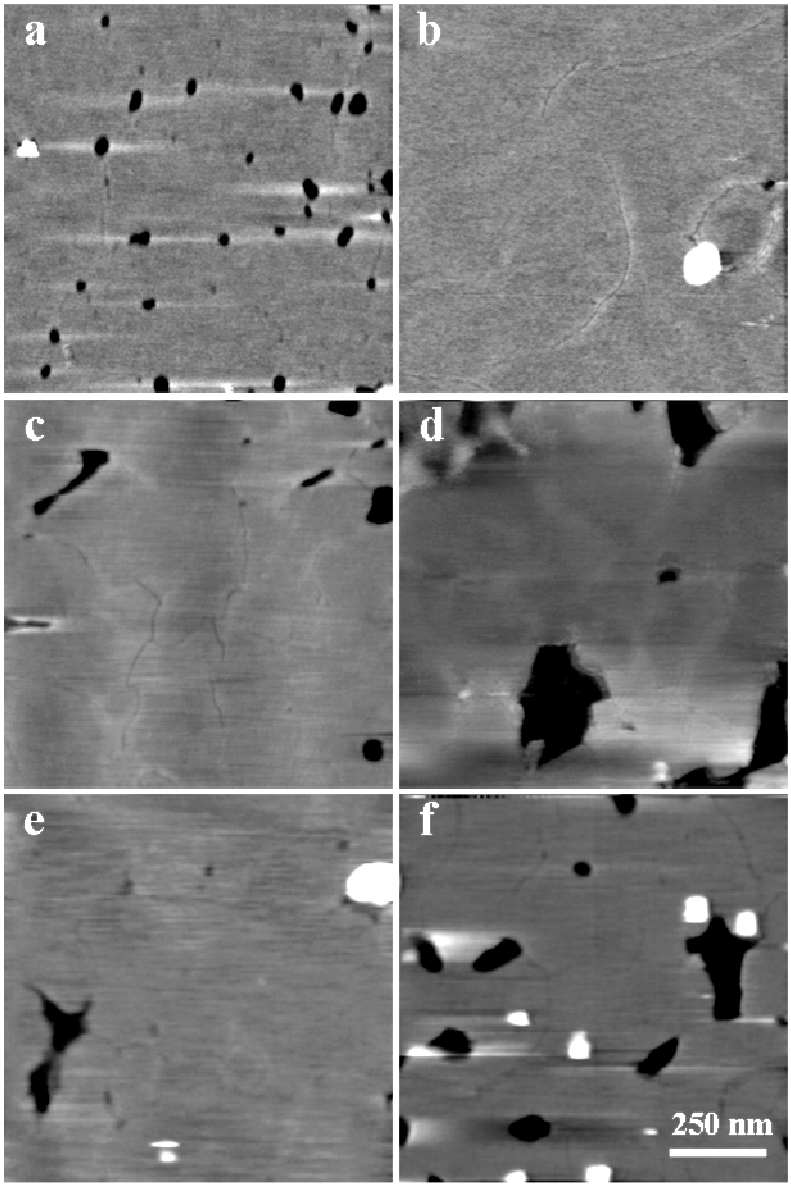

Fig. 2.2 AFM topographs of supported bilayers of saturated gel-state PC lipids with varying acyl-chain lengths *n*. **a.** *n* = 14 (DMPC), **b.** *n* = 16 (DPPC), **c.** *n* = 18 (DSPC), **d.** *n* = 20 (DAPC), **e.** *n* = 24 (DLgPC) and **f.** equimolar *n* = 16/18 (DPPC/DSPC) mixture. The grey scale indicates the relative height of features in the images, where a lighter colouring represents a higher feature. The total scale corresponds with a height difference of ~ 1 nm. All images have the same lateral dimensions

The thickness d_{bil} of the bilayers increases roughly linearly with increasing lipid length (see Fig. 2.3.a, open circles ○). The values of 5 - 6 nm are in agreement with the presence of bilayers in the gel L_{β}' phase with a layer of water of ~ 1 nm intercalated between the sample and the substrate [26, 33, 78, 149, 199, 203] (see Fig. 2.1). The total increase in d_{bil} for the whole series from n = 14 - 24 was 1.6 nm.

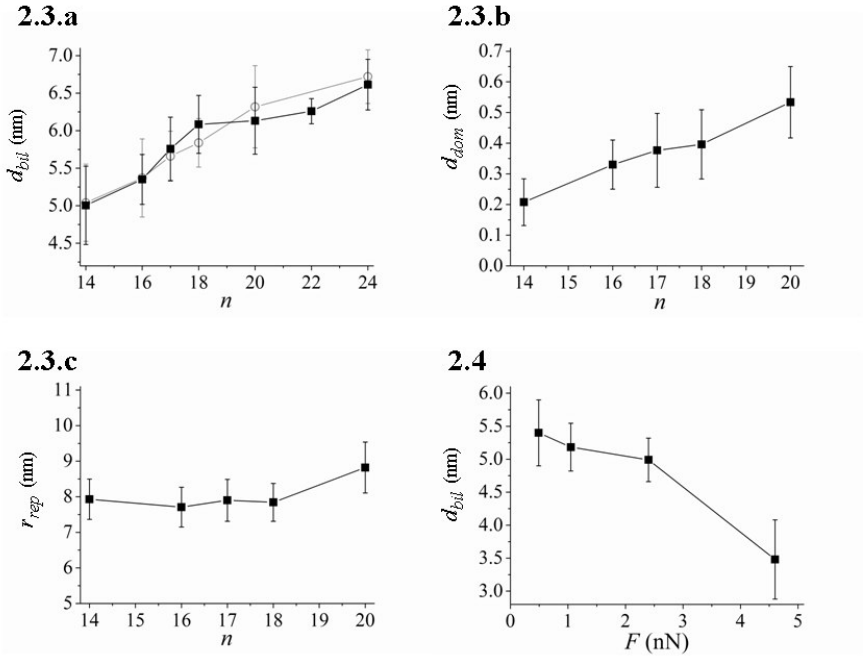

Fig. 2.3 Various characteristics as function of acyl-chain length n of di-n:0-PC lipids: **a.** measured bilayer thickness d_{bil} without (open circles ○) and with 2 mol% WALP (solid squares ■). **b.** Domain height d_{dom} and **c**. repeat distance r_{rep}. Results of the mixed DPPC/DSPC (n = 16/18) bilayer are plotted at n = 17

Fig. 2.4 Effect of the scanning or imaging force F of the AFM probe upon the measured d_{bil} for DPPC (n = 16)

These measurements were all performed at low imaging forces $F \leq 0.5$ nN. The importance of minimizing F is underlined by Fig. 2.4, where d_{bil} of DPPC (n = 16) is lowered by approximately 2 nm at a higher F of 4.5 nN. The AFM probe deforms the bilayer, leading to an apparent and lower d_{bil}. The 'real', unperturbed bilayer thickness can be found by extrapolating the curve to zero force, which leads to a value of 5.7 nm (first-order polynomial fit). A very large scanning force of $F \geq 5$ nN damaged the layer irreversibly, leading to holes (data not shown, [54]). This irreversible break-through occurs when the tip punctures the bilayer down to the mica [145, 205].

No changes in topology or layer thickness d_{bil} of DPPC bilayers were found when the pH of the aqueous medium was varied between 4 and 10 (data not shown). An increase in the NaCl concentration led to a monotonous increase of d_{bil} from 5.3 ± 0.5 nm at 2 mM to 6.1 ± 0.4 at 2 M NaCl. The morphology of the layer did not change (data not shown).

2.3.b Mixed di-*n*:0-PC/WALP23 bilayers

Incorporation of small amounts of WALP23 (0.5 mol%) in DPPC bilayers led to the appearance of single, dark lines that were broader than the grain boundaries in pure DPPC bilayers. The lines were often bordered by lighter strips with an increased height of 0.1 - 0.2 nm, as shown in Fig. 2.5. These are probably lipids with a slightly altered conformation [117].

A concentration of 1 mol% WALP23 or higher gave rise to well-defined domains that had an increased height d_{dom} = 0.3 - 0.4 nm compared to the surrounding, featureless bilayer areas (see Fig. 2.6.a). The total area of the domains increased with the amount of WALP23 and complete coverage of the sample with the striated phase occurred at ~ 12 mol% (data not shown). The close-up of a domain in Fig. 2.6.d shows the rigidly ordered pattern of alternating, parallel lighter and darker lines. The width of the darker lines in the AFM pictures was 2 - 3 nm and their measured depth was 0.2 - 0.4 nm. The real depth may be larger as the relatively large radius of the AFM tip of 5 - 20 nm could preclude accurate tracking of these small features. This effect is commonly known as tip convolution [209, 210]. The repeat distance r_{rep} between two dark stripes was almost constant at 7.7 ± 0.6 nm. Well-defined angles of almost exclusively 120° were formed where the lines changed direction or met [122].
Striated domains with an identical appearance and r_{rep} (7.5 ± 0.3 nm, see Table 2.I) were observed in a secondly stacked DPPC bilayer (Fig. 2.7), which is characterized by a step height d_{2nd} of 5 - 6 nm with respect to the first bilayer of Fig. 2.6.a. This was formed when a large amount (> 150 µl) of vesicle-suspension was applied to the mica.

The other bilayers of di-*n*:0-PC/2 mol% WALP23 contained striated domains for acyl-chain lengths from *n* = 14 to 20 carbon units and for the *n* = 16/18 mixture. AFM micrographs are shown in Figs. 2.8.a - f (on page 32). The morphologies of the domains were very similar, with only minor differences in the repeat distance and number of curves in the lines. The total area of the striated domains was strongly reduced from ~ 15 % for *n* = 16 to ~ 2 - 5 % for *n* = 20. This is not immediately apparent from the presented micrographs as these close-ups are not representative of the whole sample. The thicker bilayers of di-22:0-PC and di-24:0-PC did not display any striated domains (see Fig. 2.8.e), but only random lines similar to those in the mixed DPPC (*n* = 16)/0.5 mol% WALP23 bilayer in Fig. 2.5.
Figs. 2.3.a to c, respectively, give the bilayer height d_{bil} (solid squares ■), domain height d_{dom} and repeat distance r_{rep} as function of lipid length *n* for the WALP-containing bilayers. Both d_{bil} and d_{dom} show a progressive increase with *n*, while r_{rep} remains largely constant.

No changes in topology were detected when the pH of the aqueous medium was changed from 4 to 10. All repeat distances r_{rep} fell in the range of 7.6 - 8.0 (± 0.5) nm and all domain heights d_{dom} in the range of 0.3 - 0.4 (± 0.1) nm (data not shown). Neither did the topology of the striated domains change over a large range of NaCl concentrations (2 - 4000 mM, data not shown). d_{dom} lay between 0.3 ± 0.1 at 2 mM and 0.4 ± 0.1 nm at 2 M NaCl. The repeat distance r_{rep} remained unmodified with values between 7.5 ± 0.3 and 8.0 ± 0.5 nm.

Table 2.I Measured bilayer thickness d_{bil}, domain height d_{dom} and repeat distance r_{rep} of gel-state DPPC bilayers and striated domains at various concentrations of WALP23 and for Pa-WALP23

system	d_{bil} (nm)	d_{dom} (nm)	r_{rep} (nm)
DPPC	5.4 ± 0.5	-	-
DPPC/0.5 mol% WALP23	5.3 ± 0.3	-	-
DPPC/2 mol% WALP23	5.4 ± 0.3	0.3 ± 0.1	7.7 ± 0.6
DPPC/12.5 mol% WALP23	-	-	7.5 ± 0.3
DPPC/2 mol% Pa-WALP23	5.2 ± 0.7	0.4 ± 0.1	8.9 ± 1.2

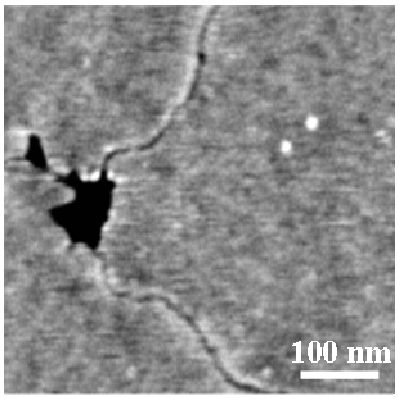

Fig. 2.5 Mixed DPPC/WALP23 bilayer with 0.5 mol% WALP23, taken at a low scanning force of $F \leq 0.5$ nN

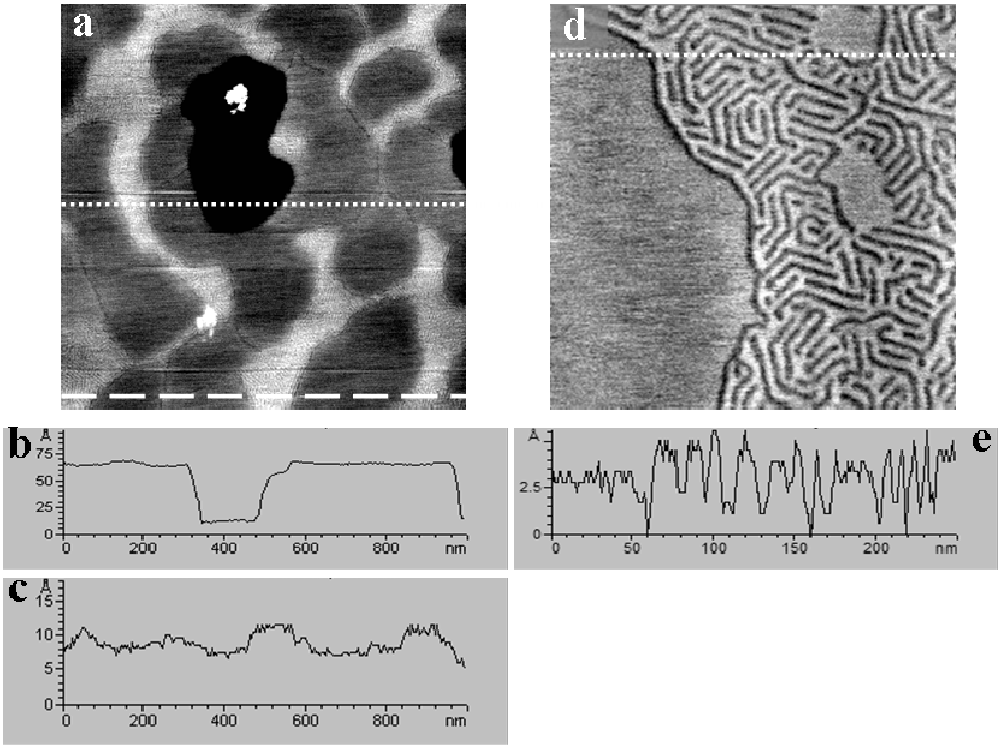

Fig. 2.6.a. AFM micrograph of a DPPC/2 mol% WALP23 bilayer (1 x 1 μm scan) with **b.** the height profile (*i.e*. relative height along the line) taken at the position of the short-dotted line. This shows a hole piercing the bilayer. **c.** gives the height profile at the position of the long-dotted line and shows the increased height of the domains. **d.** is a close-up of one domain (250 x 250 nm) and **e**. the corresponding height profile at the dotted line, which shows the alternating higher and lower lines of the striated phase

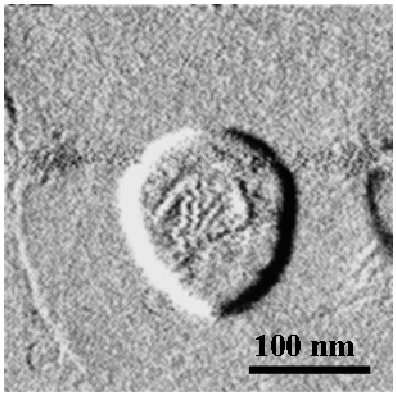

Fig. 2.7 Deflection image of a double DPPC/2 mol% WALP23 bilayer (in the middle) containing a small area of the striated phase. The background is the level of the first bilayer. Imaging of this second layer is more difficult and distortion of the lines by the AFM probe is visible. Deflection mode is used here as this gives a clearer view than the topographic image, although information on height is lost

2.3.c Palmitoylated WALP23

Palmitoylation of WALP23 (Pa-WALP23) did not remove its ability to form striated domains in gel-state DPPC bilayers (see Fig. 2.9). The stripes in the domains were more curved and met at less well-defined angles than those of the unpalmitoylated WALP23 in Fig. 2.6.d. The average repeat distance r_{rep} was increased from 7.7 to 8.9 nm (Table 2.I). The relatively large variance of r_{rep} reflects the partial loss of order of the stripes. The domain height d_{dom} was not altered significantly by the palmitoylation.

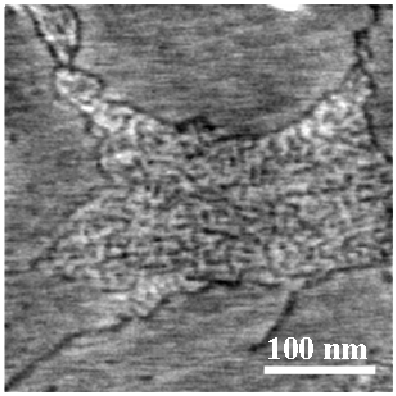

Fig. 2.9 Height image of a DPPC bilayer with 2 mol% palmitoylated Pa-WALP23

2.4 Discussion

2.4.a Gel-state di-*n*:0-PC bilayers

The value of the thickness d_{bil} of the DPPC bilayer (at low scanning forces) of 5.4 ± 0.5 nm is somewhat smaller, but still in fair agreement, with other reported AFM values of 5.8 - 5.9 [122], 5.8 ± 0.4 nm [212], 5.5 ± 0.2 nm [78, 152] and 5.6 nm [85]. Differences in applied scanning force [207], ionic strength [43, 141] and calibration could account for the fluctuations between the different AFM studies. The measured thickness also agrees with the bilayer thickness d^0_{bil} of 4.4 - 4.7 nm [29, 39, 213] found by X-ray diffraction when one realizes that the layer of d_w ~ 1 nm [33, 199, 203] separating the bilayer from the substrate is included in the AFM data but not in the X-ray diffraction data. In other words, d^0_{bil} (X-ray) = d_{bil} (AFM) + d_w (see Fig. 2.1 for definitions and Table 2.II for the measured and literature values).

The n = 16/18 mixture gave a single lipid bilayer with a d_{bil} that falls more or less halfway between those of the pure n = 16 and n = 18 bilayers. This indicates mixing of the two lipids. ^{2}H-NMR [237], ESR [238], DSC [67, 80] and fluorescence studies [239] confirmed (almost)

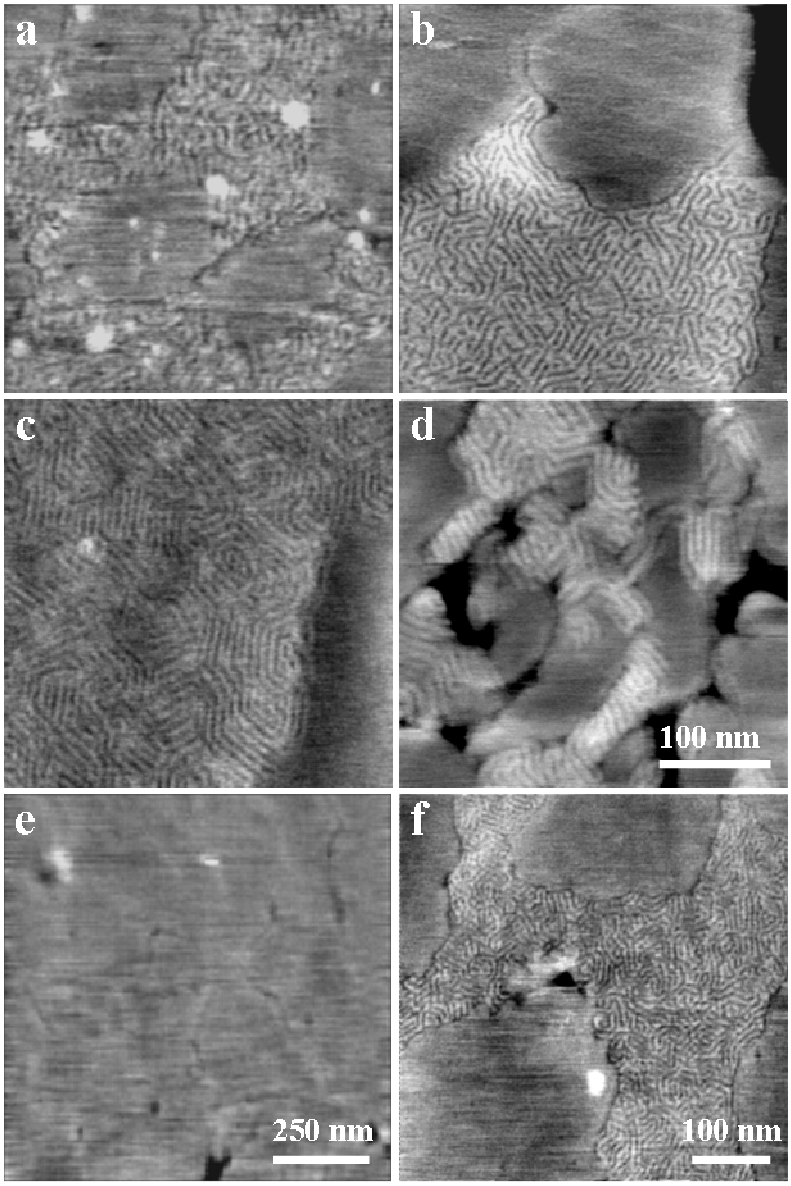

Fig. 2.8 AFM images of mixed lipid/2 mol% WALP23 bilayers formed with different saturated PC lipids with **a.** n = 14 (DMPC), **b.** n = 16 (DPPC), **c.** n = 18 (DSPC), **d.** n = 20 (DAPC), **e.** n = 24 (DLgPC) and **f.** equimolar mixture of n = 16 (DPPC) and 18 (DSPC). Figs. **a - d** have the same lateral dimensions, **e** and **f** differ. Total height scale ~ 1 nm for **a** - **f**. All are imaged at a scanning force F of approximately $\leq$ 0.5 nN

ideal miscibility of saturated PC lipids that differ two methylene units in length (di-14:0-PC/ di-16:0-PC and the used di-16:0-PC/di-18:0-PC) in the solid state.

Table 2.II Measured and literature values (X-ray and neutron diffraction) of the bilayer thickness d_{bil} and d^0_{bil} for gel-phase bilayers of different PC lipids

lipid name	**acyl-chain composition (*n*: *u*)**	**d_{bil} measured (nm)**	**d^0_{bil} literature values (nm)**
DMPC	14:0	5.0 ± 0.5	4.1 - 4.3 [29, 84]
DPPC	16:0	5.4 ± 0.3	4.4 - 4.7 [29, 39, 213]
DSPC	18:0	5.9 ± 0.4	4.6 - 4.7 [29, 84, 213]
DAPC	20:0	6.2 ± 0.6	5.1 - 5.2 ***a***
DBPC	22:0	6.3 ± 0.2	5.5 - 5.6 ***a***
DLgPC	24:0	6.6 ± 0.3	6.0 - 6.1 ***a***
DPPC/DSPC	16:0/18:0	5.7 ± 0.4	4.5 - 4.7 ***b***

a Assuming a total increase of the bilayer thickness of 0.45 nm per 2 methyl additions to the lipid tail [87]

b Average of DPPC and DSPC

The compressing effect of the AFM probe on d_{bil} (Fig. 2.4) can in principle be explained by local, elastic deformation of the bilayer and/or by penetration of the tip between the headgroups of the lipids. Considering that the relatively large tip interacts with several lipid molecules at a time [127, 134, 204 - 206], the first option seems the most likely. Differences in the elasticity of the layer and axial compression modulus (Young's modulus) in the gel and fluid phase are reflected by the indentation characteristics [127, 204 - 206], which would not be the case if the decrease in height was caused by penetration of the headgroup region only. However, some additional slight conformational adaptations of the headgroups under the lateral and axial stresses exerted by the AFM probe are likely to occur [207, 208]. The extent of the imposed deformation depends strongly on experimental variables like the exact radius and shape of the tip and the individual spring constant of the cantilever on which the tip is mounted. Large variations are known to exist, even among tips of the same type [127, 207]. However, the indentation of ~ 0.3 nm at 1 nN reported by Shao *et al.* [127] for DPPC bilayers in the gel phase seems to be of the same order of magnitude as the data in Fig. 2.4.

Finally, the lack of influence of the pH on the bilayer characteristics shows that the pH does not alter the lipid packing over a wide range from pH = 4 - 10. Protonation of the PO_4^- group does not take place till pH < 3 - 4 [29, 214], which is outside the scope of this study. Monovalent salts like NaCl are also known to leave the thickness of the hydrophobic core of the bilayer [215, 216] and bending rigidity [215] largely unmodified. On the other hand, the orientation of the headgroups [217, 218], the surface potential [218, 219], and the thickness of the interlamellar layer of water in multi-walled liposomes [215] are altered. The observed increase in d_{bil} with [NaCl] is presumably not related to any direct modifications in the bilayer,

but rather to altered interactions between the AFM probe and the substrate [43, 220]. A similar increase in d_{bil} for DPPE supported bilayers with ionic strength was observed with AFM by Müller *et al*. [43] and was attributed to screening of the electrostatic, repulsive tip-mica interactions by NaCl [43, 134, 220]. The smaller surface charge of the lipid bilayer leads to much smaller changes in the interactions between the tip and surface of the bilayer [43]. The tip-mica interactions dominate, thus altering the apparent d_{bil}, which is measured as the difference between the top of the bilayer and the substrate. Electrostatics play a distinct role in tip-sample interactions, as both the Si_3N_4 tip and the mica are negatively charged [141, 220] when they are in contact with water. This is due to dissociation of surface groups, such as the hydroxyl groups of the layer of silicon oxide on the tip.

2.4.b Mixed di-*n*:0-PC/WALP23 bilayers

General properties

The peptide WALP23 incorporates readily in PC bilayers, where it adopts a transmembrane, perpendicular orientation with respect to the bilayer surface [33]. Its low solubility in gel-state bilayers, however, leads to exclusion to the grain boundaries [122]. Random (lateral) mixing of the lipids and peptides would result in a loss of the Van der Waals interaction energy between the tightly packed gel-state lipid acyl chains [117, 122]. This loss is apparently larger than the entropy gained by mixing. Accumulation of impurities at packing defects is a common feature in biological and non-biological systems [86, 221 - 223]. Other AFM studies showed that both phospholipase A2 [211] and the model peptide C14 [224] also inserted preferentially into packing defects.

Only a limited number of WALP23 molecules can be accommodated in these grain boundaries. Raising the amount of WALP to 1 mol% already leads to an excess of peptide molecules that have to find a different location where their presence creates the least perturbation. This leads to segregation into distinct domains with an enhanced height and a stratified appearance (Fig. 2.6). The lipid/WALP23 composition is 8:1 - 10:1 [110, 117, 122]. Note that this corresponds to a spacing of 4 - 5 lipids between the lines of WALP owing to the presence of a bilayer. Nucleation of the striated phase starts when the solubility of WALP is lowered drastically upon the transition from the fluid to the gel phase [75] during the sample preparation at points where two or more grain boundaries intersect. The constant repeat distance r_{rep} forces newly-formed lines to curve accordingly to the previous lines (or terminate).

The measured thickness of the striated domains d_{dom} of 0.3 - 0.4 nm is approximately half of the 0.6 nm [110] measured by X-ray diffraction. It seems very plausible that AFM only probes the upper half of the bilayer and, hence, half of the total thickening caused by the loss of tilt of the lipids. The part of the thickening that protrudes on the underside of the bilayer is invisible for AFM (see Fig. 2.1). The bilayer outside the striated domains is believed to be a pure lipid phase devoid of peptide [122]. Indeed, d_{bil} in the WALP-containing systems (measured outside the striated domains, solid squares ■ in Fig. 2.3.a) matches that of the respective pure PC bilayers (open circles ○ in Fig. 2.3.a).

The detailed molecular organization within the striated domains has been previously studied with a variety of techniques [33, 75, 110, 119, 122]. The localization of WALP in these striated domains has been confirmed by gold-labelling of a modified SH-containing WALP analogue [110], while fluorescence techniques showed that the peptide molecules are assembled in single rows in an anti-parallel way (N next to C terminus, see Fig. 2.10) [75]. The dipoles of the peptide's helix [225 - 227] interact more favourably in an anti-parallel than in a parallel orientation [75, 228]. The rows of WALP are observed as the dark lines in the domains.

The white lines contain lipids with a different conformation than those in the pure DPPC L_β' state. Most notably, the presence of WALP reduces the tilt angle of the lipid acyl chains from the regular 30 - 32° [19, 20, 29] to a much lower value in the striated phase. The increase in thickness of 0.6 nm found by X-ray diffraction indicates a remaining tilt angle of about 6° [110] in the domains. The diffraction pattern of the lipid acyl chains is typical of the hexagonally packed gel phase [110]. This sets the 120° intersection angles of the lines in the striated domains. Both ^{2}H-NMR and X-ray diffraction showed a slightly lowered average acyl-chain ordering [110]. It is assumed that only the lipids next to the WALP have disordered chains, while those further away have stretched, gel-like chains. The reduced effective length of these chain-disordered lipids bridges the mismatch in length that would otherwise exist between DPPC and WALP23. Maintaining the mismatch would lead to an unfavourable exposure of the hydrophobic parts of the longer, stretched DPPC molecules to their aqueous surroundings or shifts of the anchoring Trp groups away from their favoured position in the bilayer [63, 119]. Additionally, more fluidized lipid chains may pack more efficiently against the rough surface of the WALP molecule [74, 190, 196, 229]. The typical length scale r_{rep} of ~ 8 nm most likely involves the distance over which the WALP-induced perturbations of the lipid packing extend.

A schematic representation of the molecular organization of the striated domains is given in Fig. 2.10. Lipids are depicted by a spherical headgroup and two 'tails', while WALP is depicted as a grey cylinder with its N terminus white and C terminus black. The altered conformation of the lipids is clearly visible. On the left hand side, a small part of the unperturbed PC bilayer is shown, where the lipids have a substantial tilt angle (~ 30°) with respect to the bilayer normal.

The striated pattern is believed to be determined by competing lipid-lipid and lipid-WALP interactions, independently of specific chemical details. The lipids tend to form an unperturbed layer, while attractive lipid-peptide interactions favour mixing. Without this latter interaction, a complete phase separation into a distinct lipid and peptide phase would be favoured as this minimizes the contact between the two species. Computer simulations on a simple model of these molecules confirmed that a striated phase is formed when the interactions between both species have some intermediate value between complete mixing and complete phase separation [124]. The insensitivity of the striated phase to the exact nature of the (uncharged) anchoring groups of the peptide [33] underlines the general character of the interactions involved. The

observed independency of the properties of the striated phase to the pH and ionic strength of the liquid medium shows that specific (electrostatic) interactions are not essential.

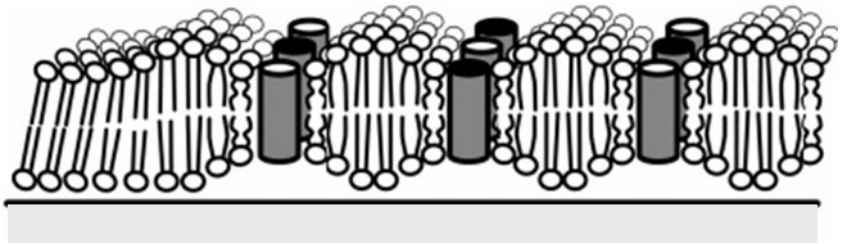

Fig. 2.10 Representation of the proposed molecular packing within the domains. The cylindrical units represent the peptide in its anti-parallel orientation. White indicates the N terminus and black the C terminus. The lipids are represented by a spherical headgroup and two tails. The lipids between the rows have a lower tilt angle than the pure DPPC bilayer (= the 3 lipid molecules on the left hand side) [75, 110]. The lipids bordering the peptide have disordered acyl chains. Adopted from [119]

Mica-bilayer interactions do not determine any of the characteristics of the striated domains, as AFM images of secondly stacked bilayers (Fig. 2.7) showed comparable striated features. This was also observed in cryo-TEM images of non-supported DPPC/WALP liposomes [33]. Secondly stacked and non-supported bilayers do not border a substrate and have properties that are, in some respects, more similar to free-standing bilayers [150, 231, 232]. These results, however, indicate that single supported bilayers are representative of free-standing bilayers in the case of the formation of striated domains.

Hydrophobic mismatch

Remarkably, the features and characterizing length scale r_{rep} of the striated domains do not alter substantially for lipids with different acyl-chain lengths from n = 14 to 20 (Fig. 2.3.c). It is assumed that WALP23 does not change its conformation much in response to mismatch under conditions of negative mismatch [33, 190]. The domain height d_{dom} increases with n (Fig. 2.3.b). d_{dom} is determined by the difference between the projected lengths of the lipid acyl chain on the z-axis (= in the direction of the bilayer normal) in the tilted and non-tilted orientation. An estimation of the expected domain height ($d_{dom,calc}$) can be calculated from the hydrophobic thickness of the tilted bilayer d_{HPH} through formula (1). d_{HPH} can be obtained by subtracting 1.1 nm [233] for the polar region from d^{0}_{bil} in Table 2.II. The final tilt angle in the domains is assumed zero.

$$d_{dom,calc}\,(\mathrm{nm}) = 0.5 \text{ x } d_{HPH}\left(\left(\frac{1}{\cos\theta}\right)-1\right) \qquad (1)$$

where θ is the angle between the lipid acyl chain and the bilayer normal in the unperturbed bilayer, taken from literature (see Table 2.III). The factor 0.5 emerges because AFM probes only half of the total thickening

Results are given in Table 2.III. Agreement with the measured d_{dom} is reasonable. Some small deviations could occur through compression of the domains or the surrounding pure lipid bilayer by the AFM probe or uncertainties in θ.

The insensitivity of the spatial length scale r_{rep} to hydrophobic mismatch is especially noticeable as the mismatch covers a relatively large interval. The magnitude of r_{rep} in Fig. 2.3.c implies that the lines of WALP are spaced by a similar number of lipids for $14 < n < 18$, *i.e.* 4 - 5 lipids [117]. The increase of r_{rep} from 7.8 nm at $n = 18$ to 8.8 nm at $n = 20$ could imply that one more lipid molecule is involved, broadening the row to 5 - 6 lipids (using the diameter of one ordered gel-state DPPC lipid = 0.8 nm [30, 235]). Rinia *et al.* [122] also found minor changes in the striated domains when varying the extent of mismatch through the length of the $(Ala\text{-}Leu)_X$-repeat of WALP. Other examples are known of (model) proteins that respond hardly or not at all to the presence of mismatch. Their aggregation [105], partitioning [236] and binding properties [69, 89] depend on other factors.
This is in contrast to the many (theoretical) studies that predict an increase of the coherence length (and hence r_{rep}) over which lipid deformations emanate from an embedded protein with increasing mismatch [87, 102]. The invariance of r_{rep}, however, suggests that this mechanism does not dominate and that its magnitude is set by some other property. The nature of this property will be investigated further in the following chapters. Apparently, most changes in the mismatch are absorbed by the small strip of 1 - 2 chain-disordered lipids [117] that border the lines of WALP (see Fig. 2.10). The difference in the extent of disorder of these boundary lipids or variations in the possible small remaining tilt angle of the acyl chains in the striated domains may account for the observed differences in the number of curves of the stripes for different n.

Table 2.III Calculated and measured $d_{dom,calc}$ and d_{dom} for gel-state PC lipids with different lengths n. The hydrophobic thickness d_{HPH} of the tilted bilayer and polar tilt angles θ from literature are used to calculate $d_{dom,calc}$

lipid name	**acyl-chain composition (*n*:*u*)**	**d_{HPH} (nm) literature**	**θ (°) literature**	**$d_{dom,calc}$ (nm)**	**d_{dom} (nm) measured**
DMPC	14:0	3.0 - 3.2	26 [232], 24 [234]	0.1 - 0.2	0.2 ± 0.1
DPPC	16:0	3.3 - 3.6	30 - 32 [19, 29, 30]	0.3	0.3 ± 0.1
DSPC	18:0	3.5 - 3.6	33.5 [8], 40 [29]	0.3, 0.5	0.4 ± 0.1
DAPC	20:0	4.0 - 4.1	35.2 [30]	0.4 - 0.5	0.5 ± 0.1
DPPC/DSPC	16:0/18:0	3.4 - 3.6	- [a]	0.4	0.4 ± 0.1

a No literature values were found

Very large mismatch conditions at $n \geq 20$ are met by (partial) exclusion of the WALP as the energetic cost of lipid disordering gets too high and exclusion becomes more favourable [71, 190, 191]. For di-22:0-PC and di-24:0-PC bilayers, inclusion of WALP seems limited to ~ 0.5

mol% as these surfaces showed a large similarity to the 0.5 mol% WALP-system in Fig. 2.5. Insertion of WALP and other model peptides is known to be limited or even prohibited when the hydrophobic mismatch is large, for both negative and positive values [71, 190, 191].

Finally, the mixed di-16:0-PC/di-18:0-PC/2 mol% WALP23 bilayer in Fig. 2.8.f shows striated domains with r_{rep} = 7.9 ± 0.6 nm. d_{dom} falls between the values for n = 16 and 18.
The presence of WALP does not induce large-scale separation into regions of shorter and regions of longer lipids ('lipid sorting'). Such heterogeneity in lipid composition was observed in fluorescence studies where proteins surrounded themselves with the best-matching lipids [240, 241]. It was shown previously, however, that WALP23 does not induce lipid sorting in mixed fluid di-14:-PC/di-18:1-PC or di-16:1-PC/di-20:1-PC bilayers [242]. It is believed that the small cross-sectional radius of the α-helix lets WALP23 interact differently with the surrounding lipids than larger proteins do [70]. This makes adaptations of the lipid around WALP energetically less costly, while larger proteins are more likely to induce lateral separation of the lipid mixture [70, 74, 242, 243].

2.4.c Palmitoylated WALP23

Attachment of a palmitoyl chain does not alter the peptide's propensity to form striated domains, indicating that no large shifts in the lipid-peptide and peptide-peptide interactions take place. The packing is somewhat altered as an increase in the repeat distance r_{rep} and a decrease in the regularity of the striated packing are observed. It will be assumed here that those changes are not related to any shifts in the backbone of the peptide, in correspondence with ^{2}H-NMR results for palmitoylated gramicidin A [244, 245]. Rather, the presence of the additional Pa-'tail' is likely to interfere with the ordered assembly of Pa-WALP and lipids into parallel lines. Probably, the first part of the fatty-acid chain in the vicinity of the amide-bond with the N terminus of the WALP will be stiff and contain a bend, as was determined for Pa-gramicidin A [244]. The latter part of the C16 chain adopts a conformation that is very similar to the surrounding lipids [244], which should be partially disordered in this case to match the lipids bordering the peptide [110]. The insertion of the upper part of the fatty-acid chain is probably incompatible with the hexagonal lipid packing and the spacing between the peptide rows increases to allow better accommodation of the Pa chain. The less ordered packing leads to less rigid intersection angles between the lines, accounting for the more curved appearance of the lines within the domains.

2.5 Conclusion

Striated domains form spontaneously in mixed gel-state bilayers of di-*n*:0-PC lipid/1 - 12 mol% WALP23 bilayers for n = 14 - 20 C-atoms. These domains can be observed with AFM and consist of alternating higher and lower lines with a repeat distance of ~ 7.5 - 8 nm. The total area of these domains increases with the amount of WALP23, with complete coverage of the surface at a lipid:peptide molar ratio of 8:1 - 10:1. The domains are elevated by ~ 0.3 nm

with respect to surrounding lipid bilayer. The lines show a distinct hexagonal packing as they curve at angles of 120°. The underlying substrate does not influence the observed topology as more free-standing double bilayers show exactly the same striated features. Changes in the ionic strength or the pH do not substantially alter the properties of the striated domains either. The area outside the striated microdomains contain PC lipids in the unperturbed, tilted gel L_{β}' phase.

The proposed molecular organization within the striated WALP/lipid phase is given in Fig. 2.10. Summarizing, single rows of WALP are separated by 4 - 5 lipids which have gel-like packed acyl chains but with a significantly reduced tilt angle. The ~ 1 - 2 lipids immediately adjacent to the peptide molecules have a reduced chain order to bridge the mismatch with the shorter WALP23 [110, 117]. The formation of the striated domains is driven by the low solubility of WALP in the gel-state bilayers, which expels the peptide to regions where it interferes less with the ordered lipid packing. Competition with attractive lipid-peptide interactions is thought to lead to a mixed lipid/peptide striated phase.

The length of the PC acyl chains between n = 14 - 20 does not alter the spacing between the stripes to a great extent. Only minor changes in appearance are detected as the number of straight segments of lines increase with the lipid length. However, incorporation of WALP becomes too limited to form striated domains in the longer n = 22 and 24 PC bilayers. This indicates a negligible role of hydrophobic mismatch in the formation and properties of the striated domains, except through the amount of WALP present.

Finally, covalent linking of a palmitoyl (C16:0) chain to the N terminus of WALP23 alters the packing behaviour of the peptide as the additional chain does not fit easily into the hexagonal packing of the lipids. As a result, the striped pattern becomes less well defined and the repeat distance is slightly enhanced.

Chapter 3

AFM study of the thermotropic behaviour of DPPC and DPPC/WALP23 supported bilayers

Abstract

Temperature-controlled Atomic Force Microscopy (TC-AFM) is used here to study the effect of the transmembrane model peptide WALP23 upon the melting kinetics of DPPC bilayers. Melting from the gel $L_{\beta'}$ phase to the fluid L_{α} phase begins at packing defects (grain boundaries) in pure DPPC bilayers. The exact measured value of the melting temperature T_M is determined largely by the force exerted by the AFM probe. The reverse process of cooling from the fluid L_{α} phase shows that grain boundaries form at the borders where different gel areas meet. A faster rate of cooling increases the number of these lines.

The presence of WALP in gel-phase DPPC bilayers leads to the formation of domains with a mixed lipid/WALP striated phase. The lipids in the striated domains have a lower T_M than those in the pure DPPC bilayers, which can be ascribed to effects of hydrophobic mismatch. The striated pattern seems to disperse around T_M. Upon cooling, the striated domains are re-formed. A lower rate of cooling leads to larger striated domains, but other properties of the striated phase remain unaffected.

3.1 Introduction

Phase behaviour of lipids has been widely investigated for decades (see for example [3, 14, 19, 29, 81] and references cited therein). This interest has been largely motivated by the comprehension that the introduction of lipids with a different physical state into biological membranes plays a role in various processes, such as membrane fusion [12, 49], microdomain formation [48, 96], and protein insertion, translocation, aggregation and functioning [3, 12, 13, 84, 88, 89, 92, 109]. The phase adopted by the lipid bilayer is closely related to factors such as the individual chemical composition of the polar heads or methylene chains of the lipid molecules [11, 14, 15], temperature [14, 19, 20], hydration [12, 19] and the presence of various additives [12, 14, 25, 26]. Proteins themselves have been shown to play an active role in affecting lipid phase behaviour. They can substantially shift and/or broaden phase transitions, alter the accompanying enthalpy or lead to the formation of new phases that are not encountered in pure bilayers under the same conditions [3, 60, 66, 76, 81, 98, 100, 246].

An attractive model system to study this complicated interplay of lipid and protein interactions in relation to phase behaviour is that of the model peptide WALP23 in DPPC bilayers. The presence of the single α-helical WALP gives rise to lateral heterogeneity in the otherwise smooth gel-state DPPC bilayers as mixed lipid/peptide domains with a striated appearance are formed spontaneously [33, 110, 117, 122]. The striated ordering is strongly dependent on lipid phase behaviour as fluorescence spectroscopy indicates a disaggregation of WALP upon entering the high-temperature fluid L_α phase [110]. Moreover, DSC analysis has revealed a WALP-induced shift and loss of cooperativity of the main melting transition of DPPC bilayers [33, 67, 80].

In this chapter, both the influence of the lipid phase on the striated domains and the influence of WALP23 on the melting behaviour of DPPC bilayers are investigated with AFM. This melting process involves the transition from the solid gel $L_{\beta'}$ phase to the fluid or liquid-crystalline L_α phase (see Fig. 1.4) [3, 10, 28]. This transition is accompanied by a large increase in lateral and rotational motions, which are severely limited in the gel phase [247]. The order of the lipid's acyl chains decreases at the expense of the interchain Van der Waals interactions [10, 247] when the chain isomerism changes from a predominantly *trans*-state towards one with a substantial number of *gauche*-kinks [3, 34, 36, 37]. The chain order decreases from $S_{gel} = 0.98$ to $S_{fluid} = 0.58$ [29]
[2] and is accompanied by an expansion of the headgroup's in-plane area [38, 39] and a concomitant decrease in bilayer thickness of ~ 16 % [40].
Temperature-controlled Atomic Force Microscopy (TC-AFM) is used here to directly image the mechanism by which melting and crystallization of supported DPPC bilayers in the presence and absence of WALP23 proceeds. TC-AFM has been used successfully in the past to

[2] The order parameter S is a measure for the ordering of the acyl chains and can be measured by ^{2}H-NMR. $S = ½ < 3 (\cos^2 \theta) - 1 >$ with θ the angle between the bilayer normal and a chemical bond between a C and ^{2}H atom [72, 248]

image melting processes in pure lipid bilayers [54, 144, 152, 205] and peptide-containing bilayers [151], and can complement results obtained previously with indirect techniques.

3.2 Materials & Methods

Supported lipid and mixed bilayers of DPPC/2 mol% WALP23 were prepared via the vesicle fusion method [127, 147], as described in section 2.2. Samples were imaged on the same day of preparing the supported bilayer and within 0 - 3 days after vesicle preparation. Details of the AFM imaging and height determinations are also described in section 2.2. Features provided by the PicoScan 5.2 software (Molecular Imaging Corporation, Phoenix, USA) were used to determine the relative areas of L_α phase.

In this chapter, d_{gel} is defined as the height difference between the top of the gel state membrane and the mica support (see Fig. 3.1) and can be measured through holes in the sample. d_{gel} is the sum of the thickness of the pure bilayer d^0_{gel} and that of the layer of water d_w. The thickness of the fluid bilayer d_{fluid} was calculated from the height differences at the borders between gel and fluid patches ($\Delta d_{gel\text{-}fluid}$) in the coexistence-region, but was measured directly through infrequently encountered holes in the bilayer at temperatures above the gel-fluid coexistence-region (T > 44 - 46 °C). d_{dom} gives the difference in height between the higher, whiter parts of the striated domains and the top of the surrounding bilayer. All presented images are in the topographic mode, unless stated otherwise.

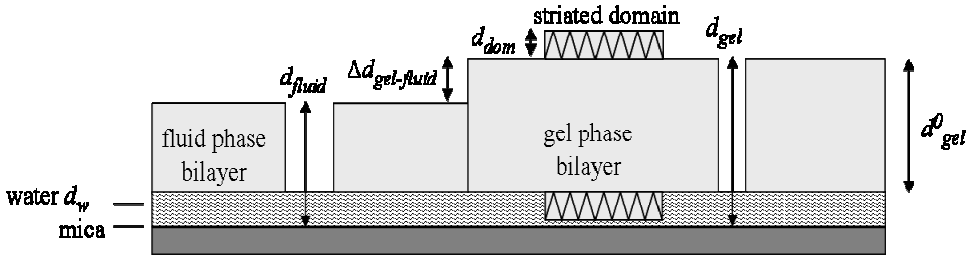

Fig. 3.1 Definition of the various heights measured with AFM. The grey rectangle denotes the supported bilayer, which is separated from the mica substrate by a layer of water of thickness d_w. d_{gel} and d_{fluid} are the bilayer thicknesses of the fluid (left) and gel phase (right). The difference between the gel and fluid phase $\Delta d_{gel\text{-}fluid}$ can be measured directly at the edges of coexisting gel and fluid patches. The height of the striated domain on top of the bilayer (d_{dom}) is measured as the difference between the higher lines of the domain and the top of the surrounding gel-phase bilayer. d^0_{gel} gives the thickness of the bilayer without the layer of water

Samples were heated and cooled by placing the hydrated, supported bilayer on top of a sample stage with an adjustable temperature: a heating stage for temperatures above room temperature and a 1x Peltier stage below room temperature (Molecular Imaging Corporation, Phoenix, USA). A LakeShore Model 330 Temperature Controller regulated the temperature of these

devices. The temperature on top of the sample was found here and by [54] to deviate from the chosen setpoint temperature, which is measured at the underside of the sample stage. A Pt-100 sensor mounted with a flat metal disk as probe (Ø 4.8 mm; Sensycon, Alzenau, Germany) was used to calibrate the temperature on top of the sample while it was immersed in measuring liquid. All temperatures mentioned in this chapter are corrected values and have an error of ~ 1 - 2 % due to thermal fluctuations of the heater. For large temperature steps of $\Delta T \geq 5$ °C, the scanning was stopped and the temperature was increased with a 5 °C/min ramp, followed by a 15-minute equilibration period. For small steps ($\Delta T = 0.5$ - 1 °C, ramp rate 5 °C/min), scanning was continued while the force setpoint of the AFM tip was adjusted simultaneously to compensate for the swelling or shrinking of the sample and tip. The sample was monitored for at least 15 minutes at each temperature to check that no further changes in morphology occurred. The temperatures that are used here to characterize the melting transition are T_{onset} and T_{end}. These are defined as the temperature where the first amount of fluid phase is observed (T_{onset}) and the temperature where no gel-phase material is left (T_{end}).

The cooling rate of the $L_\alpha \rightarrow L_\beta'$ transition mentioned in the text refers to the speed by which the sample is cooled after the final heating step of the sample preparation (heating at 65 °C). This was varied by either turning off the insulated oven and letting it cool to room temperature (cooling rate ~ 0.6 °C/min), removing the sample from the oven (~ 10 °C/min) or rinsing it immediately with a 20 mM NaCl solution precooled on ice (> 50 °C/min).

3.3 Results

3.3.a Supported DPPC bilayers

Supported gel-state DPPC bilayers exhibited no significant changes in their overall bilayer height d_{gel} of 5.2 - 5.4 nm (■ solid squares in Fig. 3.2.a) or overall surface topology (Fig. 3.3.a) in the temperature range from 5 to 35 °C. A number of packing defects (grain boundaries) were visible as thin lines with a depth of ~ 0.2 - 0.3 nm [53, 117, 211]. Above $T \approx 35$ °C, some minor features altered as holes puncturing the bilayer became progressively rounder and smaller (data not shown). d_{gel} decreases. Remaining unopened vesicles on top of the bilayer collapsed during scanning at approximately $T > 32$ °C. These punctured vesicles unfolded and merged with the bilayer, leaving circular indentations at its edge (Fig. 3.4.a and [250]).
A second phase with a significantly reduced height was formed at $T \geq 40.4$ °C (□ open squares in Fig. 3.2.a). The average height d_{fluid} of this liquid-crystalline L_α phase was 3.7 ± 0.4 nm and the average direct difference $\Delta d_{gel\text{-}fluid}$ was ~ 0.7 nm.

The observed phase transition can be ascribed to the main phase transition from the gel L_β' to the fluid or liquid-crystalline L_α phase [54, 131, 151]. This phase transition was subjected to closer inspection by increasing the temperature stepwise with increments of 0.5 or 1 °C, while scanning a single area of the DPPC bilayer. A selection of these scans is shown in Figs. 3.3.a - f. All these topographs were obtained approximately 5 minutes

after the temperature step, although all changes in temperature were reflected immediately upon the topology and no further changes took place upon repeated imaging during 10 - 15 minutes. Subsequent scans could not be made at exactly the same *xy*-coordinates, as lateral drift caused movement of the scanned area. Fortunately, some distinctly shaped features (*e.g.* a V-shaped branch or holes) provided anchoring points by which the relative position of the different images could be determined. These are marked with identical symbols in the different scans of Fig. 3.3.

Upon heating of the bilayer, a noticeable widening of the grain boundaries (Figs. 3.3.b, c) marked the onset of the melting transition at T_{onset} = 40.4 °C for relatively high scanning forces of F = 0.7 - 0.9 nN. They continued to expand progressively while the lower, liquid-crystalline L_α phase grew at the expense of the higher, gel L_β' phase region. The conversion was completed at T_{end} = 44.4 °C (Fig. 3.3.f). The progress of the $L_\beta' \rightarrow L_\alpha$ transition is quantified in Fig. 3.2.b (solid squares ■) where the relative area covered by the L_α phase is given as function of temperature. The shallow initial slope (T = 40.4 - 41.4 °C) is followed by a much steeper slope at T = 42.4 - 44.4 °C.

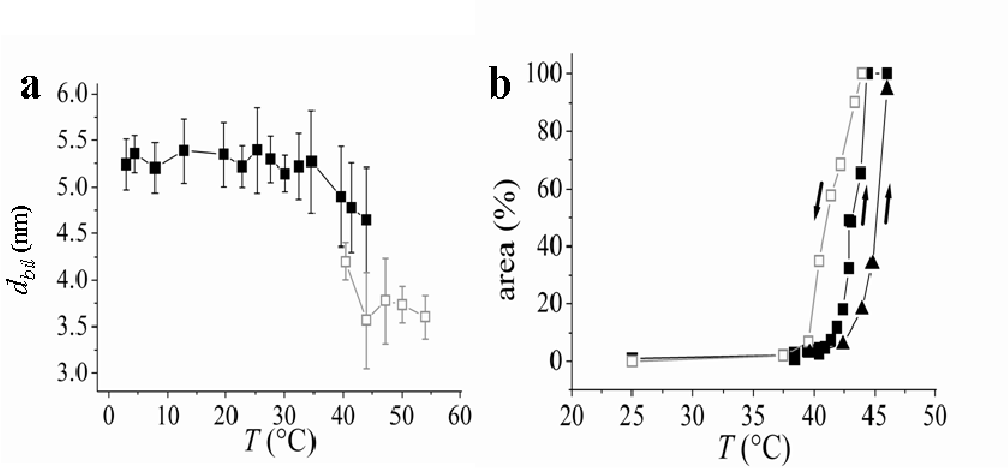

Fig. 3.2.a. Thickness of the bilayer in the gel L_β' (d_{gel}, ■) and liquid-crystalline L_α phase (d_{fluid}, □) as function of temperature T. **b.** Area covered by the liquid-crystalline L_α phase as function of temperature T: heating scans at low (▲, F = 0.1 - 0.6 nN) and high (■, F = 0.7 - 0.9 nN) imaging forces F and cooling scan at F = 0.7 - 0.9 nN (□)

Determination of transition temperatures with AFM is not unambiguous, as is shown by the two heating-curves in Fig. 3.2.b. These differ only in the force exerted by the AFM tip during scanning. Lowering the force postponed the onset of the transition T_{onset} from 40.4 °C (solid squares ■, F = 0.7 - 0.9 nN) to 42.4 °C (solid triangles ▲, F = 0.1 - 0.6 nN) and T_{end} from 44.4 °C to 46.0 °C. This is also illustrated in Figs. 3.5.a - c where the same surface region is imaged at three imaging forces, causing the area of L_α phase to change from ~ 0.5 to 2 %.

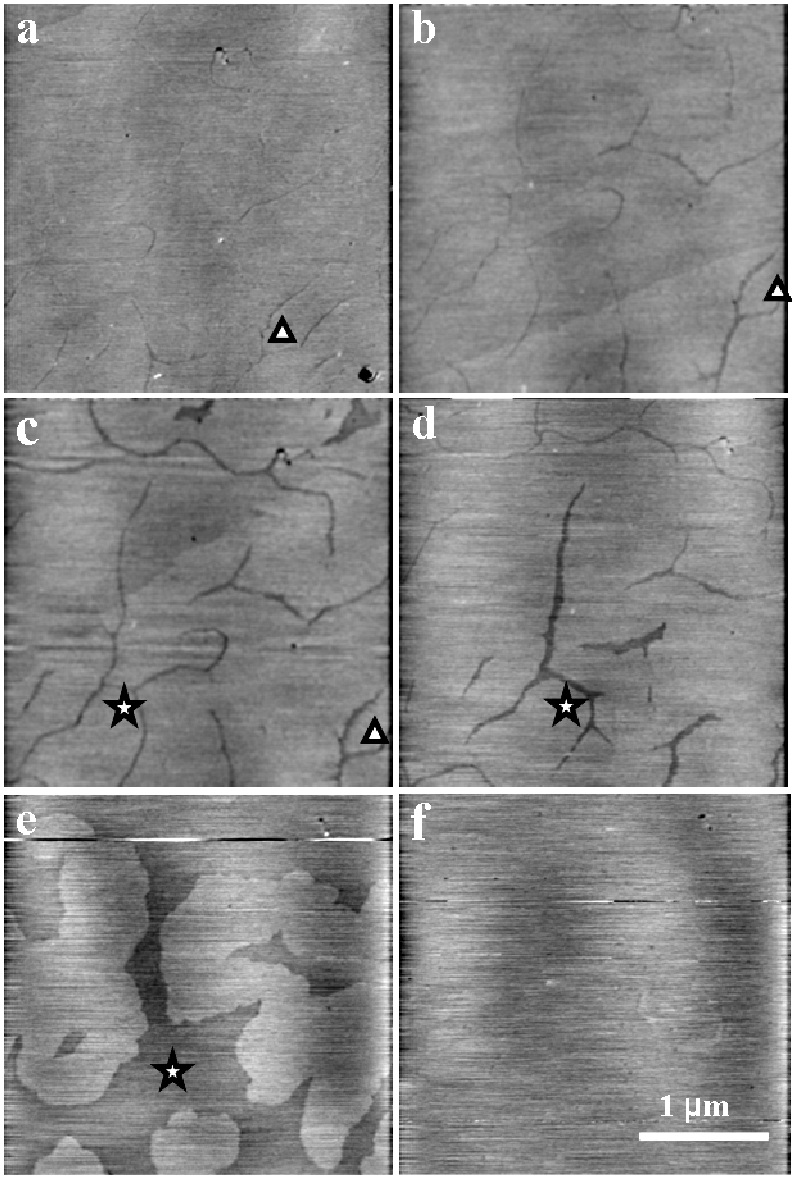

Fig. 3.3 Subsequent AFM scans of the melting of a supported DPPC bilayer at **a.** 39.4 °C, **b.** 40.4 °C, **c.** 40.9 °C, **d.** 41.9 °C, **e.** 43.9 °C and **f.** 44.3 °C at a relatively high scanning force *F* of 0.7 - 0.9 nN. Identical symbols mark the same characteristic features in the scans. All images have the same lateral and height scale. The total height scale is approx. 1 nm.

The reverse process of cooling the L_α DPPC bilayer led to the reappearance (Fig 3.6.a) and growth of L_β' domains. The different gel patches approached each other and met (Figs. 3.6.b - e), thus creating the characteristic line-type packing defects at their borders (Fig. 3.6.f). Holes appeared and expanded during the cooling process. A pronounced hysteresis of ~ 2 - 3 °C with the heating curve is observed (Fig. 3.2.b, □).
The rate used to cool a supported DPPC bilayer from the L_α to L_β' phase manifested itself through the amount of grain boundaries and continuity of the layer. The number of these boundaries was enhanced by a faster cooling rate. Table 3.I gives an approximation of the cumulative length of these lines per area unit (boundary line density ρ_{line}). The number of holes and unopened vesicle remnants also increased with the cooling rate for the same initial amount of vesicle dispersion (data not shown).

Table 3.I Approximation of the boundary line density ρ_{line} (error ~ 20 %)

cooling rate (˚C/min)	ρ_{line} **(µm/µm^2)**
0.6	1
10	3
> 50	5

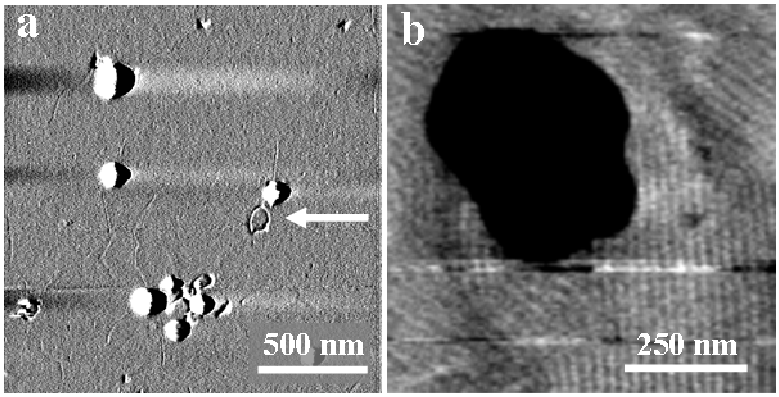

Fig. 3.4.a. Circular indentation (indicated by the white arrow) resulting from the collapse of an unopened vesicle, together with partially flattened vesicle features (white spherical structures). The deflection image is shown here rather than the topographic image as this gives a clearer view, although information on height is lost. **b.** Ripple P_β' phase formed at 38 °C on a double bilayer with a large hole. The ripple periodicity of 16 ± 1 nm is in agreement with literature values of 15 nm for the so-called Λ/2-ripple phase [150]

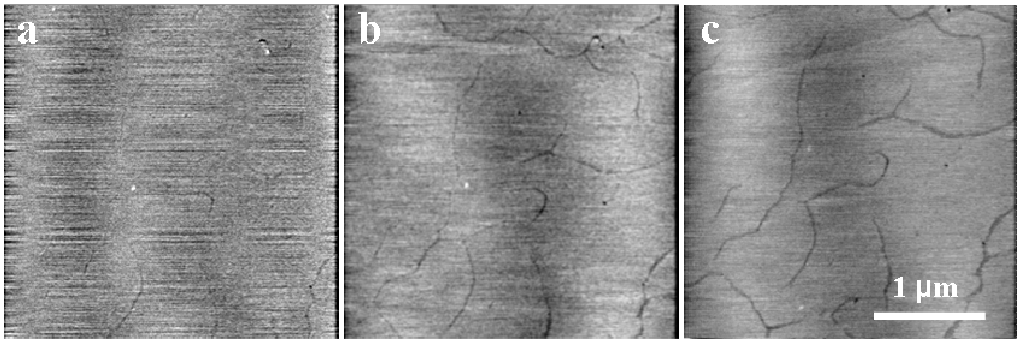

Fig. 3.5 Effect of the imaging force F upon the amount of L_α phase at 40.9 °C. The area occupied by this phase increases from **a.** < 0.5 % at $F \approx 0.4$ nN via **b.** 1 % at $F = 0.9$ nN to **c.** 2 % at $F = 2$ nN

3.3.b Mixed DPPC/WALP23 bilayers

Striated domains that are elevated with respect to the surrounding lipid areas are formed in mixed DPPC/2 mol% WALP23 bilayers ([33, 117, 119, 122] and Figs. 2.6 and 3.8.a). These domains contain rows of lipids with a modified packing, which alternate with single rows of the shorter WALP23 [110]. The spacing r_{rep} between the stripes remained fixed at ~ 7.7 nm (Table 3. II) between $T = 8$ - 35 °C. Neither did the domain height d_{dom} show any appreciable deviations from 0.3 - 0.4 nm in the gel-phase region between T = 3 and 25 °C (first part of Fig. 3.7), but a slight reduction was observed between 25 - 35 °C. A crossing over of d_{dom} to negative values took place at a higher temperature T_{dom}. This 'sinking-in' or melting of the complete domain with respect to the surrounding bilayer is shown in the AFM micrographs of Fig. 3.8.
The exact transition temperature T_{dom} was again force dependent. It was postponed from T_{dom} = 39.6 °C at relatively high scanning forces ($F = 0.7$ - 0.9 nN) to 40.4 °C at low forces ($F = 0.1$ - 0.6 nN). The two AFM micrographs in Figs. 3.9.a and b show one region at $T = 39.6$ °C imaged at two scanning forces. The higher force converted the higher striated domain (stripes barely visible) to a featureless, lower-lying area with the same contours. The used forces did not lead to any changes of d_{dom} at room temperature (data not shown).
The lipids outside the striated domains did not melt until ~ 44 °C.

The striated domains reappeared unaltered ($r_{rep} = 7.9 \pm 0.4$ nm) upon returning to room temperature after the heating steps (data not shown). A faster cooling rate of this $L_\alpha \rightarrow L_\beta'$ transition led to smaller, intercalated domains (Figs. 3.10.a - c, Table 3.III). The total area of the striated areas remained the same, as this is determined by the total WALP concentration of 2 mol% ([117, 122]).

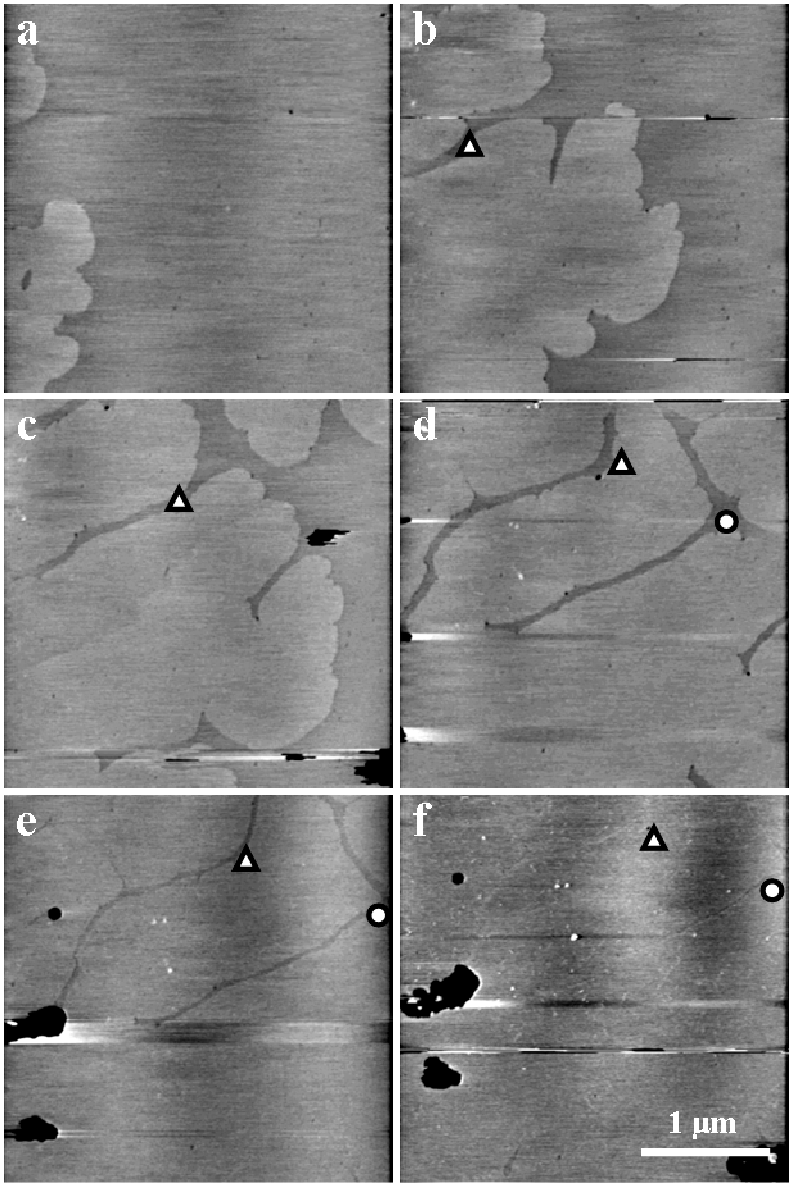

Fig. 3.6 Subsequent AFM scans of the cooling of a DPPC bilayer at **a.** 43.3 °C, **b.** 41.4 °C, **c.** 40.4 °C, **d.** 39.4 °C, **e**. 37.5 °C and **f.** 35.5 °C. In **f**, grain boundaries remain faintly visible. Identical symbols mark the same characteristic features in the scans. All images are 3 x 3 µm and have a total height (z) scale of ~ 1 nm

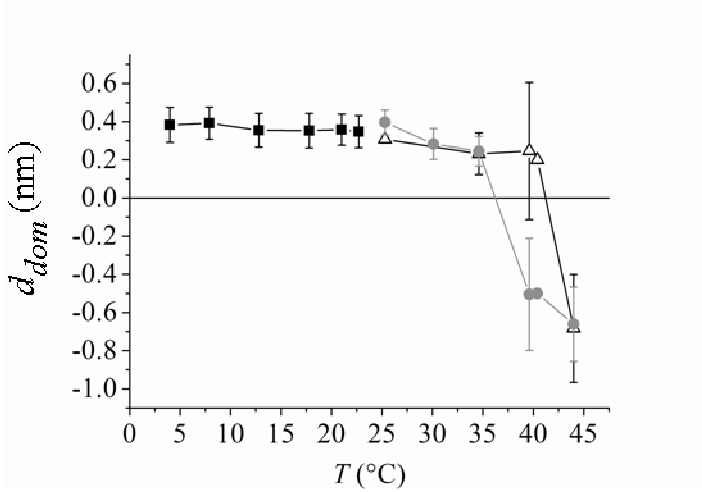

Fig. 3.7 Domain height d_{dom} as function of temperature T: ■ imaging forces F = 0.1 - 0.9 nN, Δ low force F = 0.1 - 0.6 nN and ● high force F = 0.7 - 0.9 nN

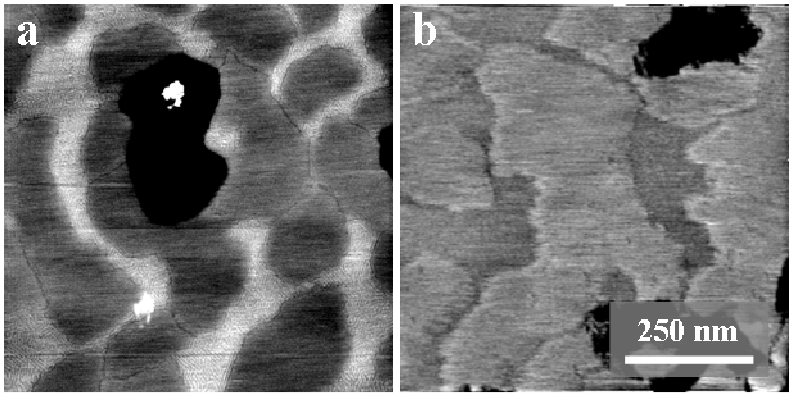

Fig. 3.8 Melting of the striated domains. **a.** Solid striated domains at 25.3 °C (lighter areas). The individual stripes are barely visible on this scale. **b.** Molten domains (darker grey areas) at 40.0 °C at a different position on the sample

Table 3.II Repeat distance r_{rep} at different temperatures T

T (°C)	r_{rep} (nm)
7.9	7.7 ± 0.5
12.8	7.6 ± 0.4
21.3	7.7 ± 0.5
30.1	7.7 ± 0.4
34.6	7.7 ± 0.6

Table 3.III Effect of the cooling rate upon the estimated diameter of the striated domains, domain height d_{dom} and repeat distance r_{rep} as function of the cooling rate of the $L_\alpha \rightarrow L_\beta'$ transition

cooling rate (˚C/min)	**typical length scale of domains (nm)**	d_{dom} **(nm)**	r_{rep} **(nm)**
0.6	801 ± 262	0.37 ± 0.09	7.8 ± 0.6
10	285 ± 119	0.33 ± 0.08	7.7 ± 0.5
> 50	63 ± 23	0.32 ± 0.09	7.7 ± 0.5

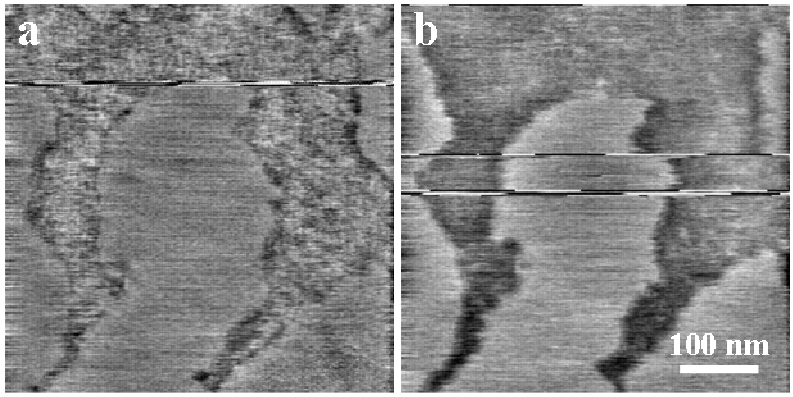

Fig. 3.9 Effect of the scanning force upon a striated domain at 39.6 °C. **a.** F = 0.6 nN and **b.** F = 0.9 nN

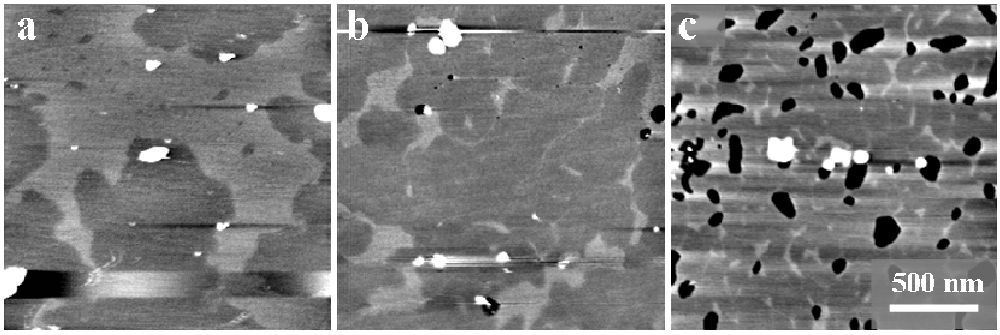

Fig. 3.10 Effect of cooling rate upon sample morphology at **a.** 0.6 °C/min, **b.** 10 °C /min and **c.** > 50 °C /min. The light-grey areas are the striated domains and the darker grey areas the surrounding lipid bilayer

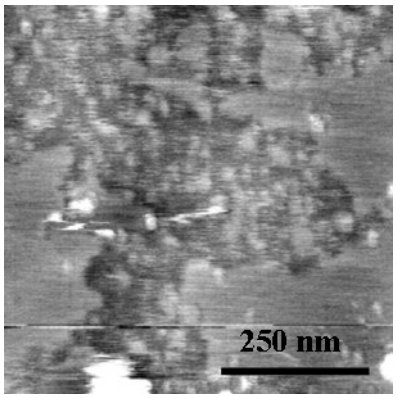

Fig. 3.11 Intermediate structure found near T_M (40 °C)

3.4 Discussion

3.4.a Supported DPPC bilayers

Phase behaviour

DPPC bilayers are in the solid gel $L_{\beta'}$ phase in the region from T = 5 to ~ 40 °C [29]. Other authors have observed no or only minor changes of typically a few percent for the tilt angle [77, 251], X-ray spacings [28, 252], chain ordering [36], and molecular area [32] and volume [253, 254] with temperature in this region. These slight changes have a minimal effect upon the bilayer thickness and fall within the error of d_{gel} (see Fig. 3.2.a). The slight reduction of d_{gel} at T > 35 °C is probably related to mechanical changes of the bilayer [38, 54, 127, 255], making it softer and thus more susceptible to deformation by the scanning tip. Additionally, the mechanical changes could cause the observed collapse of unopened vesicles at elevated temperatures of T > 32 °C. The low lateral diffusivity of the lipids in the gel state [256, 257] prevents subsequent sealing of the boundaries between the collapsed vesicle and the surrounding bilayer.

The liquid-crystalline L_α phase becomes visible as a lower phase at T_{onset} = 40.4 °C (high F) or 42.4 °C (low F). This is near the bulk main transition temperature T_M of 41.4 °C for DPPC [21, 29, 33, 258]. The measured average d_{fluid} of 3.7 ± 0.4 nm is comparable to the 3.6 nm obtained with AFM by Tokumasu *et al*. [131]. These values are underestimated as X-ray diffraction and neutron reflectivity predict a value for d_{fluid} of 4.6 - 4.9 nm (= sum of d^0_{fluid} of 3.6 [29] - 3.9 [39] nm and the layer of water with d_w of 1 nm [33, 199, 203] that is included in the AFM measurements, see Fig. 3.1). Again, deformations of the layer by the AFM probe could lead to deviations in height [133, 259].

Membrane melting on a solid substrate is a two-state process as no observable intermediates were found in either this or other AFM studies [151, 205] in this temperature range. Neither the

crystalline L_c' phase nor the ripple P_β' phase were observed here (see Fig. 1.4), although DSC and diffraction studies indicate their presence at respective temperature intervals of ~ 0 -20 ˚C [20, 21]) and 35 - 41 ˚C [19, 35]. The formation of the L_c' phase is kinetically limited and takes several days to form from the metastable L_β' phase at 0 - 4 ˚C [20, 21]. This is well outside the time scope of our experiments. Restricting bilayer-substrate interactions are thought to inhibit the formation of the P_β' phase in single supported bilayers, possibly by suppression of the surface undulations [152, 232, 260]. Ripple phase formation has been observed for more free-standing, doubly stacked bilayers ([35, 150], Fig. 3.4.b).

Initiation of the main transition and further growth

The initiation [3] of the new liquid-crystalline L_α phase proceeds from well-defined starting points rather than randomly throughout the gel phase. Newly-formed L_α lipids require additional space within the tightly packed gel state bilayer due to the disordering of their chains and related expansion of the in-plane hexagonal crystal packing [3, 37 - 39]. Naturally present defects provide a convenient starting place for melting as the crystal packing is already significantly interrupted. Such defects are provided by the observed boundary lines, which are thought to demarcate areas of different azimuth lipid tilt angles (see also section 2.3.a and Fig. 5.3) [122, 211, 261]. The lipid's methylene chains could already possess some initial disordering and/or altered tilting at these grain boundaries at temperatures far below T_M. From there, it is an energetically small step towards the highly disordered L_α conformation. Note that it is a common phenomenon for crystal surfaces to act as initiation sites for melting and melt below the bulk melting point ('surface melting' [262 - 264]). This is observed in a wide range of non-biological systems, *e.g.* for crystals of Si, Au and deposited 2D-films of $Sn(CH_3)_4$ [265 - 267]. For lipid bilayers, initiation of a new phase at the grain boundaries was already predicted theoretically [268, 269].
Conversely, Tapping-Mode AFM studies on DMPC and DPPC bilayers [131, 152] show no boundary lines at low temperatures, either due to resolution differences [133] or a lack of the lateral stresses induced by Contact-Mode AFM, which could artificially 'stretch' the boundary lines. Nevertheless, the Tapping-Mode studies in [131] and [151] on DMPC do show a growth pattern that is very similar to that in Fig. 3.3.

The initiation of the melting transition is characterized by an initial slow increase of the area of the new phase with temperature in the first part of Fig. 3.2.b. Further growth, *i.e.* melting of the 'bulk' lipids outside the grain boundaries, leads to a steeper slope. Propagation of the new phase proceeds from the interface where contact with the gel phase takes place. This increases as the transition progresses. The more mobile and disordered acyl-chain configuration of the L_α phase is accompanied by an increase in lateral diffusivity [37, 221, 270] and an expansion of the area by 15 $Å^2$ [39] per lipid molecule. This leads to the rounding and shrinking of the naturally present holes starting just below T_{onset} (these data, [151, 152]). Holes are energetically unfavourable as they allow contact of the aqueous environment with the non-

[3] The word 'initiation' in used here rather than 'nucleation' as this latter process involves the crossing of an energy barrier, which is not the case here

polar membrane interior. In contrast, holes in the gel $L_{\beta'}$ phase continue to exist for long periods of time (this study and [54, 205]), owing to the low lateral diffusion rates of the lipids [203, 257].

The main transition temperature T_M

The melting transition is largely completed within the temperature interval of ~ 42.4 - 46 °C at low *F*. Other AFM studies have reported ranges of 44.8 - 51.4 °C [54] and 46.5 - 49 °C [151] for supported DPPC bilayers. These large differences can be attributed to experimental variations in heating rate, equilibration time and imaging speed and force. Another source for discrepancies could be ageing of the vesicle suspensions as samples of 4 - 5 days old had a T_{onset} that was increased by 1 - 2 °C. This might be due to chemical degradation of the sample by hydrolysis of the ester bonds. All presented data are therefore obtained from fresh vesicle suspensions not older than 3 days.

The melting temperature is susceptible to the imaging force of the AFM probe *F* (see Figs. 3.2.b and 3.5). The distinct broadening of the lines of L_α phase at higher *F* is likely to be due to an axial compression of the lipids in the immediate vicinity of the gel-fluid border. The $L_{\beta'}$ lipids near this boundary probably have a slightly modified chain ordering as the border between the $L_{\beta'}$ and L_α phase may be expected to extend itself over several lipid molecules. The scanning probe pushes down these softer $L_{\beta'}$ lipids more readily, thus creating an apparent T_M below the real $T_{M,real}$ that corresponds to zero force. Extrapolation of the two data sets leads to a crude estimate of $T_{onset,real} \approx 43$ °C and $T_{end,real} \approx 47$ °C.

In general, supported lipid bilayers have a less cooperative, broader melting range with a higher T_M than unsupported ones [54, 151, 205, 231, 271]. DSC thermograms of DPPC suspensions commonly span a total range of $\Delta T \approx 2$ °C [3, 14] and show one sharp, symmetrical endothermic peak centred around 41.4 - 41.5 °C [21, 29, 33, 260]. The total melting process in this study, however, spans a ΔT of ~ 4 °C. A DSC study of Yang *et al.* [231] where DPPC was adsorbed on fragmented mica shards, revealed that competing lipid-substrate interactions stabilize the gel phase and cause a substantial broadening of the main transition. The polar headgroups of the lower leaflet of the DPPC bilayer interact electrostatically with the negatively charged mica support [128, 137, 272]. This competes with direct lipid-lipid interactions.

The T_{onset} (DSC) of 42 °C of the DSC study of Yang *et al.* [231] is in accordance with the observed $T_{onset} = 42.4$ °C at low scanning forces. T_{onset} and T_{end} are chosen here rather than T_M as the former parameters are more clearly defined for both techniques. T_M (DSC) is indicated by the maximum of the excess heat-curve, which does not necessarily coincide with the midpoint of the transition as observed by AFM. T_{onset} will be defined here as the onset of broadening of the grain boundaries for AFM or as the point where the heat-capacity curve starts deviating from the baseline for DSC, respectively. T_{end} marks the point where the DSC trace returns to the baseline or where the area of L_α first reaches 100 % for AFM. The

measured T_{end} (AFM) ≈ 46.0 °C for low forces compares favourably with the temperature where the second DSC curve of Yang *et al.* [231] drops back at 47 °C (see below).

Yang *et al.* [231] also observed a splitting of the endothermic peak into two symmetrical sub-peaks with maxima at 42.4 and 44.5 °C. This was attributed to a conformational decoupling of the two leaflets of the bilayer. The lower-temperature peak then originates from the melting of the upper leaflet, whereas the higher-temperature peak originates from the melting of the substrate-stabilized leaflet. The temperature interval found in our AFM study encloses both these thermal peaks. The images in Fig. 3.3, however, do not indicate any decoupling as this would add a third phase of intermediate height with one leaflet molten and the other solid [273]. Such an intermediate phase with a height difference of a few Ångstroms should fall within the resolution capabilities of AFM [129, 140]. [4] On the other hand, a more gradual transformation process without clearly defined borders between these soft and deformable phases might obscure its detection. The thickness d_{fluid} shows a slight reduction at higher temperatures, which might suggest a two-step melting process that is not clearly resolved by AFM. The large error in d_{fluid}, however, makes a definite conclusion impossible. Note that a study of DPPC bilayers on a spherical silica support does not show any decoupling between the two leaflets [260].

However, a second phase transition is reported in some AFM studies on supported DMPC and DPPC bilayers [54, 151, 205]. Its onset lies much higher ($T_{onset,2nd}$ = 53 ºC [54, 205] for DPPC) than that of the second maximum in the heat-capacity curve of Yang *et al.* (44.8 ºC [231]). It seems unlikely that they correspond to the same thermal event. This temperature falls outside the scope of [231] and this study, where the focus lay primarily on the onset of melting. The nature of this transition is a matter of debate and has been attributed to either the formation of a high-temperature –possibly interdigitated– phase [205] or to the melting of the lower, substrate bordering leaflet [151]. No such high-temperature phase has been recorded for non-supported liposomes [34].

Crystallization process

Crystallization generally follows a two-stage mechanism comprising a nucleation step and a growth regime. This is also the case during the L_α to $L_{\beta'}$ transition. A sufficiently high supersaturation (≡ T_M - T_{actual}) during cooling drives the initiation of stable gel-state clusters that act as nuclei for further growth. These are the first lighter areas observed in Fig. 3.6.a. They proceed to grow from the boundaries outwards, until they meet. The growth rate slows down considerably near the completion of the transition at T = 39.5 °C, as indicated by the lower second slope in Fig. 3.2.b (open squares □). A computer simulation study on a coarse-grained lipid model predicted similar behaviour in the region where the expanding patches of gel phase start interacting [274].

[4] Theoretically, a maximal difference in height of 0.5 x $\Delta d^0_{gel\text{-}fluid}$ (X-ray) ≈ 0.4 - 0.6 nm (4 - 6 Å) is expected for this partially molten phase [29, 39, 200]

Lipids within different growing gel areas all have a polar angle of 30 - 32° [19, 29, 30] with respect to the bilayer normal, but are likely to possess different azimuth angles [122, 211, 261]. After complete solidification, the areas with a different tilt direction are each separated by a line-type boundary, *i.e.* a grain boundary. As far as we know, this is the first time the formation of these lines has been demonstrated in a microscopy study.
The pronounced hysteresis with the heating curve (Fig. 3.2.b) is unlikely to be due to slow dynamics of the transition. Rather, a shift of 1 - 2 °C has been reported for supported bilayers under the influence of lipid-substrate interactions [271]. Non-supported lipid vesicles exhibit a hysteresis of 0.4 °C at the most [21, 25].

The large effect of the cooling rate on the number of boundary lines is governed by the kinetics of the transition. The nucleation step just below T_M is likely to be the rate-limiting step [275]. Transport of lipids to the solid phase is not expected to be rate-limiting as the density of lipids is large and they do not need to bridge large distances to reach the growing new phase. Moreover, lateral diffusion is fast (in the order of 10^{-7} - 10^{-8} cm^2/s) in the L_α phase [257, 270], compared to 10^{-9} cm^2/s in the L_β' phase [270].
A faster cooling rate induces a larger average supersaturation during the time interval in which nuclei are formed as there is a finite time-lag before a steady-state nucleation rate is built up. Classical nucleation theory [276] states that a larger number of particles will be formed under these conditions. This will eventually lead to a larger number of continuous crystalline patches with a smaller size and hence more boundary lines. A similar dependency was observed by [201] for lipid monolayers.

3.4.b Mixed DPPC/WALP23 bilayers

The striated domains of DPPC/WALP23 remain unaltered below $T < 35$ °C. No significant changes in the properties of the DPPC lipids take place in this interval [28, 36, 77, 251 - 253], although the mechanical softening of the layers [38, 54, 255] leads to some reduction of d_{dom} with T (Fig. 3.7). WALP23 itself is expected to be unaffected by temperature and retain its α-helical conformation [82]. The disappearance of the higher-lying domains above $T > 35$ °C can be ascribed to melting of the lipids within the domains from their predominantly gel-like phase to the fluid L_α phase. The reduction of the domain thickness Δd_{dom} by 0.9 - 1 nm upon proceeding from the higher, solid domains to the sunken-in, molten ones corresponds to a final height of these molten domains of 0.5 - 0.7 nm below the gel bilayer outside the domains. This matches the $\Delta d_{gel\text{-}fluid}$ of 0.7 nm between the molten and gel-state lipids in the absence of WALP23.

The presence of WALP23 reduces the onset-temperature (T_{dom}) by $\Delta T_{WALP23} = 2.0$ °C (low F) and 0.8 °C (high F) compared to the T_{onset} of pure DPPC. DSC thermograms of DPPC liposomes already showed a lowering of the main transition temperature T_M of 0.8 °C induced by WALP23 [33] and an even larger lowering of T_{onset} by ≈ 1.8 °C because of a reduced cooperativity and broadening of the endothermic peak. This agrees with $\Delta T_{WALP23} \approx 2.0$ °C at low F. The downward shift of T_M is induced by the hydrophobic length of WALP23, which is

shorter than that of the $L_{\beta'}$-state DPPC bilayer. This causes stabilization of the thinner L_{α} phase over the thicker $L_{\beta'}$ phase [80, 102]. Stabilization of the phase with the closest matching hydrophobic length has been encountered in a large number of protein/lipid systems [33, 82, 87, 98]. The bilayer outside the molten domains remains unperturbed. Its higher T_{onset} of ~ 44 °C matches the value found for pure DPPC bilayers in the previous section.

An interesting question is whether the change of lipid packing properties upon transformation from the $L_{\beta'}$ to L_{α} phase affects the observed morphology of the striated domains. Unfortunately, any structures formed by the WALP-peptides within the molten domains will not be discernible as the length of the peptide is close to that of the L_{α} lipid phase [80]. However, careful inspection in the region just below T_{dom} reveals an irregular pattern (Fig. 3.11). This could be caused by disordering or partly disaggregating of the lines of peptide. Previous fluorescence spectroscopic [75, 110] and ESR measurements [74] indicated a disaggregation of WALP into mono- and dimers upon reaching the fluid state. Disaggregation in response to an altered lipid packing mode seems to be a more general phenomenon and is encountered for a number of proteins and peptides, *e.g*. bacteriorhodopsin [88], gramicidin A [76], (Mg^{2+}- Ca^{2+}) - ATPase [109], γM4 [277] and poly-leucine model peptides [69]. For WALP, disaggregation is probably related to an increase in lateral solubility when the bilayer converts from the gel to the fluid phase [110].

Finally, upon returning to the gel phase, the striated domains reappear. The average size of the domains is inversely proportional to the cooling rate (Table 3.III). The formation of large areas of unperturbed bilayer and large domains is favourable as the total interfacial contact area and hence the total free energy will be minimized. Slow cooling of the sample allows the peptides more time to diffuse towards the growing domains and accomplish this energy reduction. A qualitatively similar effect was observed by Rinia *et al*. [122]. The underlying physical interactions of stripe formation are not influenced as all other properties of the domains remain constant.

3.5 Conclusion

The advantage of a direct technique like AFM over indirect techniques in the study of lipid phase behaviour is evident from the presented results. Membrane regions have been identified that act as specific starting points for melting from the gel $L_{\beta'}$ to the liquid-crystalline L_{α} phase; an achievement not possible with non-microscopic techniques. Both phases can be distinguished clearly by the difference in thickness that accompanies the chain-disordering during melting. The pure DPPC supported model membranes start melting at grain boundaries where the crystal packing is perturbed. Interactions with the substrate stabilize the gel phase and broaden the associated temperature interval. Previous suggestions that a complete decoupling of the lower, substrate-bordering and upper leaflet of the bilayer takes place (DSC data of [231]) are not corroborated by these AFM data.

All measured transition temperatures are dependent on the force exerted by the AFM probe and are lowered as the force increases. This underlines the importance of minimizing the imaging force in the study of thermal transitions with AFM.

The reverse process of solidification of a DPPC bilayer from the $L_\alpha \rightarrow L_\beta'$ phase starts with the formation of small gel-state nuclei. Lipids in different areas are expected to have different azimuth angles, but similar polar angles of ~ 30° [29, 30]. The areas grow and meet during further cooling, resulting in the grain boundaries mentioned above. Faster cooling rates lead to a substantial increase of these line defects. This can be explained by the classical nucleation theory, where an increase in the number of nuclei and hence increase in the number of grain boundaries is predicted under these circumstances.

The DPPC lipids in the striated domains that are formed in the presence of the transmembrane peptide WALP23 melt at a temperature that is 1 - 2 °C lower than that of the surrounding WALP-free bilayer. The temperature-depressing effect of WALP23 can be explained by hydrophobic matching principles [102], which indicate a stabilization of the best-matching (fluid) lipid phase. Some dispersal of the lines of WALP seems to occur just below T_M, in agreement with the almost complete disaggregation of WALP found in fluorescence studies [110]. This indicates the importance of the lipid environment on the lateral distribution of the peptides.
Identical striated domains reappear upon cooling from the $L_\alpha \rightarrow L_\beta'$ phase at various speeds. This indicates a general and speed-independent underlying mechanism. Their size, however, is inversely proportional to the cooling rate.

Chapter 4

Effects of lipid packing upon the striated domains: the influence of DPPE, hexadecane and unsaturated acyl chains

Abstract

Striated domains are known to form in gel-phase bilayers of saturated PC lipids in the presence of the transmembrane model peptide WALP23. In this chapter, the influence of an altered lipid environment on the formation of these striated domains is investigated. PE and unsaturated lipids were chosen because of their biological abundance. First, increasing amounts of DPPC are replaced by DPPE in mixed WALP/PC/PE bilayers, which leads to disordering of the striped pattern into meandering lines and a reduction of the amount of WALP that is incorporated in the bilayer. It is shown that these changes can be attributed to structural changes in the bilayer. The loss of ordering of the striated domains can be specifically related to the loss of the intrinsic tilt angle of the DPPE acyl chain. This is confirmed by the similarity with a DPPC bilayer to which *n*-hexadecane is added, which also reduces the tilt angle.
In the second part of this chapter, PC lipids with an unsaturated *cis*-bond in their acyl chains were used. Pure bilayers of di-*n*:1-PC (*n* = 20, 22, 24) and (16:0,18:1)-PC (POPC) in the low-temperature phase show a corrugated surface with a substantial amount of line-type packing defects. Incorporation of WALP does not lead to any striated domains, but increases the number of packing defects. These results are discussed in terms of lipid packing, which is less efficient for the kinked, unsaturated lipid acyl chains than for saturated ones

4.1 Introduction

This chapter focuses on the relation between the lateral assembly of the model peptide WALP and lipid structure. The very regular, self-assembled striated microdomains that are formed by the single α-helical model peptide WALP in DPPC bilayers lend themselves well for the evaluation of the various parameters that influence the mutual packing of lipids and proteins [33, 110, 117, 122]. Within the striated structure, the peptides are aligned in linear aggregates of single molecules. These are spaced by rows of approximately 4 - 5 gel-state lipids with an altered conformation compared to the pure DPPC gel state (see Fig. 2.10) [110, 117]. Thus far, only PC lipids have been used in the study of striated domains, but it would be interesting to determine whether the propensity to form striated domains is influenced by the type of lipid used. Other studies have shown that altering the structure and conformation of the participating lipids within biological and model membranes can have large consequences for the lateral organization, the mode and extent of association with the membrane, as well as the conformation and functioning of various proteins [11, 13, 53, 57, 75, 79, 88, 92 - 95, 97, 109, 113, 277]. This is of biological relevance.

In the first part of this chapter, the addition of DPPE (1,2-dipalmitoyl-*sn*-glycero-3-phospho-ethanolamine, di-16:0-PE) lipids to mixed gel-state DPPC/WALP bilayers is investigated. This choice is motivated by the high abundance of PE lipids in natural membranes [38, 361]. DPPC and DPPE have almost identical chemical structures [3, 247]: they are both zwitterionic and neutrally charged over a wide range of pHs [3]. In fact, the only difference is that the three terminal methyl groups in PC are substituted by hydrogen groups in PE, as shown in Fig. 1.2.a. PE and PC bilayers have a substantially different packing, however. Unsaturated PE lipids have a large tendency to form non-lamellar structures [17, 18, 50, 279], unlike unsaturated PC lipids. Long-chained, saturated PE and PC members, such as DPPE and DPPC, form lamellar bilayer structures at ambient temperatures and pH [29, 203, 256]. Both DPPC and DPPE have a comparable backbone conformation [281] and similar hexagonal packing of their all-*trans* acyl chains [17, 23, 31, 282]. The packing of DPPE in the gel phase differs from that of DPPC as the hydrocarbon chains of the former adopt a non-tilted L_β-configuration [17, 46, 203, 283], in contrast to the tilted $L_{\beta'}$-configuration of DPPC [17, 19, 31, 32, 254, 284] (see Fig. 4.1). Additionally, the PE polar groups form a tightly packed network by intermolecular hydrogen bonding between the ammonium group and the phosphate group [15, 285, 286]; a capability that is absent in the methyl-capped PC headgroups [283]. The apparent ambiguity in packing mode is explained by steric effects: the PC group has a much larger cross-sectional area (47 - 47.9 $Å^2$ [3, 235, 251]) than the smaller and less hydrated [15, 29] PE group (area 41 - 42 $Å^2$ [148, 206, 287]). In PC, this exceeds the area of the two acyl chains together (40.8 $Å^2$ [3, 10, 19, 235, 288], Fig. 4.1.a). The lipid hydrocarbon chains tilt away from the bilayer normal until their projected area matches the molecular area of the headgroup to prevent voids in the packing and maximize the mutual interchain Van der Waals attractions (Fig. 4.1.b). The

smaller headgroup area of PE does not impose such packing constraints and no need for tilt arises (see Fig. 4.1.c) [31].

Another way to decrease the tilt angle of the acyl chains is by adding *n*-hexadecane (HXD, $C_{16}H_{34}$) to DPPC bilayers. Comparing the results of this system to those of the DPPE containing bilayers allows discrimination between the effects of acyl-chain tilt and other effects of DPPE. The reduction of the tilt angle by HXD [47, 288 - 290] is due to an enlargement of the projected area of the lipids as each alkane molecule aligns parallel to the lipid methylene chains [44, 46, 289] and adds 20.4 $Å^2$ [288, 291] (see Fig. 4.1.d). This eliminates the driving force for tilting. The alkanes do not affect membrane properties such as the curvature and bending modulus [292].

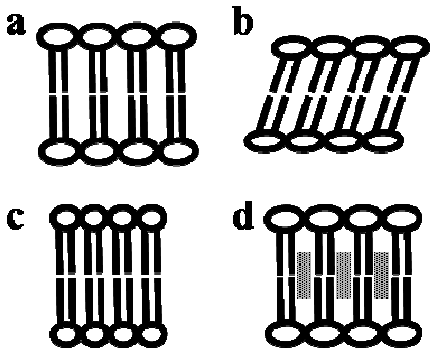

Fig. 4.1 Schematic representation of the packing in **a.** a non-tilted DPPC bilayer, which shows the voids between the acyl chains created by the mismatch in area between the PC headgroup and acyl chains, **b.** the much more favourable packing of a tilted DPPC bilayer, **c.** a DPPE bilayer [10] and **d.** a hexadecane-containing DPPC bilayer. Lipids are depicted as a spherical headgroup and two tails and hexadecane as grey rectangles

In the second part of this chapter, the role of another type of lipids is investigated, *i.e.* unsaturated lipids. Most lipids in biological membranes contain one or more *cis*-unsaturated bonds in their hydrocarbon chains [3, 10, 29, 293]. This hinders the lateral packing in the bilayer as the unsaturated bond induces a kink in the lipid chains, which is not compatible with the most efficient parallel packing of the chains. The chain disorder and area per lipid are increased [294]. This destabilizes the packing and drastically lowers the main transition temperature T_M and associated enthalpy ΔH_M [295, 296]. For example, bilayers of di-20:0-PC and di-20:1*c*11-PC have a T_M of 75 °C and - 4.3 °C, respectively [29, 295]. The experiments in this chapter are performed in the low-temperature solid state, as the tighter lateral packing of this solid phase is an essential requirement for the formation of striated domains in DPPC (see Chapter 3). Long, symmetrically di-unsaturated di-*n*:1-PCs (with n = 20, 22 or 24) and the asymmetric mono-unsaturated *sn*1-(16:0)-*sn*2-(18:1)-PC (POPC) were used. These all contain a *cis*-double bond between C9 and C10 from the chain terminus (see Fig. 4.2). These lipids

were chosen because they have a relatively easy attainable solid phase as their respective T_M's range from 27 to - 4 °C. Liquid-Atomic Force Microscopy (AFM) is used throughout to image changes in the morphology of the striated phase arising from changes in the lipid packing.

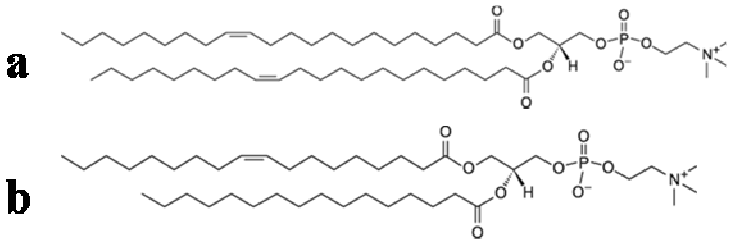

Fig. 4.2 Chemical structure of a **a.** di-22:1-PC (DErPC) and **b.** (16:0,18:1)-PC (POPC) lipid molecule. The kink in the acyl chain caused by the C=C bond is not shown, but was shown in Fig. 1.2.b. for OPPC

4.2 Materials & Methods

Supported bilayers were prepared by the vesicle fusion method of section 2.2 with some minor adjustments, as described below. All lipids were obtained from Avanti Polar Lipids Inc., Alabaster, USA at > 99.0 % purity. They were used as received without further purification. A 20 mM NaCl solution (Merck Darmstadt, Germany, p.a. grade; pH ~ 5.6) prepared with MilliQ-water with a resistivity of 18 MΩ/cm was used as aqueous phase, unless stated otherwise. Details of the (AFM) imaging and height determinations were also described in section 2.2. All experiments were performed at temperatures corresponding to the solid or gel phase of the lipids, which was room temperature (~ 22 °C) for DPPE/DPPC and HXD/DPPC, but lower for the unsaturated lipids. 2 mol% WALP23 was used, unless stated otherwise. This amount ensures that a sufficient number of the bilayer surface is covered by striated domains, if any are present.

DPPE/DPPC mixtures

Mixed DPPE/DPPC vesicles were made by mixing solutions of DPPC (1,2-dipalmitoyl-*sn*-glycero-3-phosphocholine) and DPPE (1,2-dipalmitoyl-*sn*-glycero-3-phosphoethanolamine; both in chloroform $CHCl_3$) in the appropriate amounts before adding the solution of WALP (in TFE = 2,2,2-trifluorethanol, Sigma-Aldrich, 99,5+ % NMR-grade). The temperature of all heating steps was increased to ~ 67 °C to compensate for the higher main transition temperature T_M of DPPE (64.0 °C) in comparison to that of DPPC (41.5 °C) [21, 29, 33]. Hydration of the dry, PE-containing lipid films was much slower than for pure DPPC films. This is a well-known property of PE lipids [31, 283]. Moreover, the dispersions remained slightly turbid, even after prolonged sonication. This indicates the presence of larger, aggregated or possibly multi-lamellar particles in the dispersion. This effect grew stronger with increased DPPE content. All vesicle dispersions were used within hours of their preparation as

larger aggregates became visible upon storage. In addition, the samples were measured within 3 hours after deposition on the mica substrate. The molar ratio of DPPE x_{DPPE} is defined as the initially added molar content of DPPE relative to the total lipid molar content (= [DPPE]/[DPPC + DPPE]).

HXD/DPPC

Mixed DPPC/*n*-hexadecane (HXD, $C_{16}H_{34}$, Janssen Chimica, 99 %) bilayers were prepared by dissolving the alkane in a 3:1 v/v $CHCl_3$/MeOH mixture and adding this to the DPPC (in $CHCl_3$/MeOH 1:3 v/v) or the premixed WALP (in TFE)/DPPC solutions. This method is similar to the one used by Boggs *et al.* [286] and McIntosh *et al.* [289]. The vacuum-drying step was omitted here as this led to evaporation of the hexadecane. Applying this same procedure to a HXD-free DPPC/WALP23 system did not influence the morphology of the sample. The initial HXD concentration is expressed in terms of the molar ratio x_{HXD} (= [HXD]/[HXD] + [DPPC]). Ratios x_{HXD} of 0.03, 0.08, 0.13, 0.38, 0.88 and 0.94 were used. These do not necessarily match the final amounts that are incorporated into the bilayer after sample preparation.

Unsaturated PCs

Long-chained, unsaturated PC lipids were used as the temperatures where they adopt the solid phase are more accessible than those of their shorter analogues. Di-unsaturated di-20:1*c*11-PC (1,2-dieicosenoyl-*sn*-glycero-3-phosphocholine, DEiPC; where *c*11 denotes a *cis*-unsaturated bond at C11), di-22:1*c*13-PC (1,2-dierucoyl-*sn*-glycero-3-phosphocholine, DErPC), di-24:1*c*15-PC (1,2-dinervonoyl-*sn*-glycero-3-phosphocholine, DNPC) and mono-unsaturated (16:0,18:1*c*9)-PC (1-palmitoyl-2-oleoyl-*sn*-glycero-3-phosphocholine, POPC) were used. The main transition temperatures of di-20:1-PC (T_M = - 4.3 °C [29, 295]), di-22:1-PC (T_M = 13.2 °C [29, 295]), di-24:1-PC (T_M = 26.7 °C [29, 295] and (16:0,18:1)-PC lipids (T_M = -0.8 °C to -4 °C [29, 287 - 289]) necessitated cooling to ensure the presence of a solid phase. Measuring temperatures of -6 °C for di-20:1-PC and (16:0,18:1)-PC, 4 °C for di-22:1-PC and 13°C for di-24:1-PC were obtained by mounting the sample on a Peltier I or II 3X sample stage (Molecular Imaging Corporation) that was connected to a LakeShore 330 Temperature Controller. The samples were cooled from room temperature to the desired measuring temperature at a rate of 1 °C/min, unless stated otherwise. Salinity was increased from 20 mM to 2 M for di-20:1-PC and (16:0,18:1)-PC to prevent formation of ice. 2 M NaCl depresses the freezing point of water by 8 °C [290]. This NaCl concentration did not have any effect on the properties of the striated domains in DPPC/2 mol% WALP23 bilayers (section 2.3.b). Other studies confirm that monovalent salts such as NaCl and KCl leave the structure of bilayer essentially unmodified [215, 216, 291]. Some deviations in measured heights were observed, however, for DPPC (section 2.3.a) and DPPE [43] due to altered interactions between the AFM probe and the sample [43, 134, 220].

Unsaturated lipids differ from saturated ones as they have a more loosely organized packing [288, 289, 292, 294, 295]. To investigate this further, a preliminary test was performed by

adding 1 - 4 vol% TFE (2,2,2-trifluorethanol, Sigma-Aldrich, 99.5+ %, NMR-grade) to the DPPC and DPPC/2 mol% WALP23 vesicle suspensions prior to applying it to the mica substrate. TFE also leads to a looser organization of the bilayer [13]. Imaging was done in the same 20 mM NaCl/(1 - 4 vol%) TFE-medium.

4.3 Results

4.3.a DPPE/DPPC

Mixed, gel-state bilayers with varying ratios of DPPE/DPPC showed flat, uniform surfaces with holes (see Figs. 4.3.a - e). Some thin line defects (grain boundaries [53, 117, 211]) were visible at $0.1 < x_{DPPE} \leq 0.4$, but were absent at $x_{DPPE} \geq 0.5$. A substantial amount of lipid debris was found on top of the surface and on the bottom of the holes at higher x_{DPPE} (data not shown). This consisted mainly of unopened vesicles and small regions with double bilayers. The hydrogen-bonded network of the PE-PE polar groups probably limited the unfolding and spreading of the vesicles.

The total bilayer thickness d_{bil} could be measured through holes piercing the bilayer and is plotted in Fig. 4.4.a as function of x_{DPPE}. An upward trend is unmistakably present in the first part of the plot, despite the large standard deviation. Levelling-off is observed at $x_{DPPE} > 0.5$.

4.3.b DPPE/DPPC/WALP23

The inclusion of 2 mol% WALP23 in pure gel-state DPPC model membranes gives rise to the formation of microdomains with a striated morphology (see Chapter 2). This pattern was made up of alternating single rows of the peptide WALP23 and lipid molecules with an adjusted conformation [110, 117].
The mixed DPPE/DPPC/2 mol% WALP23 bilayers with $0 < x_{DPPE} < 0.25$ contained striated domains that closely resembled those found in pure DPPC/WALP23 bilayers (Fig. 2.6). Neither their morphology (Figs. 4.5.a, b), nor the domain height d_{dom} (Fig. 4.4.b) nor repeat distance r_{rep} between the lines (Fig. 4.4.c) altered appreciably.

This is in contrast with the bilayers that contained larger amounts of DPPE ($x_{DPPE} \geq 0.25$), where the height of the striated domains d_{dom} with respect to the surrounding bilayer diminished as function of x_{DPPE} (Fig. 4.4.b). Secondly, the total area of the domains and the number of black lines decreased with increasing x_{DPPE}. Thirdly, the appearance of the striated phase was altered as the lines became more curved (Figs. 4.5.c - e) and their repeat distance

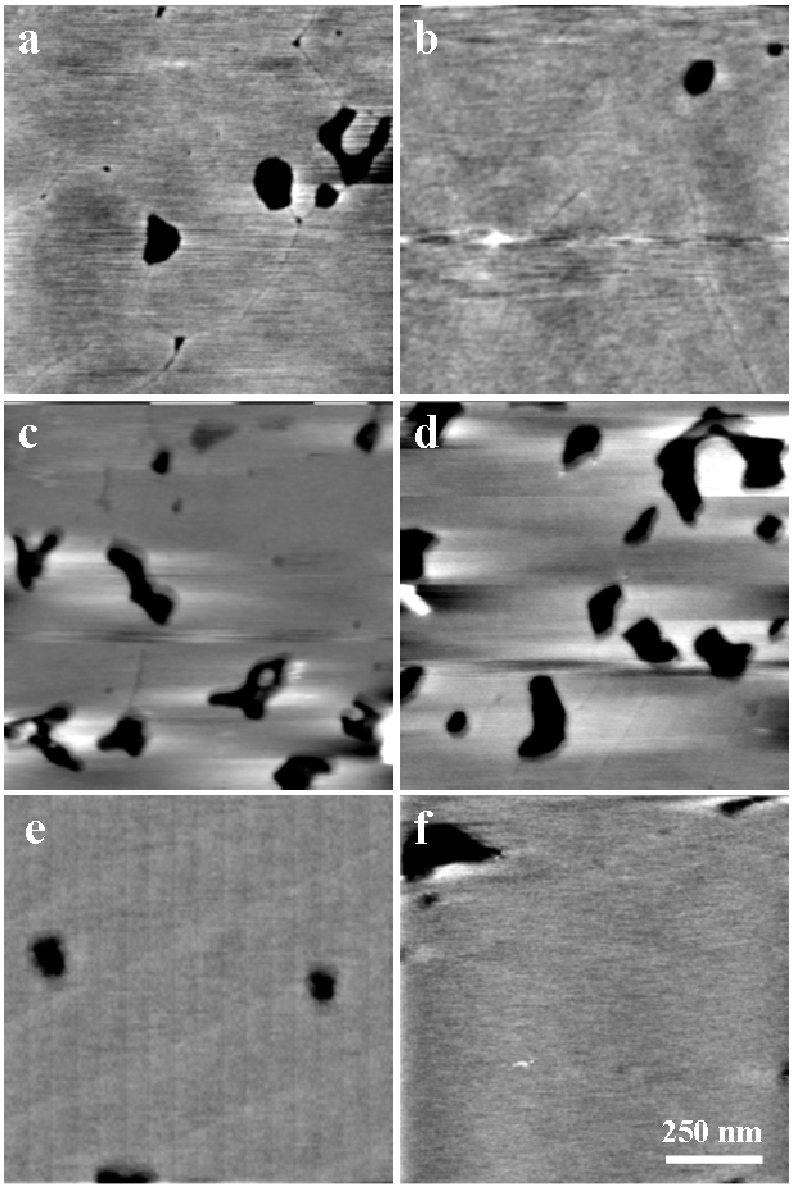

Fig. 4.3 AFM images of mixed DPPE/DPPC bilayers at a molar ratio x_{DPPE} of **a.** 0.1, **b.** 0.25, **c.** 0.3, **d.** 0.4, **e.** 0.6, **f.** 1. Flat surfaces with holes (black features) or unopened vesicles (white spherical features) are observed. Grain boundaries are visible as faint thin lines in **a** - **d**. All images have the same lateral dimensions. The regular raster pattern in **e** is a measuring artefact

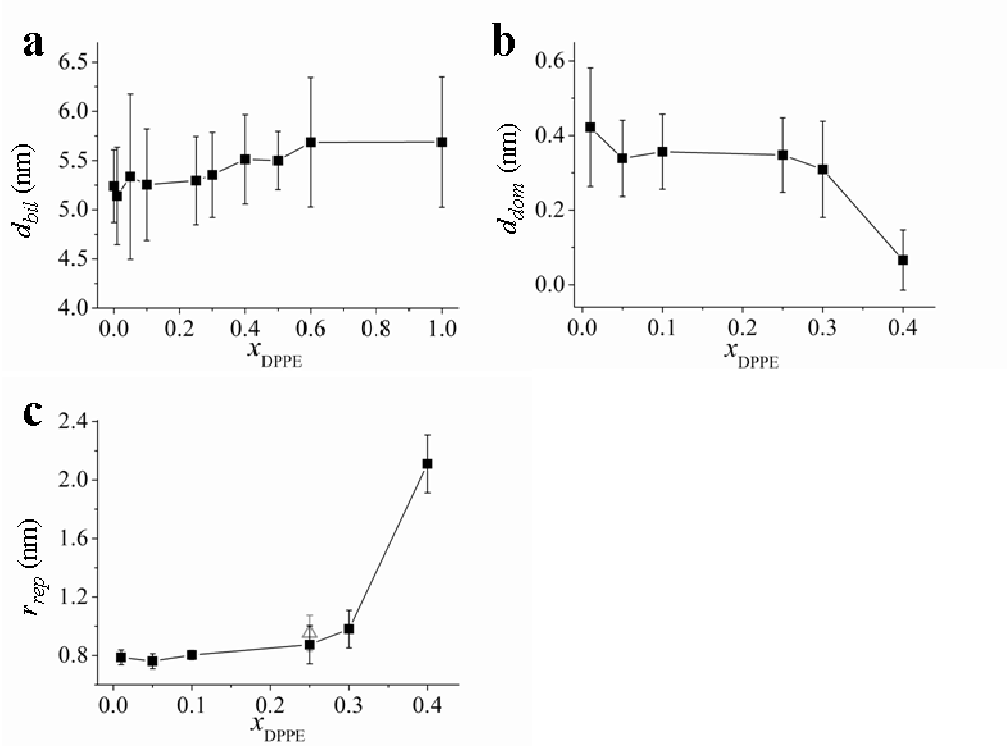

Fig. 4.4.a. Bilayer thickness d_{bil} of mixed DPPE/DPPC bilayers as function of x_{DPPE}. **b.** Domain height d_{dom} and **c.** repeat distance r_{rep} of the striated domains as function of x_{DPPE} for a mixed DPPE/DPPC/2 mol% WALP23 bilayer. The open triangle Δ in **c** is the result for a 12 mol% WALP23/lipid bilayer

r_{rep} increased (Fig. 4.4.c). The striated pattern was completely absent at $x_{DPPE} > 0.4$, where patterns of meandering lines with a depth of 0.2 - 0.4 nm remained (Figs. 4.5.d, e). The total amount of WALP is approximately 1 mol%, assuming that the lines are single lines of WALP (see discussion).

Finally, some areas with a total area < 5 % with an ill-defined, hazy appearance could be distinguished at $x_{DPPE} > 0.40$ (data not shown). This appears to be some debris on top of the bilayer structures and is sweeped off at high scanning forces F (data not shown).

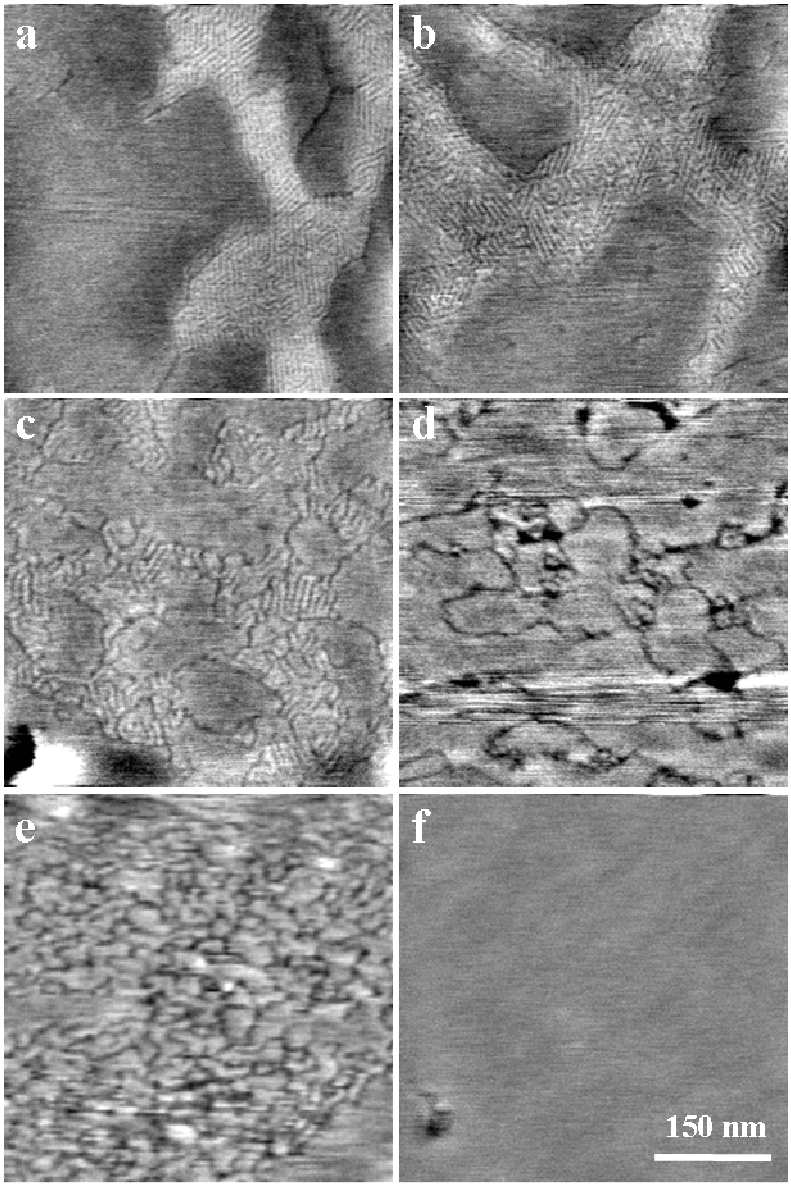

Fig. 4.5 AFM images of supported DPPE/DPPC bilayers containing an initial amount of 2 mol% WALP23 at x_{DPPE} = **a.** 0.05, **b.** 0.1, **c.** 0.3, **d.** 0.4, **e.** 0.5 and **f.** 1.0. All images have the same lateral dimensions

4.3.c HXD/DPPC

Two distinct phases appeared in a bilayer of DPPC when a low concentration of *n*-hexadecane was added (mole fraction x_{HXD} = 0.03, see Fig. 4.6.a). The measured difference in height between the two lipid phases Δd (indicated by the black arrow in Fig. 4.6.b) depended strongly on the force exerted by the AFM tip and varied from 0.6 ± 0.1 nm at low force $F \leq 0.4$ nN to 1.1 ± 0.4 nm at a relatively high force of $F \approx 1.5$ nN. The higher phase had a total thickness d_{bil} = 5.9 ± 0.3 nm, which was virtually independent of the scanning force F between 0.4 - 1.5 nN.
The relative area of the higher phase became larger as x_{HXD} increased, until only the higher phase remained at x_{HXD} = 0.13 (Fig. 4.6.c). Further increases in x_{HXD} did not have any effect other than the appearance of a clearly visible oily alkane-layer on top of the aqueous lipid dispersion at x_{HXD} = 0.88 and 0.94.

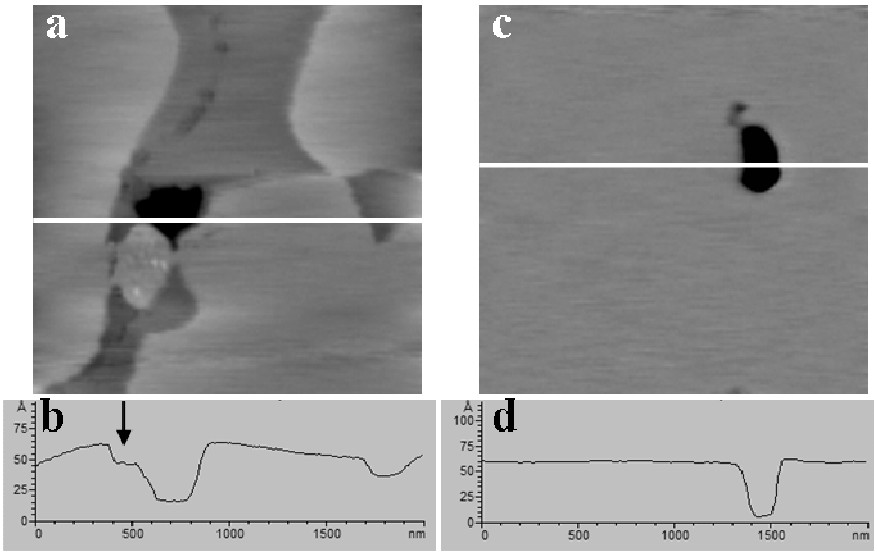

Fig. 4.6 Topographic images (2 x 2 µm) and corresponding height profiles showing a DPPC bilayer with x_{HXD} = 0.03 (**a** and **b**) and 0.13 (**c** and **d**). In **a**, a hole and a higher and lower phase are observed, which correspond to a non-tilted and tilted gel phase, respectively. In **c**, only the higher phase (and one hole) remains. The height profiles in **b** and **d** are taken at the position of the white horizontal lines in **a** and **c**. The arrow in **b** indicates the difference in height between the two phases

4.3.d HXD/DPPC/WALP23

The presence of HXD (x_{HXD} = 0.13) had a profound effect upon the formation of striated domains in WALP23-containing DPPC bilayers. Localized regions with loosely ordered line-type depressions were visible (Fig. 4.7) with a spacing of ~ 10 - 40 nm. These regions were not elevated above the level of the pure DPPC bilayer, like those in HXD-free DPPC/WALP23 bilayers (Fig. 2.6, [110, 122]). Note the similarity of these structures to the mixed x_{DPPE} = 0.5 DPPE/DPPC system of Fig. 4.5.e.

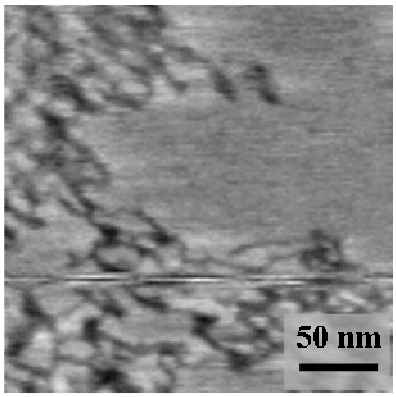

Fig. 4.7 AFM micrograph of a mixed HXD/DPPC/WALP bilayer at x_{HXD} = 0.13. The black, meandering lines are presumably linear aggregates of WALP (see discussion)

4.3.e Unsaturated PCs

Supported bilayers of symmetrical, di-unsaturated di-20:1-PC, di-22:1-PC or di-24:1-PC all showed almost identical topological features in the low-temperature solid state (see Fig. 4.8.a for di-22:1-PC). A corrugated surface was observed where narrow terraces with a typical size of ~ 50 - 275 nm were intersected by a large amount of evenly distributed, branched lines, which showed a long-range directional ordering. For instance, three distinctly different oriented regions can be observed in Fig. 4.8.a (top left, middle and bottom right). These regions are rotated with respect to each other at angles close to 60 or 120°. The width of the intersecting lines was ~ 6 - 12 nm at low scanning forces $F \leq 0.5$ nN. Their measured depth was ~ 0.5 - 1 nm, although this could be largely underestimated as the relatively large radius of the scanning tip may not reach the bottom of these lines [209, 210]. The lines probably pierce the bilayer to the level of the substrate as scanning at high imaging forces ($F > 1$ - 2 nN) led to broadening of the lines and eventually, after a few scans, the formation of holes (Fig. 4.8.a, bottom left). Rough estimates of the density of these lines ρ_{line} (≡ cumulative length of the lines per nm^2) are given in Table 4.I (top row). ρ_{line} decreases with n for the symmetrically unsaturated di-n:1-PCs and is much higher for the asymmetrically unsaturated (16:0,18:1)-PC.

Moreover, ρ_{line} of di-24:1-PC was virtually independent of the cooling rate (0.2 - 40 °C/min) during the transformation from the fluid to the low-temperature phase (data not shown). The depth d_{bil} of these holes of ~ 5 - 6 nm matches the expected thickness of bilayers in the solid phase (see Table 4.II). No literature values were found for this phase, but estimates were made based on X-ray diffraction data of the liquid-crystalline phase, to which 0.6 nm [296] was added to correct for the larger thickness of the solid phase. An additional 1 nm was added to include the layer of water between the bilayer and the substrate that is measured with AFM [33, 199, 203], but not with X-ray diffraction (see Fig. 2.1). The d_{bil}'s of the saturated PC lipids from section 2.3.b are given in the third column for comparison.

Table 4.I Line densities ρ_{line} of unsaturated PC bilayers (in μm/nm^2, error approximately 2 μm/nm^2 for di-*n*:1-PC and 10 μm/nm^2 for (16:0,18:1)-PC). The contributions of the different lipids are given in the different columns, while the concentration of WALP increases from top to bottom. The initially added mol% of WALP23 is given in brackets

lipid	ρ_{line}	**lipid**	ρ_{line}	**lipid**	ρ_{line}	**lipid**	ρ_{line}
di-20:1-PC (**0%**)	10	di-22:1-PC (**0%**)	6	di-24:1-PC (**0%**)	4	(16:0,18:1)-PC (**0%**)	27
-	-	-	-	di-24:1-PC (**0.5%**)	5	-	-
-	-	-	-	di-24:1-PC (**1%**)	10	-	-
di-20:1-PC (**2%**)	-[a]	di-22:1-PC (**2%**)	14	di-24:1-PC (**2%**)	8	(16:0,18:1)-PC (**2%**)	90
-	-	di-22:1-PC (**4%**)	13	di-24:1-PC (**4%**)	10	-	-

a Poor quality of the scans hindered a reliable determination

Table 4.II Bilayer thickness d_{bil} for the unsaturated and corresponding saturated PC lipids in the solid phase, and d_{bil} based on the literature values (see text)

type of lipid	d_{bil} **measured (nm)**	d_{bil} **of saturated lipid (nm)**	**'corrected'** d_{bil} **literature values (nm)**
di-20:1-PC	6.3 ± 0.4	6.2 ± 0.6	6.2 [84]
di-22:1-PC	6.3 ± 0.3	6.3 ± 0.2	6.1 [233, 296]
di-24:1-PC	6.6 ± 0.4	6.6 ± 0.3	6.5 [233, 296]
(16:0,18:1)-PC	6.1 ± 0.4	5.9 ± 0.4[a]	6.2 [297][b]

a Value for DSPC (di-18:0-PC)

b Direct value from an AFM study

Regions of a second, lower, liquid-crystalline phase were observed in the di-22:1-PC bilayer upon heating above T = 7 °C (Fig. 4.8.b). The difference Δd with the higher phase was 0.8 - 1.5 nm. The cumulative area of the lower, fluid phase expanded with increasing temperature, until complete coverage was reached at $T \approx 12$ °C. In the coexistence-region, the solid regions had faceted, crystal-like edges where they border the fluid regions. The onset of melting at 7 °C is lower than the reported main transition temperature T_M of 13.2 °C [29, 295]. This agrees with the reported broad melting transition of unsaturated lipids [287, 289, 295], which could be broadened even further by bilayer-substrate interactions [128, 137, 272].

Bilayers of the asymmetrically unsaturated (16:0,18:1)-PC (Fig. 4.10.a) showed distinct patterns with a large number of interconnected dark lines (width ~ 9 - 15 nm, depth ~ 0.3 nm). The morphology is different from the di-*n*:1-PC bilayers as the lines have longer straight stretches and show no preferential orientations. ρ_{line} and d_{bil} are given in Tables 4.I and 4.II, respectively. The size of the crystalline domains was ~ 30 - 130 nm.

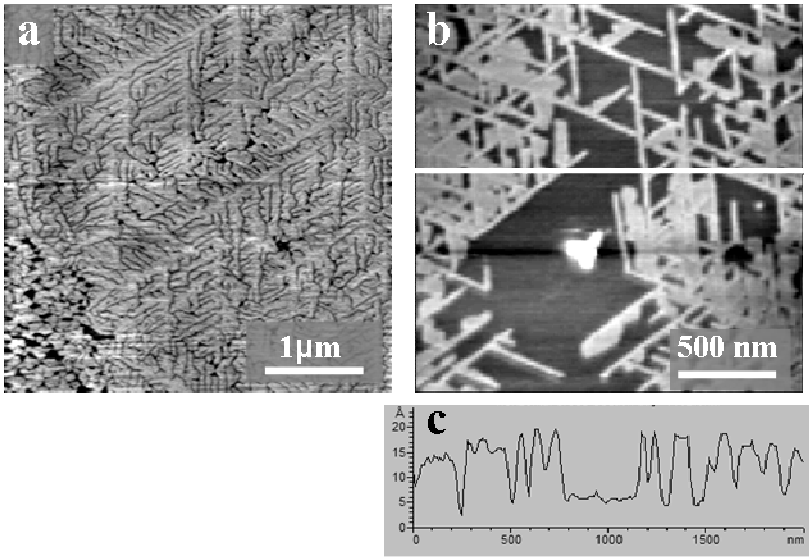

Fig. 4.8.a. AFM image of a pure di-22:1-PC bilayer in the solid state at 4 °C, showing a bilayer with a large number of packing defects. The edges of the solid domains show faceted edges. The holes in the bottom left part of the scan are due to damage from a previous scan at higher scanning force. **b.** Crystalline facets are formed in the di-22:1-PC bilayer of **a** at the edges between the low-temperature solid and high-temperature L_α phase when it is heated to 7 °C. The height profile in **c** is recorded at the position of the white line in **b**.

4.3.f Unsaturated PCs/WALP23

Inclusion of 2 mol% WALP23 in any of these unsaturated lipid bilayers did not lead to the formation of the striated domains that were observed in saturated PCs. In fact, the only discernible change was a refinement in the pattern of the lines, which led to a (more than) doubling of the line densities ρ_{line} (Figs. 4.8 - 4.10 and Table 4.I) and concomitant decrease in the size of the terraces between the lines. Estimated domain sizes are 35 - 160 nm for di-22:1-PC/2 mol% WALP23 and 20 - 60 nm for (16:0,18:1)-PC/2 mol% WALP23.
Table 4.I shows that the doubling of ρ_{line} was already achieved at 1 mol% WALP23 in di-24:1-PC and further increases in the concentration of WALP did not lead to additional changes.

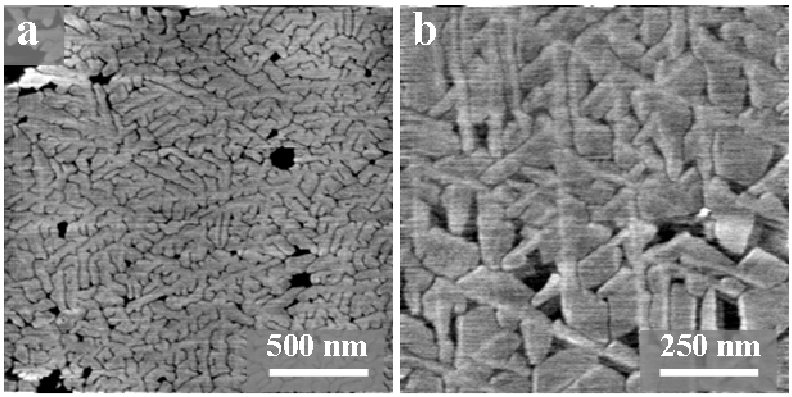

Fig. 4.9 A di-22:1-PC bilayer with **a.** 2 mol% WALP23 and **b.** close-up of a 4 mol% WALP23, showing linear packing defects. Note that these pictures have a different scale than those in Fig. 4.8

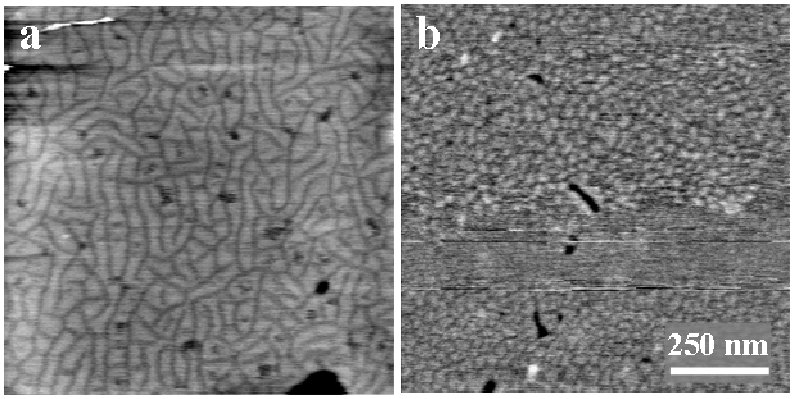

Fig. 4.10 A (16:0,18:1)-PC (POPC) bilayer **a.** without and **b.** with 2 mol% WALP23 (both 1 x 1 μm). The apparent absence of structure in the middle of **b** was an artefact due to a temporary high scanning force $F \approx 1$ nN

4.4 Discussion

4.4.a DPPE/DPPC

Pure DPPE and DPPC bilayers are in the non-tilted L_β [17, 46, 203] and tilted L_β' gel state, respectively at 22 °C [17, 31, 32, 46, 254, 283, 284]. The measured d_{bil} of pure DPPC of 5.2 ± 0.4 nm is comparable, but a little smaller than that of other AFM and X-ray diffraction studies (see section 2.4.a). The average d_{bil} for pure L_β-DPPE (x_{DPPE} =1) of 5.7 ± 0.7 nm is close to literature values of 5.4 ± 0.1 nm [149], 5.3 ± 0.5 nm [43] and 5.6 ± 0.2 nm [148] that were obtained in other AFM studies. It is, however, lower than the expected d_{bil} (DPPE) = 6.4 nm that is derived from neutron reflectivity [203] by adding 1 nm for the layer of water d_w [33, 199, 203] to the measured d^0_{bil} (neutron refl.), see Fig. 2.1. In this case, d_{bil} (DPPE) may be underestimated by combined effects of compressing the soft membrane with the AFM probe and the large number of holes with debris on the bottom. This hampers accurate measurements. A limited number of 'clean' holes (n = 3 at x_{DPPE} =1) had a larger thickness d_{bil} of 6.0 - 6.1 nm. The difference $\Delta d_{DPPE\text{-}DPPC}$ = 0.6 nm (= 6.0 - 5.4 nm) that accompanies the transition of the lipid acyl chains from a tilted (pure DPPC) to a perpendicular (pure DPPE) orientation then matches the 0.6 - 0.7 nm from [46].

The increase of d_{bil} with x_{DPPE} in Fig. 4.4.a reflects changes in the tilt angle of the lipid acyl chains, which decreases as more of the perpendicular oriented DPPE molecules are included in the tilted DPPC packing. The levelling-off of d_{bil} at high x_{DPPE} in Fig. 4.4.a is more likely to be an intrinsic property of the mixed lipid packing than the result of (partial) phase separation that arrests further incorporation of DPPE into the layer. First, no additional phases are observed in the AFM scans, although AFM should be able to resolve the difference in height between separate DPPE-enriched and DPPC-enriched patches [129, 140]. Secondly, complete miscibility of DPPE and DPPC in the gel-gel phase was also predicted by a number of literature studies (for example [284, 298 - 302]), although this is a matter of some discord. The (partial) phase separation, however, predicted in some studies (for example [238, 285, 303 - 305]) can be allocated to side effects of (fluorescent) probes [298, 303] or improper equilibration [299]. One of the most complete phase diagrams [299] - including the previously disregarded subgel and ripple phases - shows mixing under the conditions used here. It is therefore concluded here that DPPE and DPPC mix at all x_{DPPE}.

The observed trend of d_{bil} at high x_{DPPE} can then be attributed to a gradual change in the DPPC-like, tilted structure towards a DPPE-like, non-tilted phase. This transformation seems complete at $x_{DPPE} \approx 0.5$ and no further changes are detected at larger x_{DPPE}. This agrees with ^{13}C- and ^{2}H-NMR studies of Blume *et al.* [298], where a similar non-linear relationship between bilayer structural properties and PE content was found, with a transition occurring at x_{DPPE} = 0.4 - 0.5. The absence of grain boundaries at high x_{DPPE} in Fig. 4.3 is also an

indication of a vanishing tilt angle θ of the lipid chains as these boundaries are thought to demarcate areas with different (azimuth) tilt angles of the lipid acyl chains.

Summarizing, binary gel-gel DPPE/DPPC supported bilayers form smooth bilayers of which the acyl-chain tilt angle decreases when going from $x_{DPPE} = 0$ to 1. The packing seems to saturate around $x_{DPPE} \approx 0.5$.

4.4.b DPPE/DPPC/WALP23

The DPPE content of mixed DPPE/DPPC/2 mol% WALP23 bilayers does not influence the properties of the striated to a large extent when $0 < x_{DPPE} \leq 0.25$. The bilayer retains a packing that bears enough resemblance to that of pure DPPC to form a comparable striated phase. However, in the region $0.25 < x_{DPPE} < 0.5$ (Figs. 4.5.a - e), the rigid striped ordering gradually dissipates (increased r_{rep}), and the total area occupied by the striated domains and the domain height d_{dom} decrease as a conversion from a tilted L_{β}' to a non-tilted L_{β} phase takes place [76] (Figs. 4.4 and 4.5). Increases in x_{DPPE} reduce the average θ of the lipid acyl chains in the bilayer outside the domains and reduce d_{dom} as this is measured between the top of the striated domains and the surrounding, less and less tilted, bilayer surface (see Fig. 2.1).

The observed loss of ordering and increased repeat distance r_{rep} with $x_{DPPE} \geq 0.25$ (see Figs. 4.4.c and 4.5) reflect the organizational differences within the lipid's hydrophobic region. Modifications in the interactions between the peptide's anchoring tryptophan moiety and the polar groups [306] can arise when PC is replaced by PE. This is expected to be of minor importance for the striated structure because of the chemical similarities between PE and PC and the relative insensitivity of the striated domains to altered interactions of the polar region with the anchoring group of the peptide [33]. Presumably, the striated phase is gradually affected by the changes in the tilt angle θ that are introduced with x_{DPPE}. The rigid stripes dissipate into assemblies of loosely organized, dark lines when the DPPE-like packing is reached near $x_{DPPE} = 0.4 - 0.5$. The gradual transformation of the darker lines from a striped pattern to these meandering features with a comparable width suggests that these lines still consist of single rows of WALP molecules [110].
A similar role of lipid acyl-chain tilt on the formation of striated domains was deduced from an AFM study on sphingomyelin/WALP bilayers, where features similar to those in Fig. 4.5.e were observed. The absence of the striated phase was ascribed to the zero lipid acyl-chain tilt in these membranes (unpublished results of D. N. Ganchev). It will be shown in the computer simulations of Chapter 5 that the presence of a tilt angle alters the lateral length scale over which WALP-induced conformational changes of the lipids stretch. This can be related to the tendency of these bilayers to form a striated phase.

Some lipid sorting might take place on a localized scale at low $x_{DPPE} < 0.25$ as the composition of the lipids in the lighter stripes might deviate from the surrounding PE/PC bilayer. This was tested by measuring a sample with $x_{DPPE} = 0.25$ and 12 mol% WALP23. Here, the striated

phase should cover the entire surface [117], forcing all DPPE and DPPC molecules to participate. No inhomogeneities in lipid composition should take place. This led to a slightly enlarged repeat distance r_{rep} (open triangle in Fig. 4.4.c), which implies that the DPPE content in the striated phase at 12 mol% WALP is raised compared to that at 2 mol% WALP (9.5 ± 1.2 m versus 8.7 ± 1.3 nm respectively). In this latter system, some DPPE is thus expelled from the striated phase to the surrounding bilayer, although the effect is small considering the small increase in r_{rep}.

Finally, the marked reduction of the total area of the striated domains in Figs. 4.5.c - f with increasing x_{DPPE} could be due to a reduced incorporation of WALP in this part of the membrane or to an increased solubility, and disaggregation, of WALP in the bilayer. The distinction between these two can not be made with AFM, but it can reasonably be expected that WALP does not mix in these bilayers. Both DPPE and DPPC bilayers are in the gel state at room temperature and have tightly packed hydrocarbon chains. WALP has a low miscibility in gel-phase DPPC membranes [117, 122] and it seems likely that this is also low in the mixed gel-state DPPE/DPPC membrane. In fact, solubility may be expected to be even lower in DPPE as inclusion of the peptide disrupts the more interconnected, hydrogen-bonded network of the PE polar groups to a larger extent than that of the non-hydrogen-bonded PC groups [67, 68]. This is supported by DSC measurements of poly-leucine/alanine model peptides $(LA)_x$ and $WL_{22}W$ [67, 68], where the larger peptide-induced shifts of T_M in bilayers of DPPE compared to DPPC were also attributed to disruption of the hydrogen bonds between the PE polar groups [67, 68].
It is therefore concluded that part of the WALP23 is expelled from the DPPE bilayer, and is probably located in the debris located on top of the bilayer surface or is removed from the sample in one of the washing steps during sample preparation.

4.4.c HXD/DPPC

The two phases that were observed in a DPPC bilayer upon addition of small amounts of HXD (Fig. 4.6.a) can be ascribed to a DPPC L_β' phase and a HXD-containing, higher, L_β phase. The total area of the L_β phase increases with x_{HXD} until the entire bilayer is transformed at x_{HXD} = 0.13 (Fig. 4.6.b). The non-tilted L_β phase is formed by insertion of HXD in the hydrocarbon region of the DPPC bilayer. The HXD molecules are probably located halfway between the bilayer leaflets as no phase with an intermediate thickness was observed (see Fig. 1.4.d). Such an additional phase would form if one HXD molecule affects one leaflet only, while the opposing one is free of HXD.
The difference between the two phases Δd at low scanning forces F of 0.6 nm is in close agreement the difference of 0.6 - 0.7 nm found by both X-ray diffraction and calculation [46, 289] when a transition in tilt from $\theta \sim 30$ - 32° [25, 38, 39] to 0° occurs.
The doubling of Δd at larger scanning forces is surprising and suggests a difference in the axial compressibility of the two phases as the L_β phase seems to withstand the pressure exerted by the AFM probe better than the pure DPPC L_β' phase (see Fig. 2.4 for the relation between F

and d_{bil} for the DPPC L_β' phase). The reason for this is not clear, although one can imagine that the HXD chains add mechanical rigidity to the layer in the vertical *z*-direction. Some rigidifying of the acyl chains could occur upon insertion of an alkane, although this effect can not be large as the available area per lipid of HXD-containing DPPC monolayers in the liquid condensed LC phase [47, 288, 307] closely resembles that of HXD-free DPPC monolayers [47, 73, 308, 309]. LC monolayers are generally acknowledged as having corresponding properties to bilayers in the gel phase [73, 309].

The optimal packing requirements for the perpendicular L_β phase seem fulfilled at $x_{HXD} = 0.13$. No further uptake of HXD in the membrane takes place beyond this as the $L_\beta' \rightarrow L_\beta$ transformation is completed. [5] This is supported by the observation in [288] that the already favourable, perpendicular packing of the lipids within DPPE layers precludes the inclusion of HXD.
The limiting $x_{HXD} = 0.13$ for DPPC is in agreement with the maximal solubility of $x_{HXD} = 0.10$ - 0.14 found with DSC by McIntosh *et al.* [289]. Initially, both the main transition temperature T_M and corresponding melting enthalpy ΔH_M increased with x_{HXD}, but they remained constant above $x_{HXD} \approx 0.10$ - 0.14 [289]. Excess alkane ($x_{HXD} > 0.13$) accumulates in a separate phase (here and [44, 286, 289, 290]), which becomes visible as a layer of oil at extremely high x_{HXD}.

4.4.d HXD/DPPC/WALP23

2 mol% WALP23 was incorporated in mixed DPPC/HXD bilayers with $x_{HXD} = 0.13$, where the complete bilayer has adopted the L_β phase. Only loosely organized, dark lines were found (Fig. 4.7), with a topology that was very similar to that of DPPE ($x_{DPPE} = 0.5$/DPPC/WALP23 in Fig. 4.5.e). The meandering, black lines in Fig. 4.7 are expected to consist of single rows of WALP, following the similarity with the DPPC/DPPE bilayers. Hexadecane affects tilt only and leaves other properties of the DPPC gel-state bilayer essentially unaffected [288, 289, 292]. It has the same hydrophobicity as the (C16:0) lipid chains. Possible direct WALP-lipid interactions, such as tryptophan anchoring or interactions in the non-polar region, are therefore expected to remain unaffected. The possible small rigidifying of the lipid chains (see above) might serve to exclude some WALP from the bilayer, in analogy to the tightly packed polar region of the DPPE bilayer. It seems unlikely, however, that this small effect leads to the complete dispersal of the ordered, striated pattern.

Rather, the reduced polar tilt angle θ in the HXD/DPPC bilayer seems the most obvious factor influencing the tendency to form striated phases. The analogous morphologies of the HXD- and DPPE-containing DPPC/WALP bilayers can then both be explained by these shifts in θ.

---

[5] $x_{HXD} = 0.13$ corresponds to 1 HXD molecule for every 6 - 7 DPPC molecules. As each alkane adds 20 $Å^2$, this amounts to ~ 3 $Å^2$ per lipid. The mismatch in area between the acyl chains and PC polar region of 7 $Å^2$ is largely, but not completely, bridged if one assumes that the HXD inserts halfway the bilayer midplane and thus affects two leaflets simultaneously

4.4.e Unsaturated PCs

Bilayers of unsaturated PC lipids in the solid phase show a markedly different topography than those of saturated PC lipids (compare Figs. 4.8.a and 4.10.a to Fig. 2.2). The d_{bil}s in Table 4.II, however, are very similar to those of the corresponding saturated PC lipids and the values obtained from literature. Evidently, the *cis*-bond does not contribute much to the total bilayer height. This was deduced by [233] for the L_α phase, but seems surprising for the gel phase with its relatively rigid acyl-chain packing.

AFM micrographs of the bilayers of di-monoenoic di-*n*:1-PC lipids and (16:0,18:1)-PC in Figs. 4.8 and 4.10 all show small, interconnected solid bilayer domains bordered by lines. The interpretation of these observed topologies is not immediately clear, as the low-temperature phase of these systems has not been widely investigated [288, 289, 292, 295]. The overall packing, however, is largely influenced by the acyl chains, which have a kink at the position of the C=C *cis*-double bond [163, 288, 310, 311]. A molecular-mechanics study has shown that the adjacent single bonds conform to ensure the most optimal packing of the chain as a whole, which was described as a 'crankshaft-like' motive [292, 312]. Nevertheless, close-packing of the lipids is severely hindered and a looser packed solid phase is formed, where each lipid chain occupies a larger area than saturated ones do [29, 288, 294, 295]. The acyl chains have an overall tilt angle with respect to the bilayer normal [295, 296, 313].

The solid phase of the di-*n*:1-PC bilayers is more likely to be a crystalline L_c' phase than a gel L_β' phase [295]. This remains somewhat speculative, however, as the exact physical state of the bilayers cannot be determined by AFM. It is known that the conversion from the metastable gel to the thermodynamically stable crystalline phase takes place on a much faster time scale in unsaturated lipid bilayers [295] than for their saturated counterparts [20, 21]. Only one solid phase was observed here with AFM, so it can be concluded that this transition is instantaneous (or falls within the 10 - 15 minutes it takes to equilibrate the samples prior to measuring) or that the transition does not occur or is not visible with AFM. The first possibility seems the most likely as the presence of a crystalline L_c' structure seems indicated by the long-range orientational order observed at the edges of the solid terraces at the line defects (Fig. 4.8.a) and at the border with the fluid phase (Fig. 4.8.b). The structure strongly resembles that of single crystalline, dendritic crystals [421 - 424].
The crystalline domains of the di-*n*:1-PC bilayers are bordered by dark lines that seem to traverse the bilayer completely and are interpreted here as line-type lattice defects. The presence of line defects is in agreement with data from Raman spectroscopy [289] and the observation of fluorescent probe enrichment into these line defects [314] for unsaturated bilayers. The broad melting range of these bilayers is also indicative of a large number of packing defects [287, 289, 295].

Possible origins of these defects could be packing frustrations or rate-limiting transport dynamics during the formation of the solid-state bilayers. Packing frustration arises when molecules are not positioned or aligned according to the long-range translational order of a crystalline phase. The resulting frustration is relieved by forming defects. Such misplacements may be enhanced by rapid formation of the solid phase and could be amplified by the inflexible bend in the lipid acyl chains at the position of the double C=C bond [163, 292, 310, 311]. Metso *et al.* [314] suggested that it is the high bending modulus of solid-state long-chained di-*n*:1-PC lipid bilayers that causes the surface to crack into small lamellar regions.
On the other hand, the highly-branched, dendrite-like morphology of the solid phase can be a result of limited transport dynamics during the transition of the fluid to solid phase [315 - 317]. Dendrites can form when the diffusion of properly oriented lipids to the crystalline patches is slow compared to the growth (*i.e.* the attachment of lipids to the solid phase). Lateral diffusion of unsaturated PCs in the L_α phase is generally slower than that of saturated PCs [29, 270, 318].
Dendritic patterns are also formed in a comparable system of Langmuir-Blodgett monolayers of erucic (C22:1*cis*13) and nervonic (C24:1*cis*15) fatty acids [319]. These fatty-acid crystallites have an almost, but not exact, hexagonal ordering as intersection angles are close to 60º. This close-to hexagonal ordering is also observed in Fig. 4.8.a, where the lipids in the bilayer contain two such fatty-acid chains. It is difficult to discriminate between the two mechanisms of packing frustration and mass transport based on AFM. Moreover, they do not necessarily exclude each other.

The density of the line defects ρ_{line} varies for the different di-*n*:1-PC lipids and becomes smaller for larger *n* (*i.e.* the size of crystallites becomes larger, see Table 4.I). Most likely, the increase in ρ_{line} is related to the position of the C=C bond along the lipid's hydrocarbon chain. The stability of the hydrophobic region (and hence T_M) is maximally lowered when the C=C bond is located in the middle of the chain [16, 310]. In this study, the double bond becomes further removed from the PC group upon going from di-20:1-PC to di-24:1-PC; *i.e.* from 55 % to 63 % of the acyl chain. The packing is thus most perturbed for the shorter di-20:1-PC, leading to a larger ρ_{line}.

Bilayers of the mono-unsaturated (16:0,18:1)-PC (Fig. 4.10.a) show no large scale directional ordering. This could be due to the presence of a gel phase [289, 292, 311], instead of the more crystalline L_c' phase of the di-unsaturated di-*n*:1-PC bilayers. The larger ρ_{line} (Table 4.I) could be a result of the asymmetry between the oleoyl and palmitoyl chain. This makes parallel alignment of the chains even more difficult than for the symmetrical di-unsaturated lipids [289, 312]. The saturated *sn*-1 16:0 hydrocarbon chains are fully extended and pack with a tilt angle with respect to the bilayer normal [200, 389], whereas the unsaturated *sn*-2 18:1 chains can pack only partially parallel to the *sn*-1 chains. Of course, the origin of the observed lines could be different than those of di-*n*:1-PC. It was suggested in [288] that parts of the bilayer leaflets of (16:0,18:1)-PC could be interdigitated. The lines could then be interdigitated regions and can not be compared to those of the di-*n*:1-PC bilayers. Alternatively, the different phase and

structure of the lipids could alter the dynamics of nucleation and growth and affect ρ_{line}. Nucleation could be faster here, as the size of the solid domains is smaller (higher ρ_{line}).

4.4.f Unsaturated PCs/WALP23

Incorporation of WALP into these unsaturated bilayers does not lead to the formation of striated domains. In fact, the only morphological change is a refinement of the pattern that was observed without WALP (see Table 4.I and Figs. 4.9 and 4.10.b). The number of packing defects ρ_{line} in the di-24:1-PC bilayer reaches a steady state at 1 mol% WALP23. More WALP23 either leaves the topology of the bilayer unaffected or is not included in the bilayer. Limited inclusion of the peptide was observed in saturated lipid/WALP membranes when there is a large mismatch in length between the hydrophobic parts of the lipid and peptide (see section 2.4.b and [190]). This probably occurs here as well. The amount of incorporated WALP should be somewhat larger for the shorter, better-matching unsaturated lipids than for di-24:1-PC.

In principle, the presence of 1 mol% WALP should be enough to form some detectable striated domains (see [110, 122] and section 2.3.b). One of the necessary conditions for the formation of striated domains is fulfilled here, *i.e.* the presence of tilted acyl chains [163, 295, 296, 313]. The other condition is the presence of a rigidly packed solid phase (see Chapter 3, [75, 110]). The kinked acyl chains of the unsaturated lipids, however, interfere with the optimal organization of the bilayer and reduce the ordering of the lipid packing in both the polar and non-polar region. The unsaturated bond in (16:0,18:1)-PC expands the in-plane area per molecule of a LB monolayer in the liquid-condensed LC phase from ~ 45 - 50 $Å^2$ for saturated DPPC [47, 294] to ~ 55 - 60 $Å^2$ [294, 320]. Order parameter profiles [6] show that the chain ordering of the oleoyl (18:1) chain in (16:0,18:1)-PC is reduced to $S \approx 0.75$ in the gel phase, compared to $S = 0.9$ of the palmitoyl 16:0 chain. Thus, S of the oleoyl chains in the gel phase is closer to $S = 0.65$ of a palmitoyl chain in the fluid phase than to the palmitoyl gel phase [320].

The reduced ordering of the lipid chains facilitates solubility of WALP in the layer and hence reduces the driving force for segregation of WALP into localized domains. A strong possibility is that part or all of the WALP molecules are dissolved in the bilayer and are distributed there randomly as single molecules or small oligomers that are too small to be detected by AFM. This is supported by the relatively low values of ρ_{line}, where no more than 0.2 - 0.3 mol% WALP can reside for di-24:1-PC (ρ_{line} = 8 - 10 μm/nm^2, using a diameter of 1 nm for WALP [75, 110] and an area/lipid = 0.6 nm^2 [29, 294, 320]). This is based on the assumption that the WALP molecules form single, linear aggregates, like in the saturated gel-state bilayers. At least ~ 0.7 mol% of the peptide must then be associated with the bilayer outside the line defects.

[6] The order parameter $S = ½ <3 (\cos^2 \theta) -1>$ with θ the angle between the bilayer normal and a bond between a C and ^2H atom This can be measured with NMR [72, 248]

The inclusion of WALP has a visible effect on ρ_{line}, although the manner by which this is induced is not clear. One possibility is that the increase in ρ_{line} is related to the need to create more space for the WALP molecules in the line defects. The final ρ_{line} = 33 μm/nm^2 that would be necessary to accommodate the full 1 mol% of WALP is not reached, possibly due to intrinsic properties of the packing. Alternatively, the dissolved WALP may increase ρ_{line} in a more indirect way, for instance by altering collective packing properties of the membrane through the elastic or bending modulus [66, 321] or by altering the kinetics of nucleation and growth. This, in turn, can affect the morphology and size of the solid domains.

Finally, a different situation exists for (16:0,18:1)-PC/WALP bilayers, where ρ_{line} is theoretically large enough to accommodate 2.7 mol% WALP. In this case, all WALP could be located in the observed lines, although this does not explain why the pattern of the lines is altered in the presence of WALP. This latter effect could again be due to an indirect influence of the (partly) dissolved peptide on the packing or the formation kinetics.

4.4.g TFE/DPPC/WALP23

An additional test was performed to elucidate the effect of a looser lateral lipid organization. Small amounts (1 - 4 vol%) of the solvent 2, 2, 2-trifluoroethanol (TFE) were added to a DPPC bilayer. The bilayer thickness d_{bil} lay between 5 - 5.5 nm for all these TFE concentrations, indicating the continued presence of a single, gel-state bilayer. The appearance, r_{rep} and d_{dom} of the striated areas in the mixed DPPC/2 mol% WALP23/TFE bilayers remained unaffected between 0 - 3.5 vol% TFE. At 4 vol%, however, the striated pattern vanished and was replaced by assemblies of dark lines (see Fig. 4.11).

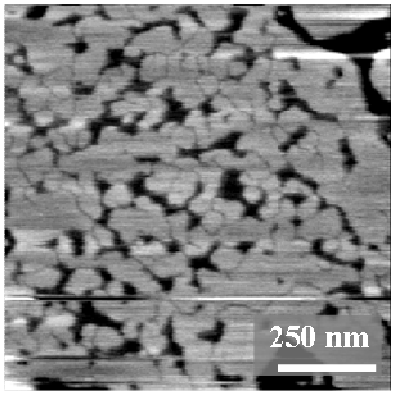

Fig. 4.11 AFM image of a DPPC bilayer with 2 mol% WALP23 and 4 vol% TFE. The striated phase is replaced by looser organized black lines, presumably single lines of WALP

These lines are expected to be linear aggregates of WALP, in analogy to those in the DPPC/HXD/WALP and DPPE /DPPC/WALP systems (see previous sections). The disappearance of the striped pattern can be ascribed to a TFE-induced disordering of the lipid acyl chains. TFE molecules partition selectively into the PC headgroup region and reduce the order of the acyl chains [13]. These results are a further confirmation that the lateral organization of the lipid packing plays an important role in the overall lateral peptide-lipid distribution.

4.5 Conclusion

The results of this chapter show that modifications in the packing of the bilayer can largely affect the formation and structure of the striated domains that are formed by phospholipids and the model peptide WALP. Replacement of DPPC by DPPE leads to the formation of striated domains at low DPPE mole fractions x_{DPPE}, but the incorporation and lateral distribution of WALP are affected at higher $x_{DPPE} > 0.25$. The reduction of the amount of WALP in the bilayer at high x_{DPPE} can be related to the tighter hydrogen-bonded network formed between the PE groups. The progressive disordering of the striated pattern with x_{DPPE} can be related to the vanishing tilt angle of the lipid acyl chains with the bilayer normal. DPPE has a non-tilted conformation, in contrast with the polar angle of 30 - 32º of DPPC [19, 29, 30]. The importance of tilt is confirmed by the similar, loosely organized pattern of WALP-containing lines in mixed *n*-hexadecane/DPPC/WALP bilayers in the non-tilted L_β phase.

Lipids with an unsaturated bond in their methylene chains (di-*n*:1-PC with $20 \leq n \leq 24$ and (16:0,18:1)-PC) form gel or crystalline bilayers with a large number of line-type packing defects. Inclusion of WALP into these bilayers is limited to ~ 1 mol% in the di-24:1-PC bilayer, probably because of the large hydrophobic mismatch. No striated domains are formed. This is ascribed to the less efficient and rigid packing of the bilayer owing to the unsaturated acyl chains. This increases the solubility of WALP in the layers and eliminates the driving force for forming separate peptide/lipid domains. The presence of the WALP23, however, affects intrinsic properties of the bilayer and leads to an increase in the number of the line-type defects. Addition of 4 vol% TFE to a DPPC/WALP23 bilayer also removes the tendency to form striated domains through a similar process of increasing the area per lipid.

These data show that changes in the lipid composition of a membrane can have large consequences for the lateral distribution of lipids and peptides through the stiffness of their packing and tilt angle of the acyl chains with respect to the bilayer normal. A tightly packed gel phase and a non-zero tilt of the lipid acyl chains are crucial for the formation of striated domains in lipid/WALP bilayers.

Chapter 5

Coarse-grained simulations of WALP/lipid mixtures

Abstract

Domains of a striated phase have been observed with AFM in mixed bilayers of phospholipids and the model peptide WALP. The conformation of the lipids and the peptide WALP in this striated phase are studied here with computer simulations. A coarse-grained model is used in which both the lipid and peptide molecules are built up from a number of connected 'beads' that describe a group of atoms. The Dissipative Particle Dynamics (DPD) simulation technique is used [180, 181].

First, the phase behaviour and characteristics of bilayers of tilted DPPC- and non-tilted DPPE-mimicking lipids are investigated, following similar work in [179]. Next, the molecular arrangement of the lipids in the vicinity of a single row of immobile WALP molecules is investigated. This is in analogy to the single rows of WALP that are found in the striated domains. The lipids close to the peptides have an altered conformation compared to those at large distances. Profiles of the bilayer thickness, shape and polar angle of the DPPC lipids as function of the distance to the WALP shows that these perturbations show distinct maxima or minima. It is proposed that the experimentally observed repeat distance between the stripes can be related to overlap of the different maxima and minima between two rows of peptide. The substantially different profiles of non-tilted DPPE lipids and of fluid DPPC lipids show why no striated domains are observed experimentally in these systems. Variations in the hydrophobic mismatch between gel-phase PC bilayers and the peptide have only a limited effect on the perturbation profiles, explaining the experimentally observed insensitivity of the repeat distance between the stripes of the striated phase.

5.1 Introduction

The structure of the striated domains that are formed in mixtures of the model peptide WALP and phospholipids has been studied by AFM ([33, 122, 123], this thesis), X-ray diffraction, fluorescence techniques and ^{2}H-NMR [110], but direct information on a molecular scale is still lacking. Computer simulations have been used successfully in the past to complement experimental data and various structural, mechanical and morphological properties of bilayers with and without proteins have been investigated in the past with various simulation techniques [103, 158, 159, 165, 189, 240, 243, 322]. Simulations may be expected to perform equally well in describing the striated domains.

Computer simulations on any system require a number of choices as to which simulation technique (*e.g.* Monte Carlo MC or Molecular Dynamics MD) and model to use. In this case, choosing a model is not easy because of the large number of physical parameters involved in the assembly of lipids and proteins in membranes. Previous studies either used a realistic atomistic representation or eliminated a certain amount of chemical details that should not be essential for the process under investigation [158, 162, 172, 322]. Atomistic MD studies give the most detailed and accurate description [57, 165, 166], but are limited to length and time scales far below those necessary for describing a number of features, owing to their high computational cost. Phase separation phenomena, such as the segregation of peptides into striated domains, are not described adequately [160, 162, 322]. Longer and larger simulations that can describe lateral heterogeneities have been made feasible by introducing some degree of coarse graining. This can be achieved by grouping together a number of atoms into one spherical particle or 'bead' with an effective potential [124, 162, 171, 175, 176, 182, 323, 324]. Such a coarse-grained model has been implemented into the Dissipative Particle Dynamics (DPD) approach [171, 179, 182, 325] that was first developed by Hoogerbrugge and Koelman [180] and later refined by Español and Warren [181]. The DPD simulation technique is derived from MD and its main purpose is to describe complex fluids on a mesoscopic scale [180]. The forces acting on one particle act as thermostat while hydrodynamic flow behaviour is reproduced correctly on the used length and time scales. Speeding-up of the simulations is achieved by setting the inter-particle force as a soft repulsion, instead of the Lennard-Jones potential traditionally used in MD. An adapted MD scheme gives particle trajectories based on the total force $\boldsymbol{f}_i$. For full reviews and mathematical justifications of the technique, the reader is referred to [158, 161, 180, 181, 185 - 187].

The coarse-grained (CG) lipid model developed by Kranenburg and Venturoli *et al.* [179, 182, 183] accurately reproduces the various phases that are encountered in experimental PC lipid bilayers [3, 19]. Moreover, lipid adaptations caused by the insertion of one cylindrical peptide could be studied [183]. In this chapter, this lipid model is used in the DPD simulation scheme to get more insight into the molecular packing and underlying physics of the striated domains. First, in section 5.3, various properties of pure CG bilayers are studied as function of

temperature and lipid tilt to act as reference point for the studies of the mixed WALP/lipid striated phase. Tilted DPPC and non-tilted DPPE lipids are used.
Next, in section 5.4, mixed WALP/lipid bilayers are considered. Emphasis lies on the conformational perturbations of the lipids induced by WALP, rather than on the self-assembly of the lipids and peptides into striated domains. The peptide is modelled as an immobile barrier with a width of one molecule, in analogy of the single rows of WALP that are known to exist in the striated phase. The acyl-chain tilt, shape, and length of the lipid molecules in the low-temperature gel phase are monitored as function of the distance to this line of WALP molecules. The shape of these profiles leads to an understanding of the possible origins of the favoured repeat distance of 8 nm found for striated domains of DPPC/WALP.

Moreover, the previous chapters have shown that two essential requirements for the formation of ordered striated domains are the presence of tilted lipids and a gel-state packing where the lipid acyl chains are rigid and tightly packed. The role of these issues is investigated here by using DPPE lipids that have no intrinsic tilt in the gel phase and by using DPPC lipids in the high-temperature fluid phase. The WALP-induced perturbations in these systems fall off much faster than in gel-state DPPC bilayers. This can be related to the propensity of these systems to form striated domains.
Additionally, the effect of the length of the peptide is studied. This alters the extent of hydrophobic mismatch between the DPPC bilayer and peptide. The experimental results of Chapter 2 showed that no major modifications occurred in the appearance of the striated phase when varying the length of the lipid acyl chain from C14 to C20. It is shown that this insensitivity is reflected by the simulation results.

5.2 Methodology

5.2.a DPD method

The force acting on particle i, $\boldsymbol{f}_i$, is given as the pairwise additive sum of three forces [161, 180]:

$$\boldsymbol{f}_i = \sum_{j \neq i} \left(\boldsymbol{F}_{ij}^{C} + \boldsymbol{F}_{ij}^{D} + \boldsymbol{F}_{ij}^{R} \right) \qquad (1)$$

where $\boldsymbol{F}_{ij}{}^{C}$ is the conservative force determined by the inter- and intra-particle interactions. The dissipative force $\boldsymbol{F}_{ij}{}^{D}$ and the random force $\boldsymbol{F}_{ij}{}^{R}$ are given by [179, 182, 183]:

$$\boldsymbol{F}_{ij}^{D} = -\eta\, \omega^{D}\left(r_{ij}\right)\left(\hat{\mathbf{r}}_{ij} \cdot \mathbf{v}_{ij}\right)\hat{\mathbf{r}}_{ij} \qquad (2)$$

$$\boldsymbol{F}_{ij}^{R} = \sigma \omega^{R}\left(r_{ij}\right)\varphi_{ij}\hat{\mathbf{r}}_{ij} \qquad (3)$$

where $\mathbf{v}_{ij}$ = velocity difference $\mathbf{v}_i - \mathbf{v}_j$ between bead i and j, $\mathbf{r}_{ij} = \mathbf{r}_i - \mathbf{r}_j$, r_{ij} = distance $|\mathbf{r}_{ij}|$ and $\hat{\mathbf{r}}_{ij}$ = the unit vector $\mathbf{r}_{ij} / r_{ij}$.

The variable φ_{ij} is a Gaussian distributed random number. η and σ are constants giving the amplitude of the dissipative and random forces, respectively, and ω^D and ω^R are the corresponding weight factors. The forces $\boldsymbol{F}^D$ and $\boldsymbol{F}^R$ are coupled since the thermal heat generated by the random force must be balanced by dissipation [326]. The dissipation-fluctuation theorem then leads to the following relationship between ω^D and ω^R, η and σ [181 - 183, 185, 186]:

$$\omega^D(r) = \left[\omega^R(r)\right]^2 \tag{4}$$

$$\sigma^2 = 2\eta k_B T \tag{5}$$

$\boldsymbol{F}^D$ and $\boldsymbol{F}^R$ collectively act as a thermostat while preserving momentum and hence reproduce hydrodynamic (Navier-Stokes) flow on a mesoscopic scale [181].

Here, $\omega^R(r)$ is taken similar to that in [175, 179]:

$$\omega^R(r) = \begin{cases} (1 - r / R_c) & (r < R_c, \text{with } R_c = 1) \\ 0 & (r \geq R_c) \end{cases} \tag{6}$$

with R_C the cut-off radius outside which interactions are set to zero. Here, $R_C = 1$.

Time evolution of the particle configurations is given by Newton's equations of motion, which provide the derivatives of the particle positions and velocities with respect to the time t [161]:

$$\frac{d\mathbf{r}_i}{dt} = \mathbf{v}_i \tag{7}$$

$$m\frac{d\mathbf{v}_i}{dt} = \boldsymbol{f}_i \tag{8}$$

Care has to be taken how these formulas are implemented in discrete time algorithms. An adapted, self-consistent velocity-Verlet algorithm has been used (see [187, 327, 328] for details).

Beads within one molecule are connected by deformable springs, which can be described by the bond potential U_{spring} between adjacent beads i and $i + 1$ [171, 178]:

$$U_{\text{spring}} = \tfrac{1}{2}\, K_{\text{spring}} (r - r_{eq})^2 \tag{9}$$

with r the distance between beads i and $i + 1$, K_{spring} the spring constant and r_{eq} the equilibrium distance. Stiffness of the chain is included in the form of a 3-bead potential between the consecutive particles i - 1, i and $i + 1$:

$$U_{bend} = \tfrac{1}{2} K_{bend} (\theta_b - \theta_{eq})^2 \qquad (10)$$

with K_{bend} the bending constant, θ_b the angle between two adjacent bonds (i - 1, i) and (i, $i + 1$) and θ_{eq} the equilibrium angle

The intermolecular interaction was chosen as a soft repulsion of the type:

$$U_c = \tfrac{1}{2} a_{ij} (1 - r_{ij}/R_c)^2 \qquad (11)$$

with U_c the interaction potential, a_{ij} the interaction parameter, r_{ij} the distance between bead i and j.

Parameters in this chapter are expressed in reduced units with the cut-off distance R_c as the unit of length and the mass of one bead m as unit of mass. A reduced temperature T^* of 1 corresponds to $T = a/k_B$ where a is the unit of energy in which the parameters a_{ij} are expressed [183]. This is set in such a way that $a_{w\text{-}w} = 25$ reproduces the experimental compressibility of water at room temperature [187].

5.2.b Modelling of lipids and peptides

All lipid and peptide molecules consist of a number of beads representing larger clusters of atoms. Distinction is made between three different types of particles by choosing appropriate values for the intermolecular interaction parameters a_{ij} in formula 11. Water w, hydrophilic head H and hydrophobic tail T beads are used.

Water is included in the simulations as single beads of the type w. This groups together 3 'real' H_2O molecules [175]. Both the peptide and lipid are built up from both H and T beads. Distinction will be made between the beads of the lipid and peptide by using L or P for lipid or peptide, respectively, followed by the type of bead, *i.e.* L_H indicates the head beads of the lipid and P_T the tail beads of the peptide. The lipid molecules contain a polar headgroup of 3 H beads and two tails of each 6 T beads, following the $H_3(T_6)_2$ model of Kranenburg and Venturoli [179, 183]. The coarse-grained model of the lipid DPPC (di-16:0-PC) is shown in Fig. 5.1 together with its atomic representation. One tail bead represents 2 - 3 methyl groups. The interaction strengths a_{ij} are given in Table 5.I. These are adopted from Kranenburg *et al.* [179]. The large repulsion of $a_{w\text{-}H} = 80$ assures a sufficiently high hydrophobicity to allow assembly into a layer where the hydrophobic interior is shielded from the water. The lipid-lipid interactions are derived from the Flory-Huggins theory for polymers [188]. Together, these

interactions reproduce the experimental phase behaviour of a pure DMPC bilayer for the $H_3(T_5)_2$ lipid model [179, 183].

Neighbouring beads within the same lipid molecule are connected by harmonic springs with a spring constant of $K_{spring} = 100$ and equilibrium distance $r_{eq} = 0.7$. Bond angles between two neighbouring tail particles have an equilibrium value of $\theta_{eq} = 180°$ and a strength of $K_{bend} = 6$, while the equilibrium bond angle between the first bead of both tail chains and the head bead (*i.e.* between bead numbers 4 - 3 - 10 in Fig. 5.1) is set at 90° with $K_{bend} = 3$ [223]. Head beads are connected by a spring with a $K_{spring} = 100$. No preferential bond angles are included [179].

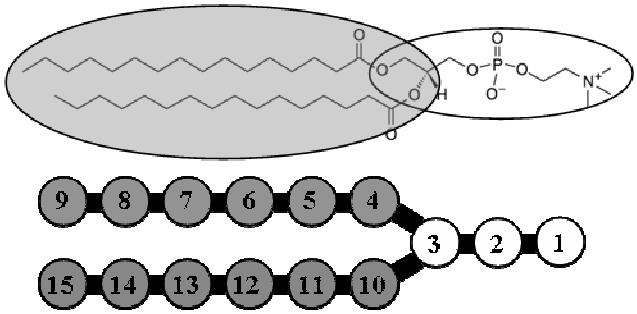

Fig. 5.1 Molecular representation of DPPC (above) and the used coarse-grained $H_3(T_5)_2$ model (below). The uniform grey region represents the hydrophobic part of the lipid and the white regions the polar headgroup region

Two different types of lipids were used: one that packs in a bilayer with a distinct polar angle θ between its acyl chains and the bilayer normal (z-axis) and one with a perpendicular orientation. The former lipids resemble DPPC and the second the perpendicularly oriented DPPE (see Chapter 4). Of course, this comparison is based on the tilt angle only as the hydrogen-bonding capability of the PE headgroups [15] is not modelled explicitly.
The average polar angle θ of these model lipids can be influenced by the choice of the L_H - L_H interactions [179]. An $a_{LH\text{-}LH}$ of 35 gives DPPC-like behaviour, while a reduction of this repulsive interaction to 10 gives DPPE-like behaviour. A reduced effective size of the PE headgroups is also thought responsible for the absence of a tilt angle in experimental DPPE bilayers [15, 31, 46].
In the remainder of this chapter, the names DPPC and DPPE will be used to identify these model lipids. The suffix (exp) or (sim) will be attached if necessary to avoid confusion between experimental and simulated systems.

The model of the peptide WALP contains a hydrophobic centre of T beads (P_T) capped by 4 H beads (P_H) on each side (see Fig. 5.2.b). The stiff, α-helical structure of the peptide was imitated by positioning the P_T beads in a helix with 4 beads per turn. One bead is connected to the next with $K_{spring} = 100$ as well as to the one immediately above it in the helix (*i.e.* bead i is connected to $i + 4$) with $K_{spring} = 200$. Bond angles were defined between beads i - 4, i and

$i + 4$ at an equilibrium angle $\theta_{eq} = 180°$ with a strength of $K_{bend} = 50$. The head beads at one terminus of the WALP molecule (P_{H1}) are different from those at the other terminus (P_{H2}). This enables us to mimic dipole-dipole interactions by choosing the interactions between like beads (P_{H1} - P_{H1} or P_{H2} - P_{H2}) attractive and those between unlike heads (P_{H1} - P_{H2}) repulsive. The remaining interactions are chosen similar to those of the lipid.

Table 5.I Intermolecular interaction strengths a_{ij} for the different types of beads: water w, lipid head L_H, lipid tail L_T, peptide tail P_T and the peptide heads P_{H1} and P_{H2}

	w	L_H	$L_T = P_T$	P_{H1}	P_{H2}
w	25	15	80	15	15
L_H	15	35 or 10[a]	80	35	35
$L_T = P_T$	80	80	25	80	80
P_{H1}	15	35	80	80	10
P_{H2}	15	35	80	10	80

a For the tilted DPPC and non-tilted DPPE lipids respectively

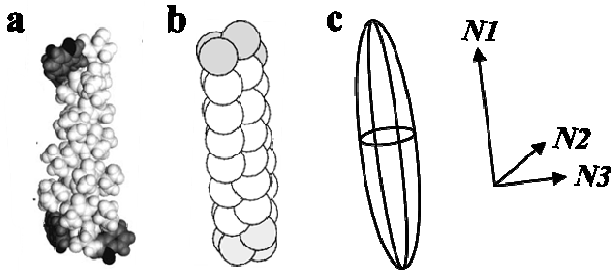

Fig. 5.2 Space-filling model of WALP23 [149] (**a**) next to the coarse-grained model of WALP-24 (**b**). Tryptophan groups are coloured grey and other amino acid groups white. In **c**, the principle axes of rotation ***N1***, ***N2*** and ***N3*** of a similarly shaped model are indicated. These are used to calculate the order parameter *S* and shape factor *P* (section 5.2.d)

5.2.c Initial configurations

Initial configurations of the pure lipid bilayers are made by placing 648 lipid molecules in a bilayer that has its surface parallel to the *xy*-plane. The remainder of the simulation box with a total *z*-height of 20 is filled with a layer of water on each side of the bilayer to eliminate interactions with the image of the simulation box created in the *z*-direction by the periodic boundary conditions. Periodic boundary conditions are used to minimize boundary effects of the simulation box in the *xy*-direction. The overall number density of beads in the system is set to $3/R_c^3$ [187].

The lipids are fully stretched (angles of 180º) and have an angle of 90º between the two tails. The initial polar angles θ_{init} of the lipids with respect to the bilayer normal are set to 30º and 0º, respectively, for DPPC and DPPE bilayers. The adopted final polar angle θ_L of the DPPC lipids is not a function of the initial orientation as placing them in an initial upright position leads to the same final polar angle after equilibration. The initial placement of lipids in a bilayer configuration is not essential as its formation from randomly placed lipids has been shown to be a self-mediated process [171, 176], but this time-consuming step was omitted here.

In section 5.4, the peptide WALP is included in the bilayer as single rows of coarse-grained WALP molecules, aligned along the *y*-axis. This is in agreement with the single linear arrays of WALP(exp) in the striated phase. The peptide molecules are rigid bodies and are centred symmetrically along the *z*-axis in a perpendicular orientation. This matches the perpendicular orientation of WALP(exp) in the striated phase that was found in Circular Dichroism measurements [33]. The choice of such a stiff peptide is justified by observations that WALP(exp) is relatively rigid [104] and does not alter its backbone conformation significantly when organized in the striated phase [110, 190], but the lipids do [110]. Immobile features have been used previously in DPD studies to simulate fluid flow between rigid walls [329 - 331]. The dipoles of WALP(sim) were arranged anti-parallel (P_{H1} next to P_{H2}), just like their experimental counterparts [110].
Typically, 18 WALPs and 35000 water beads were used. The regions between the lines of WALP were filled with DPPC or DPPE lipids in a bilayer conformation. The separation distance *D* between the lines of WALP was generally chosen large (typically ~ 30 lipid diameters), so the rows of WALP were independent. As *D* can vary during the simulation runs, the given values denote the distance after equilibration.

The length of the peptide is expressed in terms of the number of P_T beads n_T. This length is included in the name of the peptide, which is given as WALP-n_T (*e.g.* WALP-24 for n_T =24). [7] WALP-24 was used in most simulation runs, although the mismatch with DPPC is then larger than in the experimental WALP23/DPPC(exp) system (see Table 5.II). A longer model peptide (WALP-30, see Table 5.VI) should be used to reproduce the correct ratio in hydrophobic lengths. However, the effect of the shorter WALP-24 on the lipid bilayer is more explicit and hence more clearly visible.
In some simulations, the length of the hydrophobic part of the WALP molecules was varied to study the consequences of hydrophobic mismatch between lipid and WALP. The length of the peptide was varied rather than that of the lipid as changes in the length of the tail alter the phase behaviour and tilt angle of the lipids [179].

[7] Note that the number of tail beads n_T in WALP-n_T cannot be compared directly to the number of amino acids *m* in the experimental WALP*m*. Therefore, a different notation is used for these two peptides

Table 5.II Comparison of the experimental and model systems of WALP and DPPC in the gel phase. The simulation data are expressed in reduced units

	experimental			**model**		
	DPPC (nm)	WALP23 (nm)	ratio DPPC/ WALP23	DPPC bilayer at T^* =0.3	WALP-24	ratio DPPC/ WALP-24
diameter σ_L or σ_P ***b***	0.8	1	0.8	1.19	1.5	0.8
total length	4.4 - 4.7 [29, 39, 13]	3.6 [74]	1.2 - 1.3	10.6	5.43	1.9
hydrophobic length d_{HPH}	3.3 - 3.6 ***a***	2.6 [181]	1.3 - 1.4	6.8 ***b***	4.03	1.7
polar angle θ (°)	30 - 32 [19, 29, 30]	0	-	22	0	-

a By subtracting 1.1 nm from the total length [233]

b Calculated from the area/molecule A_L (Fig. 5.7.b) through $\sigma = \sqrt{(A_L/\pi)}$

5.2.d Simulation runs and calculated parameters

Equilibration runs of typically 500 000 cycles were followed by production runs of 250 000 cycles. Some systems were subsequently subjected to another 1 000 000 cycles to ensure equilibration. A time-step of integration of $\Delta t = 0.02$ is used. Imposing a constant (*N, V, T,* surface tension $\gamma = 0$) ensemble in the manner of [179, 183] ensures that the system is in a tensionless state [332]. This is done by alternating every 50 DPD cycles with one Monte Carlo step that attempts to change the area. Changes in the *x*- and *y*-direction are allowed for the pure lipid bilayers, but only in the *x*-direction for the WALP-containing layers. No expansion of the WALP rows was allowed.

The orientation and shape of the lipid and peptide molecules are characterized through their inertia tensor. The eigenvalues of the inertia tensor are the principal moments of inertia $0 \leq I_1 \leq I_2 \leq I_3$. The corresponding eigenvectors $\boldsymbol{N_1}$, $\boldsymbol{N_2}$ and $\boldsymbol{N_3}$ are the principle axes of rotation (see Fig. 5.2.c). The inertia tensor is calculated from the positions of the beads within each molecule [333]. The polar angle θ of each molecule is given by the angle between the axis of easiest rotation $\boldsymbol{N_1}$ (lipid director) and the *z*-axis. These define the average chain-order parameter *S* in the whole system through:

$$S = \tfrac{1}{2} \langle 3 (\cos^2\theta) - 1 \rangle \qquad (12)$$

S attains a value of 1 for perpendicularly oriented molecules with $\theta = 0$, a value of -0.5 when θ = 90° and 0 for randomly oriented molecules [179]. *S* is calculated differently, and probably

more accurately, in equation (12) than in [179], where the molecular director of the lipid is based on the first and last bead of the lipid tail only. Here, all beads contribute.

The given tilt angle of the lipids in the bilayer (for example, in Fig. 5.7.e) is estimated from averages of the measured polar angles (θ in Fig. 5.3) of the individual molecular directors with the bilayer normal. Additionally, an orientational distribution $N(\theta)$ is calculated for the pure lipid bilayers. This gives the number of molecules $dN(\theta)$ with a tilt angle in a small interval between θ and $\theta + d\theta$. In our simulations, $d\theta = 2°$.
The average polar angle gives a correct tilt angle when the orientational distribution $N(\theta)$ is peaked at values of θ that are far enough from the z-direction (further than the variance). However, a different situation arises at small $\theta \approx 0$, where the average θ is essentially a measure of the variance in the tilt angles of the individual lipids and gives a non-zero value. The probability distribution $P(\theta)$ should be inspected to discriminate between these two cases. In the latter case, $P(\theta)$ peaks near $\theta = 0$. The probability distribution $P(\theta, \varphi)$ to find a lipid with an orientation given by θ and φ is related to $N(\theta)$, through:

$$N(\theta) \sim \int P(\theta, \varphi) \sin\theta \, d\varphi \qquad (13)$$

φ is roughly constant in the gel phase within the interval θ and $\theta + d\theta$, while φ varies randomly from 0 to 2π in the isotropic fluid phase. In both cases, this reduces equation (13) to:

$$N(\theta) \sim \sin\theta_L \, P(\theta) \qquad (14)$$

This can be also be rationalized by considering that $N(\theta)$ can be described by an area of height $d\theta$ on the circumference of a sphere (see Fig. 5.3). This obviously leads to a much larger area near $\theta \approx \pi/2$ ('equator') than near the top of the sphere at $\theta \approx 0$. Dividing $N(\theta)$ by $\sin\theta$ corrects for this.

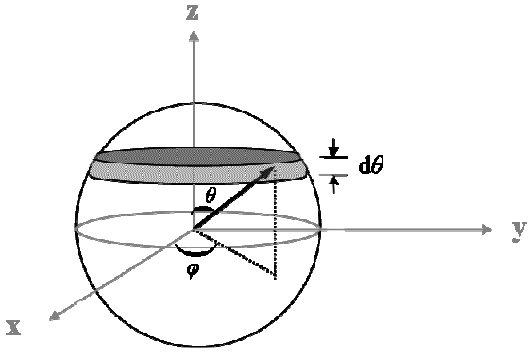

Fig. 5.3 Area occupied by the lipid director ***N1*** (black arrow) between the polar angle θ and $\theta + d\theta$. φ gives the azimuth angle

A shape factor P_L is used to monitor changes in the molecular shape of the lipids, for instance when it exchanges its elongated shape for a more compressed one upon melting. P_L is given by the ratio of the largest over the smaller principal moments of inertia:

$$P_L = 2\, I_1 / I_2 + I_3 \qquad (15)$$

P_L attains a value of 1 for spherical particles ($I_1 = I_2 = I_3$) and 0 for an infinitely long cylinder ($I_1 << I_2, I_3$).

The hydrophobic thickness d_{HPH} of the lipid or peptide gives the height of the region in the z-direction that is occupied by L_T or P_T beads, respectively. The total thickness d_L includes the head L_H or P_H beads. The area per lipid A_L is calculated by dividing the average area of the simulation box by half (because of the bilayer conformation) the number of lipid molecules. In the presence of the rigid peptide barrier of section 5.4, the parameters S_L, P_L, θ_L and d_L of the lipid bilayers are not constant in the x-direction and are described by a x-dependent profile, where the values are measured at intervals of $\Delta x = 0.5$. These are averaged over typically 500 conformations during the production run.

5.3 Pure lipid bilayers

5.3.a Results

DPPC lipids

The phase behaviour and characteristics of hydrated, pure DPPC bilayers were studied with respect to the reduced temperature T^*. DPPC lipids were organized in a lamellar bilayer configuration at all used temperatures ($0.1 < T^* < 0.8$), as is immediately evident from the snapshots in Fig. 5.4. All hydrophilic L_H beads (dark grey) are on the outside of the layer, while all hydrophobic tail L_T beads (light grey and white) are located in the interior. The terminal bead of each lipid chain (*i.e.* beads 9 and 15 in Fig. 5.1) is coloured white. Water beads are omitted for clarity. At $T^* = 0.1$ and $T^* = 0.3$ (Figs. 5.4.a and b), the bilayer is rigidly organized with a clearly defined midplane and the lipids have stretched tails that are tilted with respect to the bilayer normal. A higher temperature (Figs. 5.4 c, d) leads to an increasing disorder of the chains and headgroups. Concomitantly, the well-defined midplane vanishes and the overall bilayer thickness is reduced. Fig. 5.4.c at $T^* = 0.425$ represents a special case, where the bilayer shows a distinct modulation in its thickness (‘ripple’).

These four phases have been ascribed by Kranenburg *et al*. [179] to the experimentally observed crystalline subgel L_c', gel L_β', ripple P_β' and liquid-crystalline or fluid L_α phase. It has been shown that the lipid tails become disordered and motions of the molecules increase upon proceeding towards the high-temperature L_α phase(exp) [38, 39]. The densities of the water w, head L_H and tail L_T beads along the z-axis are given in the density profiles of Figs. 5.5.a - c.

The bilayer organization is again reflected in these profiles: the middle, interior part consists only of tail L_T beads, flanked by a region of L_H on each side. Water is present on the outside of the membrane and intercalated in the polar lipid headgroup region, but its density falls off to zero in the hydrocarbon tail region. Each of the separately distinguishable peaks at $T^* = 0.1$ represents one bead. All 2 x 3 head beads and 2 x 6 tail beads of the two bilayer-leaflets are accounted for. Water shows a layered profile, indicating a highly ordered packing. Higher temperatures lead to a less rigidly organized packing and the separate peaks of the heads and tails broaden progressively ($T^* = 0.3$) until they merge completely ($T^* = 0.8$).

The statistical distribution $N(\theta_L)$ of the lipid polar tilt angles θ_L in Fig. 5.6 shows that the lipid director is narrowly distributed around θ_L = 19º and 180 - 19º at $T^* = 0.1$. The curve is zero in the intermittent region between the peaks. The peaks broaden with increasing temperature (T^* = 0.3 and 0.425) and the maximum shifts towards larger polar angles of 23º and 27º, respectively. A contribution around 90º appears between the maxima at temperatures of $T^* > 0.65$ (shown for $T^* = 0.8$).

Six parameters are used to characterize the DPPC bilayers at different temperatures: the total bilayer thickness d_L, the thickness of the hydrophobic tail region d_{HPH}, the area per molecule A_L, the shape factor P_L (see equation 15), the order parameter S_L and the related average polar angle θ_L (see equation 12). The dependency of these parameters on the temperature T^* is shown in Figs. 5.7.a - e (solid symbols). These were measured in the direction of increasing T^*. The downward, cooling scans coincided exactly with the heating curves (data not shown). This indicates that the system is close to equilibrium.
Some general trends can be observed upon increasing T^* from 0.1 to 0.8: d_L, d_{HPH} and S_L decrease, while A_L, P_L and θ_L increase. The rates by which these curves increase or decrease are not constant, however, and four intervals with a different slope can be identified. The slopes are close to zero in the initial region between $0.1 < T^* < \sim 0.275$ - 0.3 for all parameters. Two different, steeper slopes can be distinguished in Figs. 5.7 a - c between $0.275 < T^* < 0.425$ and $0.425 < T^* < 0.525$. Above $T^* = 0.525$, the slope levels off. The curve of S_L (Fig. 5.7.d) shows a maximum in the region $0.425 < T^* < 0.525$, which leads to a minimum in the corresponding curve of θ_L in Fig. 5.7.e. The changes in slope mark the transitions between the four different phases, *i.e.* the subgel L_c', the gel L_β', the ripple P_β' and the liquid-crystalline L_α phase. The corresponding phase transition temperatures T_{tr} are given in Table 5.III.

Table 5.III Measured phase transition temperatures T_{tr} in reduced units. Literature values from [179] are given in brackets

lipid	$L_c \rightarrow L_\beta'$ or L_β [a]	$L_\beta' \rightarrow P_\beta'$	$P_\beta' \rightarrow L_\alpha$	$L_\beta \rightarrow L_\alpha$
DPPC	0.275 (0.3)	0.425 (0.375)	0.525 (0.475)	-
DPPE	0.225 (0.25)	-	-	0.675 (0.7)

a L_β' for DPPC and L_β for DPPE

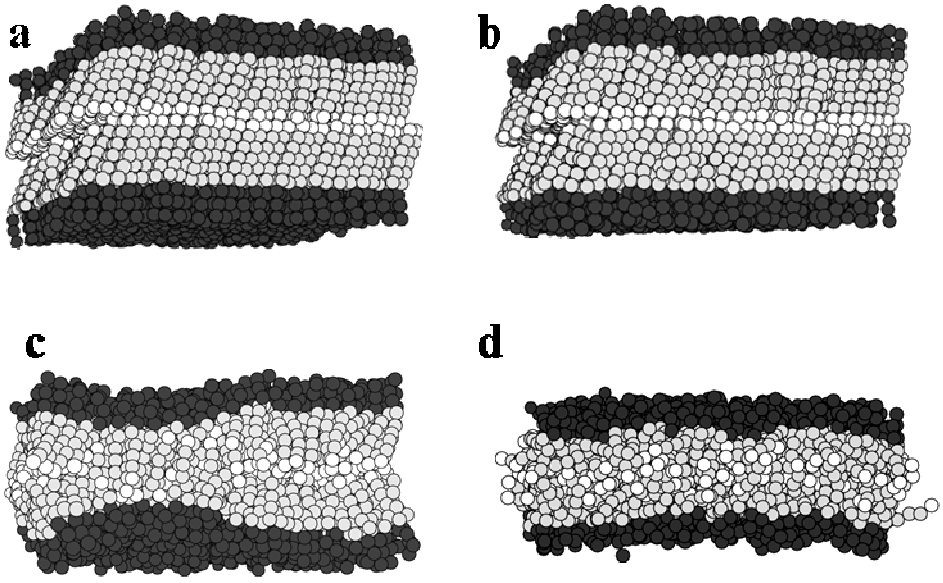

Fig. 5.4 Snapshots of each of the DPPC phases: **a.** the crystalline subgel L_c' at $T^* = 0.1$, **b.** the gel L_β' phase at $T^* = 0.3$, **c.** the ripple P_β' phase at $T^* = 0.425$, showing one ripple, and **d.** the fluid liquid-crystallineL_α phase at $T^* = 0.8$. L_H groups are coloured dark grey, terminal L_T beads white and other L_T groups light grey. Beads are shown at 85 % of their real size for clarity

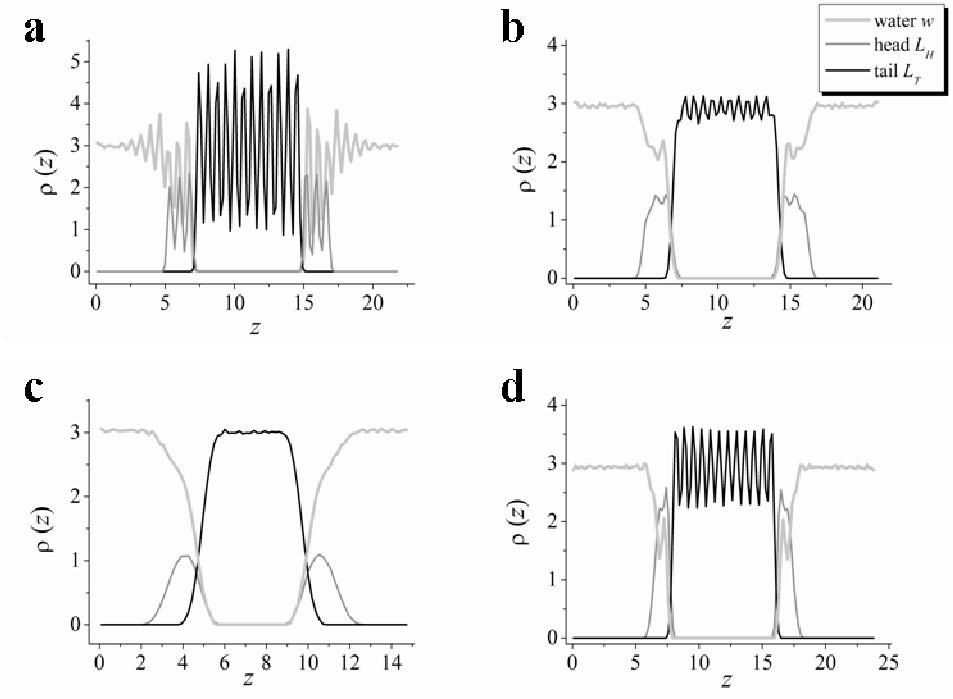

Fig. 5.5 Density profiles of DPPC bilayers at **a.** T^*= 0.1, **b.** T^*= 0.3 and **c.** T^*= 0.8, corresponding with the L_c', L_β' and L_α phase. **d.** DPPE at T^*= 0.3 in the L_β phase. With increasing z, contributions for water w (light grey), the lipid headgroups L_H (dark grey), the lipid tails L_T (black), L_H and w are encountered, respectively. The area of each curve is scaled to represent the total number of beads of that respective type

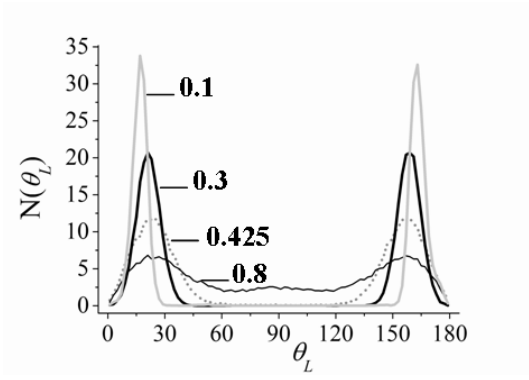

Fig. 5.6 Distribution $N(\theta_L)$ of the lipid polar angles θ_L for a DPPC bilayer at the reduced temperatures T^* given in the figure. $N(\theta_L)$ gives the number of lipid molecules which have an angle in the interval θ_L + 2 as function of θ_L

DPPE lipids

The characteristics of a DPPE bilayer as function of temperature T^* are shown in Figs. 5.7.a - e (open triangles). These curves show the same qualitative behaviour with T^* as DPPC : d_L, d_{HPH} and S_L show a general decrease and A_L, P_L and θ_L an increase as the tails of the lipids become more fluidized and lateral and rotational motions of the molecules increase. Surprisingly, the differences in the inter-headgroup repulsion $a_{\text{LH-LH}}$ between DPPC and DPPE do not lead to large differences in the initial region from $0.1 < T^* < 0.225$ in Figs. 5.7.a - e. This interval corresponds to a tilted, crystalline subgel L_c' phase [179], of which the snapshot is given in Fig. 5.8.a. The overlap of the curves of d_{HPH}, A_L, P_L and θ_L for the DPPE and DPPC bilayers indicate similar conformations of the lipid tails in this L_c' phase. d_L is the only exception and is larger for DPPE than for DPPC. The different total thicknesses d_L and identical hydrophobic thickness d_{HPH} for DPPE and DPPC suggest a dissimilarity in the packing of the headgroup region (see the discussion).

Major differences between DPPC and DPPE bilayers become apparent, however, upon increasing the temperature above $T^* = 0.2$. This leads to a distinct jump in the plots for DPPE (Figs. 4.7.a - e) as a transition from the L_c' to the gel L_β phase takes place [179]. This is accompanied by a large reduction in the average lipid polar angle θ_L to ~ 7º (see Fig. 5.7.e); in contrast to the continuing high $\theta_L \approx 20$ - 25º of DPPC.
The snapshot of the DPPE gel phase ($T^* = 0.3$) in Fig. 5.8.b shows the almost perpendicular orientation of the lipids with the bilayer normal, although some small deviations are visible. In this case, the non-zero value average $\theta_L = 9°$ at $T^* = 0.3$ is the result of fluctuations of the lipid director around the bilayer normal (see text above Fig. 5.3). The presence of a phase that is on average non-tilted is supported by the plot of the probability $P(\theta_L)$ in Fig. 5.9.b, which centres around $\theta_L = 0$. The DPPC gel phase is on average tilted and has a maximum around $\theta_L = 20°$.

The packing of the DPPE L_β phase becomes gradually less ordered with increasing T^*. The slopes of the various parameters in Figs. 5.7.a - e have an almost constant value between $0.2 < T^* < 0.5$ - 0.6, after which the slope gradually increases but becomes constant again at $T^* \geq 0.675$. The onset of the fluid L_α phase lies at $T^* = 0.675$. The choice of $T_{tr} = 0.675$ as phase transition temperature instead of $T^* = 0.5$ - 0.6 is based on the polar angle distribution $N(\theta_L)$ (Fig. 5.9.a) and the snapshots (data not shown). $N(\theta_L)$ indicates that the onset of a phase with less orderly distributed angles starts at $T^* = 0.65$, where a small non-zero contribution first appears between the maxima. This becomes more pronounced at $T^* = 0.675$.

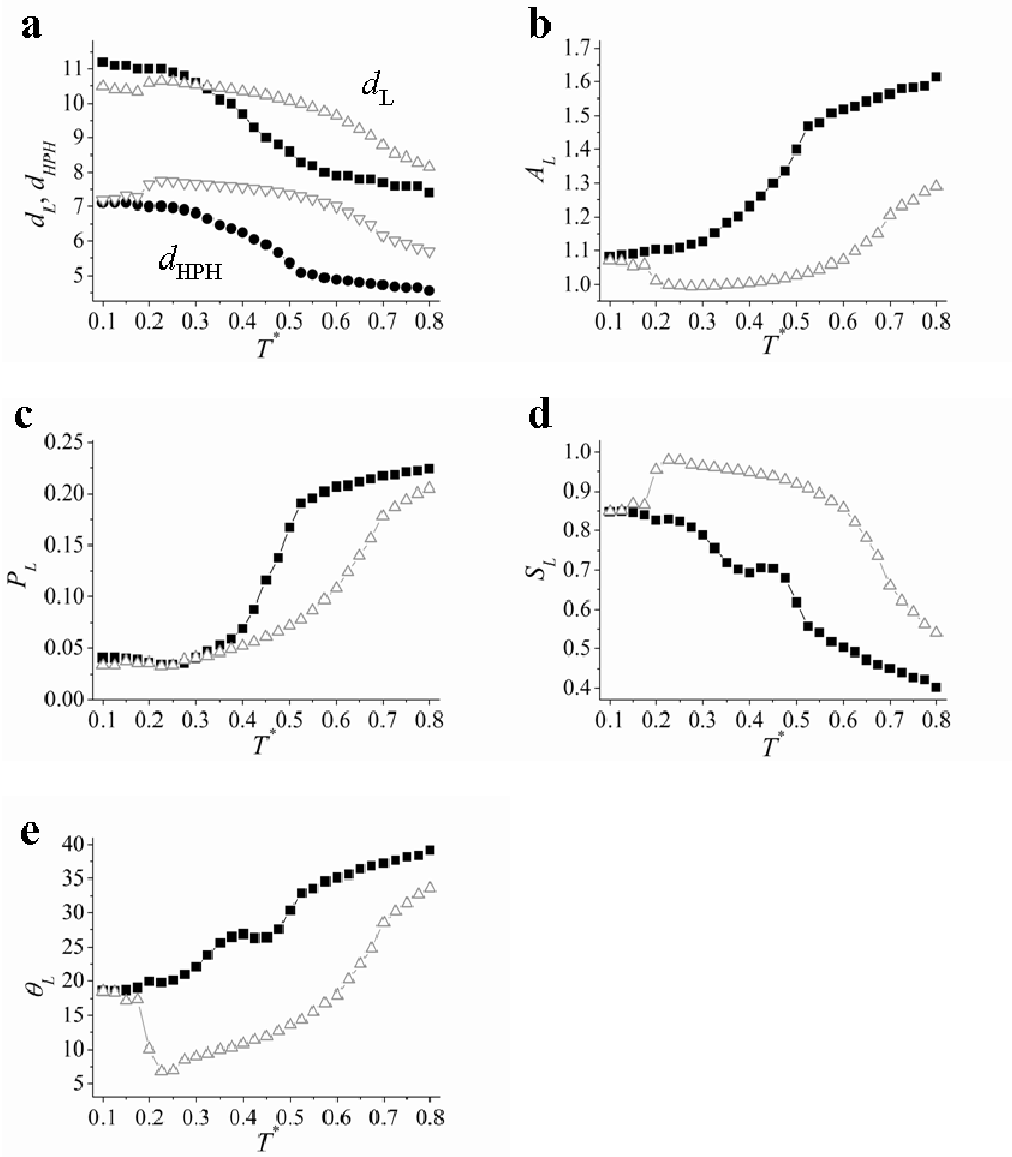

Fig. 5.7 Plots of **a.** total and hydrophobic bilayer thickness d_L (upper curves) and d_{HPH} (lower curves), **b.** area per lipid A_L, **c.** shape factor P_L, **d.** order parameter S_L and **e.** average polar angle θ_L as function of temperature T^*. Solid symbols are results for DPPC and open symbols for DPPE. The fluctuations increase monotonously with T^* from ~ 5 % at low T^* to ~ 80 % at T^*= 0.8 (not shown). Note that the given average θ_L in **e** can be interpreted as the average tilt angle in the tilted gel phase of DPPC, whereas it gives the variance in the tilt angle in the non-tilted gel phase of DPPE and in the fluid phase (see text above Fig. 5.3)

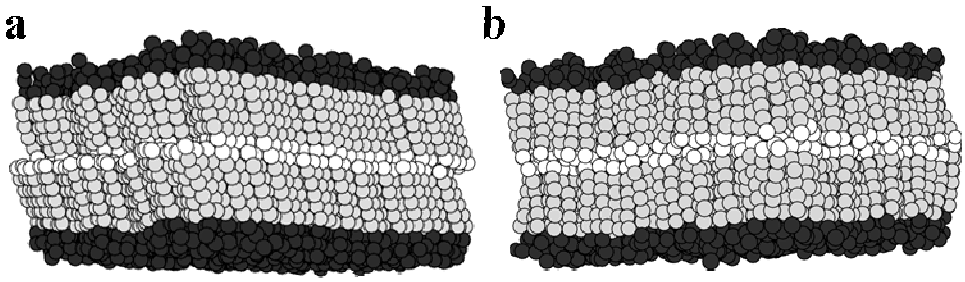

Fig. 5.8 Snapshots of a DPPE bilayer **a.** in the crystalline L_c phase at T^*= 0.1 and **b.** in the non-tilted gel L_β phase at T^*= 0.3. L_H groups are coloured dark grey, terminal L_T beads white and other L_T groups light grey

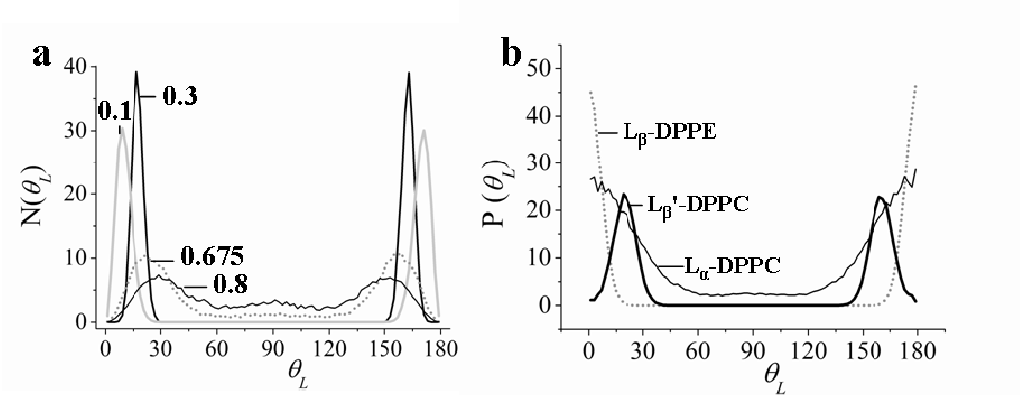

Fig. 5.9.a Distribution $N(\theta_L)$ of the polar angles of a DPPE bilayer at different temperatures T^*. Note that the polar angle in the gel phase (T^*= 0.3) is considerably lower than that of DPPC in Fig. 5.5. **b.** Probability distribution $P(\theta_L)$ of finding the lipid director between and θ_L and θ_L + $d\theta_L$ (see equation 14). Both curves for the bilayers of DPPE in the L_β phase (T^*= 0.3) and DPPC in the L_α phase (T^*= 0.8) peak around θ_L = 0 and are on average not tilted, while DPPC in the L_β' phase (T^*= 0.3) is tilted

The transition temperatures T_{tr} of the $L_c' \rightarrow L_\beta$ and $L_\beta \rightarrow L_\alpha$ phase transitions are given in Table 5.III.

In the L_α phase, the curves of the various parameters of Fig. 5.7 of DPPE converge with those of DPPC after being well-separated in the gel phase.

Note that the ripple phase P_β' was not observed in these DPPE bilayers. The presence of a tilt of the acyl-chain is a prerequisite for the formation of the corrugated P_β' phase, which is therefore neither observed here nor in DPPE(exp) bilayers [3, 10, 29, 179].

5.3.b Discussion

DPPC lipids

DPPC lipids form bilayers at all T^*. The positions of the headgroups, hydrophobic tails and water in Fig. 5.5 is consistent with comparable electron density plots derived from X-ray diffraction for hydrated DPPC(exp) multi-layers [39, 334, 335]. Some water of hydration is present in the polar headgroup regions [14, 30], but hardly any water penetrates into the hydrophobic core of the membrane. The bilayer configuration effectively shields the lipid tails from the aqueous surroundings.

Four distinct phases are found in the simulations, which correspond to the four consecutive phases found for DPPC(exp) bilayers with increasing temperature [19, 29]: L_c', L_β', P_β' and L_α. The corresponding phase transition temperatures T_{tr} are in close agreement with those of Kranenburg *et al.* [179] (see Table 5.III). The minor discrepancies can be ascribed to the ambiguity in the assignments of T_{tr}, as each of the individual parameters shows its discontinuity at a slightly different T^*. An average value is chosen here, which may differ slightly from that of [179]. Moreover, S_L is calculated differently here and an additional parameter is used: the shape factor P_L.
The phase transitions in the simulations do not proceed through discrete steps. This contrasts with the stepwise changes in thickness [40], molecular area [29] and volume [253] that are observed for the experimental systems at the main transition from the solid to fluid phase. This transition is generally acknowledged as being a first-order phase transition according to the Ehrenfest classification [247, 255, 336]. The continuous phase transitions in the simulations are most likely a consequence of the relative small system sizes [179].

Lipids in the low-temperature L_c' phase are known to have almost completely stretched, rigid acyl chains, whose order and rotational movements increase slightly upon entering the gel L_β' phase [3, 21]. Lateral and rotational motions increase and the order of the lipid tails decreases when the temperature is increased further. The bilayer passes from the L_β' through the ripple P_β' [19, 35] to the disordered L_α phase [19, 21, 32, 234]. Both the progressive disordering of the lipid tails with temperature and the formation of the corrugated surface of the ripple phase P_β' (one ripple) can be observed in the snapshots of Figs. 5.4.b - d. The less rigid and efficient packing leads to the disappearance of a well-defined midplane between both leaflets of the bilayer. The decreased ordering is also evident from the broadening of the peaks of the density profiles in Fig. 5.5. The snapshots of the fluid phase show highly disordered lipid tails, which sometimes lie almost parallel to the bilayer *xy*-plane or turn back on themselves.
The periodicity of the single ripple in the P_β' phase will most likely be imposed by the boundaries of the simulation box. The reader is referred to [179] where a more extensive study and discussion of this phase is given.

The gradual fluidization of the lipid tails with T^* reduces the observed bilayer thickness d_L and d_{HPH} (Fig. 5.7.a), while enlarging the lateral dimensions of the lipid molecules (A_L, Fig. 5.7.b).

Experimentally, the area per lipid increases by 40 % from ~ 0.5 nm^2 in the gel L_β' phase of DPPC [30, 235, 251] to 0.7 nm^2 in the liquid-crystalline L_α phase [29]. This corresponds roughly with the observed increase of ~ 30 % in A_L (Fig. 5.7.b). The decrease in d_L of approximately 20 - 30 %, is also roughly of the same order as the experimental value of ~ 20 % [40]. Much smaller steps in molecular volume [253] and bilayer thickness [29] are observed in experimental systems at the $L_c' \rightarrow L_\beta'$ and $L_\beta' \rightarrow P_\beta'$ transitions.
The increased lateral dimensions and reduced height of the molecules lead to an increase of P_L (Fig. 5.7.c). A value of $P_L = 0$ would indicate an infinitesimally long and thin molecule, while a value of 1 indicates a spherical shape. Even in the L_α phase, the lipid tails retain a predominantly elongated, cylindrical shape with $P_L \approx 0.2$. A more spherical shape would probably prevent the lipids to pack into a bilayer configuration where the L_H groups form a close-packed layer on the outside. Gaps in this polar region would lead to penetration of water into the hydrophobic region of the membrane, which is clearly an unfavourable situation in view of the large repulsion between the L_T and water w beads.

The average polar angle θ_L of 22 - 27º in the gel phase ($0.275 < T^* < 0.425$, Fig. 5.7.e) is a little less, but close to the 30 - 32º reported for hydrated DPPC bilayers [19, 29, 30]. The progression to the fluid phase is accompanied by an increase in the measured polar angle θ_L in Fig. 5.7.e and a reduced cooperativity in the polar tilt angles (Figs. 5.4 and 5.6). This phase in on average non-tilted, however, as the probability distribution $P(\theta)$ in Fig. 5.9.b peaks around $\theta_L = 0$ (see text above Fig. 5.3). The average polar angle is determined by the large fluctuations away from $\theta_L = 0$.

The plots of A_L and d_L agree with similar plots in [179], as does the low-temperature part of the plot of S_L of the L_c' and L_β' phases. Nevertheless, the values of S_L are systematically higher in the P_β' and L_α phase (Fig. 5.7.d, $0.425 < T^* < 0.8$) than those of [179]. This could be due to the different method of calculating S_L. In this study, the direction of the lipid molecule is based on all the beads instead of only the first and last tail beads, like in [179]. This probably gives a more accurate value of S_L and θ_L, especially as some lipid chains bend.
The origin of the pronounced deviation in the ripple P_β' phase ($0.425 < T^* < 0.675$), where S_L suddenly increases, is not clear. The ripple phase was shown to consist of a coexisting solid and fluid phase [179, 249]. The higher S_L of the L_c' phase could dominate the total value of S_L, leading to a net increase. Alternatively, the increased S_L could be due to constraints imposed on the bilayer to fit one ripple period in the relatively small simulation box.

DPPE lipids

The main difference between the DPPE and DPPC lipids is the L_H - L_H interaction $a_{LH\text{-}LH}$ [179]. This alters the packing of the bilayer and reduces the number of phases to three, as only a crystalline L_c', a non-tilted gel L_β and liquid-crystalline L_α phase are encountered in DPPE. The P_β' ripple phase that was observed for DPPC is absent.

First, in the subgel L_c' phase ($0.1 < T^* < 0.2$), the different curves for DPPE in Figs. 5.7.a - e are close to those of DPPC or overlap completely. This suggests that DPPE packs in a fashion that is very similar to DPPC. Possibly, the frozen-in close packing of the tails in the crystalline matrix dominates over the L_H - L_H interactions in determining the adopted conformation. The lower total bilayer thickness d_L of DPPE compared to DPPC (at $0.1 < T^* < 0.325$) suggests that differences occur in the headgroup region, where the packing of the PE headgroups is less ordered (see the snapshots in Figs. 5.4 and 5.8). This leads to a thinner L_H region, as is also clear from the more narrow peaks of L_H in the density profile of DPPE (Fig. 5.5.d) compared to DPPC (Fig. 5.5.b). Measurements of the thickness of the headgroup region of a similar lipid model by [179] confirm that this is indeed the case. The increased ordering is probably due to the larger repulsive interactions between the PC headgroups, which leads to a tendency to minimize contact between the headgroups by maximizing the space between them. The voids in between are filled with water. The density plots of Figs. 5.5.b and d of DPPC and DPPE in the gel phase show that the curve for water falls off faster in the PE headgroup region than for PC, indicating that less water intercalates in the less ordered PE polar region than in the ordered PC polar region. Experimentally, PE groups are also hydrated by a smaller number of water molecules than PC groups [14].

The influence of the smaller repulsion parameter $a_{LH\text{-}LH}$ between the PE headgroups becomes more important upon entering the gel L_β phase at $T^* > 0.2$. The reduced repulsion leads to an essentially non-tilted orientation of the DPPE molecules. This is immediately evident from the probability distribution $P(\theta)$ in Fig. 5.9.b, which peaks around $\theta_L = 0$. The non-zero value of the measured polar angle $\theta_L \approx 9°$ at $T^* = 0.3$ in Fig. 5.7.e reflects the fluctuations of the tilt director around zero.
The smaller polar angle of the DPPE lipids reduces the projected area on the *xy*-plane (smaller A_L, open triangles in Fig. 5.7.b) and increases the vertical projected length of the hydrophobic tails (larger d_{HPH}; open triangles in Fig. 5.7.a) compared to DPPC (solid squares). Above $T^* > 0.325$, the contribution of the tails to the total bilayer thickness d_L dominates that of the relatively thin headgroup region and the curve of d_L crosses over to become larger for DPPE than for DPPC.

The shape factor P_L is independent of the tilt angle (see equation 15). P_L is practically identical for the DPPE and DPPC gel phases up to $T^* \approx 0.3$, after which DPPE has a lower P_L. This indicates a similarity in the overall shape of the DPPE and DPPC molecules in the solid L_c' and L_β phases that persists almost to the onset of the DPPC P_β' phase. The onset of the P_β' phase of DPPC alters the packing characteristics considerably, leading to the observed larger divergence of the curves for the two lipids in Figs. 5.7.a - e. Finally, the conformation of both lipids becomes more similar in the disordered fluid L_α phase and the curves converge.

5.4 Peptide/lipid mixed systems with rigid peptides

5.4.a Results

DPPC bilayer with WALP-24

WALP is included in the gel-phase, DPPC bilayer as single rows of rigid GC molecules. The snapshot of a mixed WALP-24/DPPC bilayer is shown in Fig. 5.10.a (top-view). Two single rows of WALP are present, which are aligned with the *y*-axis. The water w and lipid polar L_H beads have been omitted for clarity. The two different termini of the peptide have an anti-parallel orientation with respect to each other, with P_{H1} next to P_{H2}. The side-view in Fig. 5.10.b shows the bilayer arrangement of the lipids between the shorter rows of WALP. A number of lipids bordering the WALP (boundary lipids) have a distorted acyl-chain conformation with a reduced thickness and polar angle as compared with the lipids located halfway between the two lines of WALP.

The modification of the DPPC packing near the peptide is quantified in Fig. 5.11.a - c (black lines) where profiles of the thickness d_L, the shape factor P_L and the polar angle θ_L of the DPPC lipids are given as function of the position on the *x*-axis. The *x*-values are scaled with the separation distance between the rows of WALP *D* to make comparison with other systems possible. The first row of WALP-24 peptide is then located at $x/D = 0$ and the second row at $x/D = 1$. For DPPC, $D = 39.1$ after equilibration, which corresponds to a spacing of ~ 32 rows of lipids between the rows of WALP-24 (*i.e.* ~ 64 lipids in the bilayer configuration). This should be sufficient to represent isolated, independent rows of WALP-24.

The parameters that describe the conformation of the lipids display a pronounced deviation from the intrinsic values in the pure lipid phase (straight horizontal lines in Fig. 5.11) close to WALP. The thickness d_L is reduced in the bilayer regions bordering the lines of WALP. d_L increases towards larger x/D and passes through a broad overshoot with a maximum around $x/D = -0.20$ and 0.20 and again at 0.80 (= 1 - 0.20) and 1.20 (= 1 + 0.20). This corresponds to a distance of $n(\sigma_L) \sim 6$ lipid diameters σ_L from the edge of the peptide, when using the parameters of Table 5.II. In the remainder of this chapter, only the first positive value of x/D will be mentioned. The position of the maximum or minimum of the overshoot region will be denoted by x_{max}.

The thickness of the bilayer gradually decreases at larger distances, until d_L reaches a value that is close to the 10.6 of a pure DPPC bilayer. This point will be defined as x_{bulk}/D and can be considered as the perturbation length after which the peptide no longer has any influence and the bilayer resumes the packing of a pure lipid bilayer. x_{bulk}/D is measured as the value where the tangent of the curve and the value on the *y*-axis of the horizontal steady-state value (Figs. 5.11.a - c) intersect. Here, $x_{bulk}/D \approx 0.39$.

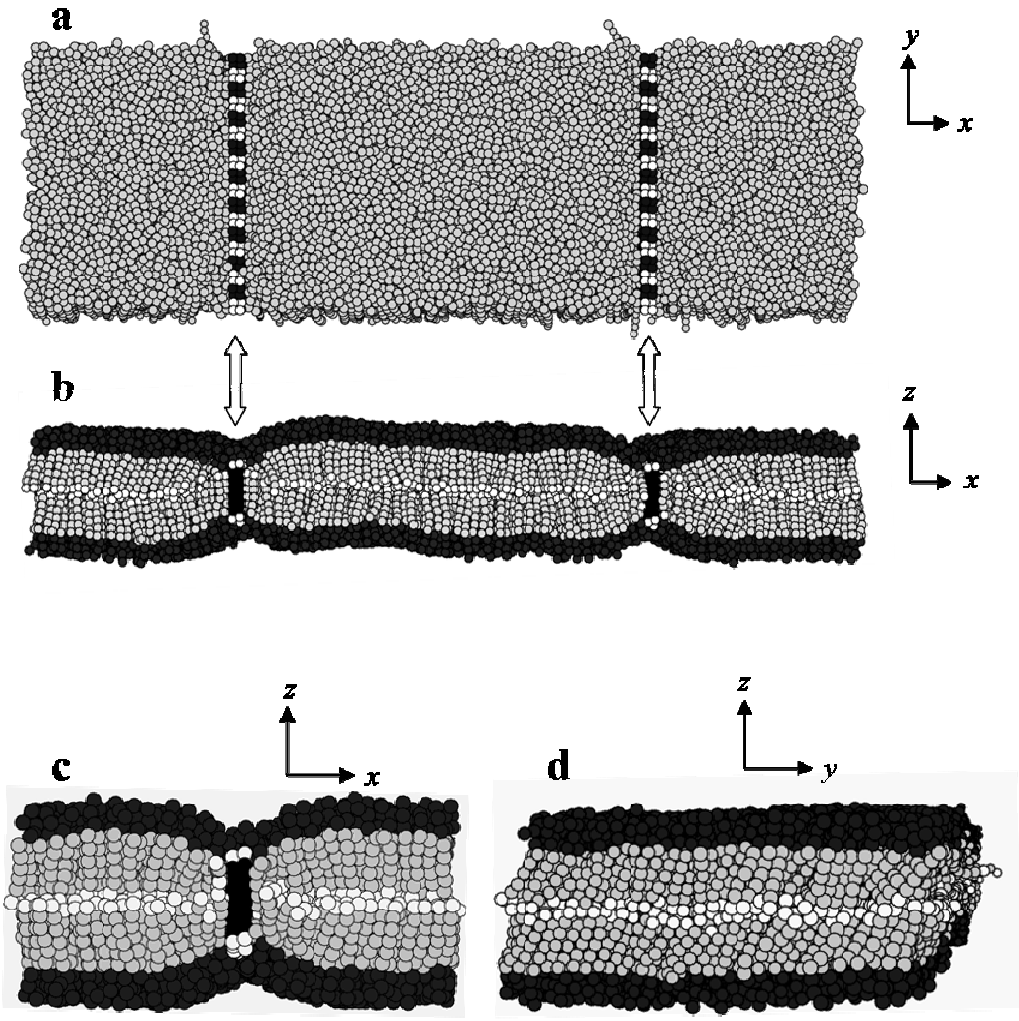

Fig. 5.10 Snapshots of a DPPC bilayer with the positions of the two rows of WALP-24 indicated by white arrows. Lipid headgroups L_H are depicted in dark grey and the tail beads L_T medium grey and the terminal L_T white. In the top-view in **a**, the two different headgroups of WALP P_{H1} and P_{H2} are black and white, whereas they are all coloured white in the side-views **b** to **d**. The P_T-core of WALP is coloured black. **b.** gives the side-view of the whole system (*xz*-plane) and **c.** is a close-up of the lipid configurations around one row of WALPs. **d.** gives the side-view in the *yz*-plane, where the tilted conformation of the DPPC lipids is visible

The shape factor P_L in Fig. 5.11.b drops off sharply from its initial maximum next to the peptide at $x/D < 0.05$. P_L then passes through a broad minimum (undershoot) with $x_{max}/D \approx 0.18$ before returning to the value of unperturbed DPPC of 0.041 at a distance $x_{bulk}/D \approx 0.34$. This corresponds to an initial layer of so-called boundary lipids with partially fluidized acyl chains (more rounded molecular shape). This is followed by a region where the lipids have a more elongated shape, before the bulk packing is resumed at larger x/D.
The polar angle θ_L shows a more complex behaviour as function of x/D. θ_L is small next to the WALP. Then it shows, in consecutive order, a maximum at $x/D \approx 0.08$ and a broad undershoot with a minimum around $x_{max}/D \approx 0.22$. At $x_{bulk}/D \approx 0.38$, θ_L assumes a steady-state value of 23º. This is close to the 22º that was found for the unperturbed DPPC bilayer(sim) in section 5.3. The positions of x_{max}/D and x_{bulk}/D for the different parameters are summarized in Table 5.IV.

Table 5. IV Values of x_{max}/D and x_{bulk}/D in the lipid/WALP-24 systems. The corresponding number of lipid diameters from the edge of the peptide $n(\sigma_L)$ is given in brackets

	DPPC x_{max}/D , $n(\sigma_L)$ [a]	**DPPC** x_{bulk}/D, $n(\sigma_L)$	**DPPE** x_{bulk}/D, $n(\sigma_L)$
d_L	0.20 (6)	0.39 (12)	0.18 (5)
P_L	0.19 (5)	0.34 (11)	0.18 (5)
θ_L	0.22 (7)	0.38 (12)	0.24 (7)
average	0.20 (6)	0.37 (12)	0.20 (6)

a $n(\sigma_L) = (x_{max} - 0.5 \times \sigma_P) / \sigma_L$ with the diameters of DPPC (σ_L(DPPC)) and WALP (σ_P) taken from Table 5.II. σ_L(DPPE) = 1.13, calculated from A_L

The values of the parameters P_L, d_L and θ_L of the first layer of lipids that border the rows of WALP (the boundary lipids) are given in the first row of Table 5.V, labelled *f(max)*. These are measured at the first maximum for θ_L and P_L ($x/D \approx 0.08$). The value next to the row of WALP-24 is used for $f = d_L$ as this curve contains no maximum in this region. For comparison, values of the pure lipid bilayers are given in the second column (labelled *f(bulk)*). Values for the situation where the acyl chains are maximally fluidized, as in the liquid-crystalline bulk phase, are given in the third row, labelled *f(fluid)*. In this case, temperature effects were compensated for by extrapolating the parameters of the fluid L_α phase ($0.5 < T^* < 0.8$) from Figs. 5.7.a, c and e to $T^* = 0.3$. The data in Table 5.V show that the disorder of the lipid tails next to the WALP-24 is less than in the L_α phase, but is much larger than in the pure lipid bilayers.

The density profile of WALP-24 in Fig. 5.12.a shows the relative location of the water beads and the P_H and P_T beads on the z-axis. No water penetrates into the hydrophobic core of the WALP-24, although some is present in the P_H region. Fig. 5.12.b shows the contributions of WALP-24 again (shaded areas), together with the contributions of the L_H and L_T beads of the first two layers of lipids (black lines) and of the lipids further away from the WALP-24

Table 5.V Measured values of the maxima of d_L, P_L and θ_L (*f(max)*) of the boundary lipids, of pure DPPC and DPPE lipid bilayers (*f(bulk)*) and estimated values of a completely disordered fluid phase, obtained by extrapolation to $T^* = 0.3$ (*f(fluid)*), see text)

	DPPC at T^*= 0.3			**DPPE at T^* = 0.3**		
	f(max)	***f(bulk)***	***f(fluid)***	***f(max)***	***f(bulk)***	***f(fluid)***
d_L	6.2	10.6	8.6	5.3	10.5	11.9
P_L	0.12	0.041	0.18	0.13	0.041	0.07
θ_L	34.8	22.1	29.5	34.1	9.03	6.0

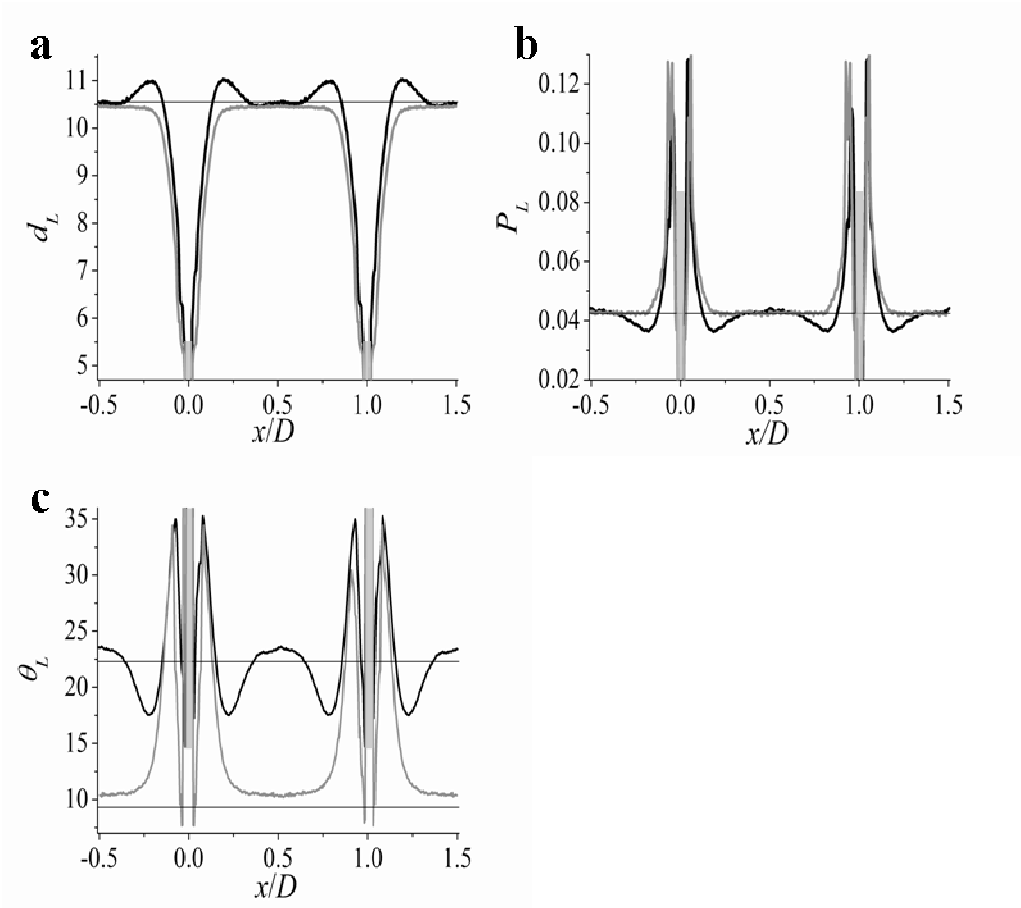

Fig. 5.11 Profile of **a.** total bilayer thickness d_L, **b.** shape factor P_L and **c**. average polar angle θ_L as function of the distance *x/D* for DPPC (black) and DPPE (grey). D = 39.1 for DPPC and D = 36.5 for DPPE. The rows of WALP-24 are indicated by the grey rectangles at *x/D* = 0 and 1 and have the correct total height d_P in **a**, whereas the height in **b** and **c** is arbitrary. The thin horizontal lines give the values for the pure lipid bilayers

($x/D > 0.3$, light grey lines). These latter molecules are regarded as having returned to the unperturbed, bulk-like conformation that they would naturally adopt in pure lipid bilayers.

The hydrophobic L_T region of the bulk lipids is broader than that of the peptide, indicating that the lipids are longer. The peaks of the WALP-bordering boundary lipids, however, have shifted so the P_H groups are positioned between the L_H and L_T groups. This is in correspondence with the proposed anchoring function of the tryptophan groups of WALP(exp), which are described here by the P_H groups [63, 119, 120]. The shift in position of the boundary lipids corresponds with the reduced value of d_L in the immediate vicinity of WALP in Fig. 5.11.a.

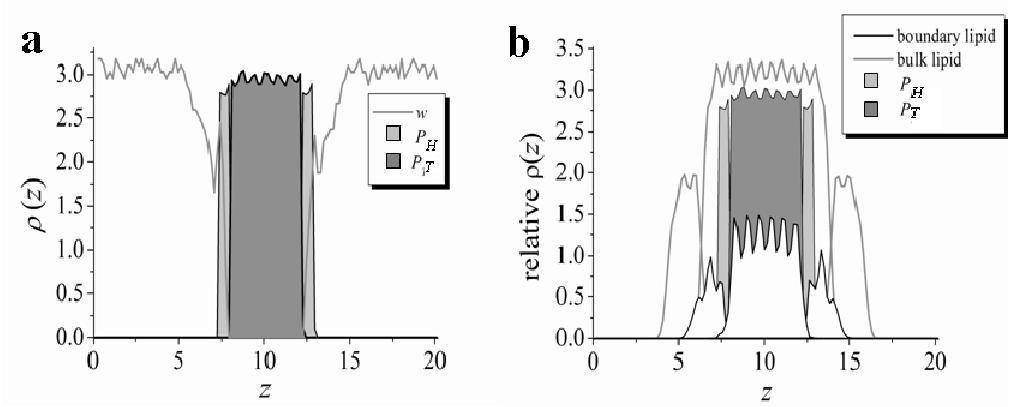

Fig. 5.12 Density profile of the various beads along the z-axis, showing the relative number of beads at a given position. The shaded peaks represent the tail and head contributions of WALP. **a.** shows the profiles of the w beads, peptide heads P_H and tails of P_T. **b.** includes the lipids, but water is omitted for clarity. The black thick lines give the contributions of the heads and tails of the boundary lipids, while the light-grey curves show those of the bulk lipids at large x. The areas in **b** do not correspond to the true number of beads, but are scaled to provide the best view

The influence of the separation distance D of the two rows of WALP on the profiles of d_L is shown in Fig. 5.13.a. P_L and θ_L show a similar dependency on D (data not shown). At $D > 20$, two distinct maxima (x_{max}) in the lipid profiles are visible; one originating from each row of WALP-24. This corresponds to the situation of independent rows. A smaller $D < 20$, however, leads to overlap of the two peaks until they merge into one broad peak. A narrowing of the profile towards smaller x-values and slight increase of the height of the maximum are observed for $D < 17$ (~ 14 σ_L). The shifts in x_{max} with D are even more evident in Fig. 5.13.b. The shallow slope of the latter part of the plot at $D \geq 17$ indicates that no major modifications in x_{max} take place, whereas the steeper slope in the former part ($D < 17$) shows a different regime where x_{max} is largely influenced by D. This corresponds to a situation where the lipids feel both rows of WALP-24 and are no longer independent.

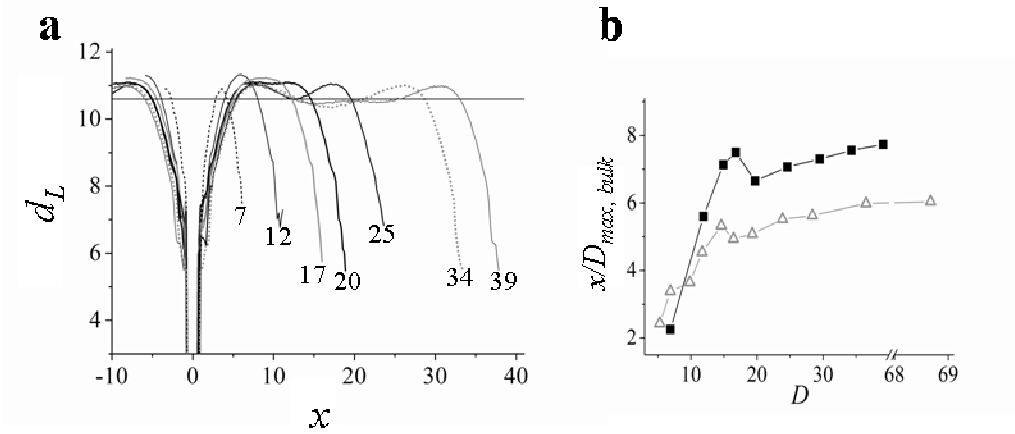

Fig. 5.13.a. Profile of the bilayer thickness d_L at different equilibrium spacings D between the rows of WALP-24 **b.** gives the positions of the maxima of the curves as function of D for DPPC (solid squares) and DPPE (open triangles), see text. x_{max} is used for DPPC and x_{bulk} for DPPE at large x

Changes in the intermolecular interactions (*i.e.* L_H - P_H, L_H - P_T, L_T - P_H, L_T - P_T, P_H - P_T, P_T - P_T and L_T - L_T) were made for a WALP-24/DPPC system with $D \approx 29$ (*i.e.* non-interacting WALP rows). They were chosen in such a way that non-physical values (*e.g.* attractive interactions between P_T or L_T and w) were avoided. The altered interactions did not affect the profiles of d_L, P_L and θ_L as they all overlapped (data not shown). The only parameter that generated a different response was the L_H - L_H interaction, which altered θ_L. In fact, a reduction in $a_{LH\text{-}LH}$ to 10 gives the model for DPPE lipids of section 5.3. This special case is described separately in the next section.

Effect of tilt: DPPE bilayer with WALP-24

DPPE has properties different from those of DPPC. A snapshot of a WALP-24/DPPE system at large D in the gel is shown in Fig. 5.14. The more perpendicular alignment of the DPPE molecules is in contrast to the tilted conformation of the DPPC molecules in Fig. 5.10.

The profiles of P_L, θ_L and d_L of DPPE in Figs. 5.11.a - c (grey lines) are different from those of DPPC (black lines). The profiles of P_L and θ_L showed the narrow region of fluidized boundary lipids at small $x/D \approx 0.06$ - 0.08 (with respectively a sharp maximum and minimum), but the broad under- and overshoots that characterized the plots of DPPC were absent. Instead, the profiles of θ_L, d_L and P_L at $x/D > 0.08$ showed a monotonous increase or decrease with x/D until they reached a steady value at $x_{bulk}/D = 0.21$ - 0.25 (~ 6 - 7 σ_L with the diameter σ_L (DPPE) = 1.13, calculated from A_L at $T^* = 0.3$ from Fig. 5.7.b, see Table 5.IV).

Variations in the separation distance D again lead to overlap of all profiles for $D \geq 15$ (~ 13 lipid diameters). For $D < 15$, a compression takes place, similar to that observed for DPPC in Fig. 5.13.a (data for DPPE not shown). For large D, x_{bulk} can be defined from the levelling-off of the curves in a manner similar to that of the previous section. For small D, however, overlap of the profiles causes a maximum to appear between the rows of WALP-24. x_{bulk} and the position of this maximum are plotted in Fig. 5.13.b as function of D. Two different slopes are present in the intervals $5 < D < 15$ and $15 \leq D < 36$. The change in slope corresponds to the situation where both WALP rows stop being independent and the lipid packing is influenced by both rows simultaneously.

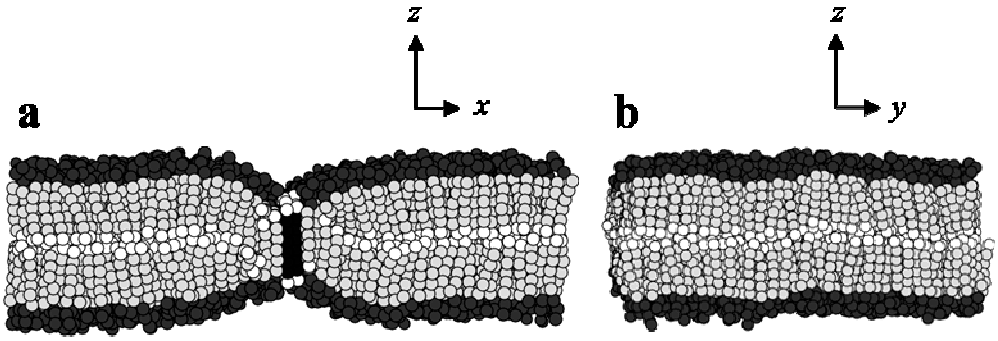

Fig. 5.14 Snapshots of a DPPE bilayer in the gel phase with one row of WALP at $T^* = 0.3$ with $D = 36.5$. Views of the *xz*- (**a**) and *yz*-plane (**b**) are given. WALP is coloured dark grey (P_T) and white (P_H). The DPPE L_H beads are dark grey, the intermediate L_T beads light grey and the terminal ones white. Water is omitted for clarity. Note that the lipid acyl chains are on average non-tilted at a large distance from the WALP

Effect of mismatch on DPPC bilayers

Mismatch conditions between DPPC and WALP-n_T were varied by modifying the hydrophobic length of the peptide d_{HPH}(WALP-n_T) from n_T = 20 to 48. The relative lengths of the tilted DPPC bilayer and the hydrophobic core of the WALP are given in Table 5.VI for the model and experimental systems. The hydrophobic length d_{HPH} of the hydrophobic Ala-Leu stretch of WALP23(exp) is 2.55 nm [181], while d_{HPH} of the PC bilayers(exp) are literature values taken from Table 2.III.

The hydrophobic length d_{HPH} of DPPC(sim) is taken from Fig. 5.7.a at $T^* = 0.3$. The mismatch is expressed in terms of the ratio of these hydrophobic lengths (d_{HPH}(DPPC)/d_{HPH}(WALP). A ratio of 1 then corresponds to complete matching of lipid and peptide and a ratio < 1 to positive mismatch conditions with d_{HPH}(DPPC) < d_{HPH}(WALP). WALP-20 to 36 give a negative mismatch and WALP-44 and 48 a positive mismatch with the DPPC bilayer. The P_T region of WALP-40 matches the L_T region of the DPPC bilayer. Snapshots of these three different situations are shown in Fig. 5.15.

The plots for all negative mismatch conditions ($20 \leq n_T \leq 36$) in Figs. 5.16.a - c show quantitatively the same behaviour as function of x, with broad over- and undershoot regions. The thickness d_L of the boundary region is shifted in a way that reflects the length of the peptide (*i.e.* a lower d_L for a shorter WALP-n_T). The positions of x_{max} shift only slightly with n_T, as shown in Fig. 5.17.
However, an additional undershoot ($x/D \sim 0.3$) develops after the first maximum in d_L with increasing n_T, which is most pronounced for $n_T = 36$. In fact, the bulk packing does not seem to be reached for this peptide length. The curves for WALP-36 seem to constitute an intermediate between those for negative mismatch and the matching WALP-40 (see below). The snapshot in Fig. 5.15.a shows that the lipids bordering the peptide have a disordered conformation in order to bridge the mismatch with the peptide.

Surprisingly, the almost matching case of DPPC/WALP-40 gives rise to substantial perturbations of the surrounding lipid bilayers, especially at larger x. The starting values of d_L, P_L and θ_L near $x/D = 0$ are close, but not completely identical, to those of the pure DPPC bilayer. The curves are not uniform, however, and still show a small maximum or minimum at x_{max}. The position of the first overshoot x_{max} is lower than for $20 \leq n_T \leq 36$ (Fig. 5.17). Additionally, an under- or overshoot is formed at relatively large $x/D \approx 0.3$ - 0.35. The snapshot in Fig. 5.15.b of the WALP-40/DPPC system shows that the acyl chains of the boundary lipids are minimally disordered. They have adopted the perpendicular orientation of the peptide.

Finally, a positive mismatch (WALP-44 and 48) reverses the profiles with respect to those of negative mismatch: minima become maxima and vice versa (Fig. 5.16.a - c). The lipids immediately adjacent to the peptide have an increased d_L and a reduced P_L and θ_L. The position of x_{max} is shifted to larger values (see Fig. 5.17), but x_{bulk} is similar to those of WALP-20 and -24. The snapshot in Fig. 5.15.c shows that the lipids-tails adapt to accommodate the longer peptide in the bilayer without unfavourable contact of polar with non-polar regions.

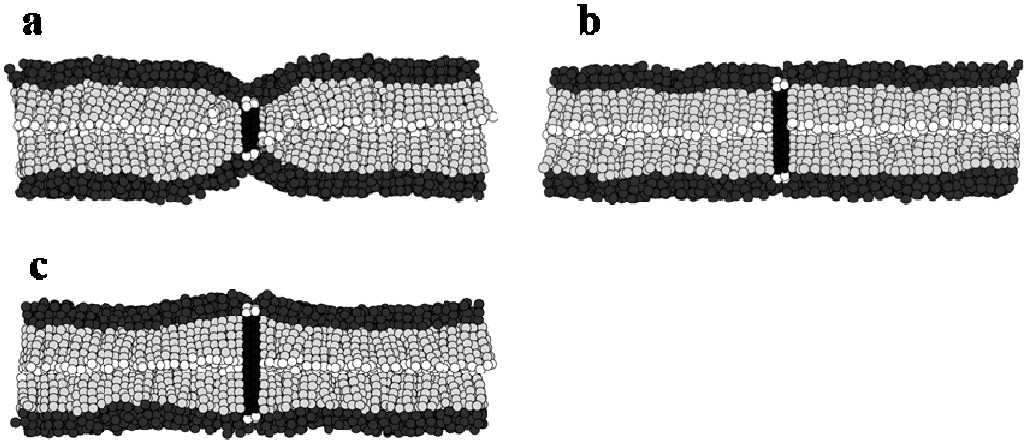

Fig. 5.15 Snapshots of mixed WALP-n_T/DPPC bilayers with **a.** n_T = 20 (large negative mismatch), **b.** n_T = 40 (matching) and **c.** n_T = 48 (positive mismatch). Only one row of WALP is shown. The different mismatch conditions lead to different responses of the lipids bordering the peptide

Table 5.VI Ratio of the hydrophobic lengths of lipid d_{HPH}(PC) and WALP d_{HPH}(WALP) in the experimental (from section 2.3.b) and model systems. Comparable systems are shown in the same row

experimental system		**model system**	
system	d_{HPH}**(DPPC)/** d_{HPH}**(WALP23)**	**system**	d_{HPH}**(DPPC)/** d_{HPH}**(WALP-**n_T**)**
di-24:0-PC/WALP23	1.94	DPPC (di-16:0-PC)/WALP-20	2.05
di-22:0-PC/WALP23	1.75	DPPC/WALP-24	1.69
di-20:0-PC/WALP23	1.59		
di-18:0-PC/WALP23	1.39	DPPC/WALP-28	1.44
di-16:0-PC/WALP23	1.35		
di-14:0-PC/WALP23	1.22	DPPC/WALP-32	1.26
		DPPC/WALP-36	1.11
		DPPC/WALP-40	1.00
		DPPC/WALP-44	0.90
		DPPC/WALP-48	0.83
L_α-DPPC/WALP23	1.47	L_α-DPPC/WALP-24	1.13 [a]

a Average hydrophobic thickness d_{HPH} of L_α-DPPC taken from Fig. 5.7.a at $T^* = 0.8$

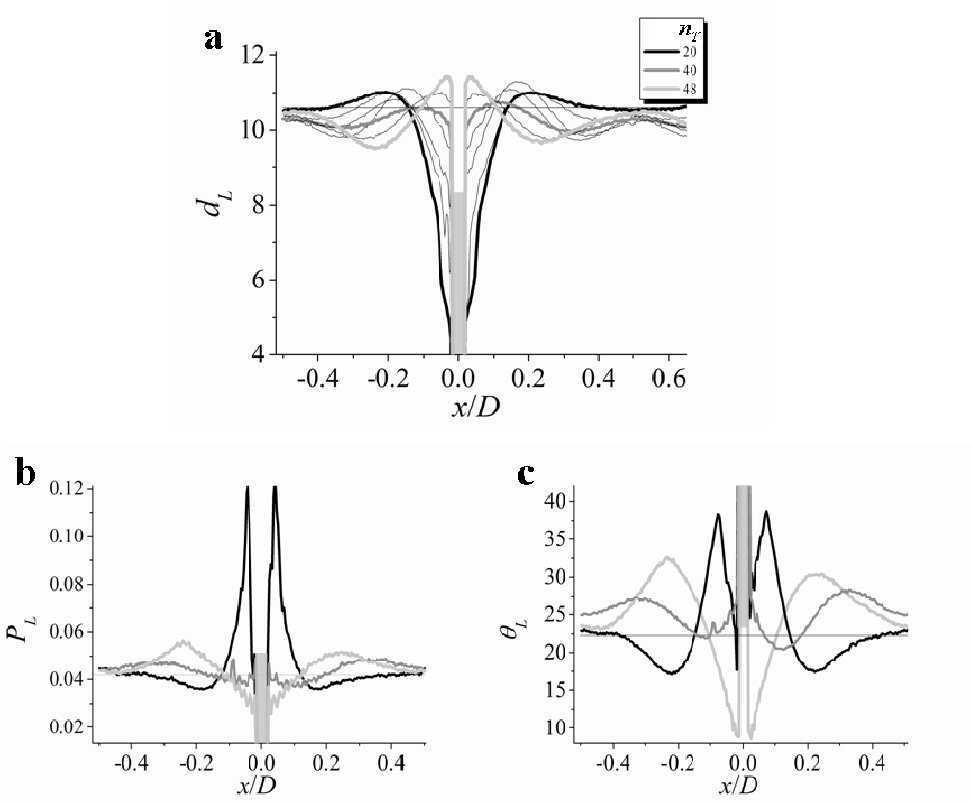

Fig. 5.16 Profiles of **a.** d_L, **b.** P_L and **c.** θ_L for DPPC lipids with WALP-n_T at $D \approx 39$. The curves for negative mismatch ($n_T = 20$), matching ($n_T = 40$) and positive mismatch ($n_T = 48$) are shown by thick lines. The additional thin black lines in **a** are contributions for $n_T = 28$, 32, 36 and 44, whose values at the WALP border increase with n_T

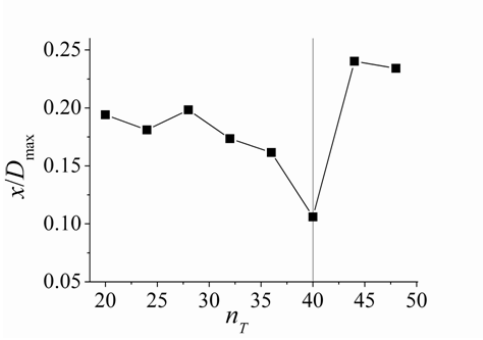

Fig. 5.17 Position of x_{max}/D, taken from the data of d_L in Fig. 5.16.a, as function of n_T where $20 \leq n_T \leq 36$ represents a negative mismatch, $n_T = 40$ zero mismatch, and $n_T = 44$ and 48 a positive mismatch. For $n_T = 40$, x_{max} is defined by the first overshoot in Fig. 5.16.a

Effect of temperature on the WALP-24/DPPC system

The effect of the lipid phase on the conformational profiles was probed in a WALP-24/DPPC system. Figs. 5.18.a - c show the profiles of d_L, P_L and θ_L in the gel L_β' state at $T^* = 0.3$ (black lines) and the liquid-crystalline L_α phase at $T^* = 0.8$ (grey lines). A snapshot of the DPPC/WALP-24 bilayer at $T^* = 0.8$ is shown in Fig. 5.19.

In the high-temperature phase, the thickness d_L at the edge of the peptide is lowered slightly, followed by a very small overshoot (at $x_{max}/D \approx 0.13$, ~ 3 σ_L with $\sigma_L = 1.43$, derived from A_L at $T^* = 0.8$ from Fig. 5.7.b) before returning to a steady-state value around 5 σ_L. The thickness d_L at large x/D remains lower than of the pure bilayer at $T^* = 0.8$, which is given by the thin horizontal, grey line. The shape factor P_L shows an almost imperceptible maximum at $\sigma_L \approx 3$, which barely exceeds the level of the fluctuations before assuming a steady-state value. The boundary lipids have a low polar angle θ_L, but this increases rapidly within 3 σ_L to a steady-state value that is close to that measured in the pure bilayers. These trends are in contrast with the larger perturbations that stretch over longer distances of the gel phase lipids at $T^* = 0.3$ (black lines).

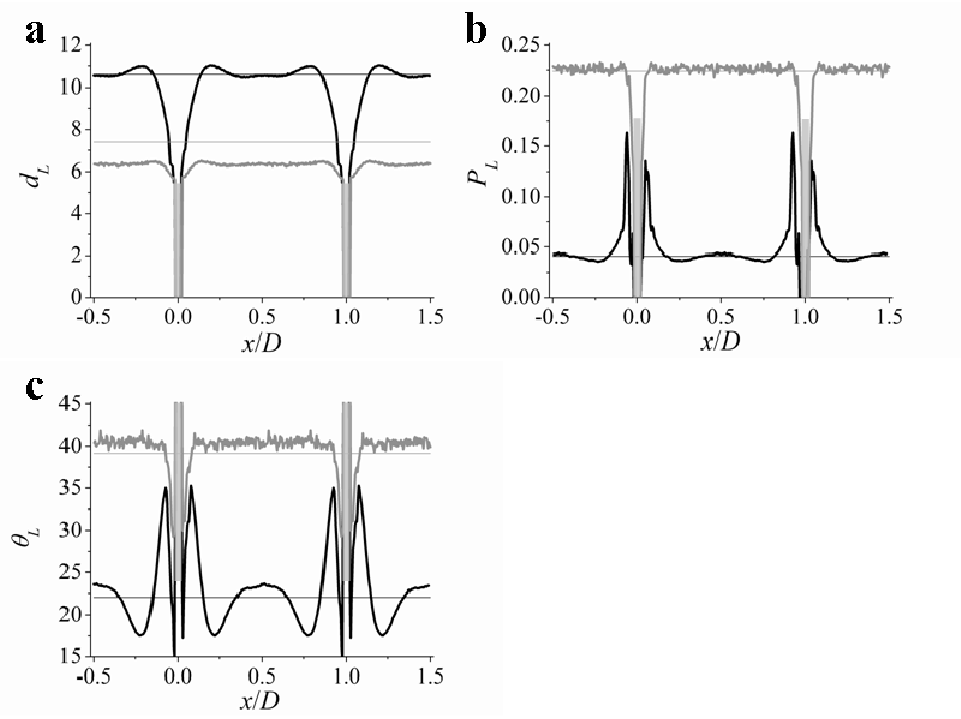

Fig. 5.18 Profiles of **a.** d_L, **b.** P_L and **c.** θ_L for DPPC bilayers with WALP-24 in the gel phase at $T^* = 0.3$ (black) and in the liquid-crystalline phase at $T^* = 0.8$ (grey). Thin horizontal lines mark the values found for the pure lipid bilayers. D(gel phase) = 39.1 and D(fluid phase) = 37.8

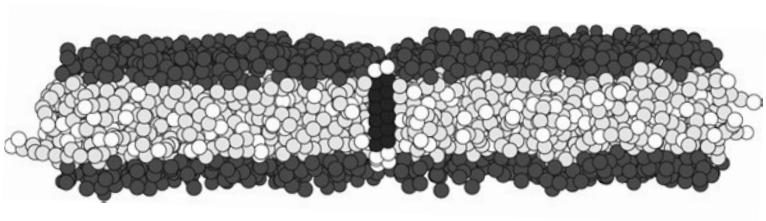

Fig. 5.19 Snapshot of the DPPC bilayer with one row of WALP-24 (*xz*-plane) in the liquid-crystalline L_α phase at $T^* = 0.8$, using the same colouring as in the previous images

5.4.b Discussion

DPPC and DPPE bilayers with WALP-24

WALP induces conformational changes in both DPPC and DPPE bilayers. Both these systems have a narrow strip of ~ 2 lipid diameters bordering WALP with a reduced length (lower d_L) and polar angle θ_L, but increased shape factor P_L (see Fig. 5.11). Over the next few lipid diameters, the polar angle increases to ~35º. This points towards a more fluidized shape of the boundary DPPC and DPPE lipids. The first lipid layers have adapted to the perpendicular orientation of the peptide. The larger polar angle of 35º of the next lipid layers does not correspond to a preferred tilt angle but is probably due to orientational fluctuations of the partially fluidized lipids.

These observations agree with experimental evidence that the lipids in the immediate vicinity of the peptide have a markedly altered conformation as compared to the pure lipid phase ([110, 117], Chapter 4). The lipids adjust their length to the adjacent, shorter WALP by disordering the acyl chains. The driving force is either hydrophobic shielding of the hydrophobic L_T units to the aqueous surroundings or hydrophilic P_H groups [62, 91], or the preferred position of the anchoring tryptophan groups [63, 120] in the polar-apolar interface of the bilayer. The density profile of Fig. 5.12.b confirms that disordering of the acyl chains allows the tryptophan groups (modelled by P_H) of the peptide to fulfil their anchoring function in this interfacial region.

At larger x, the profiles of DPPE and DPPC start to deviate considerably from each other. The parameters for DPPE return gradually to a steady-state value over a relative small distance x_{bulk} (~ 6 σ_L). The magnitude of the steady-state values are very close to those of the pure DPPE bilayer (indicated by the thin horizontal lines in Fig. 5.11). It can be safely assumed that x_{bulk} marks the x-value beyond which the perturbing influence of the peptide does not extend.
In contrast, the curves for DPPE in Figs. 5.11.a - c lack the overshoot region that characterizes DPPC.

For DPPC, however, all profiles of d_L, P_L and θ_L show a pronounced over- or undershoot before reaching the bulk packing at a larger perturbation length x_{bulk} (~ 12 σ_L). The lipids in the

maximum or minimum at x_{max} are elongated (low P_L) and have a reduced polar angle θ_L. This increases the local thickness of the bilayer d_L. The presence of a number of DPPC lipids that have an increased height and reduced polar angle is in agreement with the higher lines in the AFM images of the striated domains (see Figs. 2.6.d and 2.10) and with X-ray diffraction data of Sparr *et al*. [110]. Moreover, the X-ray diffraction pattern showed that the lipids have a hexagonal packing, which suggests stiff, elongated chains in a gel-like conformation.

The values of x_{max} and x_{bulk} are comparable for θ_L, P_L and d_L (see Table 5.IV), indicating that the perturbations of the different parameters are (almost) coupled. The positions of x_{max} and x_{bulk} for DPPC correspond to positions of respectively $n(\sigma_L)$ ~ 5 - 7 and 11 - 12 lipid diameters from the edge of the WALP row when one assumes that the lipid diameter is similar to that of an unperturbed DPPC lipid in Table 5.II. This can lead to some overestimation as the first lipids next to WALP have a larger diameter because of their fluidized tails.

Note that overshoots in thickness profiles were also found in other DPD [183] and MD [337] simulation studies of a coarse-grained, fluid DMPC bilayer in the presence of a shorter, transmembrane, cylindrical inclusion. x_{max} was smaller in these fluid systems than in our gel-state lipid bilayers (typically 3 σ_L versus 5 - 7 σ_L, respectively). The stiffer gel-state bilayer probably needs a longer length scale to adjust than the fluid bilayer. The presence of an overshoot was attributed to constraints imposed on the bilayer by the tilt and the necessity of a constant density [183].

The AFM images of the striated domains suggest that all lipids between the lines of WALP in the striated domains are perturbed, as they all have an increased height. They do not return to the bulk packing. This can be explained by overlap of the perturbed regions emanating from two opposite rows of WALP(sim). Overlap of the perturbation profiles will be energetically favourable as this reduces the overall number of affected lipids [106, 338, 339]. Moreover, a theoretical study of Marčelja [106] confirms that overlap of lipid order profiles can give rise to an attraction between two proteins. Other studies also find an attractive well upon decreasing the distance between the proteins, but this is bordered by an energetic barrier [324, 340, 341] owing to the loss of conformational energy of the lipids. No maximum could be found in this study in plots of the energy as function of the separation distance between the rows of WALP D (data not shown). This could be due to the non-exact interaction potential chosen here.

However, the effect of the overlap of the perturbed lipid zones upon decreasing the separation distance D between the two peptide rows can be determined from Figs. 5.13.a and b. The two profiles do not influence each other and both have a well-defined x_{bulk} at $D > 20$ (~16 σ_L). The maxima of the profiles start to overlap at $D \leq 20$, until only one maximum remains at $D \leq 17$. This overlap is neither accompanied by shifts in the position of x_{max} nor the height of the maximum, indicating that the overall lipid packing is not substantially altered.
Further reduction of $D \leq 12$ (~ 9 σ_L), however, leads to an overall change in the lipid packing as the profiles become substantially compressed and the maximum slightly higher (see Fig.

5.13). This indicates a larger conformational perturbation of all lipids between the two rows of WALPs. In this case, the lipids feel both peptide rows simultaneously. The small spacing D could reduce their conformational freedom and affect the overall packing [340]. This sets a scale for the experimentally observed r_{rep}, as overlap below $D \leq 12$ (~ 9 σ_L) seems unfavourable because of this. The maximal r_{rep} could then correspond to the spacing where the perturbed regions just start touching, *i.e.* at $D \leq 20$ (~16 σ_L). In principle, a further overlap of the maxima at 2 x x_{max} (≈ 10 - 14 σ_L, $D \approx 13$ - 17) is expected to give a larger energetical gain.

The absence of a similarly ordered, striated lipid/WALP phase in DPPE/WALP(exp) bilayers (Chapter 4) can then be explained by considering the different shapes of the perturbation profiles for DPPE and DPPC. DPPE lacks the broad over- and undershoot regions and no reduction in the number of perturbed lipids will be obtained by approaching and ordering of the lines of WALP, which will lead to a concomitant reduction of the entropy. Overlap of the boundary lipid regions at $D < 15$ is probably not favourable due to the restrictions of the conformations of the lipids, just like for DPPC (see above and Fig. 5.13).

The origin of the overshoots in the profiles of DPPC can be sought in the tendency to tilt. The tilted DPPC tails show an adjusted chain order and polar angle to conform to the perpendicularly oriented WALP. The DPPE tails only adjust their chain order as their naturally adopted polar angle of ~ 0° is commensurate with that of WALP. The additional perturbation of the lipid tilt director for DPPC leads to a longer perturbation length x_{bulk} than for DPPE. Theoretical studies [340, 342, 343], using continuum descriptions of the bilayer to which an independent term for lipid tilt was added, have deduced a similar role for lipid tilt. A non-zero tilt angle of the protein led to a much larger perturbation length for non-tilted, fluid lipids than a non-tilted protein.

The repeat distance r_{rep} of 10 - 14 lipids predicted in this way is obviously much larger than the experimentally observed 4 - 5 lipids. Nevertheless, the generic principles underlying the formation of striated phase are demonstrated here. The insensitivity of x_{max} to the interaction strength a_{ij} between the various particles suggests that specific interactions do not play a role and general packing effects dominate. A similar weak influence of direct lipid-peptide and peptide-peptide interactions on the striated phase has also been shown in an AFM study, where other uncharged groups replaced the anchoring tryptophan groups of WALP [33]. The position of x_{max} is sensitive to the exact model of the lipids and WALP and variations in the rigidity and surface roughness of the molecules could reduce x_{max}.

Effect of mismatch on DPPC bilayers

Three separate cases were investigated for WALP-n_T/DPPC systems: negative matching, (almost) matching and positive matching. These conditions are fulfilled respectively by the situation where $20 \leq n_T \leq 36$, $n_T = 40$, and $n_T = 44$ or 48. For all n_T's, the bilayer thickness d_L next to the peptide ($x/D \approx 0.02$, Fig. 5.16.a) follows the length of the WALP-n_T and increases with d(WALP). This requires less disordering (decreasing P_L and θ_L) when n_T becomes larger and the mismatch smaller. A positive mismatch ($n_T = 44$, 48) reverses the profiles and the starting values of d_L, P_L and θ_L indicate more ordered and less tilted acyl-chain conformations of the boundary lipids.

These general trends indicate that the responses of the lipids bilayer are aimed at minimizing the difference in length between the bilayer and the peptide. Stretching or disordering of the lipid chains has been observed for a number of systems in experimental [14, 33, 74, 76, 82, 87, 98] and simulation [76, 104, 183, 243, 341, 344, 345] studies. ^{2}H-NMR and ESR studies [62] showed small but systematic changes in the bilayer thickness and area per lipid near WALP upon altering the mismatch. Additionally, the disordering of the lipid chains in the presence of a shorter WALP lowers the main transition temperature T_M (exp) [80].
The simulations do not take into consideration any compensatory modifications in the backbone or orientation of the peptide. This might not be entirely correct, as WALP has been shown to possess a non-negligible polar-tilt angle under positive mismatch conditions [346].

The model systems of DPPC/WALP-n_T with $20 \leq n_T \leq 32$ correspond to the mismatch conditions that were probed experimentally in Chapter 2 (see Table 5.VI). The relatively small shifts in the position of x_{max} for these peptides (Fig. 5.17) could correlate with the observed small effects of the repeat distance r_{rep} of the striated domains(exp) with hydrophobic mismatch in Fig. 2.3.c. The changes in mismatch in this region can be accommodated within the first layers of lipids and do not extend beyond this distance.

A different situation exists for the (almost) matching conditions of WALP-36 and -40 (Fig. 5.16), where the boundary lipid bordering the matching WALP-40 show values of d_L, P_L and θ_L that are very close to those of the pure, WALP-free bilayer (horizontal lines in Figs. 5.16.a - c). The small deviations at small x could be caused by factors that are not related to the extent of mismatch, such as the packing of the lipids at the slightly irregular, non-smooth surface of the peptide [74, 347]. The following, ordered region could be a result of the limitation of the number of attainable conformations of the (fluidized) lipids imposed by the inclusion [340, 344]. Surprisingly, the total perturbation stretches over a much larger distance x under matching conditions than for both negative and positive mismatch. The bulk-packing seems not to be completely reached in this relatively small system. The origin of this is unclear.

Effect of temperature on the WALP-24/DPPC system

The number of lipids with an adapted conformation bordering the row of WALP is lowered drastically from approximately 12 σ_L in the gel phase L_β' at $T^* = 0.3$ to 2 - 5 in the fluid L_α phase at $T^* = 0.8$ (Fig. 5. 18). This latter corresponds to the 3 σ_L of the DPD study of [230] on a fluid DMPC bilayer.
The magnitude of the observed deformations (y-values) is also smaller, as can be expected in a fluid-like disordered phase where the packing is much less rigid than in the solid gel phase. These lipids adapt more easily to conform to inclusions such as WALP. This is in agreement with the experimentally observed disaggregation of the linear aggregates of WALP(exp) in the domains upon entering the more loosely organized L_α phase [75, 110]. The larger solubility of WALP eliminates the driving force for expelling them from the rigid gel phase into striated domains. Such dynamic effects can obviously not be observed here owing to the static nature of the rows of WALP. The smaller perturbing effect of WALP on the L_α bilayers is clear, however.

The boundary lipids have a slightly reduced d_L to bridge the mismatch with the thicker L_α DPPC phase (see Table 5.VI). The lower P_L, however, shows a more elongated shape, which is presumably due to a reduction of the number of attainable conformations near the stiff peptide. At larger x/D ($\approx 5\ \sigma_L$), a small overshoot in d_L is observed before the steady-state $d_L = 6.3$ is reached. This is significantly lower than the $d_L = 7.4$ found in the absence of WALP (Fig. 5.7.a). Possibly, the shorter length of the WALP induced an overall reduction in the length of the easily deformable lipids. Alternatively, the relative small size of the lipid bilayer between the rows of WALP could impose some overall constraints on the lipid packing.

5.5 Conclusion

It is demonstrated in this chapter how computer simulation studies can provide complementary information of the packing in the mixed lipid-WALP striated phase that has been studied experimentally with AFM, fluorescence spectroscopy, X-ray diffraction and ^{2}H-NMR [110]. Coarse-grained model lipids (tilted DPPC and non-tilted DPPE) and peptides were used, which retain enough of the structure of the lipids and peptides to allow evaluation of the packing of the lipids and WALP on a molecular scale.

Four phases with increasingly disordered packings were found for DPPC bilayers with increasing temperature. The DPPE-mimicking lipid bilayer has three phases. The presence of these phases and their characteristics are in correspondence with experimental phase diagrams and similar simulations from [179].
The insertion of rows of rigid WALP molecules in these bilayers affects the packing of the lipids. DPPC lipids next to a row of the shorter WALP-24 peptides show large conformational perturbations that emanate over a relatively large distance of ~12 lipid diameters. First, a small

region of disordered boundary lipids is present that bridge the mismatch with the peptide. This is followed by a broader region with a lowered polar angle and elongated lipid shape. A similarly reduced polar-angle was also proposed for the lipids in the striated domains to explain their increased height compared to a pure DPPC phase (see Fig. 2.10, [110]). Overlap of these perturbation profiles presumably gives rise to a favoured spacing between the rows of WALP and could lead to the experimentally observed spacing r_{rep} of 8 nm.

DPPE lipids have a much smaller perturbation length of ~ 6 lipids, which serves to bridge the mismatch with the shorter peptide. It is probably not favourable for these boundary regions to overlap as decreasing the spacing D between the rows of WALP to such a large extent affects the whole packing unfavourably. In contrast, overlap of the maxima x_{max} of the broad overshoot regions of DPPC does not alter the shape of the profile and, hence, the packing. These differences give an acceptable explanation for the absence of a well-defined repeat distance for the bilayers of the intrinsically perpendicularly oriented lipids in the AFM studies of Chapter 4 (*i.e.* DPPE/DPPC and DPPC/HXD bilayers). This clearly shows the large role of the lipid acyl-chain tilt in forming striated domains.

A mismatch in length between WALP-n_T and DPPC bilayer leads to adapted conformations of the lipids in order to bridge the gap. This leads to a local disordering or ordering for respectively conditions of negative (d_{HPH}(WALP) < d_{HPH}(DPPC)) or positive mismatch (d_{HPH}(WALP) > d_{HPH}(DPPC)) that are aimed at minimizing this gap.
The extent of negative mismatch does not substantially shift the position of the maximum x_{max} of the overshoot regions. The boundary lipids seem to absorb the differences in mismatch without substantially altering the length scales involved. This is in agreement with the experimentally observed weak dependence of the repeat distance r_{rep}(exp) to mismatch in Chapter 2. The simulations show that the presence of the peptide itself alters the lipid packing even under matching conditions.

Finally, DPPC lipids in the fluid phase adapt more readily to the presence of a peptide-barrier than those in the gel phase. The perturbations are smaller and they emanate over smaller distances. The adaptability of the lipids is the reason for the increased solubility and concomitant disaggregation of WALP indicated by fluorescence measurements [75].

Chapter 6

Summary and concluding discussion

6.1 Summary

In this thesis, the self-assembly of striated domains in bilayers of phospholipids and the model peptide WALP23 has been investigated. These highly ordered striated domains consist of a mixed phase with a lipid/WALP ratio of 8/1 - 10/1 [33, 110, 117, 122]. Previous studies [33, 110, 119, 122, 123] showed conclusively that these domains consist of single rows of the peptide that alternate with lines of 4 - 5 lipids that have an adjusted conformation [110, 117]. A representation of the proposed packing in the striated domains is given in Fig. 1.6.b.
In this work, the formation and properties of this striated phase in hydrated lipid bilayers with WALP were studied with Atomic Force Microscopy (AFM) and through Dissipative Particle Dynamics (DPD) computer simulations on a coarse-grained model. Emphasis was placed on investigating the role of the packing of the lipids. The specifics of the lipid environment have been shown to influence peptide lateral packing and functioning in many biological systems [11, 13, 53, 57, 87 - 93, 113].

In Chapter 2, some general properties of the striated phase were shown, such as the hexagonal packing and well-defined periodicity of ~ 8 nm. The morphology of the striated domains was shown to be independent of the mica substrate used to immobilize the bilayer for imaging, as an identical striated phase is formed in a more free-standing, doubly stacked bilayer. Variations in pH and ionic strength also left the structure of the striated phase unmodified. Increasing the length of the acyl chains of the saturated PC lipids (di-*n*:0-PC with n = 14 - 20) had a marginal effect on the morphology of the striated domains, but a too large mismatch (n = 22, 24) inhibited incorporation of WALP23 in the bilayer [65, 190, 191].
The observed increase in the separation distance r_{rep} between the stripes and the reduced ordering of palmitoylated (C16:0)-WALP (Pa-WALP23) demonstrated how steric effects can also affect the packing in the striated phase. This was ascribed to the inability of the additional C16 chain to fit in the surrounding DPPC lipid matrix.

In Chapter 3, it was shown that WALP23 specifically lowered the melting or main transition temperature T_M of the DPPC lipids within the striated domains, compared to the unaffected DPPC areas outside the domains. The shorter WALP stabilizes the thinner fluid phase. Moreover, the well-defined stratified pattern seemed to disperse around the melting transition. This is in agreement with fluorescence data [75, 110] that indicate disaggregation of WALP and an increased lateral solubility in the much more loosely organized fluid phase.

In Chapter 4, other aspects of the packing of the lipids were studied. First, DPPC lipids were replaced with gel-state DPPE lipids. Highly ordered striated domains with the same properties as those formed in pure DPPC bilayers were found when the DPPE mole fraction was below 0.25. A number of changes occurred at higher DPPE content. The first was a reduction of the amount of WALP incorporated in the bilayer. This was attributed to the tight hydrogen-bonded network of the headgroups of DPPE [15, 285, 286]. Additionally, a disordering of the previously straight and parallel stripes took place and the repeat distance increased. It was

argued that this is due to a gradual elimination of the acyl-chain tilt when introducing increasing fractions of DPPE in the bilayer [17, 46, 203, 283]. This hypothesis was confirmed by the observation of comparable, loosely organized patterns of dark lines in WALP/DPPC bilayers to which *n*-hexadecane was added. Insertion of this alkane also removes the tilt of the DPPC lipids [46, 47].
The second modification investigated was the presence of a *cis*-unsaturated bond in the lipid's acyl chains. Bilayers of di-*n*:1-PC(with $20 < n < 24$) and (16:0,18:1)-PC in the solid state were used. The absence of striated domains is presumably a consequence of the less efficient packing of the kinked, unsaturated chains, which increases the solubility of the peptide in the bilayer.

Finally, computer simulations in Chapter 5 showed how various local parameters that characterize the bilayer (*i.e.* bilayer thickness, tilt angle and a shape factor describing the fluidization of the lipid molecule) were affected by insertion of rows of rigid WALP molecules. The lipids have adapted conformations in the vicinity of the peptide (see Fig. 1.6.b). An initial region of 1 - 2 lipid layers with disordered chains is followed by a region where the profiles show a pronounced under- or overshoot. Here, the lipids have more ordered chains and a reduced tilt angle. At large distances from WALP, the conformational profiles of the DPPC lipids returned to their unperturbed values.
It was proposed that overlap of the minima or maxima of the overshoot regions is related to the observed separation r_{rep} between the stripes in DPPC bilayers (see the discussion in section 5.4.b). This leads to a predicted r_{rep} of 10 - 14 lipids in the simulations.

Changes in the length of the peptide did not significantly alter the position of the maxima (and spacing r_{rep}) under conditions of negative mismatch when the hydrophobic length d_{HPH} (WALP) < d_{HPH}(bilayer). Positive mismatch led to a reversal of the profiles as the lipids bordering the WALP stretch to accommodate their length to the WALP. The presence of a matching peptide induced substantial deviations from the favoured bulk packing of the lipids at large distances from the peptide.
The absence of striated domains in liquid-crystalline DPPC bilayers is corroborated in the simulations by the smaller perturbations of the lipid packing, which emanate over much smaller distances from the WALP than for those in the gel phase. This could lead to the observed increase in solubility of WALP and its disaggregation (Chapter 3 and [75, 110]). Finally, the conformational profiles of DPPE bilayers did not show a region with an under- or overshoot, but only a thin layer of ~ 6 lipids with fluidized chains.

In the following sections, the relation between these and previous findings and the proposed model of the striated domains is discussed by considering the molecular packing of the constituting lipids and WALP. This information allows better understanding of the forces governing the formation of the striated phase. Alternative descriptions of membrane-related effects have been used in literature, based on the lateral pressure profile [16, 139] and/or spontaneous monolayer curvature R_o [57, 92, 112]. These different descriptions are related as changes in the type of lipid alter both the lateral pressure profile [13, 115] and R_o [11, 12, 113]

through changes in their effective molecular shape [111]. However, the use of these concepts does not add much to the understanding of the striated domains and is omitted here as limited data is available for gel-phase bilayers.

6.2 The conformation of WALP and lipids in the striated domains

WALP adopts a perpendicular orientation with respect to the bilayer surface in the striated domains [33] (see Fig. 1.6.b). This maximizes the effective length of the peptide, which minimizes the mismatch in length between the shorter peptide and the lipid bilayer [117, 122]. The peptide behaves as a rigid unit in the bilayer and no appreciable modifications of the α-helical backbone were detected under conditions of negative mismatch [62, 190].

Contact with the perpendicularly oriented peptide forces the more adaptable saturated PC lipids in the striated domains to reduce their polar angle accordingly [110, 117, 122]. The naturally adopted tilted configuration of the acyl chains of these lipids in the bulk gel phase (polar angle θ_{DPPC} = 30 - 32º [19, 29, 30]) is reduced to approximately 6º [110]. The lipids could theoretically keep these large polar angles and align with their azimuth angle parallel to the rows of WALP if this would involve a smooth, non-interacting, cylindrical peptide. This is clearly not the case. Surface roughness, steric hindrance of the anchoring tryptophan groups of WALP or of the fluidized lipid chains (see below), or favourable attractions between the tryptophan group and the polar – non-polar interface of the bilayer could prevent this [63, 67, 119].

The first one or two layers of lipids bordering the peptides have partially fluidized acyl chains, as was indicated by [110] and by the computer simulations of Chapter 5. This serves to bridge the mismatch in length between WALP and the DPPC bilayer, which is most likely driven by the large affinity of the Trp groups of WALP for the lipid interfacial region [63, 119] or the penalty of exposing hydrophobic units to the aqueous environment or polar headgroup region of the bilayer [62]. Additionally, more disordered chains might facilitate close packing of the lipids around the relatively rough surface of the Ala-Leu helix [74, 101].

The increase in the projected area (on the *xy*-plane) of the hydrocarbon chains upon partial fluidization could lead to a reduction of the tendency to tilt. Geometrical arguments indicate that tilting of gel-state DPPC lipids is necessary to avoid voids in the packing caused by non-concomitant areas of the headgroup and non-polar region in gel-phase DPPC (see Fig. 4.1 and accompanying text) [31]. Fluidization of the boundary lipids enlarges the hydrocarbon area of DPPC and removes the need for tilting. The lipids beyond this fluidized, boundary layer have a gel-phase packing [110] but their tilt angle and conformation probably remain affected by the first layer.

6.3 Formation of the striped pattern

6.3.a Interactions promoting peptide aggregation

Association of WALP in the striated phase could be favoured by both the lipid packing and the dipole moment of the WALP-helix. The inclusion of a differently shaped and oriented molecule, such as WALP, would interfere with the ordered and tightly packed lipid matrix, resulting in a loss of Van der Waals interactions between the lipid acyl chains and of the interactions in the polar PC region. Aggregation of WALP and occlusion to naturally occurring packing defects (at low concentrations) or regionalized areas (striated domains at higher concentrations) minimizes this perturbation.
The role of the lipid packing in the formation of the striated domains is conveyed through the angles of 120º of the lines, which reflect the hexagonal lipid lateral organization. Large changes occur in the morphology of the striated domains when varying the type of lipid or phase of the bilayer. The flexible and loosely packed acyl chains of the liquid-crystalline phase allow a higher solubility of WALP in the bilayer (Chapters 3 and 5). WALP disaggregates [74, 110, 348] and the striated phase disappears. The use of unsaturated PC lipids (Chapter 4) proves that a high-temperature phase with high lateral and rotational diffusion coefficients of the lipids is not essential for disaggregation of WALP, but that a reduction in the ordering of the packing by the unsaturated bonds is sufficient. The addition of sufficient DPPE to DPPC bilayers also leads to the complete dispersal of the ordered, striped organization.
The extent of hydrophobic mismatch, on the other hand, does not lead to substantial changes in the extent of aggregation of WALP (Chapter 2 and [122]), although the presence of mismatch has been shown to promote aggregation of proteins and peptides in other systems [62, 91, 105]

A different source for aggregation of WALP could be provided by its dipole moment, which can be described as one half charge of opposite sign on each of the WALP termini [75, 225 - 227]. Attraction between helices with an opposite dipole orientation [228] leads to the observed organization of WALP molecules in an anti-parallel fashion (*i.e.* N terminus next to C terminus) [75, 110, 349]. It is not clear whether this relatively weak effect [75, 227, 228] is enough to drive the assembly into linear aggregates by itself, but it has been shown to be strong enough to favour dimerization of unflanked Ala-Leu model peptides in fluid POPC bilayers [349].

6.3.b Interactions promoting mixing of lipid and peptide

One would expect non-commensurate inclusions, such as WALP, to have a strong inclination to aggregate into completely segregated patches in order to minimize the contact area with the lipids. However, attractive lipid-peptide or repulsive peptide-peptide interactions create the opposite tendency and induce mixing.
Attractive WALP-lipid interactions could be induced by the flanking tryptophan (Trp or W) residues. These aromatic groups are encountered frequently in membrane-spanning proteins

[56, 118, 350], where they locate with the indole ring near the carbonyl moiety of the lipids [63, 120, 351 - 354] and the plane of the aromatic ring aligned roughly parallel to the bilayer normal [355]. Trp residues anchor proteins to this specific location in the bilayer [118, 120, 351]. Shifts towards a higher or lower position in the bilayer are unfavourable [63, 356]. Pulling experiments indicate that relatively large forces of 90 pN [119] are required to dislodge the Trp from its interfacial position, compared to 20 - 40 pN [357] for pulling a PC lipid out of a (fluid) bilayer. The origin of the strong preference for the bilayer-interface has been ascribed to the large bulky structure of the aromatic ring [104, 121, 358], its polarity [121, 351, 353, 358], its aromaticity (*i.e.* interactions of the delocalized π-electrons with cations [61, 353, 359]) and/or the H-bonding capability of the NH group with acceptors on the lipid headgroup [121, 351, 355, 359]. Given the strong interaction, it seems very likely that the Trp groups of WALP in the striated domains provide a strong attraction between the peptide and lipids in the striated domains, thus favouring (partial) mixing of the lipid and peptide and preventing extensive aggregation into a separate peptide phase [74, 82]. Of course, this could just be caused by steric crowding of the large Trp groups [75, 104].
Alternatively, the sidelong addition of another WALP molecule to the anti-parallel line-aggregates could lead to the unfavourable proximity of two similarly oriented dipoles to each other. The formation of linear arrays could then serve to maximize the space between like-oriented dipoles while maintaining contact between unlike-oriented ones.

It is not clear which of the above effects (dipole-dipole or Trp-lipid interactions) is the dominant factor, although the effect of the dipole is believed to be weak [227].
The use of other aromatic and uncharged flanking residues (*i.e.* phenylalanine (Phe), tyrosine (Tyr) and histidine (His) at high pH [33]) gave similar striated patterns. This could indicate a minor role for interactions of the flanking residues, but could also indicate that they all operate through a common mode of action. Trp, Tyr and Phe interact favourably with the interfacial region of the bilayer [120] and can also act as anchoring residues in transmembrane proteins [120, 354]. The ability of different XALPs (where X = Trp, Tyr, Phe or uncharged His) to induce non-lamellar phases in fluid bilayers under conditions of negative mismatch [360] indicates a similarity in the anchoring abilities of these groups. The strength of the anchoring varies somewhat, possibly because of differences in the strength of their dipole moment [360]. Presumably, the (small) favourable interaction with the interface of all these residues is sufficient to induce mixing of the lipid and XALP and prevent large-scale aggregation of XALPs in the striated domains.

WALP does not mix completely in the lipid bilayer, as would be the case if the mixing interactions exceeded the interactions that drive the peptides together [124]. The conflicting tendencies counterbalance each other and an intermediate, striped structure is formed where one WALP is surrounded by both lipid and other WALP molecules.

6.4 The repeat distance r_{rep}

The value of the repeat distance r_{rep} of 7.5 - 8 nm (~ 4 - 5 lipid diameters) in the striated phase is more likely to be correlated to the lipid environment than to the dipole-dipole repulsion between like-oriented dipoles. Theoretical work [228] shows that an inter-helix separation distance of only ~ 2 nm (= 2 - 3 DPPC lipids with a diameter of 0.8 nm [3, 235, 251]) suffices to cancel all mutual attractive and repulsive dipole-interactions. Similarly, it seems unlikely that steric or other interactions of the Trp groups extend over such relatively large distances.

The obtained AFM results for bilayers of fluid DPPC, gel DPPE, gel DPPC/HXD and unsaturated PC lipids with WALP indicate that lipid packing is the major factor in the formation and appearance of the striated phase. The most obvious length scale in determining r_{rep} is then the distance over which the WALP-induced deformations in the lipid conformations emanate (coherence length ξ). A number of theories have attempted to estimate the magnitude of ξ. The perturbed bilayer packing is described in terms of altered lipid conformations (microscopic models) [36, 344] or altered elastic properties of the bilayer, such as bending and compressibility (continuum models) [361 - 363]. The applicability of these theories to the striated phase seems limited, especially as they all assume fluid membranes and smooth proteins that usually contribute through their hydrophobic length only.

Theoretical studies do show, however, that overlap of perturbation profiles can potentially give rise to a membrane-mediated attraction between peptides [102, 106, 338, 339, 365]. Overlap reduces the overall number of perturbed lipids. Such a mechanism could stabilize a striated phase, especially as the calculated perturbation profiles of gel-state bilayers of DPPC in the DPD simulations (Figs. 5.11.a - c) show a distinct non-monotonous behaviour with a broad maximum or minimum (overshoot region). It was argued in Chapter 5 that overlap of these broad regions could be the origin of the well-defined repeat distance r_{rep} between the stripes. This leads to a r_{rep} (simulation) of 10 - 14 lipids that is larger than the experimental number of 4 - 5. This discrepancy could be an effect of the used coarse-grained model in the simulations. Refinements in the model might lead to a more realistic r_{rep}.

Detailed inspection of the AFM images of mixed DPPC/WALP bilayers supports the idea of overlapping profiles as the broad, lighter lipid rows are observed almost exclusively between two darker, WALP-containing lines. The lipids do not attain the bulk packing anywhere between the stripes. Moreover, the outer rims of the domains bordering the pure bilayer often contain much narrower regions of perturbed, lighter-coloured lipids.

The positions of the maxima of the overshoot regions, and hence r_{rep}, in the simulations are almost fixed over a range of negative mismatch conditions between the lipid bilayer and WALP. Apparently, limited changes in mismatch can be compensated for by adaptations within the first layers of lipids. This matches the experimental observations in Chapter 2. Only

when the energetic cost of lipid adaptation becomes too high, is WALP excluded from the bilayer. This was observed for the long-chained di-22:0 and 24:0-PC in Chapter 2.

The importance of the tilt angle of the lipid's acyl chains follows from the experimental data for tilted, saturated PC lipids on one hand and the non-tilted DPPE and HXD/DPPC on the other hand. The absence of tilt removes the characterizing spacing r_{rep} between the stripes. Relaxation of the tilt angle of the DPPC lipids from the WALP-imposed zero value to the unperturbed value extends over longer distances (> 10 lipid diameters in the simulations) than the relaxations of the chain disorder only (as for DPPE, 5 - 7 lipid diameters). Increases in the coherence length ξ over which protein-induced perturbations emanate were also found in theoretical work when an independent term for lipid tilting was used [340, 342, 343]. Apparently, overlap of the narrow layers of chain-disordered DPPE lipids does not lead to energetic gain or might be disfavoured by other effects, such as repulsive dipole-dipole or attractive Trp-lipid interactions. Restrictions of the possible conformations of the lipids could also play a role. WALP still forms linear aggregates, however, and meandering lines of WALP without a well-defined spacing are observed in the non-tilted DPPE and DPPC/HXD systems.

This leads to the central conclusion that overlap of the extended perturbation profiles of tilted lipids lead to a striated pattern with many parallel stripes and long straight line-sections of sometimes > 50 WALP molecules. The parallel lines indicate a cooperative effect in the formation of the striated phase upon solidification from the fluid to the gel phase. When one line curves, it forces parallel lines in its vicinity to curve similarly or terminate to keep r_{rep} constant, as can be observed in Fig. 2.6.d. From a geometric point of view, it is more favourable if lipids with the same degree of acyl chain deformation border each other. This is more difficult when many curves are present. The angles present are set by the hexagonal lipid packing and are close to 120º.

6.5 Concluding remarks

Summarizing, the formation of striated domains can be described as an interplay of lipid packing effects and peptide-peptide and peptide-lipid interactions. The obtained results emphasize the importance of the lipid environment on the lateral organization in membranes. It was already known that hydrophobic mismatch can drive aggregation in other systems [62, 102], but the work in this thesis demonstrates that effects such as lipid tilting and tightness of the lipid packing can be more important in determining the lateral organization of peptides in membranes. Tilt of the acyl-chains may be relevant in biomembranes as a curved surface of a protein can impose a favoured tilt angle on the surrounding, fluid lipids.

Striated domains self-assemble. Self-assembly is important biologically and has been shown to occur in a number of systems. Association of different membrane-spanning units of a protein through membrane-mediated effects drives the assembly of the proteins and, through this, regulates their functioning in living cells [13, 57, 79, 94, 95]. Highly ordered, self-assembled 2-

D crystalline structures have also been observed in biological systems, such as the hexagonally packed intermediate layer HPI [135] and bacteriorhodopsin [58, 135]. There is evidence that lipid-bacteriorhodopsin interactions may play an important role in its assembly [58], which suggests a large influence of the lipid matrix.

The use of the relatively simple model systems in this work has provided a way to systematically study the driving forces responsible for lateral heterogeneity and the precise role of the lipid matrix in this. This would not have been possible with large, biological proteins. The generality of the ordering mechanism presented here, however, suggests that striped ordering should not be restricted to the α-helical WALP, but should be a more general phenomenon. Indeed, another small model peptide (*i.e.* the β-helical ion-channel gramicidin A [85]) also shows distinct patterns of line-type aggregates in gel-state, saturated PC bilayers, albeit less ordered than those of WALP. Of course, it would be interesting to see if striated phases can be formed with larger proteins or if it is limited to single helices.
Finally, the underlying principles of self-assembly into striated regions can be applied to non-biological systems. Self-assembly of molecules with similar characteristics into a locally ordered structure on a nanoscale might be applied to technological devices in the future.

References

[1] A.N. Shipway, E. Katz, I. Willner, *Chem. Phys. Chem.*, **2000**, *1*, 18 - 52

[2] A. Ulman, *Chem. Rev.*, **1996**, *96*, 1533 - 1554

[3] P.L. Yeagle, '*The Structure of Biological Membranes*', CRC Press, Boca Raton, USA, **2005**

[4] H.R. Horton, L.A. Moran, R.S. Ochs, J.D. Rawn, K.G. Scrimgeour, '*Principles of Biochemistry*', Prentice Hall Int. Inc., Upper Saddle River, USA, **1996**

[5] C.R. Safinya, *Colloids and Surfaces A*, **1997**, *128*, 183 - 195

[6] L.K. Tamm, C. Böhm, J. Yang, Z. Shao, J. Hwang, M. Edidin, E. Betzig, *Thin Solid Films*, **1996**, *282 - 285*, 813 - 816

[7] E. Sackmann, *Science*, **1996**, *271*, 43 - 48

[8] K. Besteman, J.O. Lee, F.G.M. Wiertz, H.A. Heering, C. Dekker, *Nano Letters*, **2003**, *3*, 727 - 730

[9] Artist unknown, downloaded from: http://web.archive.org/web/20030608022517/ http://omega.dawsoncollege.qc.ca/ray/cellmemb/ membrane.jpg (accessed March 23, 2009)

[10] B. Gennis, '*Biomembranes, Molecular Structure and Function*', Springer-Verlag, New York, USA, **1989**

[11] K. Gawrisch, L.L. Holte, *Chem. Phys. Lipids*, **1996**, *81*, 105 - 116

[12] J.M. Seddon, *Biochim. Biophys. Acta*, **1990**, *1031*, 1 - 69

[13] E. van den Brink- van der Laan, J.A. Killian, B. de Kruijff, *Biochim. Biophys. Acta*, **2004**, *1666*, 275 - 288

[14] R.N. McElhaney, *Chem. Phys. Lipids*, **1982**, *30*, 229 - 259

[15] T.J. McIntosh, *Chem. Phys. Lipids*, **1996**, *81*, 117 - 131

[16] G. Cevc, *Biochemistry*, **1991**, *30*, 7186 - 7193

[17] J.R. Silvius, *Chem. Phys. Lipids*, **1991**, *57*, 241 - 252

[18] M.P. Nollert, H.A. Kolb, *J. Membr. Biol.*, **1998**, *161*, 227 - 233

[19] A. Tardieu, V. Luzzati, F.C.J. Reman, *J. Mol. Biol.*, **1973**, *75*, 711 - 733

[20] S.C. Chen, J.M. Sturtevant, B.J. Gaffney, *Proc. Natl. Acad. Sci. USA*, **1980**, *77*, 5060 - 5063

[21] R.N.A.H. Lewis, N. Mak, R.N. McElhaney, *Biochemistry*, **1987**, *26*, 6118 - 6126

[22] G. Cevc, *Chem. Phys. Lipids*, **1991**, *57*, 293 - 307

[23] S. Furuike, V.G. Levadny, S.J. Li, M. Yamazaki, *Biophys. J.*, **1999**, *77*, 2015 - 2023

[24] M.S. Fernfindez, M.T. Gonzfilez-Martinez, E. Calderon, *Biochim. Biophys. Acta*, **1986**, *863*, 156 - 164

[25] B.G. Tenchov, H. Yao, I. Hatta, *Biophys. J.*, **1989**, *56*, 757 - 768

[26] J. Mou, J. Yang, C. Huang, Z. Shao, *Biochemistry*, **1994**, *33*, 9981 - 9985

[27] H. Hauser, *Chem. Phys. Lipids*, **1991**, *57*, 309 - 325

[28] M.J. Ruocco, G.G. Shipley, *Biochim. Biophys. Acta*, **1982**, *684*, 59 - 66

[29] D. Marsh, '*CRC handbook of lipid bilayers'*, CRC Press Inc., Boca Raton, USA, **1990**

[30] S. Tristram-Nagle, R. Zhang, R.M. Suter, C.R. Worthington, W.J. Sun, J.F. Nagle, *Biophys. J.*, **1993**, *64*, 1097 - 1109

[31] H. Hauser, I. Pascher, R.H. Pearson, S. Sundell, *Biochim. Biophys. Acta*, **1981**, *650*, 21 - 51

[32] M.J. Janiak, D.M. Small, G.G. Shipley, *J. Biol. Chem.*, **1979**, *254*, 6068 - 6078

[33] H.A. Rinia, J.W.P. Boots, D.T.S. Rijkers, R.A. Kik, R.A. Demel, M.M.E. Snel, J.A. Killian, J.P.J.M. van der Eerden, B. de Kruijff, *Biochemistry*, **2002**, *41*, 2814 - 2824

[34] D.G. Cameron, H.L. Casal, H.H. Mantsch, *Biochemistry*, **1980**, *19*, 3665 - 3672

[35] C. Leidy, T. Kaasgaard, J.H. Crowe, O.G. Mouritsen, K. Jørgensen, *Biophys. J.*, **2002**, *83*, 2625 - 2633
[36] D.A. Pink, T.J. Green, D. Chapman, *Biochemistry*, **1980**, *19*, 349 - 356
[37] A.L. MacKay, *Biophys. J.*, **1981**, *35*, 301 - 313
[38] T. Heimburg, *Biochim. Biophys. Acta*, **1998**, *1415*, 147 - 162
[39] J.F. Nagle, R. Zhang, S. Tristam-Nagle, W. Sun, H.I. Petrache, *Biophys. J.*, **1996**, *70*, 1419 - 1431
[40] V.P. Ivanova, T. Heimburg, *Phys. Rev. E*, **2001**, *63*, 041914, 1 - 12
[41] Wikipedia contributors, "Lipid bilayer," Wikipedia, The Free Encyclopedia, http://en.wikipedia.org/w/index.php?title=Lipid_bilayer&oldid=252952150 (accessed December 14, 2008)
[42] S.M. Gruner, *Proc. Natl. Acad. Sci. USA*, **1985**, *82*, 3665 - 3669
[43] D.J. Müller, A. Engel, *Biophys. J.*, **1997**, *73*, 1633 - 1644
[44] K. Lohner, *Chem. Phys. Lipids*, **1991**, *57*, 341 - 362
[45] J. Mou, J. Yang, Z. Shao, *Biochemistry*, **1994**, *33*, 4439 - 4443
[46] T.J. McIntosh, *Biophys. J.*, **1980**, *29*, 237 - 245
[47] M. Thoma, M. Schwendler, H. Baltes, C.A. Helm, T. Pfohl, H. Riegler, H. Möhwald, *Langmuir*, **1996**, *12*, 1722 - 1728
[48] K.A. Melkonian, A.G. Ostermeyer, J.Z. Chen, M.G. Roth, D.A. Brown, *J. Biol. Chem.*, **1999**, *274*, 3910 - 3917
[49] P.R. Cullis, M.J. Hope, C.P.S. Tilcock, *Chem. Phys. Lipids*, **1986**, *40*, 127 - 144
[50] D.P. Siegel, *Biophys. J.*, **1986**, *49*, 1171 - 1183
[51] C. Hamai, T. Yang, S. Kataoka, P.S. Cremer, S.M. Musser, *Biophys. J.*, **2006**, *90*, 1241 - 1248
[52] D. Marsh, *Biophys. J.*, **1996**, *70*, 2248 - 2255
[53] S.W.Hui, A. Sen, *Proc. Natl. Acad. Sci. USA*, **1989**, *86*, 5825 - 5829
[54] S. Garcia-Manyes, G. Oncins, F. Sanz, *Biophys. J.*, **2005**, *89*, 4261 - 4274
[55] L. Stryer, '*Biochemistry*', W.H. Freeman and Company, New York, USA, **1988**
[56] R.A.F. Reithmeier, *Curr. Op. Struct. Biol.*, **1995**, *5*, 491 - 500
[57] J.A. Lundbæk, A.M. Maer, O.S. Andersen, *Biochemistry*, **1997**, *36*, 5695 - 5701
[58] M.P. Krebs, T.A. Isenbarger, *Biochim. Biophys. Acta*, **2000**, *1460*, 15 - 26
[59] D.A. Kelkar, A. Chattopadhyay, *Biochim. Biophys. Acta*, **2007**, *1768*, 2011 - 2025
[60] J.A. Killian, *Biochim. Biophys. Acta*, **1998**, *1376*, 401 - 416
[61] M.R.R. de Planque, J.A. Killian, *Mol. Membrane Biol.*, **2003**, *20*, 271 - 284
[62] J.A. Killian, *FEBS Letters*, **2003**, *555*, 134 - 138
[63] M.R.R. de Planque, B.B. Bonev, J.A.A. Demmers, D.V. Greathouse, R.E. Koeppe II, F. Separovic, A. Watts, J.A. Killian, *Biochemistry*, **2003**, *42*, 5341 - 5348
[64] S. Özdirekcan, D.T.S. Rijkers, R.M.J. Liskamp, J.A. Killian, *Biochemistry*, **2005**, *44*, 1004 - 1012
[65] S. Morein, R.E. Koeppe II, G. Lindblom, B. de Kruijff, J.A. Killian, *Biophys. J.*, **2000**, *78*, 2475 - 2485
[66] D.P. Siegel, V. Cherezov, D.V. Greathouse, R.E. Koeppe II, J.A. Killian, M. Caffrey, *Biophys. J.*, **2006**, *90*, 200 - 211
[67] F. Liu, R.N.A.H. Lewis, R.S. Hodges, R.N. McElhaney, *Biophys. J.*, **2004**, *87*, 2470 - 2482
[68] Y.P. Zhang, R.N.A.H. Lewis, R.S. Hodges, R.N. McElhaney, *Biochemistry*, **2001**, *40*, 474 - 482
[69] S. Mall, R. Broadbridge, R.P. Sharma, A.G. Lee, J.M. East, *Biochemistry*, **2000**, *39*, 2071 - 2078
[70] J.A. Killian, T.K.M. Nyholm, *Curr. Op. Struct. Biol.*, **2006**, *16*, 473 - 479
[71] R.J. Webb, J.M. East, R.P. Sharma, A.G. Lee, *Biochemistry*, **1998**, *37*, 673 - 679
[72] J.H. Davis, *Biochim. Biophys. Acta*, **1983**, *737*, 117 - 171
[73] D. Vaknin, K. Kjaer, J. Als-Nielsen, M. Lösche, *Biophys. J.*, **1991**, *59*, 1325 - 1332

[74] M.R.R. de Planque, D.V. Greathouse, R.E. Koeppe II, H. Schäfer, D. Marsh, J.A. Killian, *Biochemistry*, **1998**, *37*, 9333 - 9345
[75] E. Sparr, W.L. Ash, P.V. Nazarov, D.T.S. Rijkers, M.A. Hemminga, D.P. Tieleman, J.A. Killian, *J. Biol. Chem.*, **2005**, *280*, 39324 - 39331
[76] D. Chapman, B.A. Cornell, A.W. Eliasz, A. Perry, *J. Mol. Biol.*, **1977**, *113*, 517 - 538
[77] W. Hübner, H.H. Mantsch, *Biophys. J.*, **1991**, *59*, 1261 - 1272
[78] A. Janshoff, D.T. Bong, C. Steinem, J.E. Johnson, M.R. Ghadiri, *Biochemistry*, **1999**, *38*, 5328 - 5336
[79] J.R. Lewis, D.S. Cafiso, *Biochemistry*, **1999**, *38*, 5932 - 5938
[80] S. Morein, J.A. Killian, M.M. Sperotto, *Biophys. J.*, **2002**, *82*, 1405 - 1417
[81] R.N. McElhaney, *Biochim. Biophys. Acta*, **1986**, *864*, 361 - 421
[82] J.A. Killian, I. Salemink, M.R.R. de Planque, G. Lindblom, R.E. Koeppe II, D.V. Greathouse, *Biochemistry*, **1996**, *35*, 1037 - 1045
[83] P.C. Dave, E. Billington, Y.L. Pan, S.K. Straus, *Biophys. J.*, **2005**, *89*, 2434 - 2442
[84] M. Caffrey, G.W. Feigenson, *Biochemistry*, **1981**, *20*, 1949 - 1961
[85] J. Mou, D.M. Czajkowsky, Z. Shao, *Biochemistry*, **1996**, *35*, 3222 - 3226
[86] J. Riegler, H. Möhwald, *Biophys. J.*, **1986**, *49*, 1111 - 1118
[87] F. Dumas, M.-C. Lebrun, J.-F. Tocanne, *FEBS Letters*, **1999**, *458*, 271 - 277
[88] R.J. Cherry, U. Müller, R. Henderson, M.P. Heyn, *J. Mol. Biol.*, **1978**, *121*, 283 - 298
[89] J.M. East, A.G. Lee, *Biochemistry*, **1982**, *21*, 4144 - 4151
[90] A. van Dalen, S. Hegger, J.A. Killian, B. de Kruijff, *FEBS Letters*, **2002**, *525*, 33 - 38
[91] M.Ø. Jensen, O.G. Mouritsen, *Biochim. Biophys. Acta*, **2004**, *1666*, 205 - 226
[92] S.L. Keller, S.M. Bezrukov, S.M. Gruner, M.W. Tate, I. Vodyanoy, V.A. Parsegian, *Biophys. J.*, **1993**, *65*, 23 - 27
[93] N. Naarmann, B. Bilgiçer, K. Kumar, C. Steinem, *Biochemistry*, **2005**, *44*, 5188 - 5195
[94] T.A. Harroun, W.T. Heller, T.M. Weiss, L. Yang, H.W. Huang, *Biophys. J.*, **1999**, *76*, 937 - 945
[95] J.A. Killian, *Biochim. Biophys. Acta*, ***1992***, *1113*, 391 - 425
[96] J.T. Dunphy, M.E. Linder, *Biochim. Biophys. Acta*, **1998**, *1436*, 245 - 261
[97] T. Gil, J.H. Ipsen, O.G. Mouritsen, M.C. Sabra, M.M. Sperotto, M.J. Zuckermann, *Biochim. Biophys. Acta*, **1998**, *1376*, 245 - 266
[98] D. Papahadjopoulos, M. Moscarello, E.H. Eylar, T. Isac, *Biochim. Biophys. Acta*, **1975**, *401*, 317 - 335
[99] J.A. Killian, B. de Kruijff, *Biochemistry*, **1985**, *24*, 7881 - 7890
[100] F. Liu, R.N.A.H. Lewis, R.S. Hodges, R.N. McElhaney, *Biochemistry*, **2001**, *40*, 760 - 768
[101] P.C.A. van der Wel, T. Pott, S. Morein, D.V. Greathouse, R.E. Koeppe II, J.A. Killian, *Biochemistry*, **2000**, *39*, 3124 - 3133
[102] O.G. Mouritsen, M. Bloom, *Ann. Rev. Biophys. Biomol. Struct.*, **1993**, *22*, 145 - 171
[103] M.M. Sperotto, *Eur. Biophys. J.*, **1997**, *26*, 405 - 416
[104] H.I. Petrache, D.M. Zuckerman, J.N. Sachs, J.A. Killian, R.E. Koeppe II, T.B. Woolf, *Langmuir*, **2002**, *18*, 1340 - 1351
[105] B.A. Lewis, D.M. Engelman, *J. Mol. Biol.*, **1983**, *166*, 203 - 210
[106] S. Marčelja, *Biochim. Biophys. Acta*, **1976**, *455*, 1 - 7
[107] A.N.J.A. Ridder, W. van de Hoef, J. Stam, A. Kuhn, B. de Kruijff, J.A. Killian, *Biochemistry*, **2002**, *41*, 4946 - 4952
[108] B.Y. van Duyl, D.T.S. Rijkers, B. de Kruijff, J.A. Killian, *FEBS Letters*, **2002**, *523*, 79 - 84
[109] W.Kleemann, H.M. McConnel, *Biochim. Biophys. Acta*, **1976**, *419*, 206 - 222
[110] E. Sparr, D.N. Ganchev, M.M.E. Snel, A.N.J.A. Ridder, L.M.J. Kroon-Batenburg, V. Chupin, D.T.S. Rijkers, J.A. Killian, B. de Kruijff, *Biochemistry*, **2005**, *44*, 2 - 10
[111] J.N. Israelachvili, D.J. Mitchell, *Biochim. Biophys. Acta*, **1975**, *389*, 13 - 19
[112] D.B. Fenske, H.C. Jarrell, Y. Guo, S.W. Hui, *Biochemistry*, **1990**, *29*, 11222 - 11229
[113] A.G. Lee, *Biochim. Biophys. Acta*, **2004**, *1666*, 62 - 87

[114] P. Wiggins, R. Phillips, *Biophys. J.*, **2005**, *88*, 880 - 902
[115] R.S. Cantor, *Biophys. J.*, **1999**, *76*, 2625 - 2639
[116] B. de Kruijff, *Nature*, **1997**, *386*, 129 - 130
[117] B. de Kruijff, J.A. Killian, D.N. Ganchev, H.A. Rinia, E. Sparr, *Biol. Chem.*, **2006**, *387*, 235 - 241
[118] M. Schiffer, C.-H. Chang, F.J. Stevens, *Protein Engineering*, **1992**, *5*, 213 - 214
[119] D.N. Ganchev, D.T.S. Rijkers, M.M.E. Snel, J.A. Killian, B. de Kruijff, *Biochemistry*, **2004**, *43*, 14987 - 14993
[120] W.C. Wimley, S.H. White, *Nat. Struct. Mol. Biol.*, **1996**, *3*, 842 - 848
[121] J.A. Killian, G. von Heijne, *Trends Biochem. Sci.*, **2000**, *25*, 429 - 434
[122] H.A. Rinia, R.A. Kik, R.A. Demel, M.M.E. Snel, J.A. Killian, J.P.J.M. van der Eerden, B. de Kruijff, *Biochemistry*, **2000**, *39*, 5852 - 5858
[123] H.A. Rinia, B. de Kruijff, *FEBS Letters*, **2001**, *504*, 194 - 199
[124] J.P.J.M. van der Eerden, M.M.E. Snel, J. Makkinje, A.D.J. van Dijk, H.A. Rinia, *J. Cryst. Growth*, **2002**, *237 - 239*, 111 - 115
[125] G. Binnig, C.F. Quate, C.H. Gerber, *Phys. Rev. Lett.*, **1986**, *56*, 930 - 933
[126] G. Binnig, C.H. Gerber, E. Stoll, T.R. Albrecht, C.F. Quate, *Europhys. Lett.*, **1987**, *3*, 1281 - 1286
[127] Z. Shao, J. Mou, D.M. Czajkowsky, J. Yang, J.-Y. Yuan, *Adv. Phys.*, **1996**, *45*, 1 - 86
[128] A. Engel, C.A. Schoenenberger, D.J. Müller, *Curr. Op. Struct. Biol.*, **1997**, *7*, 279 - 284
[129] D. Fotiadis, S. Scheuring, S.A. Müller, A. Engel, D.J. Müller, *Micron*, **2002**, *33*, 385 - 397
[130] H.G. Hansma, K. Kasuya, E. Oroudjev, *Curr. Op. Struct. Biol.*, **2004**, *14*, 380 - 385
[131] F. Tokumasu, A.J. Jin, G.W. Feigenson, J.A. Dvorak, *Ultramicroscopy*, **2003**, *97*, 217 - 227
[132] Z.V. Leonenko, A. Carnini, D.T. Cramb, *Biochim. Biophys. Acta*, **2000**, *1509*, 131 - 147
[133] V.P. Ivanova, I.M. Makarov, T.E. Schäffer, T. Heimburg, *Biophys. J.*, **2003**, *84*, 2427 - 2439
[134] H.J. Butt, *Biophys. J.*, **1991**, *60*, 1438 - 1444
[135] D.J. Müller, M. Amrein, A. Engel, *J. Struct. Biol.*, **1997**, *119*, 172 - 188
[136] K. El Kirat, I. Burton, V. Dupres, Y.F. Dufrêne, *J. of Microscopy*, **2005**, *218*, 199 - 207
[137] D.J. Müller, A. Engel, M. Amrein, *Biosensors and Bioelectronics*, **1997**, *12*, 867 - 877
[138] Wikipedia contributors, "Atomic force microscope," Wikipedia, The Free Encyclopedia, http://en.wikipedia.org/w/index.h hp?title= Atomic_force_microsco pe&oldid=175755561 (Accessed December 8, 2007)
[139] B. Drake, C.B. Prater, A.L. Weisenhorn, S.A. Gould, T.R. Albrecht, C.F. Quate, D.S. Cannell, H.G. Hansma, P.K. Hansma, *Science*, **1989**, *243*, 1586 - 1589
[140] D.J. Müller, K. Anderson, *Trends in Biotechnology*, **2002**, *20*, S45 - S49
[141] A.L.Weisenhorn, P. Maivald, H.J. Butt, P.K. Hansma, *Phys. Rev. B*, **1992**, *45*, 11 226 - 11 232
[142] D.J. Müller, D. Fotiadis, S. Scheuring, S.A. Müller, A. Engel, *Biophys. J.*, **1999**, *76*, 1101 - 1111
[143] H.G. Hansma, J. Vesenka, C. Siegerist, G. Kelderman, H. Morrett, R.L. Sinsheimer, V. Elings, C. Bustamante, P.K. Hansma, *Science*, **1992**, *256*, 1180 - 1184
[144] Y.F. Dufrêne, G.U. Lee, *Biochim. Biophys. Acta*, **2000**, *1509*, 14 - 41
[145] S. Garcia-Manyes, G. Oncins, F. Sanz, *Electrochimica Acta*, **2006**, *51*, 5029 - 5036
[146] Y. Fang, J. Yang, *J. Phys. Chem.*, **1996**, *100*, 15614 - 15619
[147] A.A. Brian, H.M. McConnell, *Proc. Natl. Acad. Sci. USA*, **1984**, *81*, 6159 - 6163
[148] J.M. Solletti, M. Botreau, F. Sommer, W.L. Brunat. S. Kasas, T.M. Duc, M.R. Celio, *Langmuir*, **1996**, *12*, 5379 - 5386
[149] S.W. Hui, R. Viswanathan, J.A. Zasadzinski, J.N. Israelachvili, *Biophys. J.*, **1995**, *68*, 171 - 178
[150] T. Kaasgaard, C. Leidy, J.H. Crowe, O.G. Mouritsen, K. Jørgensen, *Biophys. J.*, **2003**, *85*, 350 - 360

[151] Z.V. Feng, T.A. Spurlin, A.A. Gewirth, *Biophys. J.*, **2005**, *88*, 2154 - 2164
[152] M.-C. Giocondi, L. Pacheco, P.E. Milhiet, C. Le Grimellec, *Ultramicroscopy*, **2001**, *86*, 151 - 157
[153] B. van Duyl, D. Ganchev, V. Chupin, B. de Kruijff, J.A. Killian, *FEBS Letters*, **2003**, *547*, 101 - 106
[154] J. Mou, J. Yang, Z. Shao, *J. Mol. Biol.*, **1995**, *248*, 507 - 512
[155] P.N.T. Unwin, P.D. Ennis, *Nature*, **1984**, *307*, 609 - 613
[156] H. Janovjak, A. Kedrov, D.A. Cisneros, K.T. Sapra, J. Struckmeier, D.J. Müller, *Neurobiol. Aging*, **2006**, *27*, 546 - 561
[157] M. Müller, K. Katsov, M. Schick, *Phys. Reports*, **2006**, *43*, 113-176
[158] M. Venturoli, M.M. Sperotto, M. Kranenburg, B. Smit, *Phys. Reports*, **2006**, *437*, 1 - 54
[159] H.L. Scott, *Curr. Op. Struct. Biol.*, **2002**, *12*, 495 - 502
[160] D.P. Tieleman, S.J. Marrink, H.J.C. Berendsen, *Biochim. Biophys. Acta*, **1997**, *1331*, 235 - 270
[161] D. Frenkel, B. Smit, '*Understanding Molecular Simulation, From Algorithms to Applications*', Academic Press, San Diego, USA, **2002**
[162] S.O. Nielsen, C.F. Lopez, G. Srinivas, M.L. Klein, *J. Phys. Condens. Matter*, **2004**, *16*, R481 - R512
[163] H. Heller, M. Schaefer, K. Schulten, *J. Phys. Chem.*, **1993**, *97*, 8343- 8360
[164] R.G. Snyder, K. Tu, M.L. Klein, R. Mendelssohn, H.L. Strauss, W. Sun, *J. Phys. Chem. B*, **2002**, *106*, 6273 - 6288
[165] P.C. Biggin, M.S.P. Sansom, *Biophys. Chem.*, **1999**, *76*, 161 - 183
[166] T.B. Woolf, *Biophys. J.*, **1997**, *73*, 2376 - 2392
[167] D.A. McQuarrie, '*Statistical Mechanics*', Harper & Row Publishers Inc., NewYork, USA, **1976**
[168] P. La Rocca, Y. Shai, M.S.P. Sansom, *Biophys. Chem.*, **1999**, *76*, 145 - 159
[169] B.R. Brooks, R.E. Bruccoleri, B.D. Olafson, D.J. States, S. Swaminathan, M. Karplus, *J. Comp. Chem.*, **1983**, *4*, 187 - 217
[170] J. Hermans, H.J.C. Berendsen, W.F. Van Gunsteren, J.P.M. Postma, *Biopolymers*, **1984**, *23*, 1513 - 1518
[171] S.-J. Marrink, A.H. de Vries, A.E. Mark, *J. Phys. Chem. B*, **2004**, *108*, 750 - 760
[172] A. Redondo, R. LeSar, *Annu. Rev. Mater. Res.*, **2004**, *34*, 279 - 314
[173] H.W. Huang, *Biophys. J.*, **1986**, *50*, 1061 - 1070
[174] P. Lagüe, M.J. Zuckermann, B. Roux, *Biophys. J.*, **2000**, *79*, 2867 - 2879
[175] R.D. Groot, K.L. Rabone, *Biophys. J.*, **2001**, *81*, 725 - 736
[176] R. Goetz, R. Lipowsky, *J. Chem. Phys.*, **1998**, *108*, 7397 - 7409
[177] C. Stadler, F. Schmid, *J. Chem. Phys*., **1999**, *110*, 9687 - 9705
[178] J.C. Shillcock, R. Lipowsky, *J. Chem. Phys.*, **2002**, *117*, 5048 - 5061
[179] M. Kranenburg, B. Smit, *J. Phys. Chem. B*, **2005**, *109*, 6553 - 6563
[180] P.J. Hoogerbrugge, J.M.V.A. Koelman, *Europhys. Lett.*, **1992**, *19*, 155 - 160
[181] P. Español, P. Warren, *Europhys. Lett.*, **1995**, *30*, 191 - 196
[182] M. Kranenburg, M. Venturoli, B. Smit, *J. Phys. Chem. B*, **2003**, *107*, 11491 - 11501
[183] M. Venturoli, B. Smit, M.M. Sperotto, *Biophys. J.*, **2005**, *88*, 1778 - 1798
[184] A.P. Lyubartsev, M. Karttunen, I. Vattulainen, A. Laaksonen, *Soft Materials*, **2003**, *1*, 121 - 137
[185] E.G. Flekkøy, P.V. Coveney, G. De Fabritiis, *Phys. Rev. E*, **2000**, *62*, 2140 - 2157
[186] P.B. Warren, *Curr. Op. Coll. Intf. Sci.*, **1998**, *3*, 620 - 624
[187] R.D. Groot, P.B. Warren, *J. Chem. Phys.*, **1997**, *107*, 4423 - 4435
[188] M. Doi, S.F. Edwards, '*The theory of polymer dynamics'*, Clarendon Press, Oxford, United Kingdom, **1986**
[189] M.C. Sabra, O.G. Mouritsen, *Biophys. J.*, **1998**, *74*, 745 - 752
[190] M.R.R. de Planque, E. Goormaghtigh, D.V. Greathouse, R.E. Koeppe II, J.A.W. Kruijtzer, R.M.J. Liskamp, B. de Kruijff, J.A. Killian, *Biochemistry*, **2001**, *40*, 5000 - 5010

[191] Y.-P. Zhang, R.N.A.H. Lewis, R.S. Hodges, R.N. McElhaney, *Biochemistry*, **1995**, *34*, 2362 - 2371
[192] R.J. Deschenes, *Encylcopedia Biol. Chem.*, **2004**, *3*, 532 - 534
[193] J. Basu, *Current Science*, **2004**, *87*, 212 - 217
[194] J. Greaves, L. Chamberlain, *J. Cell Biol.*, **2007**, *176*, 249 - 254
[195] M.D. Resh, *Science's STKE*, **2006**, 359, re-14
[196] P.C.A. van der Wel, E. Strandberg, J.A. Killian, R.E. Koeppe II, *Biophys. J.*, **2002**, *83*, 1479 - 1488
[197] D.D. Lasic, '*Liposomes: from Physics to Applications'*, Elsevier Science B.V., Amsterdam, The Netherlands, **1993**
[198] J. Jass, T. Tjärnhage, G. Puu, *Biophys. J.*, **2000**, *79*, 3153 - 3163
[199] P.S. Cremer, S.G. Boxer, *J. Phys. Chem. B*, **1999**, *103*, 2554 - 2559
[200] L. Chen, M.L. Johnson, R.L. Biltonen, *Biophys. J.*, **2001**, *80*, 254 - 270
[201] D.H. Kim, M.J. Costello, P.B. Duncan, D. Needham, *Langmuir*, **2003**, *19*, 8455 - 8466
[202] S.W. Hui, D.F. Parsons, M. Cowden, *Proc. Natl. Acad. Sci. USA*, **1974**, *71*, 5068 - 5072
[203] B. Stidder, G. Fragneto, S.J. Roser, *Soft Matter*, **2007**, *3*, 214 - 222
[204] J. Schneider, Y.F. Dufrêne, W.R. Barger Jr., G.U. Lee, *Biophys. J.*, **2000**, *79*, 1107 - 1118
[205] Z.V. Leonenko, E. Finot, H. Ma, T.E.S. Dahms, D.T. Cramb, *Biophys. J.*, **2004**, *86*, 3783 - 3793
[206] J.A.N. Zasadzinski, C.A. Helm, M.L. Longo, A.L. Wiesenhorn, S.A.C. Gould, P.K. Hansma, *Biophys. J.*, **1991**, *59*, 755 - 760
[207] M. Beckmann, P. Nollert, H.A. Kolb, *J. Membrane Biol.*, **1998**, *161*, 227 - 233
[208] J. Rädler, M. Radmacher, H.E. Gaub, *Langmuir*, **1994**, *10*, 3111 - 3115
[209] C. Wong, P.E. West, K.S. Olson, M.L. Mecartney, N. Starostina, *J. Minerals*, **2007**, *59*, 12 - 16
[210] P. Markiewicz, C.M. Goh, *Rev. Scientific Instruments*, **1995**, *66*, 3186 - 3190
[211] M. Grandbois, H. Clausen-Schaumann, H. Gaub, *Biophys. J.*, **1998**, *74*, 2398 - 2404
[212] R.L. McClain, J.J. Breen, *Langmuir*, **2001**, *17*, 5121 - 5124
[213] L.J. Lis, M. McAlister, N. Fuller, R.P. Rand, V.A. Parsegian, *Biophys. J.*, **1982**, *37*, 657 - 665
[214] D. Papahadjopoulos, *Biochim. Biophys. Acta*, **1968**, *163*, 240 - 254
[215] H.I. Petrache, S. Tristram-Nagle, D. Harries, N. Kučerka, J.F. Nagle, V.A. Parsegian, *J. Lipid Research*, **2006**, *47*, 302 - 309
[216] R. Bartucci, L. Sportelli, *Biochim. Biophys. Acta*, **1994**, 1195, 229 - 236
[217] J. Seelig, P.M. MacDonald, P.G. Scherer, *Biochemistry*, **1987**, *26*, 7535 - 7541
[218] K. Makino, T. Yamada, M. Kimura, T. Oka, H. Ohshima, T. Kondo, *Biophys. Chem.*, **1991**, *41*, 175 - 183
[219] S.A. Tatulian, *Biochim. Biophys. Acta*, **1983**, *736*, 189 - 195
[220] W.F. Heinz, J.H. Hoh, *Biophys. J.*, **1999**, *76*, 528 - 538
[221] H.G. Kapitza, D.A. Rüppel, H.-J. Galla, E. Sackmann, *Biophys. J.*, **1984**, *45*, 577 - 587
[222] L.M. Loura, A. Fedorov, M. Prieto, *Biophys. J.*, **1996**, *71*, 1823 - 1836
[223] G. Müller, J.-J. Métois, P. Rudolph,'*Crystal growth: from fundamentals to technology*', Elsevier, Amsterdam, The Netherlands, **2004**
[224] T.B. Pedersen, T. Kaasgaard, M.Ø. Jensen, S. Frokjaer, O.G. Mouritsen, K. Jørgensen, *Biophys. J.*, **2005**, *89*, 2494 - 2503
[225] W.G.J. Hol, *Adv. Biophys.*, **1985**, *19*, 133 - 165
[226] M.S. Sansom, *Prog. Biophys. Molec. Biol.*, **1991**, *55*, 139 - 235
[227] J. Aqvist, H. Luecke, F.A. Quiocho, A. Warshel, *Proc. Natl. Acad. Sci. USA*, **1991**, *88*, 2026 - 2030
[228] N. Ben-Tal, B. Honig, *Biophys. J.*, **1996**, *71*, 3046 - 3050
[229] T.K.M. Nyholm, S. Özdirekcan, J.A. Killian, *Biochemistry*, **2007**, *46*, 1457 - 1465
[230] A. Spisni, I. Pasquali-Ronchetti, E. Casali, L. Lindner, P. Cavatorta, L. Masotti, D.W. Urry, *Biochim. Biophys. Acta*, **1983**, *732*, 58 - 68

[231] J. Yang, J. Appleyard, *J. Phys. Chem. B*, **2000**, *104*, 8097 - 8100
[232] S.J. Johnson, T.M. Bayerl, D.C. McDermott, G.W. Adam, A.R. Rennie, R.K. Thomas, E. Sackmann, *Biophys. J.*, **1991**, *59*, 289 - 294
[233] B.A. Lewis, D.M. Engelman, *J. Mol. Biol.*, **1983**, *166*, 211 - 217
[234] D. Needham, E. Evans, *Biochemistry*, **1988**, *27*, 8261 - 8269
[235] W.-J. Sun, R.M. Suter, M.A. Knewtson, C.R. Worthington, S. Tristram-Nagle, R. Zhang, J.F. Nagle, *Phys. Rev. E*, **1994**, *49*, 4665 - 4676
[236] A. Vidal, T.J. McIntosh, *Biophys. J.*, **2005**, *89*, 1102 - 1108
[237] R. Jacobs, E. Oldfield, *Biochemistry*, **1979**, *18*, 3280 - 3285
[238] E.J. Shimshick, H.M. McConnell, *Biochemistry*, **1973**, *12*, 2351 - 2360
[239] M.P. Andrich, J.M. Vanderkooi, *Biochemistry*, **1976**, *15*, 1257 - 1261
[240] F. Dumas, M.M. Sperotto, M.-C. Lebrun, J.-F. Tocanne, O.G. Mouritsen, *Biophys. J.*, **1997**, *73*, 1940 - 1953
[241] A.D. Horowitz, *Chem. Phys. Lipids*, **1995**, *76*, 27 - 39
[242] A.N.J.A. Ridder, R.E.J. Spelbrink, J.A.A. Demmers, D.T.S. Rijkers, R.M.J. Liskamp, J. Brunner, A.J.R. Heck, B. de Kruijff, J.A. Killian, *Biochemistry*, **2004**, *43*, 4482 - 4489
[243] M.M. Sperotto, O.G. Mouritsen, *Biophys. J.*, **1991**, *59*, 261 - 270
[244] T.C.B. Vogt, J.A. Killian, B. de Kruijff, *Biochemistry*, **1994**, *33*, 2063 - 2070
[245] R.E. Koeppe II, T.C.B. Vogt, D.V. Greathouse, J.A. Killian, B. de Kruijff, *Biochemistry*, **1996**, *35*, 3641 - 3648
[246] C.J.A. van Echteld, B. de Kruijff, A.J. Verkleij, J. Leunissen-Bijvelt, J. de Gier, *Biochim. Biophys. Acta*, **1982**, *692*, 126 - 138
[247] M. Rappolt, P. Laggner, G. Pabst, *Recent Res. Devel. Biophys.*, **2004**, *3*, 363 - 392
[248] A. Seelig, J. Seelig, *Biochemistry*, **1974**, *13*, 4839 - 4845
[249] M. Rappolt, G. Pabst, G. Rapp, M. Kreichbaum, H. Amenitsch, C. Krenn, S. Bernstorff, P. Laggner, *Eur. Biophys. J.*, **2000**, *29*, 125 - 133
[250] N. Maeda, T.J. Senden, J.M. di Meglio, *Biochim. Biophys. Acta*, **2002**, *1564*, 165 - 172
[251] H. Binder, *Vibrational Spectr.*, **1999**, *21*, 151 - 163
[252] R. Zhang, W. Sun, S. Tristram-Nagle, R.L. Headrick, R.M. Suter, J.F. Nagle, *Phys. Rev. Lett.*, **1995**, *74*, 2832 - 2835
[253] S. Tristam-Nagle, J.F. Nagle, *Chem. Phys. Lipids*, **2004**, *127*, 3 - 14
[254] B. Tenchov, R. Koynova, G. Rapp, *Biophys. J.*, **2001**, *80*, 1873 - 1890
[255] O.G. Mouritsen, M.J. Zuckermann, *Eur. Biophys. J.*, **1985**, *12*, 75 - 86
[256] C.P.S. Tilcock, P.R. Cullis, *Biochim. Biophys. Acta*, **1982**, *684*, 212 - 218
[257] L.K. Tamm, H.M. McConnell, *Biophys. J.*, **1985**, *47*, 105 - 113
[258] Z.V. Feng, T.A. Spurlin, A.A. Gewirth, *Biophys. J.*, **2005**, *88*, 2154 - 2164
[259] A.N. Zdravkova, J.P.J.M. van der Eerden, *J. Cryst. Growth*, **2007**, *307*, 192 - 202
[260] C. Naumann, T. Brumm, T.M. Bayerl, *Biophys. J.*, **1992**, *63*, 1314 - 1319
[261] G. Weidemann, D. Vollhardt, *Thin Solid Films*, **1995**, *264*, 94 - 103
[262] U. Tartaglino, T. Zykova-Timan, F. Ercolessi, E. Tosatti, *Phys. Reports*, **2005**, *411*, 291 - 321
[263] M. Zhao, Q. Jiang, *Solid State Comm.*, **2004**, *130*, 37 - 39
[264] J.W.M. Frenken, J.F. van der Veen, *Phys. Rev. Lett.*, **1985**, *54*, 134 – 137
[265] J.G. Dash, *Proc. Natl. Acad. Sci. USA*, **1987**, *84*, 4690 - 4691
[266] H. Schechter, R. Brener, M. Folman, J. Suzanne, *Phys. Rev. B*, **1990**, *41*, 2748 - 2752
[267] V. Ignatescu, J.M. Blakely, *Surface Science*, **2007**, *601*, 5459 - 5465
[268] F. Yarrow, T.J.H. Vlugt, J.P.J.M. van der Eerden, M.M.E. Snel, *J. Cryst. Growth*, **2005**, *275*, e1417 - e1421
[269] M.J. Zuckermann, O.G. Mouritsen, *Eur. Biophys. J.*, **1987**, *15*, 77 - 86
[270] B. Lee, S.A. Mabry, A. Jonas, J. Jonas, *Chem. Phys. Lipids*, **1995**, *I78*, 103 - 117
[271] S. Schuy, A. Janshoff, *Chem. Phys. Chem.*, **2006**, *7*, 1207 - 1210
[272] M. Käsbauer, M. Junglas, T.M. Bayerl, *Biophys. J.*, **1997**, *76*, 2600 - 2605

[273] M.C. Giocondi, V. Vié, E. Lesniewska, P.E. Milhiet, M. Zinke-Allmang, C. Le Grimellec, *Langmuir*, **2001**, *17*, 1653 - 1659
[274] S.J. Marrink, J. Risselada, A.E. Mark, *Chem. Phys. Lipids*, **2005**, *135*, 223 - 244
[275] P. Yager, W.L. Peticolas, *Biochim. Biophys. Acta*, **1982**, *688*, 775 - 785
[276] D. Kaschiev, in '*Science and Technology of Crystal Growth*', Ed. J.P. van der Eerden, O.S.L. Bruinsma, Kluwer Academic Publishers, Dordrecht, The Netherlands, **1995**
[277] R.F.M. de Almeida, L.M.S. Loura, M. Prieto, A. Watts, A. Fedorov, F.J. Barrantes, *Biophys. J.*, **2004**, *86*, 2261 - 2272
[278] E. Evans, D. Needham, *J. Phys. Chem.*, **1987**, *91*, 4219 - 4228
[279] P.M. Brown, J. Steers, S.W. Hui, P.L. Yeagle, J.R. Silvius, *Biochemistry*, **1986**, *25*, 4259 - 4267
[280] D. Marsh, *Chem. Phys. Lipids*, **2006**, *144*, 146 - 159
[281] A. Blume, D.M. Rice, R.J. Wittebort, R.G. Griffin, *Biochemistry*, **1982**, *21*, 6220 - 6230
[282] D.A. Wilkinson, J.F. Nagle, *Biochemistry*, **1981**, *20*, 187 - 192
[283] H.L. Casal, H.H. Mantsch, *Biochim. Biophys. Acta*, **1983**, *735*, 387 - 396
[284] R.J. Wittebort, A. Blume, T.-H. Huang, S.K. Das Gupta, R.G. Griffin, *Biochemistry*, **1982**, *21*, 3487 - 3502
[285] H.D. Dörfler, P. Miethe, A. Möps, *Chem. Phys. Lipids*, **1990**, *54*, 171 - 179
[286] J.M. Boggs, G. Rangaraj, K.M. Koshy, *Chem. Phys. Lipids*, **1986**, *40*, 23 - 34
[287] P.J. Davis, B.D. Fleming, K.P. Coolbear, K.M.W. Keough, *Biochemistry*, **1981**, *20*, 3633 - 3636
[288] S. Leekumjorn, A.K. Sum, *J. Phys. Chem. B*, **2007**, *111*, 6026 - 6033
[289] B.J. Litman, E.N. Lewis, I.W. Levin, *Biochemistry*, **1991**, *30*, 313 - 319
[290] '*CRC handbook of chemistry and physics'*, Ed. D.R. Lide, Chapman and Hall, Boca Raton, USA, **2001**
[291] D.W. Gruen, *Biophys. J.*, **1981**, *33*, 149 - 166
[292] Z. Chen, R.P. Rand, *Biophys. J.*, **1998**, *74*, 944 - 952
[293] J. Seelig, N. Waespe-Šarčević, *Biochemistry*, **1978**, *17*, 3310 - 3315
[294] H. Yun, Y.W Choi, N.J. Kim, D. Sohn, *Bull. Korean Chem. Soc.*, **2003**, *24*, 377 - 383
[295] R.N.A.H. Lewis, B.D. Sykes, R.N. McElhaney, *Biochemistry*, **1988**, *27*, 880 - 887
[296] W.P. Williams, B.A. Cunningham, D.H. Wolfe, G.E. Derbyshire, G.R. Mant, W. Bras, *Biochim. Biophys. Acta*, **1996**, *1284*, 86 - 96
[297] A.C. Simonsen, L.A. Bagatolli, *Langmuir*, **2004**, *20*, 9720 - 9728
[298] A. Blume, R.J. Wittebort, S.K. Das Gupta, R.G. Griffin, *Biochemistry*, **1982**, *21*, 6243 - 6253
[299] J.R. Silvius, *Biochim. Biophys. Acta*, **1986**, *857*, 217 - 228
[300] P.J. Quinn, L.J. Lis, B.A. Cunningham, *J. Coll. Intf. Sci.*, **1988**, *125*, 437 - 443
[301] E. Evans, D. Needham, *Faraday Discuss. Chem. Soc.*, **1986**, *81*, 267 - 280
[302] B.A. Cunningham, W. Tamura-Lis, L.J. Lis, P.J. Quinn, *J. Coll. Intf. Sci.*, **1988**, *121*, 193 - 197
[303] T. Inoue, Y. Nibu, *Chem. Phys. Lipids*, **1999**, *100*, 139 - 150
[304] I.V. Polozov, J.G. Molotkovsky, L.D. Bergelson, *Chem. Phys. Lipids*, **1994**, *69*, 209 - 218
[305] K. Arnold, A. Lösche, K. Gawrisch, *Biochim. Biophys. Acta*, **1981**, *645*, 143 - 148
[306] S. Scarlata, S.M. Gruner, *Biophys. Chem.*, **1997**, *67*, 269 - 279
[307] D.W.R. Gruen, D.A. Haydon, *Pure & Appl. Chem.*, **1980**, *52*, 1229 - 1240
[308] F. Paltauf, H. Hauser, M.C. Phillips, *Biochim. Biophys.* Acta, **1971**, *249*, 539 - 547
[309] M.C. Phillips, D. Chapman, *Biochim. Biophys. Acta*, **1968**, *163*, 301 - 313
[310] D. Marsh, *Biophys. J.*, **1999**, *77*, 953 - 963
[311] M. Ceccarelli, M. Marchi, *Biochimie*, **1998**, *80*, 415 - 419
[312] S. Li, H. Lin, Z. Wang, C. Huang, *Biophys. J.*, **1994**, *66*, 2005 - 2018
[313] J. Ernst, W.S. Sheldrick, J. Fuhrhop, *Z. Naturforsch.*, **1979**, *34b*, 706 - 711
[314] A.J. Metso, J.P Mattila, P.K.J. Kinnunen, *Biochim. Biophys. Acta*, **2004**, *1663*, 222 - 231
[315] J.S. Langer, *Rev. Mod. Phys.*, **1980**, *52*, 1 - 28

[316] Y. Teraoka, A. Saito, S. Okawa, *Int. J. Refrigeration*, **2002**, *25*, 218 -225
[317] L. Gránásy, T. Pusztai, T. Börzsöny, J.A. Warren, J.F. Douglas, *Nature Materials*, **2004**, *3*, 645 - 650
[318] S. Frey, L.K. Tamm, *Biochem. J.*, **1990**, *272*, 713 - 719
[319] D. Vollhardt, *J. Phys. Chem. C*, **2007**, *111*, 6805 - 6812
[320] H. Binder, K. Gawrisch, *J. Phys. Chem. B*, **2001**, *105*, 12378 - 12390
[321] P. Vitovič, S. Kresák, R. Naumann, S.M. Schiller, R.N.A.H. Lewis, R.N. McElhaney, T. Hianik, *Bioelectrochemistry*, **2004**, *63*, 169 - 176
[322] M. Müller, K. Katsov, M. Schick, *Phys. Reports*, **2006**, *434*, 113 - 176
[323] D. Harries, A. Ben-Shaul, *J. Chem. Phys.*, **1997**, *106*, 1609 - 1619
[324] T. Sintes, A. Baumgärtner, *J. Chem. Phys.*, **1997**, *106*, 5744 - 5750
[325] M.J. Stevens, *J. Chem. Phys.*, **2004**, *121*, 11942 - 11948
[326] I. Vattulainen, M. Karttunen, G. Besold, J.M. Polson, *J. Chem. Phys.*, **2002**, *116*, 3967 - 3979
[327] I. Pagonabarraga, M.H.J. Hagen, D. Frenkel, *Europhys. Lett.*, **1998**, *42*, 377 - 382
[328] M.P. Allen, *J. Phys. Chem. B*, **2006**, *110*, 3823 - 3830
[329] M. Liu, P. Meakin, H. Huang, *J. Comp. Phys.*, **2007**, *222*, 110 - 130
[330] I.V. Pivkin, G.E. Karniadakis, *J. Comp. Phys.*, **2005**, *207*, 114 - 128
[331] M. Revenga, I. Zúñiga, P. Español, I. Pagonabarra, *Int. J. Modern Phys. C*, **1998**, *9*, 1319 - 1328
[332] F. Jähnig, *Biophys. J.*, **1996**, *71*, 1348 - 1349
[333] H. Goldstein, C. Poole, J. Safko, '*Classical Mechanics*', 3rd ed., Addison Wesley, San Francisco, USA, 2002
[334] S. Tristram-Nagle, H.I. Petrache, J.F. Nagle, *Biophys. J.*, **1998**, *75*, 917 - 925
[335] J.N. Sachs, H.I. Petrache, T.B. Woolf, *Chem. Phys. Lipids*, **2003**, *126*, 211 – 233
[336] G. Jaeger, *Arch. Hist. Exact Sci.*, **1998**, *53*, 51 - 81
[337] S.O. Nielsen, B. Ensing, V. Ortiz, P.B. Moore, M.L. Klein, *Biophys. J.*, **2005**, *88*, 3822 - 3828
[338] P. Lagüe, M.J. Zuckermann, B. Roux, *Biophys. J.*, **2001**, *81*, 276 - 284
[339] R.S. Cantor, *Chem. Phys. Lipids*, **1999**, *101*, 45 - 56
[340] S. May, A. Ben-Shaul, *Biophys. J.*, **1999**, *76*, 751 - 767
[341] M.M. Sperotto, S. May, A. Baumgaertner, *Chem. Phys. Lipids*, **2006**, *141*, 2 - 29
[342] J.-B. Fournier, *Eur. Phys. J. B*, **1999**, *11*, 261 - 272
[343] M. Hamm, M.M. Kozlov, *Eur. Phys. J. E*, **2000**. *3*, 323 - 335
[344] D.R. Fattal, A. Ben-Shaul, *Biophys. J.*, **1993**, *65*, 1795 - 1809
[345] S.K. Kandansamy, R.G. Larson, *Biophys. J.*, **2006**, *90*, 2326 - 2343
[346] S. Özdirekcan, C. Etchebest, J.A. Killian, P.F.J. Fuchs, *J. Am. Chem. Soc.*, **2007**, *129*, 15174 - 15181
[347] T.B. Woolf, B. Roux, *Proteins: Structure*, *Function and Genetics*, **1996**, *24*, 92 - 114
[348] W.K. Subczynski, R.N.A.H. Lewis, R.N. McElhaney, R.S. Hodges, J.S. Hyde, A. Kusumi, *Biochemistry*, **1998**, *37*, 3156 - 3164
[349] M. Gimpelev, L.R. Forrest, D. Murray, B. Honig, *Biophys. J.*, **2004**, *87*, 4075 - 4086
[350] I.T. Arkin, A.T. Brunger, *Biochim. Biophys. Acta*, **1998**, *1429*, 113 - 128
[351] K. Kachel, E. Asuncion-Punzalan, E. London, *Biochemistry*, **1995**, *34*, 15475 - 15479
[352] J.A.A. Demmers, E. van Duijn, J. Haverkamp, D.V. Greathouse, R.E. Koeppe II, A.J.R. Heck, J.A. Killian, *J. Biol. Chem.*, **2001**, *276*, 34501 - 34508
[353] S. Persson, J.A. Killian, G. Lindblom, *Biophys. J.*, **1998**, *75*, 1365 - 1371
[354] P. Braun, G. von Heijne, *Biochemistry*, **1999**, *38*, 9778 - 9782
[355] S.S. Deol, P.J. Bond, C. Domene, M.S.P. Sansom, *Biophys. J.*, **2004**, *87*, 3737 - 3749
[356] F. Liu, R.N.A.H. Lewis, R.S. Hodges, R.N. McElhaney, *Biochemistry*, **2002**, *41*, 9197 - 9207
[357] E. Evans, F. Ludwig, *J. Phys. Condens. Matter*, **2000**, *12*, A315 - A320

[358] W.-M. Yau, W.C. Wimley, K. Gawrisch, S.H. White, *Biochemistry*, **1998**, *37*, 14713 - 14718
[359] F.N.R. Petersen, M.Ø. Jensen, C.H. Nielsen, *Biophys. J.*, **2005**, *89*, 3985 - 3996
[360] M.R.R. de Planque, J.-W.P. Boots, D.T.S. Rijkers, R.M.J. Liskamp, D.V. Greathouse, J.A. Killian, *Biochemistry*, **2002**, *41*, 8396 - 8404
[361] R. Bruinsma, P. Pincus, *Curr. Op. Solid State Mater. Sci.*, **1996**, *1*, 401 - 406
[362] T.A. Harroun, W.T. Heller, T.M. Weiss, L. Yang, H.W. Huang, *Biophys. J.*, **1999**, *76*, 3176 - 3185
[363] N. Dan, S.A. Safran, *Biophys. J.*, **1998**, *75*, 1410 - 1414
[364] M.C. Sabra, J.C.M. Uitdehaag, A. Watts, *Biophys. J.*, **1998**, *75*, 1180 - 1188

List of abbreviations and symbols

γ	surface tension
Δd	difference in thickness
ΔH_M	main transition or melting enthalpy
ΔT_{WALP}	depression in T_M caused by WALP
θ	polar angle
θ_L	polar tilt angle of lipid
ξ	coherence length
ρ	density
ρ_{line}	density of linear packing defects
σ_L	diameter of the lipid
σ_P	diameter of the peptide
φ	azimuth angle
Å	Ångstrom = 10^{-10} m
A	alanine amino acid
a_{ij}	interaction parameter
A_L	area per lipid
AAC	Acoustic Alternating Current
Ac	acetyl group
AFM	Atomic Force Microscopy
Ala	alanine amino acid
CG	coarse-grained
D	equilibrium separation distance between rows of WALP
d_{bil}	bilayer thickness
d^0_{bil}	bilayer thickness (X-ray)
d_{dom}	height of the striated domains
D_{dom}	thickening at the striated domains
d_{fluid}	thickness of fluid-phase bilayer
d^0_{fluid}	thickness of fluid-phase bilayer (X-ray)
d_{gel}	thickness of gel-phase bilayer
d^0_{gel}	thickness of gel-phase bilayer (X-ray)
d_{HPH}	hydrophobic thickness
d_L	thickness of lipid bilayer
d_w	thickness of water-layer
DAPC	di-1,2-arachidoyl-*sn*-glycero-3-phosphocholine, di-20:0-PC
DBPC	di-1,2-beheneoyl-*sn*-glycero-3-phosphocholine, di-22:0-PC
DEiPC	1,2-dieicosenoyl-*sn*-glycero-3-phosphocholine, di-20:1-PC
DErPC	1,2-dierucoyl-*sn*-glycero-3-phosphocholine, di-22:1-PC
DLgPC	di-1,2-lignoceroyl-*sn*-glycero-3-phosphocholine, di-24:0-PC
DMPC	di-1,2-myristoyl-*sn*-glycero-3-phosphocholine, di-14:0-PC
DNPC	1,2-dinervonoyl-*sn*-glycero-3-phosphocholine, di-24:1-PC
DOPC	di-1,2-oleoyl-*sn*-glycero-3-phosphocholine, di-16:1-PC
DPD	Dissipative Particle Dynamics
DPPC	1,2-dipalmitoyl-*sn*-glycero-3-phosphocholine, di-16:0-PC
DPPE	1,2-dipalmitoyl-*sn*-glycero-3-phosphoethanolamine, di-16:0-PE
DSPC	di-1,2-stearoyl-*sn*-glycero-3-phosphocholine, di-18:0-PC
DSC	Differential Scanning Calorimetry
ESR	Electron Spin Resonance
EtOH	ethanol
exp	experimental
F	imaging or scanning force
$\boldsymbol{f}_i$	force on particle i
$\boldsymbol{F}_{ij}{}^C$	conservative force
$\boldsymbol{F}_{ij}{}^D$	dissipative force
$\boldsymbol{F}_{ij}{}^R$	random force
G	glycine amino acid
Gly	glycine amino acid
H	headgroup
H_{II}	inverted hexagonal phase
His	histidine amino acid
HXD	*n*-hexadecane, $C_{16}H_{34}$
IR	Infra Red

L_α	fluid or liquid-crystalline phase
L_β	gel phase, non-tilted
L_β'	gel phase, tilted
$L_{\beta I}$	interdigitated phase
L_c'	subgel phase
L_o	liquid-ordered phase
L	leucine amino acid
L_H	lipid head
L_T	lipid tail
LB	Langmuir-Blodgett
LC	liquid-condensed
Leu	leucine amino acid
MAC	Magnetic Alternating Current
MC	Monte Carlo
MD	Molecular Dynamics
MeOH	methanol
MLV	multi-lamellar vesicle
n	length of lipid acyl chain
N	number of particles
n_T	number of tail beads
$n(\sigma_L)$	number of lipid diameters
$N(\theta_L)$	orientational distribution
nm	10^{-9} m
NMR	Nuclear Magnetic Resonance
P	peptide
P_β'	ripple phase
$P(\theta_L)$	probability distribution
P_H	peptide head
P_{H1}	peptide head 1
P_{H2}	peptide head 2
P_L	shape factor of lipid
P_T	peptide tail
Pa	palmitoyl chain, 16:0
PC	phosphatidylcholine
PE	phosphatidylethanolamine
Phe	phenylalanine amino acid
POPC	1-palmitoyl-2-oleoyl-*sn*-glycero-3-phosphocholine, (16:0,18:1)-PC
POPE	1-palmitoyl-2-oleoyl-*sn*-glycero-3-phosphoethanolamine, (16:0,18:1)-PE
Q_{II}	cubic phase
r	interparticle distance
R_c	cut-off distance
r_{rep}	repeat distance
S_L	order parameter of lipid
sim	simulation
SPB	supported planar bilayer
SUV	small uni-lamellar vesicle
T	temperature
T	tailgroup
T^*	reduced temperature
T_{dom}	melting temperature of lipids in striated domains
T_{end}	temperature where melting is completed
T_M	main transition temperature
T_{onset}	temperature where melting starts
T_{pre}	pre transition temperature
T_{tr}	transition temperature
TC	Temperature-Controlled
TFE	2,2,2-trifluoroethanol
TM	transmembrane
Trp	tryptophan amino acid
Tyr	tyrosine amino acid
x_{bulk}	x-value where bulk packing is assumed
x_{DPPE}	mole fraction of DPPE
x_{HXD}	mole fraction of *n*-hexadecane
x_{max}	x-value of maximum
V	volume
w	water
W	tryptophan amino acid
WALP	model peptide

Nederlandse samenvatting voor niet-ingewijden

Alle levende organismen bestaan uit cellen. Mensen en dieren hebben een groot aantal verschillende cellen, zoals zenuwcellen en spiercellen. Binnen elke cel voltrekken zich biochemische processen die noodzakelijk zijn voor het functioneren. Zo wordt bijvoorbeeld DNA afgelezen voor de aanmaak van nieuwe eiwitten, die op hun beurt weer betrokken zijn bij allerlei belangrijke processen, zoals het omzetten van energie uit voedsel.
Cellen zijn omgeven door een membraan, dat ervoor zorgt dat de waterige inhoud van de cel bij elkaar en afgeschermd blijft. Een membraan is onder meer opgebouwd uit lipiden, die bestaan uit een water-minnende ('hydrofiele') kopgroep en meestal twee water-vrezende ('hydrofobe') staarten. Er zijn een groot aantal verschillende lipiden die elk een andere chemische samenstelling en structuur hebben (zie bijvoorbeeld figuur 1.2).
Door de tweedeling tussen kop- en staartgroepen pakken de lipiden samen in een dubbele laag (bilaag), waarin de lipiden tegenover elkaar zitten. De kopgroepen bevinden zich aan de buitenkant, zodat ze grenzen aan de waterige omgeving. De staarten zitten aan de binnenzijde zodat ze afgeschermd zijn van water (zie het onderste plaatje van figuur 1.3, waar de witte bollen de kopgroepen voorstellen en de rechte grijze lijnen de staarten). Op deze manier vormen de lipiden een flexibele, aaneengesloten laag om de cellen.

Naast lipiden bevatten cellen eiwitten die allerlei taken uitvoeren, van het opruimen van lichaamsvreemde bacteriën en virussen, signaalfuncties tot het transport van stoffen (denk aan transport van zuurstof door hemoglobine). Een aantal van deze eiwitten bestaat uit meerdere delen die door de lipide bilaag heen steken (de zogenaamde integrale of transmembrane eiwitten, zie figuur 1.1).
Vroeger dacht men dat het membraan alleen een omhulsel was waarin deze transmembrane eiwitten 'ronddreven', maar tegenwoordig heeft men bewijs dat het membraan zelf een grote invloed uitoefent op de eiwitten. Verschillende soorten lipiden kunnen gebiedjes vormen in de membranen waarin bepaalde eiwitten verblijven. Ook kunnen de relatieve posities van de verschillende eenheden van een eiwit beïnvloed worden, wat het eiwit 'aan' en 'uit' kan zetten van een actieve naar een niet-actieve vorm. Verschillende theorieën zijn bedacht om deze effecten te verklaren. Zo kan het verschil in dikte tussen de bilaag en het eiwit een rol spelen ('hydrofobe mismatch'), maar ook het soort lipide en de fase (vast of vloeibaar) van de bilaag.

Om dit soort interacties te bestuderen, wordt meestal gebruik gemaakt van vereenvoudigde systemen met een beperkt aantal soorten lipiden en een simpel eiwit. Synthetische kleine eiwitten, ook wel peptiden genoemd, hebben als voordeel dat hun lengte en samenstelling op een systematische manier te variëren zijn. Het hier gebruikte WALP is zo een peptide. Het bestaat uit een α-helix dat model staat voor één transmembrane eenheid van een groter eiwit (zie Figuur 1.5). Aan de uiteinden van de helix bevinden zich groepen die bij voorkeur aan het grensvlak tussen de kop- en staartgroepen van de bilaag gaan zitten en zo, als het ware, het peptide verankeren.

Het interessante van WALP is dat het spontaan gebieden met een gestreept uiterlijk vormt als het ingebouwd wordt in bilagen van bepaalde (fosfo)lipiden (zie Figuur 1.6.a). De streepjes bestaan uit rijen van WALP die worden afgewisseld door rijen van lipiden. De afstand tussen de lijnen is ongeveer 8 nanometer (1 nm = 0,000000001 meter of een miljoenste millimeter). De gestreepte ordening is waarschijnlijk een algemeen effect waarvoor, naast directe WALP-lipide en WALP-WALP wisselwerkingskrachten, ook een grote rol is weggelegd voor indirecte effecten via de lipide bilaag.

In dit proefschrift zijn de eigenschappen van deze gestreepte domeinen en het verband met de eigenschappen van de bilaag nader onderzocht. Dit wordt op twee manieren gedaan: via Atomic Force Microscopie ('atoomkracht microscopie' of AFM) en via computer simulaties. Bij de eerste techniek wordt het oppervlak van de bilaag gescand met een heel dun naaldje dat het hoogteprofiel van het oppervlak van de bilaag volgt. Omdat de streepjes uit hogere lipiden en lagere peptiden bestaat, is dit te zien als de donkere en lichte strepen van Figuur 1.6.a. Het voordeel van deze techniek is dat het direct een plaatje geeft van de bilaag en dat de resolutie hoger is dan bij de meeste andere vormen van microscopie. Op kristallijne materialen zijn soms zelfs de afzonderlijke atomen zichtbaar te maken. AFM is gebruikt in hoofdstukken 2 tot en met 4.

In hoofdstuk 2 is onder meer de lengte van de staarten van de lipiden gevarieerd, wat niet veel invloed blijkt te hebben op de eigenschappen van de gestreepte gebieden. Het verwarmen van de bilaag (hoofdstuk 3) leidt tot het smelten van de vaste fase (ook wel gel fase genoemd) naar de vloeibare fase. De lipiden in de strepen smelten eerder dan de lipiden buiten de strepen. De lossere lipide pakking leidt er ook toe dat de gestreepte ordening verdwijnt. Een soortgelijk effect wordt in hoofdstuk 4 gevonden voor lipiden die door een onverzadigde binding een knik in hun staarten hebben waardoor ze ook niet dicht bij elkaar kunnen komen. Een andere opmerkelijke bevinding is dat de tilthoek van de staarten van de lipiden ten opzichte van de bilaag ook uitmaakt. Het blijkt dat lipiden die helemaal rechtop staan geen gestreepte domeinen vormen, maar lipiden die een hoek van ongeveer 30° maken wel.

Computer simulaties kunnen een goede aanvulling zijn op experimenteel werk omdat de moleculen afzonderlijk bekeken kunnen worden. Een model voor de water-, lipide- en peptide-moleculen wordt ingevoerd, samen met interacties die aangeven of de deeltjes elkaar aantrekken of afstoten. Er wordt berekend hoe de moleculen zich ordenen. In dit geval kunnen we niet alle atomen van het WALP en de lipiden weergeven omdat dit maanden tot jaren rekentijd zou kosten. Er is daarom gekozen voor een zogenaamde coarse-graining procedure, waarbij groepjes van atomen samengevoegd worden tot grotere bolletjes ('beads', zie figuur 5.1 en 5.2). De gebruikte simulatietechniek waar dit model is ingestopt, heet DPD (Dissipative Particle Dynamics). Het is bewezen dat deze techniek de beweging van deeltjes in water goed weergeeft en bovendien een goede beschrijving geeft van het lipide/water systeem. Wij hebben dit gebruikt om het effect van een rij WALP (zoals in het experimentele gestreepte systeem) op de lipide bilaag te onderzoeken. Het blijkt dat de lipiden naast WALP hun conformatie aanpassen: de eerste laag van lipiden heeft minder gestrekte staarten, waarna er een gebied is

waar de lipiden rechtop staan met gestrekte staarten. Nog verder weg van de rijen met WALP nemen de lipiden hun reguliere, niet-verstoorde toestand weer aan.
De simulaties laten goed zien waarom er verschil is tussen de getilte en rechtopstaande lipiden in het vormen van gestreepte domeinen. De invloed van het rechtopstaande WALP is geen probleem voor de rechtopstaande lipiden en de verstorende invloed van WALP is klein en strekt zich niet uit over grote afstanden. De andere lipiden moeten van een rechtopstaande toestand naast WALP terugkeren naar een getilte toestand, waarvoor een grote afstand nodig is. Dit geeft een grote verstoring.
Als verschillende rijen WALP elkaar naderen, overlappen de gebieden met verstoorde lipiden. Dit is gunstig omdat dan het totale aantal verstoorde lipiden vermindert. Dit mechanisme leidt waarschijnlijk tot de gestreepte ordening met een vaste afstand tussen de lijnen die gevonden was met AFM.

Bovenstaande resultaten geven meer inzicht in de processen die de verdeling en ook werking van eiwitten in biologische, levende membranen stuurt. De volgende stap zou zijn om te kijken of deze bevindingen ook op grotere, ‘echte’ eiwitten toepasbaar zijn.

Curriculum Vitae

De auteur van dit proefschrift is op 11 mei 1973 geboren in Delft. In 1991 behaalde zij het gymnasiumdiploma aan het Sint Stanislascollege in Delft, waarna zij in het zelfde jaar begon aan de studie Scheikunde aan de Universiteit Utrecht. Het doctoraaldiploma werd in 1996 behaald (met als specialisatie Fysische en Colloid Chemie). Na onderzoeksfuncties aan de Universiteit Utrecht (Gecondenseerde Materie bij profs. J.J. Kelly en D.A.M. Vanmaekelbergh, 1997 - 1999) en bij het Wageningen Centre for Food Sciences (standplaats Wageningen Agricultural Universitity bij prof. E. van der Linden, 1999 - 2002), werd in 2002 begonnen aan het in dit proefschrift beschreven onderzoek bij de toenmalige afdeling Fysische Chemie van Grensvlakken van het Debye Instituut aan de Universiteit Utrecht. Naderhand werd dit Condensed Matter and Interfaces. De auteur heeft posterbijdragen geleverd aan verschillende internationale congressen, zoals het internationale congres over Scanning Tunnelling Microscopy/Spectroscopy in Eindhoven (2003), het congres van de International Organization for Crystal Growth in Grenoble, Frankrijk (2004) en de European Biophysical Conference in London, Engeland (2007). Daarnaast is de auteur gedurende 2,5 jaar bestuurslid geweest bij de Debye AIO Comissie.

Publications

- F. Yarrow, T.J.H. Vlugt, J.P.J.M. van der Eerden, M.M.E. Snel, *Melting of a DPPC lipid bilayer observed with atomic force microscopy and computer simulatio*n, J. Cryst. Growth, **2005**, *275*, e1417 - e1421

Expected publications resulting from this thesis (to be submitted):

- Thermotropic behaviour of DPPC bilayers in the presence and absence of the model peptide WALP studied with AFM

- The effect of the lipid acyl chain tilt on the lateral assembly of phospholipids and the model peptide WALP

- DPD simulations of striated domains formed in gel-phase bilayers with the model peptide WALP

Dankwoord

Tenslotte wil ik op deze laatste pagina iedereen bedanken die op een of andere manier heeft bijgedragen aan dit proefschrift. Mijn promotor Jan, maar ook Ben en Antoinette voor de wetenschappelijke discussies. Thijs bedankt voor je input wat de simulaties betreft: van het idee om DPD te gebruiken en 'WALP-als-muur' tot het programmeren. Margot bedankt voor het overdragen van je kennis over de AFM. Ook alle overige mede-AIO's van Grensvlakken en Laura en Gerrit bedankt voor de gezelligheid en hulp. En na de samenvoeging van onze groepen, de collega's van Condensed Matter.

Daarnaast wil ik ook alle vrienden, kennissen, familie en de leden van het Huisorkest bedanken voor hun belangstelling. Ondanks dat jullie er misschien niet zo veel van begrepen, was er altijd wel iemand die vroeg hoe het ermee ging. Erg bemoedigend!!
Tenslotte wil ik mijn ouders nog even apart bedanken (David, bedankt voor je pogingen om er beter engels van te maken) en als laatste, maar niet de minste, Bonny. Bedankt voor alles: van het bestellen van pizza als ik weer eens 's avonds aan het meten was, je hulp met de literatuur-referenties en formule's, tot het beantwoorden van moeilijke vragen ('welk plaatje is mooier') en je bemoedigende woorden. Ik heb jouw steun altijd erg gewaardeerd.